

Engineering Critical Assessments of Subsea Pipelines under High-
pressure/High-temperature Service Conditions

Ankang Cheng

Submitted for the degree of Doctor of Philosophy (PhD)

June 2019

School of Engineering

Newcastle University

Abstract

Due to the world's continuously increasing energy demand and currently limited alternatives, the exploration and exploitation activities of offshore oil and gas are heading into deep waters. In this process, subsea production systems are faced with severe challenges from development environments such as high-pressure/high-temperature reservoirs. As the part of a subsea production system that occupies most extension in space, failures of subsea pipelines may result in enormous economic loss as well as catastrophic environmental disasters. Therefore, it is of significant importance to reasonably assess the structural integrity of subsea pipelines under high-pressure/high-temperature service conditions, especially for critical issues such as corrosion fatigue and low-cycle fatigue that are highly likely to occur.

Engineering critical assessment has been widely adopted in industries for structural integrity assessment. However, the cracking and fatigue processes in the cases of corrosion fatigue and low-cycle fatigue are complicated, involving both mechanical and environmental factors. Current industrial standards for engineering critical assessment only provide limited guidance in particular for corrosion fatigue. Low-cycle fatigue is even out of their scopes. So there exists controversy about the applicability and hence the results of the current industrial standards when conducting engineering critical assessments for subsea pipelines serving high-pressure/high-temperature reservoirs.

Based on these facts, the author in this research developed an engineering critical assessment approach in particular for corrosion fatigue and established a model for predicting the crack growth under low-cycle fatigue loads. Applications have been made. Comparisons with the experimental data showed that the proposed engineering critical assessment approach and fatigue crack growth model can reasonably assess the structural integrity of subsea pipelines under high-pressure/high-temperature service conditions.

Acknowledgement

The author would like first to give his sincere gratitude and appreciation to his supervisor, Prof. Nianzhong Chen. Prof. Chen's substantial industrial experience and exceptional academic background have benefited the author a lot. Without his continuous solid support and enlightening guidance, the author would not have achieved so much.

The author would also like to show his deep thanks to Dr. Yongchang Pu, for the good support and encouragement he received to accomplish this journey.

Many thanks to Dr. Ilinca Stanciulescu and Prof. Pol D. Spanos at Rice University as well as Dr. Wanhai Xu at Tianjin University in particular for the inspiration and help the author received from them in his master and bachelor programs.

The support from all the friends and colleagues that the author has met along the years he spent as a student across countries must also be appreciated. Special appreciation goes to Lourdes Lilley and Keith Lilley. The couple made the days when the author served as the student chair of the Society of Naval Architects and Marine Engineers at Newcastle University so memorable.

Further acknowledgement must be expressed to the faculty and staff in the School of Marine Science and Technology, which is now the part of the School of Engineering, at Newcastle University, for the kind financial support the author received for his PhD research.

Last but not least, the author dedicates this research in token of affection and gratitude to his parents, his sister, and his beloved lady, Ms. Lang. They have inspired and supported him so much all the time. They are the source of his courage to go through so many difficulties.

Abstract	i
Acknowledgement	ii
Table of Contents	iii
List of Figures	v
List of Tables	ix
List of Publications	x
Chapter 1. Introduction	1
1.1 Research Background	1
1.2 Research Objectives	3
1.3 Thesis Structure	4
Chapter 2. Literature Review	6
2.1 Subsea Pipelines Serving High-pressure/High-temperature Wells.....	6
2.1.1 Environmental Loads	8
2.1.2 Corrosion Mechanisms	11
2.2 Fatigue Analysis.....	15
2.2.1 Linear Elastic Fracture Mechanics.....	16
2.2.2 Elastoplastic Fracture Mechanics.....	19
2.3 Environmental-assisted Cracking	22
2.3.1 Stress Corrosion Cracking	23
2.3.2 Corrosion Fatigue.....	24
2.4 Engineering Critical Assessment	26
2.4.1 Failure Modes	27
2.4.2 Assessing Procedures	31
2.5 Summary	33
Chapter 3. Corrosion Fatigue Assessment	35
3.1 Hydrogen-enhanced Fatigue Crack Growth	35
3.1.1 Hydrogen Embrittlement Effect.....	36
3.1.2 Fatigue Crack Growth Modelling	37
3.1.3 Discussion	48
3.1.4 Model Applications.....	50
3.1.5 Summary	54
3.2 Corrosion Fatigue Crack Growth in Seawater	54
3.2.1 Corrosion Fatigue Mechanisms	55
3.2.2 Model Development.....	56
3.2.3 Model Applications.....	65
3.2.4 Summary	72

3.3 Extended Engineering Critical Assessment Approach.....	73
3.3.1 Traditional Approach.....	74
3.3.2 Extended Approach	76
3.3.3 Applications.....	81
3.3.4 Summary.....	92
Chapter 4. Fatigue Assessment.....	95
4.1 Crack Growth under High-cycle Fatigue Loads.....	95
4.1.1 Fracture Mechanics Based Model Development.....	97
4.1.2 Energy Principles Based Model Development.....	101
4.1.3 Model Application and Discussion.....	108
4.1.4 Summary.....	117
4.2 Crack Growth under Low-cycle Fatigue Loads	118
4.2.1 Model Development	119
4.2.2 Model Application and Discussion.....	132
4.2.3 Summary.....	139
Chapter 5. Conclusions.....	141
5.1 Contributions.....	142
5.2 Future Research.....	143
References	145

Lists of Figures

Figure 1.1 Research objectives of the PhD thesis	4
Figure 2.1 World’s primary energy consumption by fuel	6
Figure 2.2 A typical subsea production system	8
Figure 2.3 Lateral buckling of subsea pipeline under high-pressure/high-temperature service conditions.....	9
Figure 2.4 Vortex-induced vibrations of free spanned subsea pipeline	10
Figure 2.5 An S-N plot showing low-cycle fatigue and high-cycle fatigue regions	15
Figure 2.6 Stress state in the polar coordinate system.....	17
Figure 2.7 J -integral path around a crack tip	20
Figure 2.8 Mechanisms of corrosion fatigue crack growth	25
Figure 2.9 The typical structure of engineering critical assessment.....	27
Figure 2.10 Schematic diagram of a normal fatigue cracking process.....	29
Figure 2.11 Existing standard approach of engineering critical assessment for corrosion fatigue.....	32
Figure 3.1 Schematic diagram of a typical hydrogen-enhanced fatigue cracking	38
Figure 3.2 Schematic diagram of the corrosion-crack correlation model.....	39
Figure 3.3 (a) ΔK_{th} - R relationship; (b) Influence of K_{IC} on ΔK_{th} (given that ΔK_0 keeps constant).....	40
Figure 3.4 Schematic diagram of stress distribution in front of crack tip.....	42
Figure 3.5 (a) f_C definition; (b) r_{EAZ} - r_p relationship	44
Figure 3.6 Relationship between K_{tran} and f	46
Figure 3.7 Comparison between predicted K_{tran} and experimental data of X65 steel.....	49
Figure 3.8 Comparison between model prediction and experimental data of X42 (a) $R = 0.1$; (b) $R = 0.8$	51
Figure 3.9 Comparison between model prediction and experimental data of X65	52
Figure 3.10 Comparison between model prediction and experimental data of X70	53

Figure 3.11 Comparison between model prediction and experimental data of X80.....	53
Figure 3.12 Corrosion fatigue behaviour patterns: (a) Type A; (b) Type B; (c) Mixed type ...	55
Figure 3.13 Experimental corrosion fatigue data in comparison with model predictions of API 579-1/ASME FFS-1 and BS 7910: (a) Simple linear model; (b) Bilinear model	56
Figure 3.14 Anodic dissolution influence on the shape of crack growth curve: (a) X65; (b) X70.....	60
Figure 3.15 Pipeline steel specimens in seawater with and without cathodic protection: (a) X65; (b) X70.....	60
Figure 3.16 Model of crack growth for the hydrogen embrittlement part of corrosion fatigue: (a) Corrosion-crack correlation; (b) Two-stage Forman equation model	63
Figure 3.17 Model application to X65 pipeline steels with R=0.5: (a) crack growth; (b) crack evolution.....	66
Figure 3.18. Loading frequency effect on K_t	68
Figure 3.19 Stress ratio effect on model performance: (a) crack growth with $R = 0.1$; (b) crack growth with $R = 0.8$; (c) crack evolution with $R = 0.1$; (d) crack evolution with $R = 0.8$; (e) remaining fatigue life with $R = 0.1$; (f) remaining fatigue life with $R = 0.8$	70
Figure 3.20 Environmental temperature effect on K_t	72
Figure 3.21 Comparison between model prediction and experimental data.....	76
Figure 3.22 Corrosion fatigue crack evolution	78
Figure 3.23 Prediction of transition stress intensity factors for X65 under corrosion fatigue with various load frequencies.....	83
Figure 3.25 Crack growth curves of X65 under corrosion fatigue with various load frequencies.....	84
Figure 3.25. Geometry and the geometry function of the single-edge notched specimen	85
Figure 3.26 Corrosion fatigue crack curves for X65 steels with initial crack size $a_i = 1$ mm: (a) Crack growth; (b) Crack evolution.....	87
Figure 3.27 Corrosion fatigue crack curves for X65 steels with initial crack size $a_i = 4$ mm: (a) Crack growth; (b) Crack evolution.....	87

Figure 3.28 Corrosion fatigue crack curves for X65 steels with initial crack size $a_i = 12$ mm: (a) Crack growth; (b) Crack evolution.....	87
Figure 3.29 Load frequency effect on corrosion fatigue life prediction for X65 steels under various initial crack sizes.....	88
Figure 3.30 Prediction by standard models for corrosion fatigue life of X65 steels with various initial crack sizes.....	89
Figure 3.31 Comparison of life prediction for X65 under various load frequencies.....	91
Figure 3.32 Proposed approach of engineering critical assessment for corrosion fatigue.....	94
Figure 4.1 Fatigue crack growth with $R = -1$	96
Figure 4.2 (a) Mechanism of crack growth under constant amplitude cyclic load; (b) Stress- strain relationship under constant amplitude cyclic load	97
Figure 4.3 Crack-tip stress distribution at the peak stress of a load cycle	100
Figure 4.4 The strain energy density required for material elements to fracture	104
Figure 4.5 Main routine implementing the proposed model for predicting fatigue crack growth	109
Figure 4.6 Subroutine for calculating the initiation crack size of fatigue crack growth	109
Figure 4.7 Comparison between model prediction and test data for A533-B1 Steel	111
Figure 4.8 Comparison between model prediction and test data for AISI 4340 Steel	112
Figure 4.9 Comparison between model prediction and test data for AISI 4140 Steel	112
Figure 4.10 Comparison between model prediction and test data for 25CrMo4 Steel	113
Figure 4.11 Comparison between model prediction and test data for 2024-T351 Al	113
Figure 4.12 Comparison between model prediction and test data for 7075-T6 Al.....	114
Figure 4.13 Comparison between model prediction and test data for 7175 Al.....	114
Figure 4.14 Comparison between model prediction and test data for Ti6Al4V Alloy	115
Figure 4.15 Model application to consider the R effect for AISI 4340 Steel: (a) R effect on fatigue crack growth rates; (b) model application.....	116

Figure 4.16 Model application to consider the R effect for 7075-T6 Al: (a) R effect on fatigue crack growth rates; (b) model application.	117
Figure 4.17 (a) Stress-strain curves under monotonic and cyclic loads; (b) stress-strain response under a specified cyclic strain load	120
Figure 4.18 Mechanism of crack growth under low-cycle fatigue conditions	123
Figure 4.19 Graphical interpretation of Neuber's rule, equivalent strain energy density (ESED) rule, and modified ESED rule	125
Figure 4.20 Strain energy density required for material elements to fracture	128
Figure 4.21 Variation of energy ratios with stress amplitude ratio	130
Figure 4.22 Flow diagram of the proposed model	131
Figure 4.23 Comparison between the test data and the model prediction for A533-B1 Steel without modification	133
Figure 4.24 Comparison between the test data and the model prediction for A533-B1 Steel with modification	134
Figure 4.25 Comparison of crack evolution data generated by tests and model for A533-B1 Steel	135
Figure 4.26 Comparison between the test data and the model prediction for AISI 4340 Steel (a) without modification; (b) with modification	137
Figure 4.27 Comparison between the test data and the model prediction for 2024-T3 Al (a) without modification; (b) with modification	137
Figure 4.28 Comparison between the test data and the model prediction for 7075-T6 (a) without modification; (b) with modification	138
Figure 4.29 Comparison between the test data and the model prediction for Ti6Al4V Alloy (a) without modification; (b) with modification	139
Figure 5.1 Whole structure of the PhD research.....	141

Lists of Tables

Table 3.1 Experimental data for API grade pipeline carbon steels	45
Table 3.2 Model predictions for API grade pipeline carbon steels	45
Table 3.3 Model parameters from experimental data	45
Table 3.4 Model calculation results for X65 pipeline steel.....	60
Table 3.5 Model calculation results for X42 pipeline steels at different stress ratios	64
Table 3.6 Material properties of API X65 steel.....	74
Table 3.7 Predicted transition stress intensity factors for X65 pipeline carbon steels under corrosion fatigue	74
Table 3.8 Parameters of corrosion fatigue crack growth curves regressed from test data.....	76
Table 3.9 Parameters of crack growth curves with $R < 0.5$ from BS 7910	77
Table 3.10 Prediction of BS 7910 simplified and bilinear models and experimental results...	78
Table 4.1 Material input parameters for model application	100
Table 4.2 Fatigue crack growth test information.....	100
Table 4.3 Input parameters of some materials for model application.....	122
Table 4.4 Test information of fatigue crack growth rate for applied materials	122

List of Publications

Journal Papers

Cheng, A., Chen, N.Z. and Pu, Y., 2019. An energy principles based model for fatigue crack growth prediction. *International Journal of Fatigue*, 128, p.105198.

Cheng, A. and Chen, N.Z., 2018. An extended engineering critical assessment for corrosion fatigue of subsea pipeline steels. *Engineering Failure Analysis*, 84, pp.262-275.

Cheng, A. and Chen, N.Z., 2017. Corrosion fatigue crack growth modelling for subsea pipeline steels. *Ocean Engineering*, 142, pp.10-19.

Cheng, A. and Chen, N.Z., 2017. Fatigue crack growth modelling for pipeline carbon steels under gaseous hydrogen conditions. *International Journal of Fatigue*, 96, pp.152-161.

Under review

Cheng, A., Chen, N.Z., Pu, Y., and Yu, J.. Fatigue crack growth prediction for small-scale yielding (SSY) and non-SSY conditions.

Cheng, A., Chen, N.Z., and Pu, Y.. Engineering critical assessment for subsea pipelines under high-pressure/high-temperature (HP/HT) service conditions.

Conference Papers

Cheng, A. and Chen, N.Z., 2018, June. A benchmark study on applying extended finite element method to the structural integrity assessment of subsea pipelines at HPHT service conditions. In *ASME 2018 37th International Conference on Ocean, Offshore and Arctic Engineering* (pp. V11BT12A037). American Society of Mechanical Engineers.

Cheng, A. and Chen, N.Z., 2017, June. Corrosion fatigue mechanisms and fracture mechanics based modelling for subsea pipeline steels. In *ASME 2017 36th International Conference on Ocean, Offshore and Arctic Engineering* (pp. V004T03A002). American Society of Mechanical Engineers.

Cheng, A. and Chen, N.Z., 2017. A modified method assessing the integrity of carbon steel structures subjected to corrosion fatigue. In Soares, C.G. (Ed.), *Progress in the Analysis and Design of Marine Structures: Proceedings of the 6th International Conference on Marine Structures (MARSTRUCT 2017)*, pp. 659-666. CRC Press.

Note

Some of the chapters (i.e. Chapter 3 and Chapter 4) in this thesis actually consist of the research works either published or under review where the author's name appears as the first author, meaning that the author has contributed the main idea and taken the most research and text work. The author has received the permission from other authors to use them in this thesis and would like to acknowledge the courtesy of the publishers. Those works have been well listed with their details in the List of Publications as well as in the Reference.

Chapter 1. INTRODUCTION

Since renewable energy is blooming worldwide and the oil price is still under some pressure, some people may question the necessity of continuous research focusing on offshore oil and gas. However, the current consensus of energy industry is that the world's main energy source is and will continue to be oil and gas in the near future, at least in the several decades to come (BP, 2019). Compared with other sources such as shale oil and gas, offshore oil and gas have their advantages and therefore are expected to continue to play important roles in the global energy supply.

1.1 Research Background

Pipelines have been employed as one of the most practical and low-price methods for large offshore oil and gas transport since 1950s. The installations of subsea pipelines have witnessed drastic increase in the past several decades. The accompanying structural failures and the associated potentially tremendous economic loss as well as disastrous effect on ocean environment are drawing more and more public attention. Many investigations have pointed to initially small flaws on the structures for initiating structural failures. But as metallic welded structures, subsea pipelines cannot avoid flaws either as a consequence of manufacturing process (i.e. deep machining marks or voids in welds) and metallurgical discontinuities (i.e. inclusions), or simply due to service loads and environments. Structural integrity is often used to describe the quality of a component/structure being whole and complete or the state of being unimpaired from undertaking its designed function. The presence of flaws can severely damage the structural integrity of a component/structure and further impose a huge risk of structural failure. Therefore, assessing the structural integrity in presence of flaws is very important from the perspective of ensuring the safety of engineering structures during operation.

Pioneer researchers proposed the concept of engineering critical assessment for evaluating the structural integrity of safety-critical structures (Kumar et al., 1981). Engineering critical assessment is a fit-for-service procedure that uses fracture mechanics principles to determine the defect tolerance of safety critical items. It enables engineers to make informed and confident decisions on the most appropriate remedial measures to take. There has been an increasing popularity of engineering critical assessment since it was proposed in the late 1970s to early 1980s. Nowadays engineering critical assessments are routinely performed in evaluating the integrity of structures such as pipelines and pressure vessels, platforms, rigs

and wind turbines. Several standards specific to engineering critical assessments for oil and gas pipelines have been developed so far. The most commonly used of these are API 1104 Appendix A (2013), BS 7910 (2015), CSA Z662 Annex K (2015) and API 579-1/ASME FFS-1 (2016). In supplement, ABS and DNVGL provide their own guidance specifically for subsea pipelines, e.g. ABS's Guide for Building and Classing Subsea Pipeline Systems (2018) and DNVGL-RP-F108 (2017). By integrating engineering critical assessment with other techniques such as non-destructive test, structured programs can be established for structural integrity management of subsea pipelines (DNVGL-ST-F101, 2017). Satisfactory results are often obtained. However, as the continuously increasing global energy demand drives the exploration and exploitation activities of offshore oil and gas into ever deeper waters, more and more high-pressure/high-temperature reservoirs are being encountered by the industry. A variety of new challenges to subsea pipelines due to the harsh environments, both internally and externally, have been introduced by the high-pressure/high-temperature service conditions. Foremost among them are corrosion fatigue and low-cycle fatigue (Pargeter and Baxter, 2009; Bai and Bai, 2014). Both corrosion fatigue and low-cycle fatigue may result in fast fracture or premature failure of the structures. However, current industrial standards provide only limited guidance on engineering critical assessments for corrosion fatigue. Specifically, unified behaviour model for subcritical fatigue crack growth is suggested although the corrosion fatigue crack growth behaviour may differ as the combination of environmental and mechanical factors changes, which often leads to either over conservatism or under estimation in assessment results (Cheng and Chen, 2018a). Subcritical crack growth of low-cycle fatigue is even out of the scope of the current industrial standards (BS 7910, 2015; API 579-1, 2016). So there exists controversy surrounding the applicability and hence the results of the current industrial standards when conducting engineering critical assessment for subsea pipelines serving high-pressure/high-temperature wells.

Individually, corrosion fatigue and low-cycle fatigue have been long researched by many researchers. But there is a lack of research performed in particular for subsea pipelines under high-pressure/high-temperature service conditions and in the aspect of engineering critical assessment. While the industry has noticed for some time that the high-pressure/high-temperature service conditions are highly likely to cause corrosion fatigue and low-cycle fatigue issues for subsea pipelines and therefore improvement of current industrial standards is necessary (Buitrago et al., 2008; Holtam, 2010; Kumar et al., 2014). Through the years limited progress has been achieved by the research carried out (Chong et al., 2016; Holtam et al., 2018). In other words, standardized guidance to conducting engineering critical

assessments with specific consideration of corrosion fatigue and low-cycle fatigue for subsea pipelines that operate under high-pressure/high-temperature conditions is currently not readily available. Related research is still in necessity.

1.2 Research Objectives

Rooted in the real industry needs mentioned above, the research focus of this PhD thesis will be engineering critical assessments of subsea pipelines under high-pressure/high-temperature service conditions accounting for corrosion fatigue and low-cycle fatigue. The main research objectives are briefly outlined as follows:

- 1) Specifying the critical issues faced by subsea pipelines under high-pressure/high-temperature service conditions and the associated mechanisms,
- 2) Developing a reasonable approach of engineering critical assessment in particular for corrosion fatigue,
- 3) Establishing a prediction model of fatigue crack growth applicable for low-cycle fatigue.

The author's most research effort will be put on the last two main objectives. Each of them can be divided into several sub-objectives and research concentrating on each sub-objective will be carried out in a sequence as the following:

In developing a reasonable approach of engineering critical assessment in particular for corrosion fatigue, consistent research work will be performed in 3 levels,

- 1) in level 1, the research work will focus on modelling the fatigue crack growth behaviour under the impact of hydrogen embrittlement only,
- 2) then a corrosion fatigue crack growth model based on the damage mechanisms will be constructed in level 2,
- 3) based on those foundations, the approach existing in current industrial standards for engineering critical assessment will be extended with particular consideration on corrosion fatigue;

In establishing a prediction model of fatigue crack growth applicable for low-cycle fatigue,

- 1) the author will start from building up an energy principles based model using the stress intensity factor range, ΔK to predict the fatigue crack growth of metallic materials subjected to high-cycle fatigue,

2) afterwards, the model for predicting fatigue crack growth in low-cycle fatigue will be established following a similar idea but using the cyclic J -integral, ΔJ to ensure the model's applicability to fatigue crack growth under both small-scale yielding and non-small-scale yielding conditions.

Figure 1.1 shows an overview of all the research objectives of this PhD thesis. Note that the purpose of this research is not to demonstrate the detailed process of performing engineering critical assessment for subsea pipelines under high-pressure/high-temperature service conditions, but rather to spotlight on some critical issues faced by the industry and to bridge the gaps between the current industrial standards and the engineering reality, which may also provide useful reference for engineering critical assessments or fatigue analysis of welded metallic structures in a broader sense.

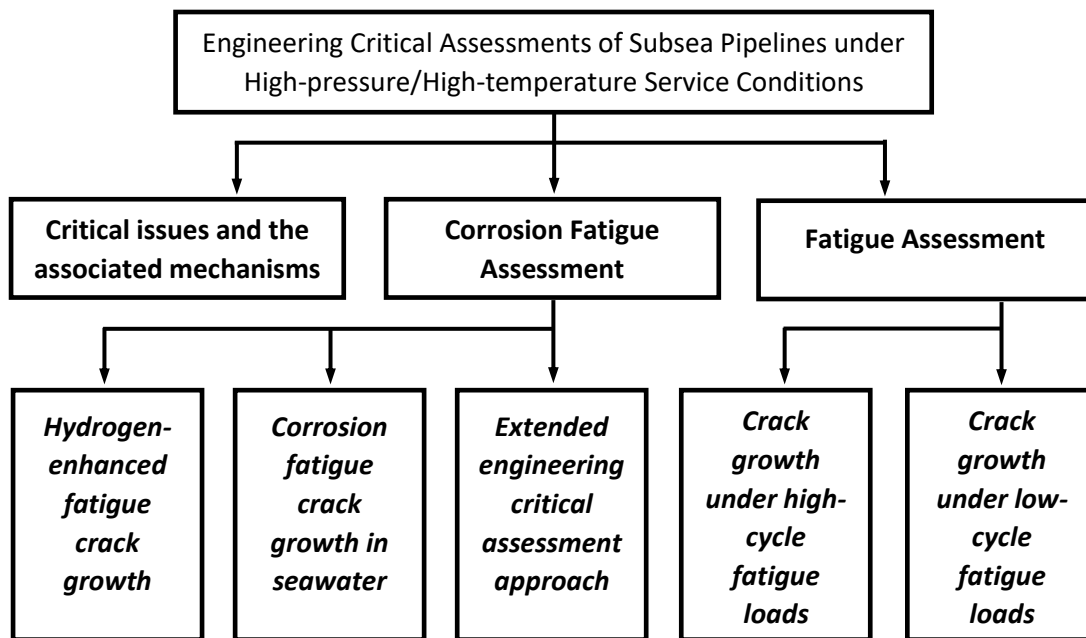


Figure 1.1 Research objectives of the PhD thesis

1.3 Thesis Structure

In accordance to the research objectives mentioned in Section 1.2, the thesis is organized into 5 chapters. Chapter 1 briefly introduces the background, objectives and the structure of the research. Chapter 2 is the literature review, where the detailed challenges faced by subsea pipelines under high-pressure/high-temperature service conditions are investigated and analysed, the current research status of associated issues such as corrosion fatigue and low-cycle fatigue are reviewed, and the state-of-the-art technologies for engineering critical assessment is introduced. In Chapter 3, an approach of engineering critical assessment in

particular for corrosion fatigue is developed consistently in 3 different levels, centring on hydrogen embrittlement, corrosion fatigue and assessment approach, respectively. While in Chapter 4, issues of fatigue crack growth under both small-scale yielding and non-small-scale yielding conditions are focused and prediction models are proposed for both high-cycle fatigue and low-cycle fatigue. Finally, Chapter 5 draws conclusions from the research work in previous chapters and points out potential future research directions under the topic of engineering critical assessments for subsea pipelines under high-pressure/high-temperature service conditions.

It should be noted that Chapter 3 and Chapter 4 are actually consisting of the research works either published or under review by the author as first author (Cheng and Chen, 2017a; Cheng and Chen, 2017b; Cheng and Chen, 2018a; Cheng et al., 2019). Hence each subchapter is fully structured and may be viewed as an individual research task, but meanwhile is well related to others and consistent in the view of this PhD thesis as whole.

Chapter 2. LITERATURE REVIEW

According to BP's 2019 Energy Outlook (2019), in the future several decades, the transition of current energy system to a lower-carbon one will be apparent. But oil and gas will keep being the world's main energy source, still totally accounting for over half of the world's primary energy consumption in the year 2040 as seen in figure 2.1. Since the world's total energy demand is expected to increase continuously, the absolute amount of energy consumption covered by oil and gas will increase remarkably as well. However, the conventional oil and gas reservoirs are dwindling. While shale oil and gas are booming for their low cost in recent years, offshore oil and gas still play important roles in the today's global energy supply and have tremendous potential of growth. This may be attributed to two basic facts. One is that the cost of offshore oil and gas production is being significantly reduced through integrating new technologies and management strategies since the steep drop of oil price in 2014. The other is that although offshore oil and gas production requires a lot of upfront investment, once operational it can keep a steady production stream for years and decades to come, overwhelming shale production in the view of business.

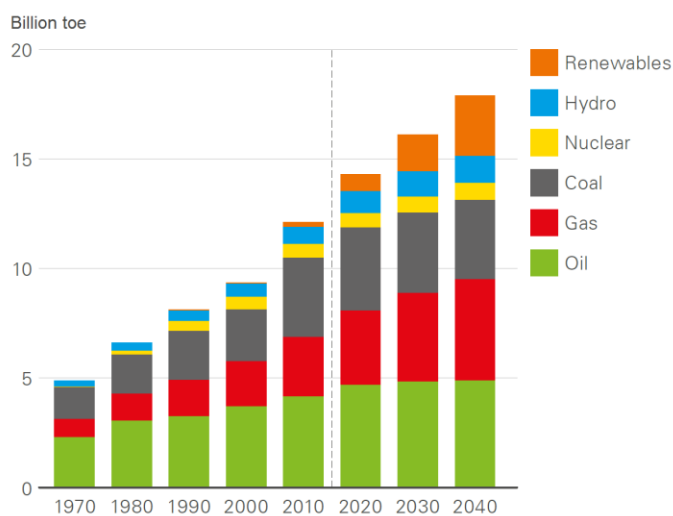


Figure 2.1 World's primary energy consumption by fuel (BP, 2019)

2.1 Subsea Pipelines Serving High-pressure/High-temperature Wells

Offshore developments of oil and gas reservoirs are one of the most challenging engineering tasks in the world. The Deepwater Horizon incident in 20 April 2010 is a prudent evidence as well as a reminder to the whole world about the safety aspect and moreover the consequences of structural failures in exploring and exploiting offshore oil and gas sources. Unfortunately, as the world's continuously increasing energy demand drives those activities to move into

deeper waters, the industry is being encountered with more and more high-pressure/high-temperature offshore oil and gas reservoirs, which brings about even more serious challenges to the structural safety.

According to API 17TR8 (2015), high-pressure/high-temperature environments are intended to be one or a combination of the following well conditions:

- 1) The completion of the well requires completion equipment or well control equipment assigned a pressure rating greater than 103 MPa or a temperature rating greater than 177°C;
- 2) The maximum anticipated surface pressure or shut-in tubing pressure is greater than 103 MPa on the seafloor for a well with a subsea wellhead or tied back to the surface and terminated with surface operated equipment; or
- 3) The flowing temperature is greater than 177°C on the seafloor for a well with a subsea wellhead or tied back to the surface and terminated with surface operated equipment.

In the later 1970s to early 1980s the Mongure Prospect and Mobile Bay projects pioneered initially dealt with 158.6 MPa and 232°C high sour gas conditions (Skeels, 2014). These projects pushed way beyond the known boundaries of conventional offshore oil and gas reservoirs. Stringently controlled high-strength alloy steels were used for casing and liner pipes to withstand the excessive mechanical loads and well pressures while being de-rated for extreme wellbore temperatures. What's worse, high H₂S and/or CO₂ concentration were found to be accompanied with production fluid of the wells, which was later proven to be mostly true for worldwide offshore high-pressure/high-temperature reservoirs. New corrosion resistant alloys such as Hastelloy C were then employed to withstand the excessive H₂S conditions associated with flow testing and producing of these wells. Since these projects, the technical interest on high-pressure/high-temperature decayed as such wells quickly became uneconomic during the economic bust of 1980s and 90s. Most of the industry's interest went back out the high-pressure/high-temperature range until the late 1990s when economic and geological conditions renewed the prospects of high-pressure/high-temperature reservoirs.

In the last decades, the oil and gas industry has come to accept the subsea production system as the technology of choice for developing deep and ultra-deep water findings. A subsea production system is comprised of a wellhead and valve tree ('x-max tree') equipment, pipelines, and structures and a piping system, and in many instances, a number of wellheads have to be controlled from a single location (Wang et al., 2012). As safety critical structures primarily used to transport oil and gas, subsea pipelines occupy the most extension through

space in a subsea production system, and are most probably trapped in harsh environmental or geological conditions. Their construction often needs giant investment and hence are often required to have a long designed service life, e.g. 20 years, for the economic reason. But subsea pipelines serving high-pressure/high-temperature oil and gas reservoirs have to face serious challenges from both the internal and external environments since the date of their commissioning, which may greatly affect the real service life. Therefore, it is of significant importance to assess the structural integrity with the challenges from high-pressure/high-temperature service conditions reasonably considered. To achieve this goal, first it is necessary to understand the impact from high-pressure/high-temperature service conditions on the structural integrity of subsea pipelines. The impact is complicated and multi-aspect. Detailed analyses will be conducted in this section.

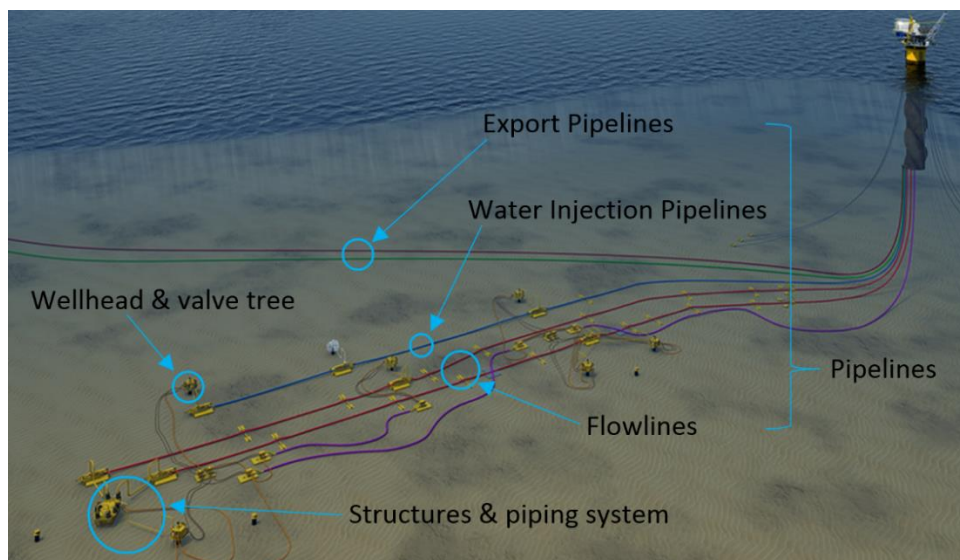


Figure 2.2 A typical subsea production system (Gavem et al., 2015, modified)

2.1.1 Environmental Loads

In the aspect of mechanics, the loads resulting from both the internal and external environments of subsea pipelines serving high-pressure/high-temperature reservoirs can be classified into the following (ABS, 2014):

- 1) Internal and external pressure
- 2) Ambient and elevated operating temperatures
- 3) Static and dynamic mechanical loads
- 4) Pressure/temperature induced loadings

More specifically, huge external hydrostatic pressure will be imposed on the pipe structure in the deep-water environment, additional static loads by thermal and pressure expansion and

contraction should also be noticed. What's more, the operations such as shut-down and start-up of subsea pipelines can induce longitudinal thermal and pressure expansions and contractions under high-pressure/high-temperature service conditions, and further cause resistance force of friction between pipelines and the seabed soil. Therefore some pipeline sections may experience large tensile and compressive loads at certain locations periodically during the service life. When the compressive load is sufficiently high, i.e. exceeding the critical buckling capacity, the pipeline section will go through global buckling. Depending on the load and constraint conditions, either upheaval or lateral buckling may happen. For subsea pipelines buried or rock dumped in trench, while lateral buckling is not likely to happen, upheaval buckling with even higher loads can occur (Carr et al., 2003). For those exposed on the seabed, the global buckling is generally in lateral direction. If the sectional pipeline is free spanned, downward buckling is also possible. In this study, the lateral buckling of subsea pipelines is focused since it's the main buckling type that may cause low-cycle fatigue, as shown in figure 2.3.

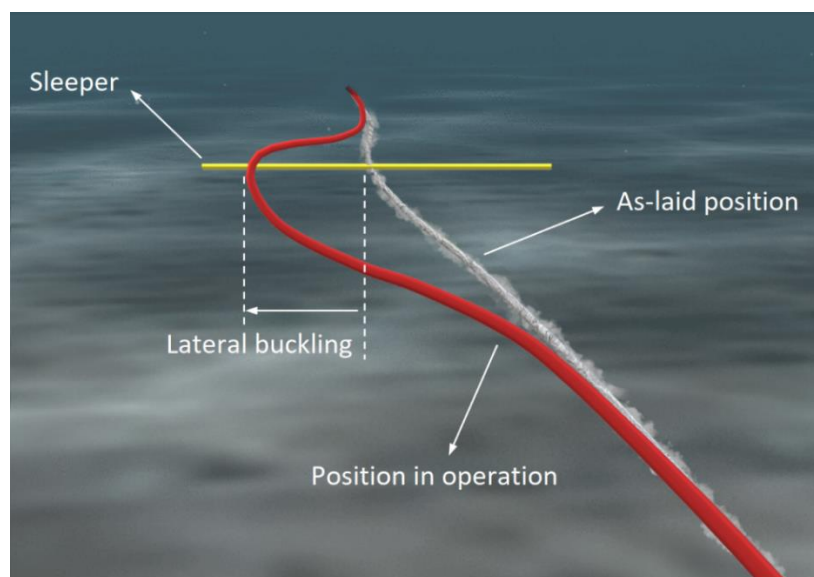


Figure 2.3 Lateral buckling of subsea pipeline under high-pressure/high-temperature service conditions

While as a load response, global buckling may impose some impact on the flow assurance of subsea pipelines, it is not a failure mode in itself. In fact global buckling can effectively relieve the compressive loads locally, but the accompanying excessive plastic strain due to the bending moment in the area around the buckle apex may exceed the yield limit, inducing serious plastic deformation, i.e. local buckling or plastic collapse, or fracture and hence pipeline failure. Records of subsea pipeline failures induced by buckling are many. For example, in January 2000, a 17km 16-Inch pipeline in Guanabara Bay, Brazil, suddenly buckled 4m laterally and ruptured, leading to a damaging release of about 10,000 barrels of

oil and a great loss to the operator (Bai and Bai, 2014). To avoid such failures, the design concept called planned buckle is introduced by the industry. In such a design, buckles in some sections of the pipeline are allowed to eliminate the possibility of rogue buckles where the bending moment and strains could exceed the allowable limits. Planned buckle is realized by setting buckle initiators, such as sleepers and buoyancy sections at a planned interval where the maximum strain in the possible buckle should be within the limit. Through proper design, potential strength problems of pipe structures could be effectively controlled (Sun et al., 2012). However, cyclic buckling/bending may still induce strains that are large even close to the material's yield strength, especially when in areas where stress concentrations exist. High-strain cycles can bring about low-cycle fatigue, severely threatening the structural integrity of subsea pipelines (Bai and Bai, 2005). In this regard, the fatigue resistance of subsea pipelines should be seriously considered.

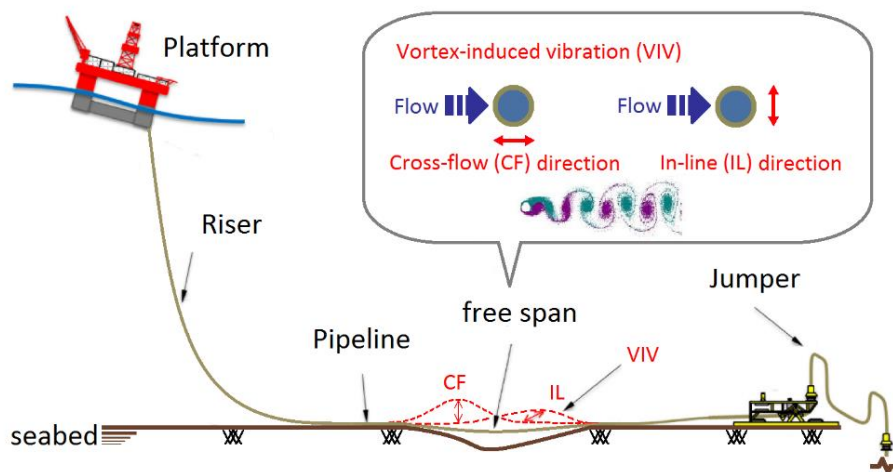


Figure 2.4 Vortex-induced vibrations of free spanned subsea pipeline

On the other hand, wave, current and other met-ocean events may also be the sources of fatigue loads for pipeline sections under the circumstances of free spanning. When flows cross the free spans, potential formation and shedding of vortices can induce changes of flow pressures on different sides of the pipe structure. In response, the free spanned pipeline section may vibrate in changing directions, called vortex-induced vibration, generating in cyclic strain/stress loads, as shown in figure 2.4. Resultantly, fatigue damage will be accumulated in the pipe structure or the girth welds depending on the situations. There have been some cases of pipeline failures due to vortex-induced vibrations of free spans. For example, 14 failures of subsea pipelines in the Cook inlet in South Alaska were reported to be caused by vortex-induced vibration between 1965 and 1976, and two local failures of Ping Hu pipeline in the East China sea during the autumn of 2000 were found to be associated with

vortex-induced vibrations of free spanned pipeline sections (Knut et al., 2013). Note that free spans may be more prone to appear for subsea pipelines under high-pressure/high-temperature service conditions (Drago et al., 2015).

Additional fatigue loads on subsea pipelines may be induced by intervention vessels as well as flow assurance problems (API 17TR8, 2015). Particularly, subsea pipelines serving high-pressure/high-temperature oil and gas wells tend to have problems such as wax, hydrate and asphalt etc.. These problems not only severely undermine the pipelines' ability of producing hydrocarbons efficiently (flow assurance), but also induce considerable internal pressure fluctuations that may affect their service lives. Therefore in recent years, flow assurance problems are receiving remarkable attention from both engineers and researchers (Mokhatab et al., 2007; Kang et al., 2014; Bomba et al., 2018). Flow assurance is a newly emerged research area that involves multiple disciplines. Substantial research work in the area is undergoing worldwide and many questions remain to be answered. Technical difficulty still exists in modelling and controlling of pipelines' internal multi-phase flow. For this reason, no detailed discussion about flow assurance and the associated internal fluctuations is carried out here. For any further interests, please refer to the work by Reda et al. (2011) and Makogon (2019).

It can be concluded from the above discussion that fatigue loads are inevitable during the service lives of subsea pipelines. For subsea pipelines serving high-pressure/high-temperature oil and gas wells, fatigue is an issue that must be carefully considered.

2.1.2 Corrosion Mechanisms

In the aspect of corrosion, subsea pipelines under high-pressure/high-temperature service conditions are highly likely to be exposed to aggressive environments both internally and externally. Subsea pipelines are usually constructed by API grade carbon steels and steel alloys for base and weld materials respectively, while the production fluid of high-pressure/high-temperature reservoirs is often found to contain chemicals such as CO₂ and/or H₂S that are highly corrosive to those materials. To protect the metal structure from corrosion, tape or coating are essential for subsea pipelines. However, either the tenting of tape or coating at the long-seam welds or under tape wrinkles on the pipeline outside may still create space for seawater contacting the bare metal. The potential contact of bare metal or girth welds with CO₂ and/or H₂S from the production fluid as well as with water/seawater will not only cause corrosion. The corrosive chemicals in the cavities of pre-existing flaws such as as-built pipeline defects including grooves and weld defects, dents caused by third-party

interference, and corrosion pits may also severely degrade the local material's mechanical properties, such as fracture resistance, and further initiating the environment-assisted cracking under previously mentioned complicated environmental loads.

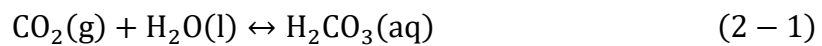
2.1.2.1 Sweet Corrosion – CO₂

CO₂ in the presence of water forms the corrosive carbonic acid, causing the most common form of sweet corrosion, i.e. uniform weight loss in carbon pipeline steels. A variety of models can be used to predict such corrosion. Factors including partial pressure of CO₂, temperature, water content, flow rate, and pH of water phase can significantly affect the corrosion rate. On the other hand, a protective scale layer may form on the metal surface depending on the temperature and pH, reducing the corrosion rate. However, if turbulent flow presents and breaks down locally the protective scale, localized corrosion may occur. The presence of oxygen or organic acids may also reduce the protectiveness of the scale.

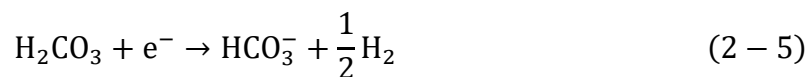
Localized corrosion may also occur in gas fields where the temperature along the pipeline falls below the dew point and gas condensate containing CO₂ begins to form along the pipe internal walls. "Top of the line" corrosion in gas field pipelines is an example of this corrosion mechanism. Sweet corrosion can be mitigated by the use of a qualified corrosion inhibitor for carbon pipeline steel (Iannuzzi, 2011).

The electrochemical reaction for CO₂ corrosion is shown below (Ossai, 2015):

- Absorption:



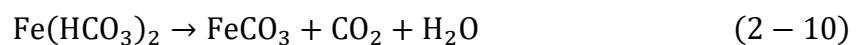
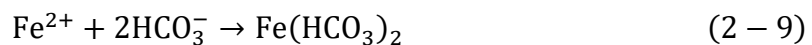
- Cathodic reaction:



- Anodic reaction:

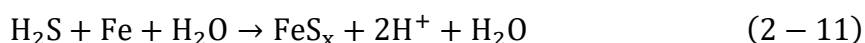


- Oxide film formation:



2.1.2.2 Sour Corrosion – H₂S

While there is a standardized definition of sour service based on the partial pressure of H₂S in production flow, it is suggested that all high-pressure/high-temperature wells should be treated as sour service and given consideration of possibly increasing H₂S content over the life of the well (Kumar et al., 2014). H₂S corrosion is highly likely to be in the form of pitting corrosion. Elemental sulphur have been reported by some researchers as being responsible for the localized corrosion appearance, however, Song et al. (2012) suggested that other substances such as SO₄²⁻, SO₃²⁻, S₂O₃²⁻ and H⁺ may also have non-negligible contribution. The general equation of H₂S corrosion is shown below:

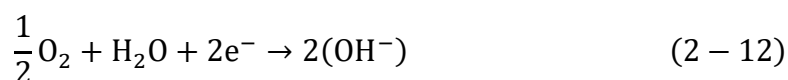


Note that the iron sulphide (FeS_x) generated may act as a protective scale preventing the chemicals (H₂S) from contacting the bare metal for further corrosion. However, just as in the case of CO₂ corrosion, erosion and turbulence in pipelines may mechanically remove it, or chemical reactions necessitated by microorganisms or operating condition of the flowing oil and/or gas may dissolve it, giving room for more corrosion (API 17TR8, 2015).

2.1.2.3 Chloride Corrosion

Chlorides can induce both general and localized corrosion in carbon pipeline steels by lowering the environmental pH. This may be addressed with coatings or the use of CRAs. However, some CRAs are prone to localized corrosion in the form of pitting or crevice in chloride containing environments. Temperature is also an important factor that may affect corrosion in chloride containing environments. Hence CRAs are selected based upon their critical pitting temperature and critical crevice temperature below which pitting and crevice corrosion does not occur. For chloride corrosion, the equations representing the general electrochemical reaction are shown below:

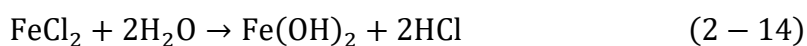
- Cathodic reaction



- Anodic reaction



- Local acidity increased



According to Ma (2012), pH of the electrolyte inside a pit by chloride corrosion can decrease from 6 to as low as 2~3, accelerating the local corrosion. Large ratio between the anode and cathode areas may accelerate the corrosion as well. Corrosion product such as $\text{Fe}(\text{OH})_3$ may protect the metal from further corrosion for some time, but finally be damaged following similar mechanisms in the cases of CO_2 corrosion and H_2S corrosion. It is worth noting that chloride corrosion consumes oxygen, as indicated by (2-12). However, there is a lack of oxygen in deep-water environment. While oxygen can be introduced inside the pipeline by injection of surficial seawater for secondary recovery, a continuous supply of oxygen is not practical. Thus for subsea pipelines, the chloride corrosion, even if occurred, can be limited and self-confined, regardless of position (i.e. inside or outside the pipeline) (Iannuzzi, 2011).

2.1.2.4 Hydrogen Embrittlement in Seawater with Cathodic Protection

Cathodic protection of metallic materials submerged in seawater may result in formation of hydrogen protons through direct seawater dissociation. The generated hydrogen protons may then diffuse into the metal and cause hydrogen embrittlement. Depending upon the specific conditions (i.e. extent of the cracking, toughness of the material, etc.), hydrogen embrittlement can lead to rapid fracture at stresses well below the yield strength. Strictly speaking, cathodic protection induced hydrogen embrittlement doesn't involve the process of "corrosion" (if it means some metal dissolution exists at least). Some researchers tend to classify it into environment-assisted cracking (Gangloff, 1990). However, it is introduced here following the ideology of API 17TR8 (2015) and will not be re-introduced when discussing environment-assisted cracking.

Methods to prevent hydrogen embrittlement include barrier coatings and material selection with hardness below a threshold value. No industry standard currently exists for more detailed ranking of alloy susceptibility to hydrogen embrittlement. But usually it is thought lower strength alloys and those containing low inclusion and precipitate are less prone to hydrogen embrittlement. Nickel-based alloys are generally superior to steels in resistance to hydrogen embrittlement.

Sometimes microbiological-induced corrosion is also mentioned for oil and gas pipelines. However, it may not be a likely source of corrosion damage for subsea pipelines under high-pressure/high-temperature service conditions since its required temperature is relatively mild in a range of 10~50°C (Chandrasatheesh et al., 2014).

Based on extensive corrosion data obtained from experiments conducted in laboratories and from field monitoring, a number of models predicting different types of corrosion have been

proposed by researchers. But since pure corrosion is not the focus of this thesis, no further discussion will be performed on in this regard. In case of any special interest from readers, the works by Fontana (2005), Palmer and King (2004), and Perez (2013) are recommended.

The widespread anti-corrosion design of oil and gas pipeline is to add a corrosion allowance in the range of 0-6 mm in the wall thickness (Masson et al., 2015). Using a uniform estimation of cumulative corrosion over the service life actually deviates from the corrosion nature, i.e. corrosion can be different from location to location along pipelines. For example, in low spots where produced water might settle out of the production, the corrosion may be more significant than other regions. Missing the due diligence to the localized effect of corrosion defects may lead to neglecting the potential initiation of environment-assisted cracking from those sites.

2.2 Fatigue Analysis

Traditional fatigue design approach often adopts S-N curves, as shown in figure 2.5. S is the applied stress range and N stands for the number of stress cycles to failure. A series of fatigue tests are required to obtain the material's S-N curve.

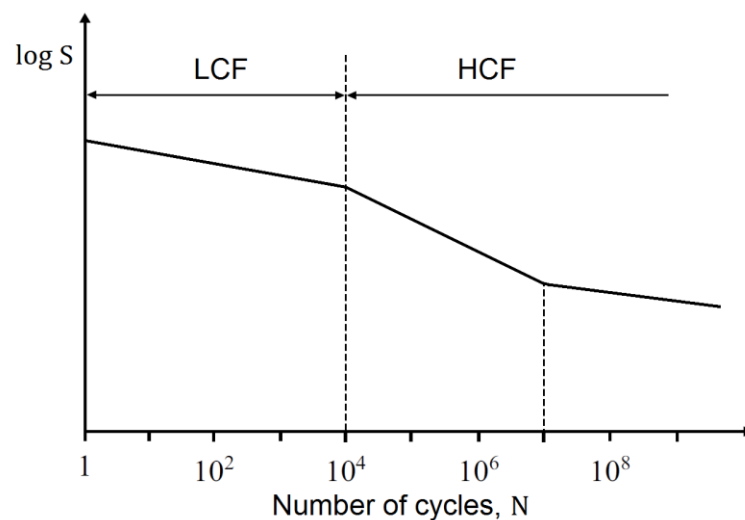


Figure 2.5 A typical S-N plot showing low-cycle fatigue (LCF) and high-cycle fatigue (HCF) regions

In the cases where the specimen is loaded with a significant stress range, it is often found to survive only a few load cycles. This is believed to be caused by the resultant large strain range exceeding the material's yield strain, both in tension and compression. Researchers divide the total strain into elastic and plastic strain. Experimental observation has proven that as the plastic strain amplitude is reduced, the specimens can bear a larger number of load cycles

before failure occurs. Thus, a gradual transition exists from fatigue under significant plastic strain to that of elastic behaviour. The former is often referred to as low-cycle fatigue and the latter is commonly called high-cycle fatigue. A more straightforward distinction between low-cycle fatigue and high-cycle fatigue can be seen in the S-N plot shown in figure 2.5.

The transition between low-cycle fatigue and high-cycle fatigue can be considered to be located in the region of 10^4 to 10^5 load cycles. However, note that in the S-N plot, the number of load cycles N includes both crack initiation and crack growth, thus it should be called as the total fatigue life. To the author's best knowledge, traditional research on fatigue has focused on the total fatigue life, either low-cycle fatigue or high-cycle fatigue, for the benefit of design (Fatemi and Yang, 1998). It is only after 1950s when linear elastic fracture mechanics was established and later 1970s-1980s when the concept of engineering critical assessment was proposed that the process of fatigue crack growth started to receive increasing research attention (Cui, 2002). The presence of a crack can significantly reduce the strength of an engineering structure/component due to brittle fracture. However, it is unusual for a crack of dangerous size to exist initially, although this can occur, as when large defects exist in the material used to make a component. In a more common situation, a small flaw that was initially present develops into a crack and then grows until it reaches the critical size for brittle fracture. Therefore the fatigue crack growth of a crack is of significant importance. Engineering analysis of fatigue crack growth is often required and can be done with the fracture mechanics. The fatigue crack growth of high-cycle fatigue is often depicted by the theory of linear elastic fracture mechanics, while the research on the fatigue crack growth of low-cycle fatigue is relatively rare (Ljustell, 2007). In the following subsections, a brief introduction to linear elastic fracture mechanics and elastoplastic fracture mechanics is made.

2.2.1 Linear Elastic Fracture Mechanics

Fracture mechanics is derived from crack-tip stress analysis. There are two early approaches to analysing stresses in cracked bodies developed by Westergaard (1939) and Williams (1952; 1957), respectively. The former approach connects the local fields to global boundary conditions providing certain configurations, while the latter considers the local crack-tip fields under generalized in-plane loading. Herein the latter approach is simply illustrated. Consider a crack tip in an infinite plane body in a polar coordinate system defined at the crack tip as shown in figure 2.6.

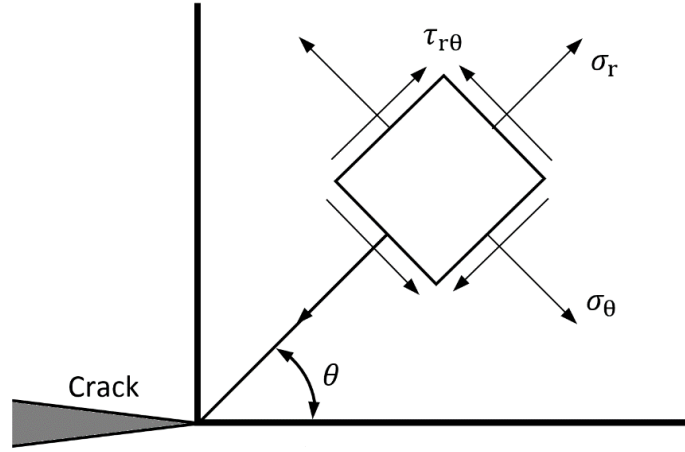


Figure 2.6 Stress state in the polar coordinate system

The different stress components can be expressed as

$$\sigma_{\theta\theta} = \frac{\partial^2 \phi}{\partial r^2} \quad (2-15a)$$

$$\sigma_{rr} = \frac{1}{r} \frac{\partial \phi}{\partial r} + \frac{1}{r^2} \frac{\partial^2 \phi}{\partial \theta^2} \quad (2-15b)$$

$$\sigma_{r\theta} = \frac{1}{r^2} \frac{\partial \phi}{\partial \theta} - \frac{1}{r} \frac{\partial^2 \phi}{\partial r \partial \theta} \quad (2-15c)$$

where ϕ is the Airy stress function. Equilibrium is automatically satisfied since the stresses are expressed through the Airy function. To ensure compatibility, when expressed in terms of the Airy function, the biharmonic equation is required to be satisfied

$$\nabla^2(\nabla^2 \phi) = 0 \quad (2-16)$$

where

$$\nabla^2 = \frac{\partial^2}{\partial r^2} + \frac{1}{r} \frac{\partial}{\partial r} + \frac{1}{r^2} \frac{\partial^2}{\partial \theta^2} \quad (2-17)$$

In order to solve equation (2-16), boundary conditions are needed. Since the crack is assumed to be traction-free, the boundary conditions become

$$\sigma_{\theta\theta} = \sigma_{r\theta} = 0 \text{ with } \theta = \pm\pi \quad (2-18)$$

While a solution of separate type is assumed

$$\phi = r^{\lambda+1} f(\theta) \quad (2-19)$$

where $f(\theta)$ is the angular function that describes the variation in the θ -direction. Inserting equation (2-19) into the equation (2-16) leads to an eigen value problem with the solution

$$\begin{aligned} \phi = & \sum_{n=1,3,\dots} r^{1+\lambda} \left[C_n \left(\cos(\lambda - 1)\theta - \frac{\lambda - 1}{\lambda + 1} \cos(\lambda + 1)\theta \right) \right. \\ & \left. + D_n (\sin(\lambda - 1)\theta - \sin(\lambda + 1)\theta) \right] \\ & + \sum_{n=2,4,\dots} r^{1+\lambda} \left[C_n (\cos(\lambda - 1)\theta - \cos(\lambda + 1)\theta) \right. \\ & \left. + D_n \left(\sin(\lambda - 1)\theta - \frac{\lambda - 1}{\lambda + 1} \sin(\lambda + 1)\theta \right) \right] \end{aligned} \quad (2 - 20)$$

where $\lambda = n/2$. Physically admissible values for λ in order to satisfy the criterion of finite displacements and bounded strain energy at the crack tip ($\phi < \infty$ when $r \rightarrow 0$) give

$$\lambda = \frac{1}{2}, 1, \frac{2}{3}, \dots \quad (2 - 21)$$

Substitution of the expression of ϕ into equation (2 - 15) and differentiation give the stress distribution around the crack. Assuming that the singular term will dominate the stress field in the vicinity of the crack tip, all but the first term will be truncated. Further rewriting the constants C_1 and D_1 into $K_I/\sqrt{2\pi}$ and $K_{II}/\sqrt{2\pi}$, respectively, gives

$$\sigma_{rr} = \frac{K_I}{\sqrt{2\pi r}} \left[\frac{5}{4} \cos \frac{\theta}{2} - \frac{1}{4} \cos \frac{3\theta}{2} \right] \quad (2 - 22a)$$

$$\sigma_{\theta\theta} = \frac{K_I}{\sqrt{2\pi r}} \left[\frac{3}{4} \cos \frac{\theta}{2} + \frac{1}{4} \cos \frac{3\theta}{2} \right] \quad (2 - 22b)$$

$$\tau_{r\theta} = \frac{K_I}{\sqrt{2\pi r}} \left[\frac{1}{4} \sin \frac{\theta}{2} + \frac{1}{4} \sin \frac{3\theta}{2} \right] \quad (2 - 22c)$$

for the Mode-I case. And

$$\sigma_{rr} = \frac{K_{II}}{\sqrt{2\pi r}} \left[-\frac{5}{4} \sin \frac{\theta}{2} + \frac{3}{4} \sin \frac{3\theta}{2} \right] \quad (2 - 23a)$$

$$\sigma_{\theta\theta} = \frac{K_{II}}{\sqrt{2\pi r}} \left[-\frac{3}{4} \sin \frac{\theta}{2} - \frac{3}{4} \sin \frac{3\theta}{2} \right] \quad (2 - 23b)$$

$$\tau_{r\theta} = \frac{K_{II}}{\sqrt{2\pi r}} \left[\frac{1}{4} \cos \frac{\theta}{2} + \frac{3}{4} \cos \frac{3\theta}{2} \right] \quad (2 - 23c)$$

for the Mode-II case. The anti-plane shearing Mode III is more straightforward to derive. K_I , K_{II} and K_{III} are the so-called stress intensity factors by Irwin (1957) corresponding to different cracking modes and defined generally as

$$K = \sigma\sqrt{\pi a} \quad (2 - 24)$$

where σ is the applied stress and a is the size of the crack in its characteristic dimension. For through-thickness cracks, a represents the half crack length, for surface cracks, a is the flaw height, and for embedded cracks, a is the half height. Since the strains and stresses in the elastic range increase in proportion to stress intensity factors and the above equations describe a first order approximation of the field quantities near the crack tip. The validity of such an approximation requires the condition that the size of the plastic zone is small compared to the crack length. In other words, the basic assumption of linear elastic fracture mechanics is small-scale yielding.

Stress intensity factor can not only be used as a parameter describing the strength of the singularity at the crack tip, but also used as a parameter describing the onset of rapid crack growth or fracture. It should be stated that for simplicity only Mode-I cracking is considered in this research. The critical value of stress intensity factor, termed “fracture toughness”, in Mode I is then labelled K_{IC} . Note that K depends on the loading and the crack size and might vary with position around a crack front.

Considering a growing crack that increases its length by an amount of Δa due to the application of a number of cycles ΔN , then the fatigue crack growth rate can be defined by the ratio $\Delta a/\Delta N$ or, for small intervals, by the derivative da/dN . Paris and Erdogan (1963) in the early 1960s proposed the famous equation as follows to describe the fatigue crack growth

$$\frac{da}{dN} = C(\Delta K)^m \quad (2 - 25)$$

where C is a constant and m is the slope on the log-log plot of da/dN vs ΔK . Note that in a load cycle, $\Delta K = K_{\max} - K_{\min}$. Named as Paris’ law, this equation actually started the application of fracture mechanics to fatigue.

2.2.2 Elastoplastic Fracture Mechanics

Stress intensity factor has been widely used to describe fatigue crack growth. However, researchers found that being based on linear elastic fracture mechanics, K doesn’t work well for situations where crack tips undergo significant plastic deformation. Even its physical meaning was questioned when large plasticity is involved. Thus, a more general parameter

capable of accounting for plasticity effects is needed for non-small-scale yielding conditions. The most likely candidate is the J -integral, which has the expression below

$$J = \int_{\Gamma} \left(W dy - \vec{T} \frac{\partial \vec{u}}{\partial x} ds \right) \quad (2 - 26)$$

As originated by Rice (1968), J is the two-dimensional path-independent line integral illustrated as figure 2.7.

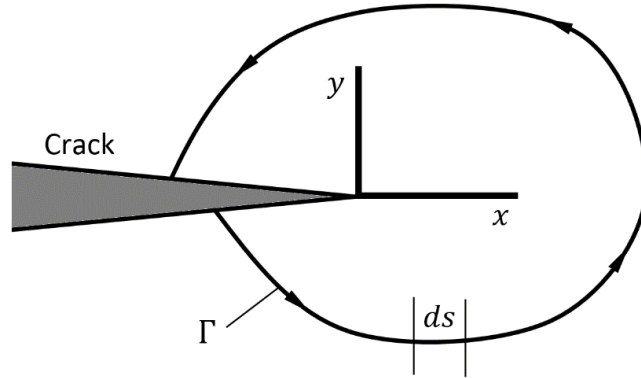


Figure 2.7 J -integral path around a crack tip

Counter-clockwise integration is performed around a path Γ connecting the crack faces, with x and y being the coordinates indicated, \vec{u} the displacement, and s the arc length along Γ . W is the strain energy density,

$$W = \int_0^{\varepsilon_{ij}} \sigma_{ij} d\varepsilon_{ij} \quad (2 - 27)$$

where σ_{ij} and ε_{ij} are the stress and strain tensors, respectively. The traction \vec{T} is a stress vector at a given point on the contour Γ . The components of \vec{T} is,

$$T_i = \sigma_{ij} n_j \quad (2 - 28)$$

where σ_{ij} is the stress component, n_j is the component of the unit vector normal to Γ .

Hutchinson (1968) and Rice and Rosengren (1968) independently showed that the J -integral characterizes crack-tip conditions in a nonlinear elastic material. They each assumed a power-law relationship between plastic strain and stress. If elastic strains are included, this relationship for uniaxial deformation becomes

$$\frac{\varepsilon}{\varepsilon_0} = \frac{\sigma}{\sigma_0} + \alpha \left(\frac{\sigma}{\sigma_0} \right)^n \quad (2 - 29)$$

where σ_0 is the yield strength, $\varepsilon_0 = \sigma_0/E$, α is dimensionless constant, and $n =$ strain-hardening exponent.

The above equation is known as the Ramberg-Osgood equation, and is widely used for curve-fitting stress-strain data. Hutchinson (1968) and Rice and Rosengren (1968) showed that in order to remain path independent, stress-strain must vary as $1/r$ near the crack tip. At distances very close to the crack tip, well within the plastic zone, elastic strains are small in comparison to the total strain, and the stress-strain behaviour reduces to a simple power law. These two conditions imply the following variation of stress and strain ahead of the crack tip:

$$\sigma_{ij} = k_1 \left(\frac{J}{r} \right)^{1/(n+1)} \quad (2 - 30a)$$

$$\varepsilon_{ij} = k_2 \left(\frac{J}{r} \right)^{n/(n+1)} \quad (2 - 30b)$$

where k_1 and k_2 are proportionality constants, which are defined more precisely below. For a linear elastic material, $n = 1$, then the above equation predicts a $1/\sqrt{r}$ singularity, which is consistent with linear elastic fracture mechanics. The actual stress and strain distributions are obtained by applying appropriate boundary conditions (Anderson, 2005):

$$\sigma_{ij} = \sigma_0 \left(\frac{EJ}{\alpha\sigma_0^2 I_n r} \right)^{1/(n+1)} \tilde{\sigma}_{ij}(n, \theta) \quad (2 - 31a)$$

$$\varepsilon_{ij} = \frac{\alpha\sigma_0}{E} \left(\frac{EJ}{\alpha\sigma_0^2 I_n r} \right)^{n/(n+1)} \tilde{\varepsilon}_{ij}(n, \theta) \quad (2 - 31b)$$

where I_n is an integration constant that depends on n , and $\tilde{\sigma}_{ij}$ and $\tilde{\varepsilon}_{ij}$ are the dimensionless functions of n and θ . These parameters also depends on the assumed stress state (i.e., plane stress or plane strain). The above equation is commonly called the HRR solution of crack-tip stress/strain field, named after Hutchinson, Rice, and Rosengren. For details of calculating I_n and $\tilde{\sigma}_{ij}(n, \theta)$, the works by Guo (1993a; 1993b; 1995) and Galkiewicz and Graba (2006) are recommended.

Dowling (1976) applied ΔJ to describe the fatigue crack growth of low-cycle fatigue, and suggested that the J -integral form of Paris' law can describe the fatigue crack growth with gross plasticity.

$$\frac{da}{dN} = C_j (\Delta J)^{m_j} \quad (2 - 32)$$

where C_j is a constant and m_j is the slope on the log-log plot of da/dN vs ΔJ . Lamba (1975) proposed that the cyclic form of J -integral may be calculated following that of the monotonic J -integral as

$$\Delta J = \int_{\Gamma} \left(\Delta W dy - \Delta T_i \frac{\partial \Delta u_i}{\partial x} \right) ds \quad (2 - 33)$$

with

$$\Delta W = \int_0^{\Delta \varepsilon_{ij}} \Delta \sigma_{ij} d\Delta \varepsilon_{ij} \quad (2 - 34)$$

The symbol Δ preceding the component stress, strain, traction and displacement designates the changes of these quantities. Note that $\Delta J \neq J_{\max} - J_{\min}$.

It is worth noting there are conditions called very large-scale yielding where J -integral loses its capability of characterizing the crack-tip stress/strain field. In component/structural level, they are manifested as failures after an extreme low number of load cycles. With very large-scale yielding, single-parameter fracture mechanics can no longer be applied. Actually, ultra-low cycle fatigue is rare in engineering practice. Even in the limited cases, general fatigue life (including initiation and a small part of propagation) instead of fatigue crack growth is what the engineers/researchers care. Relevant research is beyond the scope of this thesis. Therefore no further discussion is performed in this regard. However, if it is in the reader's interest, the works by Nip et al. (2010), Martinez et al. (2015), and Jia and Ge (2018) may serve as references.

2.3 Environment-assisted Cracking

It is well known that the cracking process of metals such as carbon steels can be severely aggravated by the aggressive environment. This phenomenon is usually called environment-assisted cracking. Unfortunately, subsea pipelines are exposed to aggressive service environments both internally and externally, and often contain stress concentrations such as as-built pipeline defects or dents caused by interference as well as corrosion pits. The contact of salts and water with the metal, either on the inside or outside pipeline surfaces, gives environment-assisted cracking a chance to happen and the stress concentrations may act as initiating sites. Potential CO_2 and H_2S in the production fluid make the situation even worse. Therefore, environment-assisted cracking has become one of the main challenges to the structural integrity of subsea pipelines under high-pressure/high-temperature service

conditions. To eliminate the failure risk during the pipeline service life, it is crucial to understand the mechanisms and kinetics of environment-assisted cracking, which is to be introduced in this section.

2.3.1 Stress Corrosion Cracking

Depending on the loading profile, there are two major categories of environment-assisted cracking: stress corrosion cracking and corrosion fatigue. As indicated by the names, stress corrosion cracking is the environment-assisted cracking under static loads, while corrosion fatigue is the environment-assisted cracking under cyclic loads. In contrast to corrosion fatigue, researches on stress corrosion cracking are relatively extensive and fruitful (Parkins, 2000; Woodtli and Kieselbach, 2000; Beavers and Harle, 2001; Fang et al., 2003).

Cracks in stress corrosion cracking are found to initiate from the bottoms of surface blemishes, and then propagate into the material either transgranularly, intergranularly or sometimes in a mixed way, affected by on the interaction of corrosion reaction and mechanical stress. For high-pH (9-13) stress corrosion cracking, cracks often grow along intergranular paths. This is thought to be associated with the strong environmental influence it receives. In reality, high-pH stress corrosion cracking is unlikely to happen to subsea pipelines. Thus, the near-neutral pH (5-7) stress corrosion cracking, which generates transgranular crack path will be discussed in detail. The transgranular crack path has been suggested to be associated with local corrosion and ingress of hydrogen, a by-product of corrosion reactions, at the crack tip. That is to say that near-neutral pH stress corrosion cracking is mixture of two damage modes, namely stress-assisted corrosion or briefly stress corrosion and hydrogen-assisted cracking.

In the case of stress corrosion, the primary driving force for crack growth comes from the localized chemical corrosion processes occurring at the crack tip, which is usually explained by the theory of anodic dissolution (Logan, 1952; Parkins, 1979). Various models for estimating the crack growth rate were proposed based on either theoretical formulae such as Faraday's law or experimental tests or both (Endo, et al., 1981).

As for hydrogen-assisted cracking, crack growth is associated with absorbed hydrogen in the material. Hydrogen may come from corrosion reactions in aqueous solutions, cathodic protection, or high-pressure hydrogen gas, and then diffuse into the material in its atomic state through a pre-existing flaw with stresses applied. Consequently, enhanced crack growth occurs and fracture happens at a lower stress level compared to that of the same material loaded in air or inert gas. This phenomenon is hydrogen embrittlement. There is still

controversy centred on the extent to which hydrogen-assisted cracking explains subcritical crack growth in metals stressed in environments that support concurrent crack tip dissolution, passive film formation, and atomic hydrogen production. Nevertheless, an agreement has been reached that hydrogen embrittlement normally prevails for subsea metal structures with cathodic protection as well as those exposed to gaseous hydrogen (Barnoush, 2011).

Numerous theories have been raised to explain the degradation of mechanical properties observed in hydrogen embrittlement. To date three of them have been widely accepted: hydrogen-enhanced de-cohesion, hydrogen-enhanced localized plasticity, and adsorption-induced dislocation emission. Arguments supporting each are not definitive, even not exclusive. A critical review was provided by Lynch in 2011. A consensus is emerging that hydrogen-enhanced de-cohesion is likely to be the dominant (Gangloff, 2008).

Conclusively, anodic dissolution and hydrogen embrittlement should be mainly responsible for the crack-tip material damage in near-neutral pH stress corrosion cracking.

2.3.2 Corrosion Fatigue

BS 7910 (2015) defines corrosion fatigue as a type of damage similar to fatigue, except that the environment is corrosive. The fatigue failure process of a component or specimen usually begins with crack initiation (stage I), and the cracks grow under continued cyclic loads (stage II), sequentially comes the rapid crack growth that finally leads to rupture (stage III). In contrast, the corrosive environment causes degradation of the material first, with the most common visible effect being pitting or etching. These notch-like flaws may act as stress raisers and become the initiating sites of nucleation, which significantly shortens the time of crack initiation (Ellyin, 2012). Once cracks are initiated, subsequent crack growth rate will be further enhanced by the environmental corrosiveness.

Given the fact that practical operations commonly generate varying working stresses in engineering structures, some researchers even consider stress corrosion cracking as a special case of corrosion fatigue where the stress ratio reaches unity (Shipilov, 2002). BS 7910 (2015) has recognized the fact that engineering structures are seldom subjected to pure static loads and the threshold of stress corrosion cracking can be considerably reduced if a cyclic component, even of very small magnitude, is superimposed on the static loading, therefore suggests assessing corrosion fatigue threshold instead of stress corrosion cracking threshold is more appropriate. Hence, it is of significant necessity to fully understand and reasonably assess the damage on structural integrity due to corrosion fatigue.

Interestingly, corrosion fatigue cracks usually follow a transgranular path. Based on the difference in crack morphology and environmental conditions, it has been pointed out that among the two basic modes of stress corrosion cracking, i.e. high-pH and near-neutral pH, the latter shares a similar morphology sometimes as well as the environmental conditions with those of corrosion fatigue. The similarity in crack morphologies and environment conditions may imply a similarity in cracking mechanisms. Further studies confirm that the mechanisms, which have generally been proposed to explain near-neutral pH stress corrosion cracking, are also applicable for corrosion fatigue (Shipilov, 2002). That is to say corrosion fatigue is also a mixture of two crack-tip damage modes, namely stress corrosion and hydrogen-assisted cracking, as illustrated in figure 2.8.

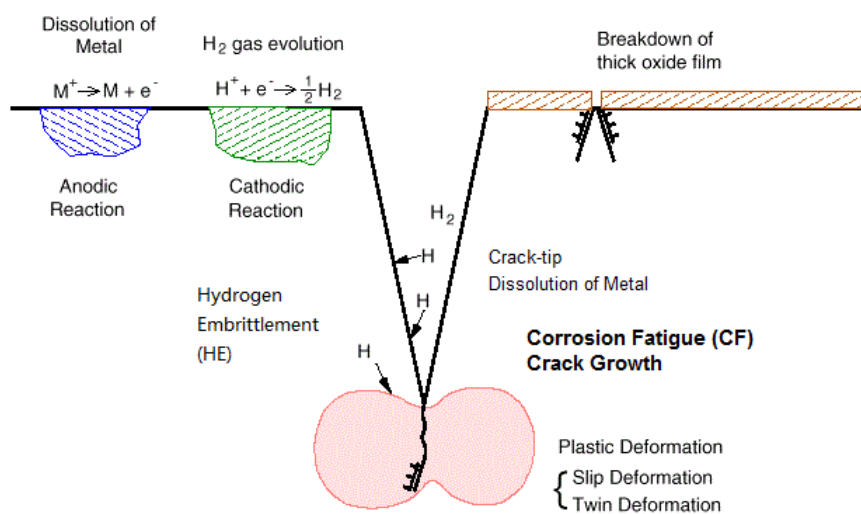


Figure 2.8 Mechanisms of corrosion fatigue crack growth (Yuyama et al., 1983)

Experimental observations (Vosikovskiy, 1975; Stephens et al., 2000; Holtam, 2010; Weng et al., 2013) have confirmed that corrosion fatigue can change the crack growth behaviour and lead to remarkably higher crack growth rate than that of fatigue in air for pipeline carbon steels such as X65. Some researchers have examined the corrosion fatigue damage in the view of the consequently lower overall fatigue life. For example, Baxter et al. (2007), based on their experimental results, found fatigue lives of steels in seawater, with or without cathodic protection, at high stress range can be a factor of three lower than those in air. Most relevant researchers have been aware that load frequency has an important influence on the crack growth in the case of corrosion fatigue, which is quite different from fatigue crack growth in dry-air environments (Yu et al., 2015). Other researchers such as Holtam (2010), has investigated the effect of crack size on corrosion fatigue crack growth.

However, current industrial standards for engineering critical assessment only provide limited guidance for corrosion fatigue, without sufficient consideration of its damage mechanisms and the resultant unique behaviour.

2.4 Engineering Critical Assessment

The structural integrity of pipelines, plant, equipment and structures is vital to ensure a continued, safe and economic operation. While the presence of flaws may severely damage the structural integrity, imposing a risk of failure during operation, flaws such as cracks, welding defects and corrosion damage may be inevitable during stages of manufacture and commissioning. But not all flaws are harmful, as some of them will not cause failure during the designed life, thus the replacement or repair of such ‘insignificant’ flaws is unnecessary and economically wasteful. Engineering critical assessment enables engineers to make the assessment that whether a detected flaw is ‘critical’ or in other words, whether the structure/component is still fit-for-service.

Beginning in the late 1970s to early 1980s, engineering critical assessment originally emerged as an alternative to traditional workmanship criteria. Previously most welding fabrication codes specify maximum tolerable flaw sizes and minimum tolerable Charpy energy, based on good workmanship, i.e. what can reasonably be expected following normal working practices. Since the workmanship criteria were developed with a limited understanding of material characteristics, their requirements tend to be somewhat arbitrary, and consequently failure to achieve them does not necessarily mean that the structure/component is at risk of failure.

While engineering critical assessment relies heavily on fracture mechanics. Its flaw acceptance criteria considered additional factors such as stress history, yield strength, fracture toughness, flaw orientation et al. (BS 7910, 2015). Together, these additional factors allow for more scientific flaw acceptance criteria, resulting in fewer unnecessarily repaired welds.

Nowadays methods for engineering critical assessment have been standardized in standards like the UK nuclear industry’s fracture assessment code R6 (2001), ISO 19902 (ISO, 2014), BS 7910 (2015) and API 579-1/ASME FFS-1 (2016) etc. are routinely used by the nuclear, oil and gas, aerospace, petrochemical and power industries to ensure the structural integrity of their safety critical components/structures. Figure 2.9 shows a typical structured program of engineering critical assessment. In this thesis, research focus is put on the engineering critical assessments in the commissioning stage of the component/structure.

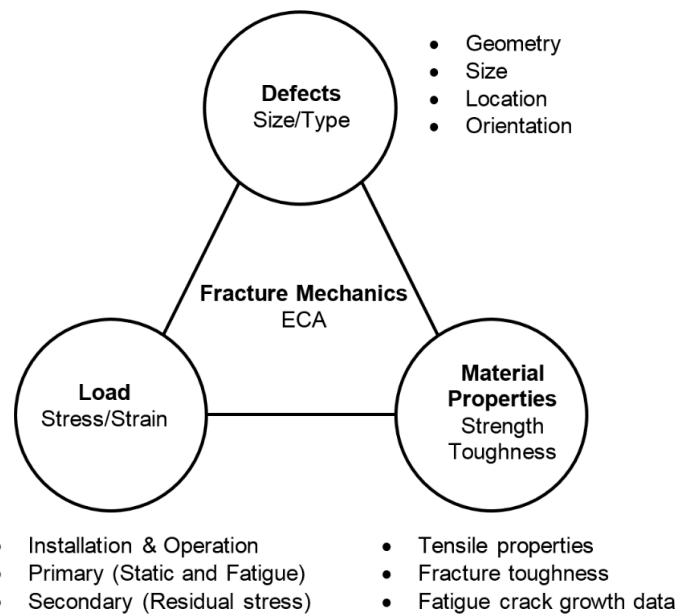


Figure 2.9 The typical structure of engineering critical assessment

2.4.1 Failure Modes

In engineering critical assessment, the following points should be assessed for each flaw:

- 1) The potential modes of final failure; and
- 2) Any possible material damage mechanisms leading to property degradation or sub-critical flaw growth.

BS 7910 (2015) suggests potential failure modes for a component/structure as follows:

- 1) failure by fracture and plastic collapse
- 2) damage by fatigue
- 3) damage by creep and creep fatigue
- 4) failure by leakage of containment vessels
- 5) damage by corrosion and/or erosion
- 6) damage by environmentally assisted cracking
- 7) failure by instability (buckling)

Some damage mechanisms associated with the aforementioned failure modes includes embrittlement, fatigue, corrosion fatigue, creep cracking, internal corrosion, external corrosion and under lagging corrosion, stress corrosion cracking, hydrogen and hydrogen sulphide related cracking, erosion and cavitation et al.. Note that material damage and sub-critical flaw growth can be affected by the material itself, design features, stress levels, time, cyclic loading, composition and concentration of process fluids and additive, flow rates, operating temperatures, external environment and so on, though not all these considerations

apply to any given material damage mechanism (BS 7910, 2015). Similarly, not all the aforementioned failure mode are relevant in all applications. In the preliminary analysis of an engineering critical assessment, all operating conditions should be screened, including start-up, shut-down, process upset and external environment, to find which failure mode is relevant to the component/structure under consideration. Then possible interaction between various damage mechanisms should be taken into account.

Among those failure modes and damage mechanisms, fracture and fatigue are the most well understood ones so far. The treatment provided for the two failure modes by industrial standards with respect to the depth and generality is inapproachable for other failure modes.

2.4.1.1 Fracture Mode

Fracture in components/structures due to tensile stress (Mode I) is normally evaluated invoking the failure assessment diagram, which combines two potential failure modes, i.e. brittle fracture and plastic collapse (ABS, 2018). Various types of imperfections are possible in girth welds. When evaluating the risk of fracture failure for girth welds, assumptions are to be made regarding types, dimensions and locations of weld defects. The most frequently seen type of planar/crack-like defect in one-sided shielded metal arc welding is lack-of-fusion defects. Such defects can be located near the surface, at the root of the weld toe or they can be surface-breaking and may have gone undetected when following the procedures of non-destructive test according to API 1104 (2013).

Despite ABS recommends three levels for assessing defects in girth welds, only the assessment using failure assessment diagram and tearing stability analysis from API 579-1/ASME FFS-1 (2016), BS 7910 (2015) or equivalent to obtain the critical stress levels with respect to failure (e.g., fracture, plastic collapse of remaining ligament) as a function of the flaw's characteristic dimension based on fracture mechanics will be briefly introduced here.

The maximum weld flaws are to be used as the basic input for the assessment. Surface flaw is chosen as the worst scenario from acceptable flaws specified in the welding procedure specifications. The defect sizes to be used in the fracture assessment are to be based on the welding methods used and the accuracy of the non-destructive test during construction. If no detailed information is available, the defects and material may be taken as provided by ABS (2018). The corresponding critical strain level is estimated assuming the material's stress-strain relationship can be depicted by Ramberg-Osgood equation. BS 7910 (2015) level 2 provides three failure assessment diagrams as options and its level 3 covers tearing instability analysis. In assessing the fracture failure capacity of the pipe or its weld due to longitudinal

strain, surface breaking flaws may be idealized as semi-elliptical surface defects of depth, a , and total length, $2c$. a and c are to be based on measurements by non-destructive test with a minimum of no less than the minimum detectable crack size of the applied non-destructive test technology. Parametric solutions for K are available in codes such as BS 7910 (2015) and API 579-1/ASME FFS-1 (2016).

2.4.1.2 Fatigue Mode

While the presence of defects such as cracks and crack-like anomalies may severely damage the integrity of structures, imposing risks of failure during operation, not all of them are immediately harmful (BS 7910, 2015). Fatigue is a time-dependent damage mechanism. Components/structures subjected to fatigue experience severe subcritical growth of defects before their final failures. Fatigue life is defined as the time it takes to develop a through-wall-thickness crack under cyclic loads. For convenience, the number of load cycles N is often used in fracture mechanics based calculation. In an inert environment, the surface of fatigue crack tends to be transgranular and follows a path normal to the maximum principal tensile stress; the crack growth in principle starts from the “stage I”, mainly being “short crack” with characteristic length < 1 mm, and grows with being “long crack” in stage II and finally enters the stage III with “rapid growth” towards fracture (Suresh and Ritchie, 1984; Pugno, 2006).

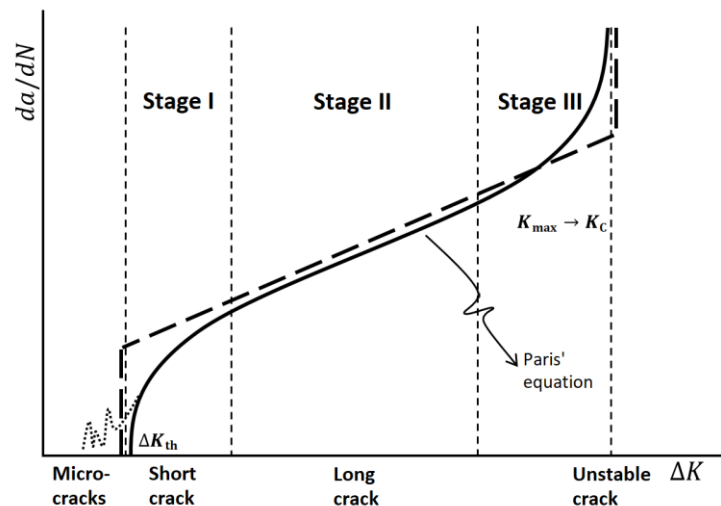


Figure 2.10 Schematic diagram of a fatigue cracking process

In engineering critical assessments, the fatigue crack growth rate of stage II is the primary concern. The reasons are as follows:

- 1) fatigue crack growth curves used by current industrial standards of engineering critical assessment for life prediction and maintenance scheduling are usually generated using

fracture mechanics specimens with crack lengths typically greater than 1mm (Suresh and Ritchie, 1984; Turnbull, 2014)

- 2) short cracks can be strongly influenced by local microstructures, implying LEFM becomes invalid for stage I crack growth (BS 7910, 2015; API 579-1, 2016)
- 3) while short crack growth may play an important role given its share of total fatigue life, in practical engineering the minimum reliably detectable flaw size of non-destructive testing (NDT) techniques is in the order of 1 mm (Tavares and De Castro, 2017; Smith et al., 2018).

Therefore, in this thesis, wherever “fatigue crack growth” is mentioned, it is referred to the stable fatigue crack growth of stage II except as otherwise specified. The fatigue crack growth rate is to be calculated using Paris’ law and the final fracture found in accordance with recognized failure assessment diagrams.

Subsea pipelines may be subjected to fatigue damage since its commissioning. Potential cyclic loads that can cause fatigue damage includes vortex-induced vibrations, wave-induced hydrodynamic loads (not applicable in the deep-water situation), floating installation movements and cyclic operation such as start-up and shut-down. Free spanned pipeline sections, welds, and cyclic buckle apex area should be considered for fatigue. The fatigue crack growth rate may be obtained following the procedure described in ABS (2018) or referring to the well-accepted industrial standards such as BS 7910 (2015), API 579-1/ASME FFS-1 (2016) or equivalent. In the assessment, the actual da/dN versus ΔK and ΔK data should be used wherever possible to fit Paris’ equation over the entire range of data or fit alternative crack growth law (e.g., Forman equation, see API 579-1/ASME FFS-1 for others). Alternatively, fitting Paris’ equation in a piecewise linear manner. The latter is preferred for fatigue crack growth in seawater with and without cathodic protection. In the absence of specific da/dN data, the upper bound relationships in BS 7910, API 579-1/ASME FFS-1 or equivalent may be used. Fatigue crack growth life versus crack size a may be predicted by transferring the $\Delta a/\Delta N$ versus ΔK relationship in the domain of a then integrating using a cycle-by-cycle approach provided a constant amplitude cyclic load.

However, it must be noted that the success of Paris’ equation describing fatigue crack growth is mainly attributed to the fact that engineering structures are usually designed to withstand loads well below the material’s yield strength, justifying the small-scale yielding assumption of linear elastic fracture mechanics and hence qualifying its application. In engineering practice fatigue with non-small-scale yielding crack-tip conditions is still possible to happen. The plasticity introduced will significantly reduce the number of load cycles to be

experienced by the structure, thus causing the so-called low-cycle fatigue. Low-cycle fatigue in marine structures have long been recognized and studied by various researchers (Garbatov et al., 2018). For instance, under rough weather conditions, the amplitudes of wave-induced cyclic stresses at locations such as welding toes in ships may be comparable to or even larger than the material's yield strength (Chen, 2016). For floating production storage and offloading (FPSO) vessels, the loading and offloading operations can introduce high-amplitude stresses (Kaminski, 2007; ABS, 2018). Similarly, subsea pipelines serving high-pressure/high-temperature reservoirs may also suffer cyclic operational stresses above the small-scale yielding limit (Bai and Bai, 2014; Cheng and Chen, 2018b). Non-small-scale yielding conditions violates the assumption of linear elastic fracture mechanics. Therefore, linear elastic fracture mechanics and models based on it can no longer be applied to predicting the crack growth under low-cycle fatigue loads. In conclusion, no current industrial standards are capable of providing guidance on conducting engineering critical assessments for structures subjected to low-cycle fatigue.

2.4.2 Assessing Procedures

Engineering critical assessment requires thorough examination by non-destructive test using techniques capable of locating and sizing flaws in critical areas. The non-destructive tests are normally carried out after any post weld heat treatment and/or proof test. A major objective of engineering critical assessment is to reduce costs by eliminating unnecessary repairs. The derivation of acceptance levels for flaws in assessments is based upon the fit-for-service principle. By this principle a component/structure is considered adequate for its purpose, as long as the conditions to cause failures are not reached. But it should be noted that engineering critical assessment is not an alternative to good workmanship for quality control. Quality control levels are usually conservative. Hence flaws that are less severe than such quality control levels as given are acceptable without further consideration. If flaws are more severe than the quality control levels, decisions on whether rejecting, down rating and/or repairing should then be based on engineering critical assessments. It is emphasized, however, that a proliferation of flaws, even if shown to be acceptable by an engineering critical assessment, is regarded as indicating that quality is in need of improvement (BS 7910, 2015).

The following general procedures are recommended for carrying out an engineering critical assessment for a known flaw (BS 7910, 2015):

- 1) Identify the flaw type, i.e. planar, non-planar or shape
- 2) Establish the cause of the flaw

- 3) Establish the essential data, relevant to the particular structure
- 4) Determine the size of the flaw
- 5) Assess possible material damage mechanism and damage rates
- 6) Determine the limiting size for the final modes of failure
- 7) Based on the damage rate, assess whether the flaw would grow to this final size within the remaining life of the structure or the in-service inspection interval, by sub-critical crack growth
- 8) Assess the consequences of failure
- 9) Carry out sensitivity analysis
- 10) If the flaw would not grow to the limiting size, including appropriate factors of safety, it is acceptable. The safety factors should take account both of the confidence in the assessment and of the consequences of failure.

Note that if engineering critical assessment is used for the purpose of design, according to ABS (2018), the design criteria for fatigue life should be at least 10 times the service life for all components. The initial flaw size should be the maximum acceptable flaw specified for the non-destructive test during manufacturing the component in question. Modelling techniques such as finite element analysis are sometimes asked to augment these standardized approaches of engineering critical assessment to determine the crack loading and collapse loads of cracked structures undergoing complex modes of loading.

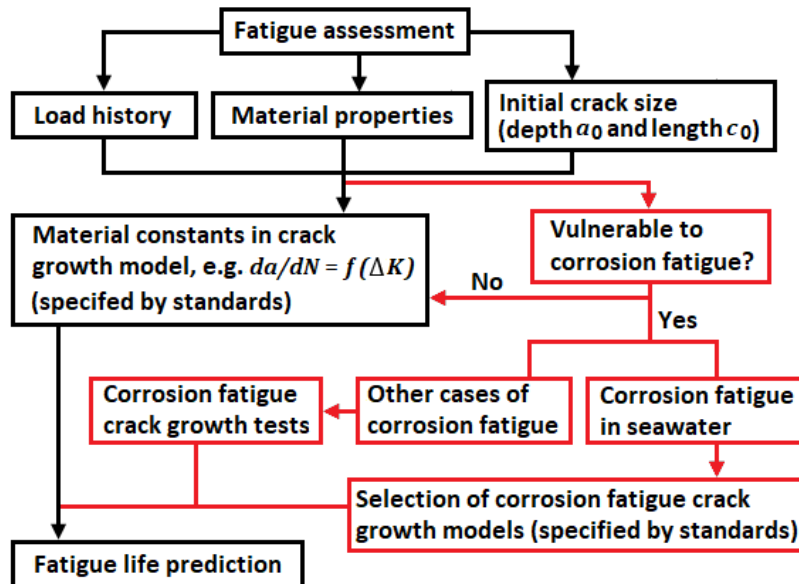


Figure 2.11 Existing standard approach of engineering critical assessment for corrosion fatigue (BS 7910, 2015; API 579-1, 2016)

The approach of engineering critical assessment for corrosion fatigue existing in current industrial standards, e.g. BS 7910 (2015) and API 579-1 (2016), is illustrated in figure 2.11

(in red). It includes two parts: for the case of corrosion fatigue in seawater, the two types of models, i.e. the simplified linear and the bilinear, can be used to describe the corrosion fatigue crack growth with provided parameters. But for other cases of corrosion fatigue, fatigue crack growth tests employing environmental and loading conditions that are representative of those encountered in service are needed.

2.5 Summary

For a component/structure subjected to fatigue loading, creep, brittle fracture and general volumetric corrosion, procedures are given in industry standards for assessing the acceptability of flaws found in service in relation to their effects on fatigue strength, both in welded and unwelded parts, or for estimating the tolerable crack sizes based on fit-for-service principles. The likelihood of failure from the operation of these failure modes and the associated damage mechanisms can be predicted with varying degrees of confidence and accuracy using current industrial standards for engineering critical assessment, such as BS 7910 (2015), API 579-1/ASME FFS-1 (2016) etc. This is because the behaviour of a component/structure subjected to these failure modes and damage mechanisms is relatively well understood.

However, the engineering critical assessment of subsea pipelines under high-pressure/high-temperature service conditions is more complicated and challenging for the lack of understanding on the material behaviour in such combined aggressive environment. While the industry has noticed for some time that the high-pressure/high-temperature service conditions are highly likely to cause corrosion fatigue and low-cycle fatigue issues for subsea pipelines, current standards (BS 7910, 2015; API 579-1/ASME FFS-1, 2016) are not able to provide as detailed, in depth and generality, and accurate treatments to corrosion fatigue as to the aforementioned failure mode and low-cycle fatigue is even left out of their scopes. Therefore, improvement of current industrial standards is necessary (Buitrago et al., 2008; Holtam, 2010; Kumar et al., 2014). This is the most critical challenge faced by engineers when reasonable engineering critical assessments for subsea pipelines under high-pressure/high-temperature service conditions are required. DNV has started systematic research on related topics since around 2014 (Kumar et al., 2014; Chong et al., 2016), however, the progress so far has been limited (Holtam et al., 2018). Standardized guidance to performing engineering critical assessments with particular consideration of corrosion fatigue and low-cycle fatigue for subsea pipelines that operate under high-pressure/high-temperature conditions is still not

readily available. Thus, the need is practical and pressing to develop a reasonable approach of engineering critical assessment in particular for corrosion fatigue and establish a prediction model of fatigue crack growth applicable for low-cycle fatigue.

Basically, the following two chapters will present the research work done in this PhD thesis to fulfil the objectives mentioned in Section 1.2 in detail.

Chapter 3. CORROSION FATIGUE ASSESSMENT

Engineering critical assessment concerns potential subcritical growth of detected flaws and utilizes fracture mechanics to determine the defect tolerance of structures. These flaws can be either original welding flaws (which are idealized as sharp cracks) or cracks formed in service by other mechanisms such as corrosion, fatigue and external interference. In the case of subsea pipelines under high-pressure/high-temperature service conditions, the structures are more prone to have free spans and cyclic buckling due to cyclic thermal and pressure expansion and contraction along periodic operations. The dynamic responses in both cases tend to cause tenting of tape or coating at long seam welds and tape wrinkles on the outside surface. The contact of corrosive medium (e.g. seawater) with metal gives corrosion fatigue, where the environmental corrosiveness accelerates the fatigue crack growth process, a chance to occur.

The research work to be presented in this Chapter is centred on developing a reasonable approach of engineering critical assessment in particular for corrosion fatigue. It consists of 3 sections. Section 3.1 deals with modelling the fatigue crack growth behaviour under the impact of hydrogen embrittlement only. Section 3.2 demonstrates the procedure of establishing a corrosion fatigue crack growth model based on damage mechanisms. Section 3.3 extends the approach of corrosion fatigue in current industrial standards to account for effects of initial size and loading frequency.

3.1 Hydrogen-enhanced Fatigue Crack Growth

As nowadays the renewable energy such as wind and solar is booming in its development, the corresponding energy storage technology is attracting more and more attention. In a possible scheme proposed, the fresh energy is converted into gaseous hydrogen by separating water, and then stored and transmitted by pipelines (Leighty et al., 2006). This idea is especially practical for offshore wind and solar farms where water supply is not a problem. Modern pipelines are usually made of medium or low strength steels and often designed by use of defect-tolerant principles, where knowledge of defect size and fatigue crack growth rate can be used to determine the remaining service life of a component. Several comprehensive reviews on the fatigue crack growth behaviour of pipeline carbon steels exposed to gaseous hydrogen were performed by Lam (2006), Nanninga (2010), and Liu (2013).

As seen from the above brief review of literature, it is clear that hydrogen embrittlement has a significant impact on fatigue crack growth behaviour of carbon pipeline steels, especially under high hydrogen pressures and varying loading frequencies. Although both corrosion fatigue and hydrogen-enhanced fatigue cracking show some frequency dependence, Nanninga (2010) pointed out that the mechanisms and models used to predict hydrogen-enhanced fatigue cracking in hydrogen may still differ significantly from those used for statically loaded applications or in fatigue situations where the hydrogen derives from aqueous liquids, which usually accompanies corrosion or/and negative potential. Moreover, unlike the situation for sustained load cracking in hydrogen environments, it was found that medium- even low-strength pipeline steels are highly susceptible to hydrogen-enhanced fatigue cracking (Liu, 2013). However, there is still a lack of such models that can rationally account for the mechanisms of hydrogen-enhanced fatigue cracking, just as what is mentioned in API 579-1/ASME FFS-1 (2016), equations/models that describe fatigue crack growth behaviour in aggressive environments are only available for limited stress intensity ranges and most often intended for aqueous liquids.

In order to solve this problem, a corrosion-crack correlation model is developed in this section based on the concepts of environment-affected zone and plastic zone. In the model, fatigue crack growth rate is predicted by Forman equation to take into account the influence from fracture toughness. The critical frequency and the “transition” stress intensity factor are derived from theoretical basis of stress-driven hydrogen diffusion and hydrogen-enhanced de-cohesion. Furthermore, an approximation formula involving the threshold stress intensity factor range and stress ratio is established to describe the phenomenon of crack growth rate plateau. In addition, a formula is proposed to estimate the final fracture toughness determined by the equilibrium between crack growth and hydrogen delivery rates.

3.1.1 Hydrogen Embrittlement Effect

A brief description for the hydrogen-enhanced fatigue cracking process of pipeline carbon steels will be presented here, with the purpose of providing a theoretical basis and clarifying physical meaning to the mathematical equations given in the next part.

As Oriani claimed in 1972, the basic notion of hydrogen-enhanced de-cohesion is that hydrogen embrittlement cracking occurs when the local opening tensile stress in front of crack tip exceeds the maximum-local atomic cohesion strength, which has been lowered by the presence of hydrogen. Based on this notion, Wang et al. (2013) established a model that can predict the degradation of fracture toughness for alloy steels exposed to gaseous hydrogen.

Good agreement was observed between the prediction and experimental data. The success of this model indicates that the theory of hydrogen-enhanced de-cohesion works well on explaining the hydrogen embrittlement of pipeline carbon steels. However, it should be noted that the degraded fracture toughness was measured by testing pre-cracked specimens under sustained loading condition (Gutierrez-Solana, 1982), where there is sufficient time for hydrogen atoms to diffuse to the maximum tensile stress location. Thus fracture resistance is degraded and cracking is enhanced to the same extent corresponding to the hydrogen pressure along the whole test. The fracture toughness measured in such a way is called the saturated fracture toughness for the ambient hydrogen pressure.

However, if crack growth goes beyond a specific speed (usually around the point when rapid unstable crack growth begins), diffusing hydrogen cannot keep pace with the growing crack, resulting in an increased resistance against the rapid crack growth and in turn the rate itself slows its acceleration to establish an equilibrium with the hydrogen delivery rate. Subcritical crack growth may then continue along the equilibrium rate toward an “equilibrium fracture toughness” (API 579-1/ASME FFS-1, 2016). Such a hydrogen-enhanced fatigue crack process can be observed in fatigue tests performed in hydrogen gas for pipeline steels spanning from low grades such as X42 (Cialone and Holbrook, 1985) to grades as high as X100 (Amaro et al., 2014).

If viewing hydrogen damage as a special case of corrosion, the foresaid process then describes the corrosion-crack correlation mechanism existing in hydrogen-enhanced fatigue cracking. Based on the typical process description, for a specimen tested in high-pressure hydrogen gas with fatigue loading, three specified types of fracture toughness are defined, namely the inherent fracture toughness, K_{IN} , which is measured in a non-aggressive environment with the same loading conditions; the saturated fracture toughness, K_{IH} , which is obtained under high hydrogen pressure using procedures defined in ASTM E1820-17 (2017); the equilibrium fracture toughness, K_{IE} , namely the final fracture toughness displayed in the fatigue test.

3.1.2 Fatigue Crack Growth Modelling

As mentioned in 2.4.1.2, for normal fatigue cracking (where aggressive environment is not applicable), in principle, crack growth starts from the “stage I” (the “initiation” phase), mainly being “short crack”, and continues with the “propagation” phase of stage II and stage III (fast crack growth), being “long crack” toward final failure (Pugno, 2006), as shown in figure 2.10.

However, the process will be changed when hydrogen embrittlement is introduced. A typical hydrogen-enhanced fatigue cracking process of pipeline carbon steels in hydrogen gas with

constant amplitude loading is shown in figure 3.1 by the solid curve. The process is consisted of three stages. In the beginning, the crack rate grows along the sigmoidal curve dictated by K_{IH} , which is recognized as stage 1. The enhanced fatigue crack growth results from the hydrogen delivered at the crack tip through diffusion. When the crack growth rate goes beyond the hydrogen delivery rate, the crack propagates into the bulk material with little hydrogen, and as a consequence encounters larger resistance. So the growth acceleration decreases, and transition happens, indicating the commencement of stage 2. An equilibrium between the crack growth rate and hydrogen delivery rate is achieved later. Due to the continuity of hydrogen charging and crack growth, the cracking rate will not drop. Instead a plateau, where the crack growth rate keeps constant at the equilibrium rate, appears in the crack growth curve and lasts over some range along the abscissa of K_{max} . Stage 3 starts when the curve merges into the sigmoid oriented by the equilibrium fracture toughness K_{IE} , which is closer to the inherent fracture toughness K_{IN} . The sigmoidal fatigue crack growth curves oriented by K_{IH} and K_{IN} are both plotted using dash lines in the same figure.

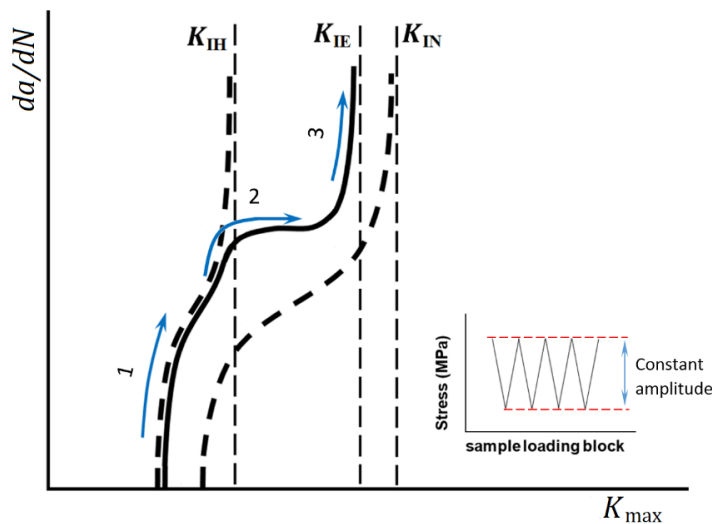


Figure 3.1 Schematic diagram of a typical hydrogen-enhanced fatigue cracking

At present, linear elastic fracture mechanics based analysis has been widely applied to engineering critical assessment for steel structures. The main purpose of the assessment is to predict the remaining service life of a component with use of Paris' law (Paris and Erdogan, 1963), which is defined as:

$$\frac{da}{dN} = A(\Delta K)^n \quad (3 - 1)$$

where A and n are the Paris coefficients, and ΔK is the stress intensity factor range, which can be calculated as

$$\Delta K = F \Delta S \sqrt{\pi a} \quad (3 - 2)$$

where F is the geometry function, and ΔS is the stress range ($S_{\max} - S_{\min}$). a is the characteristic dimension of the crack. For through-thickness cracks, a represents the half crack length, for surface cracks, a is the flaw height, and for embedded cracks, a is the half height.

It is generally agreed that linear elastic fracture mechanics can provide reasonable fatigue life estimates for long cracks (Stephens, 2000) and Paris' Law works well for predicting the fatigue crack growth rate in stage II. For more complicated fatigue crack growth curves that are not straight lines in log-log plots, multi-segment lines are usually constructed in order to model the real curve.

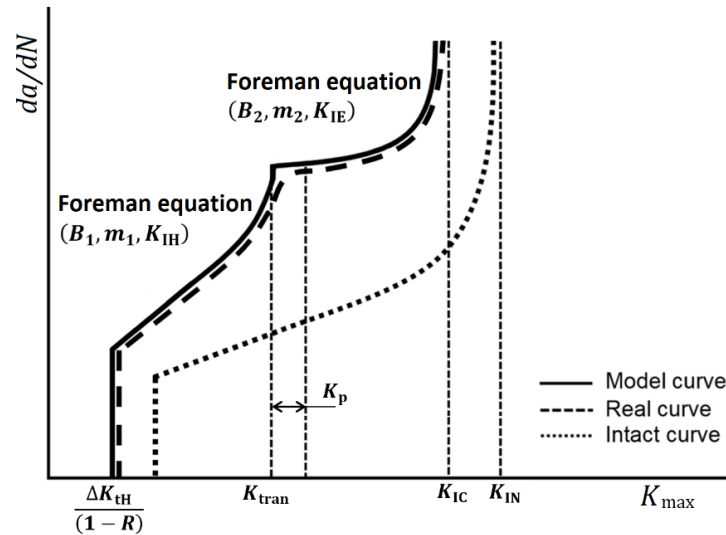


Figure 3.2 Schematic diagram of the corrosion-crack correlation model

As discussed in 3.1.1, degradation of fracture toughness of pipeline carbon steels will normally happen in high-pressure hydrogen gas. However, there is no link between crack growth rate and fracture toughness variation in Paris' Law, which is the main manifestation of material degradation in hydrogen gas. In 1967, Foreman at al. proposed an equation as:

$$\frac{da}{dN} = \frac{B \Delta K^m}{[(1 - R)K_{IC} - \Delta K]} \quad (3 - 3)$$

where K_{IC} stands for the fracture toughness in a general sense. The equation covers both stage II and III considering the fracture toughness variation. Therefore, Forman equation is adopted herein as the basic formulation for establishing the fatigue crack growth model of pipeline steels tested in high-pressure hydrogen gas. The model to be constructed is basically a two-stage Foreman equation model, as shown in figure 3.2 in comparison with the hydrogen-

enhanced fatigue crack growth curve and the fatigue crack growth curve in a non-aggressive environment. As seen from figure 3.2, to schematically describe the hydrogen-enhanced fatigue crack growth process, four key points should be seized, i.e. the threshold stress intensity factor range ΔK_{th} , the Transition stress intensity factor K_{tran} , plateau stress intensity range K_p , and the equilibrium fracture toughness K_{IE} .

3.1.2.1 Threshold Stress Intensity Factor Range

ΔK_{th} determines when crack starts advancement. Three varying parameters may affect the ΔK_{th} of pipeline carbon steels in high-pressure hydrogen gas, namely the stress ratio R , fracture toughness, K_{IC} , and hydrogen pressure.

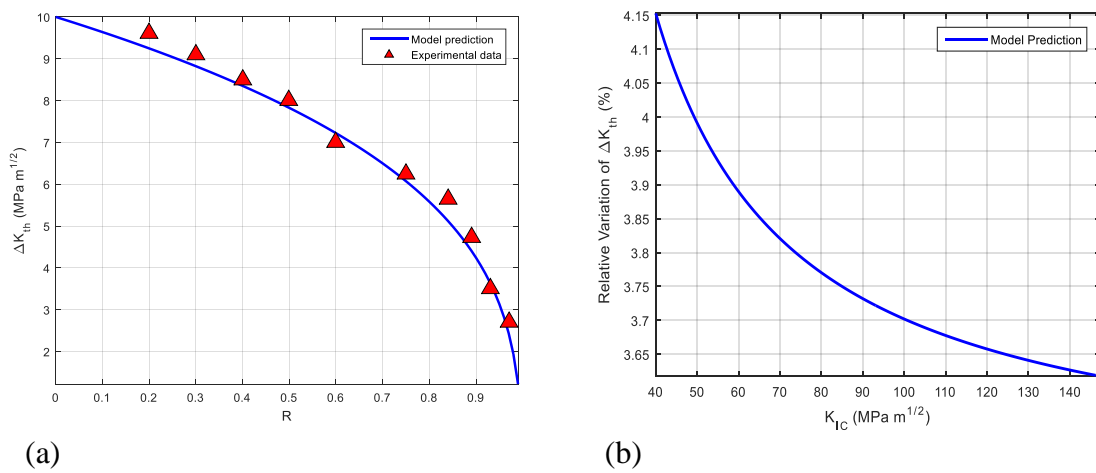


Figure 3.3 (a) ΔK_{th} - R relationship, with experimental data by Davenport and Brook (1979); (b) Influence of K_{IC} on ΔK_{th} (given that ΔK_0 keeps constant)

Based on the relation proposed by Davenport and Brook (1979), for fatigue crack cracking under non-aggressive conditions, its threshold stress intensity factor range ΔK_{th} is given by:

$$\Delta K_{th} = \Delta K_0 \left(\frac{(K_{IC} - K_{max})(1 - R)}{(K_{IC} - \Delta K_0)} \right)^{\frac{1}{3}} \quad (3 - 4)$$

where ΔK_0 represents the threshold stress intensity factor range at $R = 0$, and K_{max} is the maximum stress intensity factor. Meanwhile, it should be noted that

$$\Delta K_{th} = K_{maxth}(1 - R) \quad (3 - 5)$$

and that

$$\Delta K_0 = K_{max0} \quad (3 - 6)$$

where $K_{\max\text{th}}$ and $K_{\max0}$ correspond to the maximum stress intensity factors at ΔK_{th} and at $R = 0$, respectively. ΔK_0 is usually obtained from experiments. Based on equations (3 – 4) to (3 – 6), it follows that,

$$\frac{K_{\max\text{th}}}{K_{\max0}} = (1 - R)^{-\frac{2}{3}} \left(\frac{K_{\text{IC}} - K_{\max\text{th}}}{K_{\text{IC}} - K_{\max0}} \right)^{\frac{1}{3}} \quad (3 - 7)$$

As an example, the relation between R and ΔK_{th} of a 0.15%C-1.5%Mn steel is drawn in figure 3.3(a). The experimental data were collected from the work by Davenport and Brook (1979). On the other hand, figure 3.3(b) shows that the variation in K_{IC} gives little impact (up to 4%) on the threshold stress intensity factor range. This may be because the variation of threshold stress intensity factor range of metals exposed to hydrogen mainly comes from the change of threshold stress intensity factor range at $R = 0$ under different hydrogen pressures.

Somerday et al. (2007) gave a critical review on hydrogen influence on fatigue crack growth and concluded that at ΔK values near ΔK_{th} , the effect of hydrogen environment on both the crack growth or on the value of ΔK_{th} was not evident. This conclusion was supported by previous experiments conducted by Pendse and Ritchie (1985), and Dauskardt and Ritchie (1986). Therefore, in this research, the degradation of ΔK_{th} due to hydrogen influence is assumed to be $1 \text{ MPa}\sqrt{\text{m}}$ for all hydrogen pressures. The threshold stress intensity factor range for pipeline carbon steels tested in high-pressure hydrogen gas is assumed to be:

$$\Delta K_{\text{tH}} = \Delta K_{\text{th}} - 1 \quad (3 - 8)$$

3.1.2.2 Transition Stress Intensity Factor

Transition stress intensity factor, K_{tran} , is determined by establishing the corrosion-crack correlation model, which interprets the fatigue crack growth behaviour of pipeline carbon steel under hydrogen embrittlement influence as the manifestation of the correlation between the sizes of the environment-affected zone, r_{EAZ} , and plastic zone r_{p} . Penetration of chemical agents into a localized crack-tip region would severely damage the bulk of material near the crack tip. The damaged material no longer represents the original bulk material and exhibits accelerated crack growth rates as compared to its baseline behaviour. This damaged zone is called the environment-affected zone. In the case of hydrogen-enhanced fatigue crack growth testing, hydrogen is considered the primary source for creating the damaged zone. According to the theory of hydrogen-enhanced de-cohesion, hydrogen damage sites are located at a distance ahead of the crack tip surface where tensile stresses are maximized, namely the

plastic-elastic boundary. The elastic-plastic stress field near the crack tip was schematically plotted in figure 3.4.

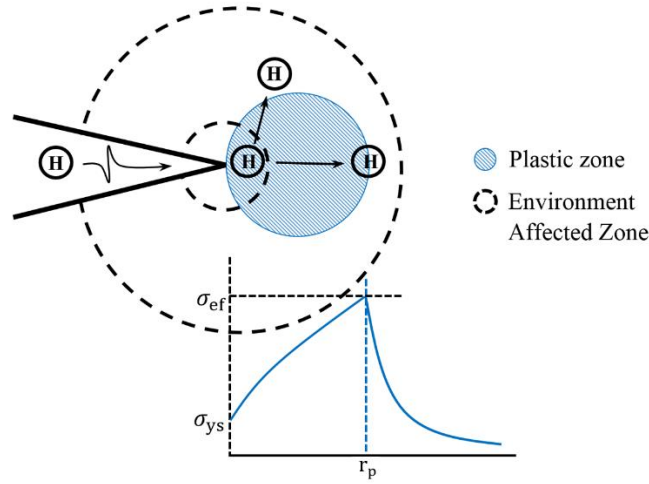


Figure 3.4 Schematic diagram of stress distribution in front of crack tip

Hill (1998) performed a detailed analysis on the stress field in front of a crack tip with crack tip radius ρ . It was found that the hydrostatic stress within plastic zone σ_h , can be expressed as

$$\sigma_h = \sigma_{ys} \left[\frac{1}{2} + \ln \left(1 + \frac{r}{\rho} \right) \right] \quad (3 - 9)$$

where r is the distance in front of the crack tip, and σ_{ys} corresponds to the yield strength.

For hydrogen atoms diffusing into the crack-tip region, their energetic driving force μ , which is created by the chemical potential can be written as

$$\mu = \mu_0 + k_B T \ln \frac{c}{1 + c} + \sigma_h V_H \quad (3 - 10)$$

where c is the hydrogen concentration at r , V_H is the partial volume of hydrogen, k_B is the Boltzmann constant, T is the temperature and μ_0 is a constant.

Thus the velocity of hydrogen atoms from the crack tip V_r has the expression

$$V_r = - \frac{D}{k_B T} (\nabla \mu)_r \quad (3 - 11)$$

where D is the diffusion coefficient, and is calculated from the ratio of hydrogen permeability and solubility for carbon steel (Gadgeel and Johnson, 1979).

Note that the H concentration $c \ll 1$ when the location is away from the immediate crack tip, so the concentration driven part is so small that any explicit concentration dependence of

diffusion can be neglected. Also, the aggregation and redistribution process of local hydrogen around the crack tip is quite short and it has no significant influence on the time required for hydrogen atoms to reach the near-crack-tip region (Song and Curtin, 2011). Therefore the dominant force driving hydrogen to diffuse is the hydrostatic pressure in front of the crack tip and the hydrogen concentration at diffusion front line can be viewed as being constant. This analysis yields the following expression for hydrogen diffusion velocity V_r ,

$$V_r = -\frac{DV_H}{k_B T} \left(\sigma_{ys} \frac{\frac{1}{\rho}}{1 + \frac{r}{\rho}} \right) \quad (3 - 12)$$

On the other hand, $V_r = -dr/dt$. So, after time t , hydrogen atoms can be spread within a distance of $r = R$ in front of the crack tip, where

$$R = \sqrt{\frac{2DV_H\sigma_{ys}}{k_B T} t} \quad (3 - 13)$$

In a stress cycle, when unloading starts, the residual stress can cause compression in front of the crack tip, since hydrogen embrittlement effect is limited to tensile stress state, only half time of a cycle contributes to the H accumulation at the near crack-tip region. This limited distance is defined as r_{EAZ} . If this distance in front of the crack tip is no larger than the plastic zone size, it can be calculated by

$$r_{EAZ} = \sqrt{\frac{DV_H\sigma_{ys}}{k_B T} \cdot \frac{1}{f}} \quad (3 - 14)$$

where f is the loading frequency.

For Mode I loading under the elastic condition, the stress σ_{yy} perpendicular to the crack plane at a distance of r off the crack tip can be expressed in a function of K_I , as

$$\sigma_{yy} = \frac{K_I}{\sqrt{2\pi r}} \quad (3 - 15)$$

The maximum principal stress happens at the elastic-plastic boundary r_c , where,

$$\sigma_{\max} = \sigma_{yy} = \omega\sigma_{ys} \quad (3 - 16)$$

ω is a magnification factor of value 3 ~ 5 accounting for the material's working hardening effect.

Accordingly, at fracture initiation point, where $K_I = K_{IN}$, equation (3 – 15) can be rewritten as

$$r_c = \frac{1}{2\pi} \frac{K_{IN}^2}{(\omega\sigma_{ys})^2} \quad (3 - 17)$$

Since the loading frequency may vary when comparing different loading cases, a critical frequency, f_c , is determined as where the environment-affected zone reaches the elastic-plastic boundary, i.e. $r_{EAZ} = r_c$. Accordingly,

$$f_c = \frac{4\pi^2 DV_H (\omega\sigma_{ys})^4 \sigma_{ys}}{k_B T K_{IN}^4} \quad (3 - 18)$$

To give a clear picture of the process described by equations (3 – 9) ~ (3 – 18), X60 steel was used as an example. Calculation was performed with the experiment data obtained by Yu et al. (2015). The definition of f_c and the r_{EAZ} - r_p relationship were both plotted in figure 3.5.

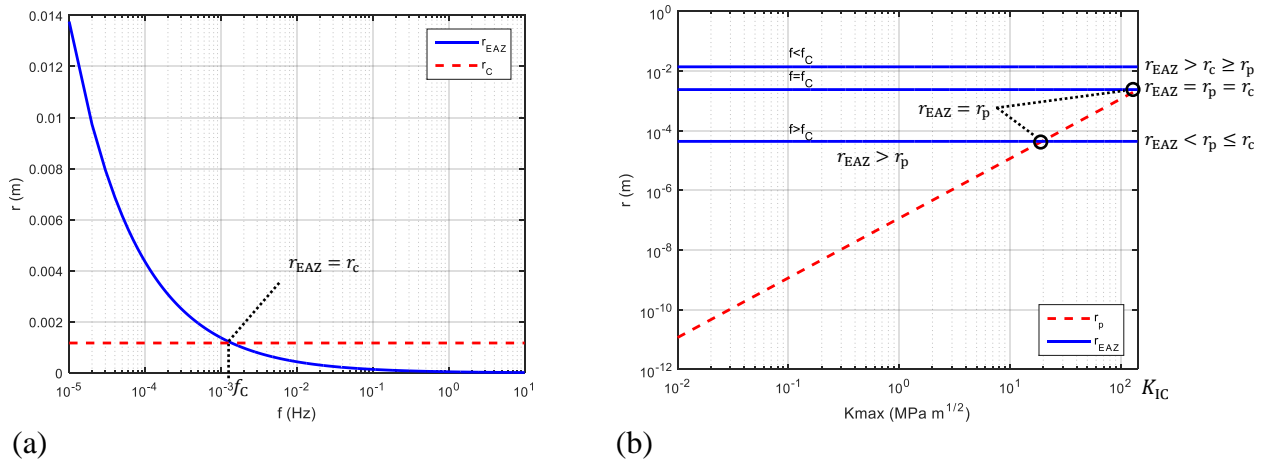


Figure 3.5 (a) f_c definition; (b) r_{EAZ} - r_p relationship

In figure 3.5(a), it can be seen that r_{EAZ} varies as the loading frequency changes. A higher loading frequency corresponds to a smaller size of environment-affected zone, and thus a weaker corrosion effect, which is in agreement with experimental observations. At the critical frequency f_c , the frontline of environment-affected zone draws back to the elastic-plastic boundary, i.e. $r_{EAZ} = r_c$. The plastic zone size r_p varies differently under different loading frequencies. If the loading frequency $f < f_c$, r_{EAZ} will be larger than r_p and the relation $r_{EAZ} > r_c \geq r_p$ holds over the whole fatigue crack growth process as shown in figure 3.5(b). If $f > f_c$, which represents a typical hydrogen-enhanced fatigue cracking process of pipeline carbon steels in hydrogen gas shown in figure 3.1, r_p maybe smaller than r_{EAZ} at first, corresponding to the stage 1 crack growth. However, as K_{max} increases, the growing r_p comes

equal to and then goes beyond r_{EAZ} at some point before K_{max} reaches K_{IC} , corresponding to the stage 1 and 3 crack growth respectively. For the whole fatigue crack growth process, $r_{\text{EAZ}} < r_p \leq r_c$ stays valid. If $f = f_c$, r_p grows and achieves the equilibrium $r_{\text{EAZ}} = r_p = r_c$ at the point where $K_{\text{max}} = K_{\text{IC}}$.

Before having an insight into the transition stress intensity factor, the assumption that r_c is independent of hydrogen (Wang et al., 2013) is introduced, thus the mechanism of hydrogen-enhanced de-cohesion can be mathematically expressed as (Oriani, 1977)

$$\sigma_{\text{maxH}} = \sigma_{\text{max0}} - \beta C \quad (3 - 19)$$

where σ_{maxH} and σ_{max0} are the maximum principal stress at r_c with and without hydrogen when cracking initiates, respectively. β is a parameter related to loss of critical cohesive stress by hydrogen impurity, and C is the local hydrogen concentration.

Insert equation (3 - 16) into equation (3 - 19), it follows that

$$\omega_{\text{H}} = \omega - \frac{\beta C}{\sigma_{\text{ys}}} \quad (3 - 20)$$

ω_{H} accounts for the material's work hardening effect with hydrogen introduced. Provided that K_{IH} and K_{IN} have been determined, then equation (3 - 20) can be written as

$$\omega_{\text{H}} = \omega \frac{K_{\text{IH}}}{K_{\text{IN}}} \quad (3 - 21)$$

Based on this model, the point where the crack growth curve starts transition is the very point where r_p grows to an equilibrium with r_{EAZ} , i.e.

$$r_p = r_{\text{EAZ}} \quad (3 - 22)$$

Inserting equation (3 - 14), equation(3 - 15), and equation (3 - 17) into equation (3 - 22), the transition stress intensity factor can be obtained as

$$K_{\text{tran}} = \omega \sigma_{\text{ys}} \frac{K_{\text{IH}}}{K_{\text{IN}}} \left(\frac{4\pi^2 D V_{\text{H}} \sigma_{\text{ys}}}{k_{\text{B}} T f} \right)^{\frac{1}{4}} \quad (3 - 23)$$

If the time interval lasts so long that the hydrogen passes the elastic-plastic boundary, diffusing into the elastic stress field, then the hydrostatic stress afterward holds the following expression (Liu, 2005)

$$\sigma_{\text{h}} = \frac{2(1 + \nu)}{3} \frac{K_{\text{I}}}{\sqrt{2\pi r}} \quad (3 - 24)$$

The size of environment-affected zone then should be a sum of hydrostatic stress contribution from both the plastic and elastic zones. But since the summated size is definitely larger than that of the critical plastic zone and maximum stress still occurs at the elastic-plastic boundary, the cracking happens in the same way with that of the situation where $r_{EAZ} = r_p$.

Note that it was observed by experiments, as mentioned in 3.1, that hydrogen influence on crack growth rate is not evident at ΔK values near threshold stress intensity factor range. This results in the lower boundary condition for K_{tran} . While the upper boundary of K_{tran} is K_{IH} . Thus, the controlling function for K_{tran} can be established as

$$K_{tran} = \min \left\{ \max \left\{ K_{tran}, \frac{\Delta K_0}{(1-R)} \right\}, K_{IH} \right\} \quad (3 - 25)$$

Equation (3 – 25) is plotted in figure 3.6 in the domain of f , using X60 steel as an example. The calculation is performed based on the experimental data provided by Yu et al. (2015).

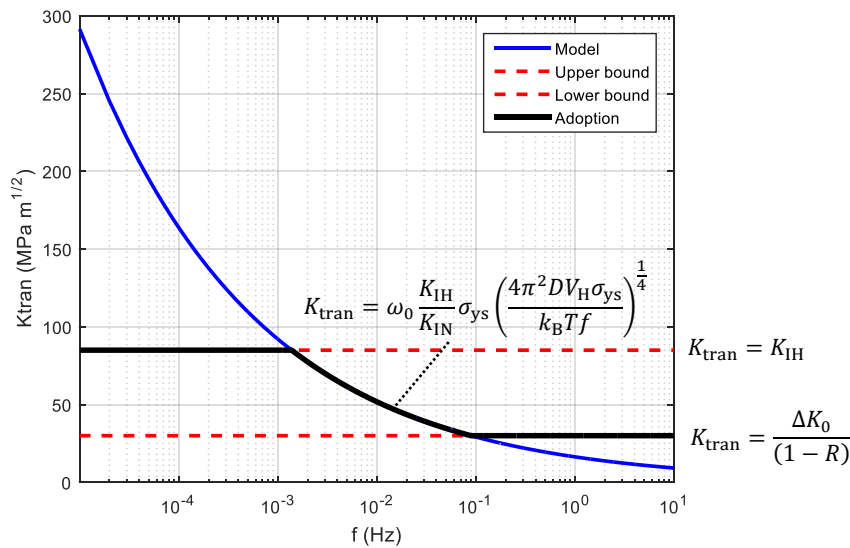


Figure 3.6 Relationship between K_{tran} and f

It can be seen that though the loading frequency f can vary in a large range ($10^{-5} - 10^{-6}$ Hz in the plotting), K_{tran} is restricted to a bounded range by the threshold stress intensity factor range and the saturated fracture toughness, as the lower and upper boundaries respectively. The value of f determines the value of K_{tran} . If K_{tran} is located at the boundary K_{IH} , it means the crack will grow with saturated hydrogen diffusion along the fatigue crack growth curve dictated by the fully degraded fracture toughness K_{IH} until final fracture happens. In other words, if the K_{tran} value calculated via equation (3 – 23) is no smaller than K_{IH} , transition behaviours may not be expected, and fractures may happen as K_{max} approaches K_{IH} . This is in

accordance with the fact that the lower the loading frequency, the stronger the corrosion effect.

3.1.2.3 Plateau Stress Intensity Range

In this research, K_p is defined as

$$K_p = \frac{\Delta K_{tH}}{(1 - R)} \quad (3 - 26)$$

K_p can be found in figure 3.2 where a nearly constant crack growth rate will be kept before the crack growth curve catches up and evolve along the new curve that has a fracture toughness locating between the K_{IN} and K_{IH} .

3.1.2.4 Fracture Toughness

As mentioned in 3.1.1, three types of fracture toughness should be determined, i.e. the inherent fracture toughness K_{IN} , the saturated fracture toughness K_{IH} , and the equilibrium fracture toughness K_{IE} .

K_{IN} is normally obtained from experiments (Gutierrez-Solana, 1982; Oh et al. 2007; Godefroid et al., 2014; Santos et al., 2010). For most of materials, the inherent fracture toughness K_{IN} can be expressed in terms of any one of the three parameters J_{IN} , CTOD and K_{IN} . If the valid data of K_{IN} are not available, K_{IN} may be approximately estimated by one of the following equations (Broek, 1974):

$$K_{IN}^2 = \frac{J_{IN} \cdot E}{(1 - \nu^2)} \quad (3 - 27)$$

$$CTOD = \frac{4}{\pi} \frac{K_{IN}^2}{E \sigma_{ys}} \quad (3 - 28)$$

where E and ν are the Young's Modulus and Poisson's ratio of material, respectively.

K_{IH} is calculated herein using Wang's model (Wang et al., 2013):

$$\frac{K_{IH}}{K_{IN}} = 1 - \beta s \frac{\sqrt{P}}{\omega \sigma_{ys}} \exp \left[\frac{2(1 + \nu)}{3} \frac{V_H}{k_B T} \frac{K_{IH}}{K_{IN}} \omega \sigma_{ys} \right] \quad (3 - 29)$$

where P is the hydrogen pressure, and s is the solubility. Once all the parameters besides K_{IH} are provided, K_{IH} is then predictable.

Based on equations (3 - 14), (3 - 17), and (3 - 18), a formula is proposed for the equilibrium fracture toughness K_{IE} as:

$$K_{IE} = \begin{cases} \left[1 - \left(\frac{r_{EAZ}}{r_c}\right)^\lambda\right] K_{IN}, & f > f_c \\ K_{IH}, & f \leq f_c \end{cases} \quad (3 - 30)$$

In general, K_{IE} is achieved by applying the corrosion-crack correlation theory and equation (3 – 30) is the correlation function of equations (3 – 14), (3 – 17), and (3 – 18). f_c is calculated from equation (3 – 18), r_{EAZ} is decided by equation (3 – 14), and r_c is obtained from equation (3 – 17). When $r_{EAZ}/r_c \geq 1 \Rightarrow f \leq f_c$, $K_{IE} = K_{IH}$; when $0 < r_{EAZ}/r_p < 1 \Rightarrow 0 < r_{EAZ}/r_c < 1 \Rightarrow f > f_c$, $K_{IE} = \left[1 - \left(\frac{r_{EAZ}}{r_c}\right)^\lambda\right] K_{IN}$; when $r_{EAZ}/r_c \rightarrow 0 \Rightarrow f \gg f_c$, $K_{IE} \rightarrow K_{IN}$. A non-negative parameter λ is used to adjust the rate with which the equilibrium fracture toughness tends toward the inherent fracture toughness. The larger the value of λ , the smaller the difference between K_{IE} and K_{IN} . Material properties and environment conditions can have an impact on the value of λ . Further investigation on this parameter may be conducted in the future. In this research, $\lambda = 1$ is adopted for demonstration purpose.

3.1.3 Discussion

The range of loading frequency in practice for pipelines transporting oil and gas is typically between 10^{-1} to 10^{-6} Hz (Yu et al., 2015). For most of the commonly used alloys, the frequency effect of constant-amplitude load on crack growth rate is negligible in dry-air environments. However, because of the presence of hydrogen, the frequency effect on fatigue crack growth behaviour appears for materials under constant-amplitude load. It is generally believed that the fatigue crack growth rate increases with lowering frequency, because lower cyclic loading frequency extends the exposure time of the material to the aggressive environment, which allows more hydrogen atoms to diffuse to a longer distance in front of the crack tip within each loading cycle. Thus the material properties near crack-tip is furtherly degraded. But observations from fatigue tests in aggressive environments have shown that there exists a critical frequency f_c , under which the material properties always show the same extent of degradation. The critical frequency changes as testing material varies (Zhao et al., 2014). The proposed equation (3 – 18) for f_c only depends on material properties and it is thus unique to the material, which agrees with the observations.

To demonstrate the validity of equation (3 – 18) for predicting the f_c , an experiment conducted by Yu et al.(2015) is utilized for a comparison between model prediction and experimental results. The experiment was performed on X60 pipeline steel and the measured critical frequency was 1.04×10^{-3} Hz. According to the experimental conditions, σ_{ys} of X60 pipeline steel = 414 MPa, $T = 303$ K, $\nu = 0.31$, $V_H = 2 \times 10^{-6}$ m³/mol. Inherent fracture

toughness K_{IN} , is assumed as 142 MPa as reported by Guedri et al. (2004). Since the material's working hardening effect ω usually ranges from 3 to 5, f_C is calculated to be in the range of 4.4×10^{-4} and $3.4 \times 10^{-3} \text{ Hz}$. While the measured critical frequency is $1.04 \times 10^{-3} \text{ Hz}$ that exactly falls in the predicted range of 4.4×10^{-4} and $3.4 \times 10^{-3} \text{ Hz}$, which shows the critical frequency of the experiment is captured by equation (3 – 18). It is thus indicated that equation (3 – 18) may provide reasonable prediction for the critical frequency of a specific material under a given loading frequency if the ω is known.

So far only a few of investigations have been done on environment-affect zone. Kim and Manning (1983) hypothesized that, the size of environment-affected zone, r_{EAZ} is in proportion to the crack-tip plastic zone size (which is a function of K_I), hydrogen diffusion coefficient for the material, and hold time in the loading profile. However, based on a vast number of experimental data obtained from fatigue tests for Inco 718 alloy under high temperature, Chang (1988) found that r_{EAZ} was a function of hold time and temperature, independent of K_I . As seen from the proposed equation (3 – 14), the estimate of r_{EAZ} is also only related to the loading frequency and it is independent of K_I , which is well supported by Chang's observation.

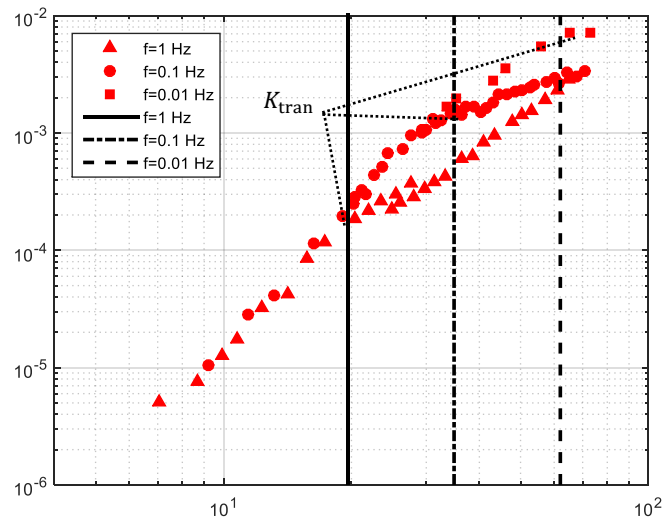


Figure 3.7 Comparison between predicted K_{tran} and experimental data of X65 steel (Vosikovsky, 1975)

Furthermore, the experimental data from tests conducted by Vosikovsky (1975) for API X65 pipeline steels under free corrosion in seawater with a series of loading frequencies can be used to confirm the validity of equation(3 – 23), since the hydrogen diffusion of a corrosion fatigue process without cathodic protection is also mainly stress-driven. As the saturated

fracture toughness is hard to be decided for a component in the free corrosion seawater environment, a degradation factor δ , with a value of 0 ~ 1, was multiplied by the inherent fracture toughness to approximate the remaining fracture toughness, namely

$$K_{IH} = \delta K_{IN} \quad (3 - 31)$$

Assume $\delta = 0.8$, i.e. 80 percent of the inherent fracture toughness is left providing a saturated diffusion condition, then the predicted transitional fracture toughness was calculated and plotted together with the test data in figure 3.7. Good agreement between model prediction (equation (3 – 23)) and experimental data is observed.

3.1.4 Model Applications

The effectiveness of the proposed corrosion-crack correlation model is demonstrated by applying it to four types of API pipeline carbon steels and comparing with experimental data, i.e., X42 (Cialone and Holbrook, 1985), X65 (Ronevich et al., 2016), X70 (Drexler et al., 2014) and X80 (Stalheim et al., 2010). X42 were tested in 6.9 MPa hydrogen gas at $f = 1$ Hz and $R = 0.1$ and $R = 0.8$. X65 were tested in 21 MPa hydrogen gas at $R = 0.5$ and $f = 1$ Hz. X70 were tested in 5.5 MPa hydrogen gas at $R = 0.5$ and $f = 1$ Hz. X80 were tested in 21 MPa hydrogen gas at $R = 0.5$ and $f = 1$ Hz. The aforementioned information are summarized in table 3.1.

API grade	R	P	f	Inherent fracture toughness	fatigue test data da/dN-ΔK
X42	0.1	6.9	1	Gutierrez-Solana (1982)	Cialone and Holbrook (1985)
X42	0.8	6.9	1	Gutierrez-Solana (1982)	Cialone and Holbrook (1985)
X65	0.5	21	1	Oh et al. (2007)	Ronevich et al. (2016)
X70	0.5	5.5	1	Godefroid et al. (2014)	Drexler et al. (2014)
X80	0.5	21	1	Santos et al. (2010)	Stalheim et al. (2010)
Unit	-	MPa	Hz	MPa√m	mm/cycle – MPa√m

Table 3.1 Experimental data for pipeline carbon steels of different API grades

The model application can be divided into two main steps. The first step is to calculate the parameters f_C and K_{tran} based on the actual experimental conditions. The second step is to achieve the Foreman coefficients using the test measured data of fatigue crack growth. The predicted model parameters are listed in table 3.2. The Foreman coefficients obtained by model calibration with experimental data are given in table 3.3. The comparison results between model prediction and experimental data are plotted in figures 3.8 ~ 3.11.

API grade	R	P	ΔK_{th}	K_{tran}	K_p	f_c	K_{IE}	ω	λ
X42	0.1	6.9	5.7	8.5	6.4	1.6×10^{-4}	145.4	4.2	1
X42	0.8	6.9	2.8	35	14.1	1.6×10^{-4}	145.4	4.2	1
X65	0.5	21	6.8	21.2	13.5	0.0013	158.4	4.8	1
X70	0.5	5.5	6.8	21.4	13.5	0.0020	188.2	4.0	1
X80	0.5	21	6.8	20	13.6	0.0014	188.7	3.2	1
Unit	-	MPa	$\text{MPa}\sqrt{\text{m}}$	$\text{MPa}\sqrt{\text{m}}$	$\text{MPa}\sqrt{\text{m}}$	Hz	$\text{MPa}\sqrt{\text{m}}$	-	-

Table 3.2 Model predictions for pipeline carbon steels of different API grades

API grade	R	P	B_1	B_2	m_1	m_2
X42	0.1	6.9	6.7×10^{-10}	1.6×10^{-6}	7.0	4.4
X42	0.8	6.9	1.0×10^{-7}	5.2×10^{-6}	4.2	4.5
X65	0.5	21	8.2×10^{-9}	1.2×10^{-5}	4.4	2.7
X70	0.5	5.5	1.7×10^{-10}	1.0×10^{-5}	6.4	3.1
X80	0.5	21	1.0×10^{-7}	2.3×10^{-6}	3.9	3.4
Unit	-	MPa	-	-	-	-

Table 3.3 Model parameters calculated from the experimental data

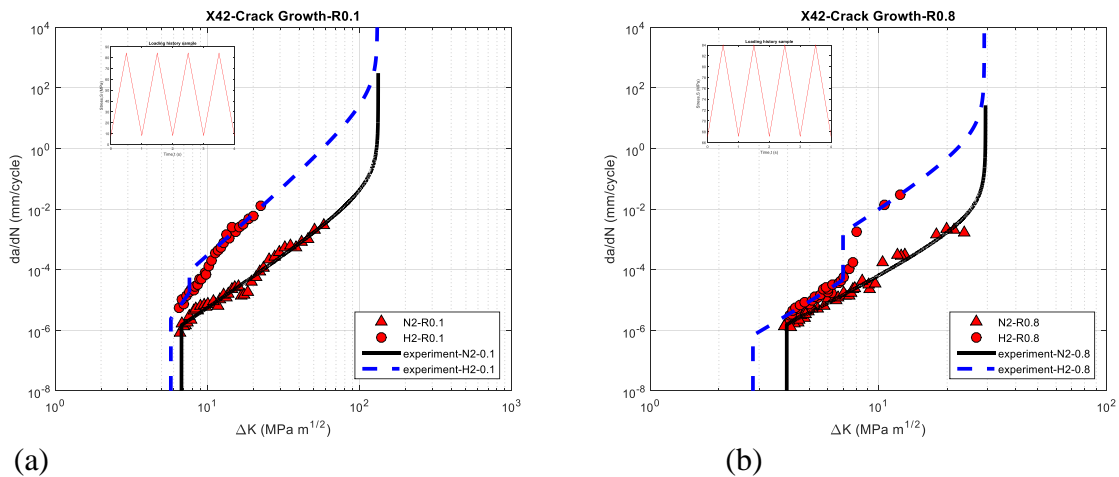


Figure 3.8 Comparison between model prediction and experimental data of X42 (Cialone and Holbrook, 1985) (a) $R = 0.1$; (b) $R = 0.8$

Figure 3.8 shows that there is significant difference in crack growth behaviour observed from the comparison between experimental data obtained under hydrogen gas and non-aggressive conditions at $R = 0.1$ and $R = 0.8$. As shown in table 3.2, the critical frequency f_c for the X42 specimen under experimental conditions calculated by equation (3 – 18) is smaller than the specific loading frequency f . Figure 3.8 also shows that the transitions in the hydrogen-

enhanced fatigue crack growth curves exactly happen at the K_{tran} predicted by equation (3 – 23), which is listed in table 3.2. As shown in figure 3.8, K_p determined by equation (3 – 26) yields a good approximation to the stress intensity range of the crack growth rate plateau and good agreements can be observed in each stage of the hydrogen-enhanced fatigue crack growth. This indicates that the model provides good prediction and also successfully captures the essence of the hydrogen-enhanced fatigue crack growth behaviour of X42 specimens tested in 6.9 MPa hydrogen gas at $f = 1 Hz$ and $R = 0.1$ and $R = 0.8$. The results show that the proposed model works well to predict the hydrogen-enhanced fatigue crack growth behaviour of X42 pipeline carbon steels under both low and high stress ratios. This illustrates that the proposed corrosion-crack correlation model can be applied to predict the hydrogen-enhanced fatigue crack growth behaviour of low-strength pipeline carbon steels under different stress ratios.

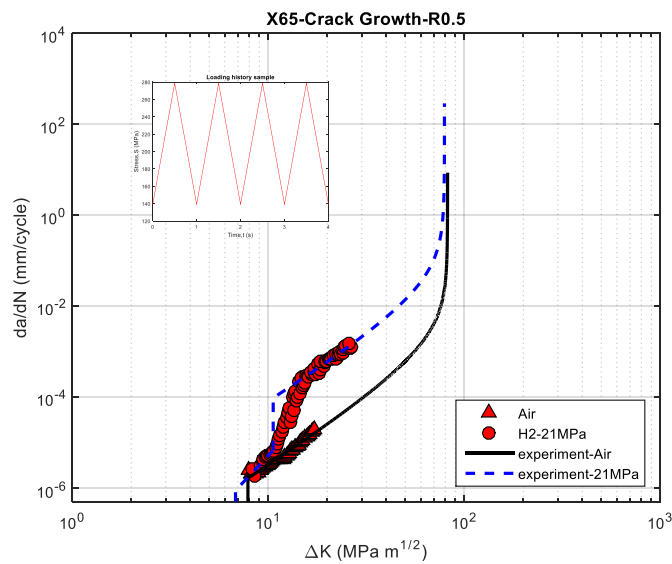


Figure 3.9 Comparison between model prediction and experimental data of X65 (Ronevich et al., 2016)

Figure 3.9 shows that the model curve agrees well with the experimental data of medium-strength carbon steel X65 tested in 21 MPa hydrogen gas at $R = 0.5$ and $f = 1 Hz$. The critical frequency f_c calculated from equation (3 – 18) for the tested X65 specimens, as listed in table 3.2, is smaller than the specific loading frequency f . As shown in figure 3.9, transition of the fatigue crack growth curve occurred at the point on the abscissa as predicted by equation (3 – 23) and then a plateau of crack growth rate appeared and lasted over a range of $K_p(1 - R)$. As K_{max} is increased continually, the crack propagates with a rapid crack growth rate approaching the critical size determined by K_{IE} . It is found that in each stage of the hydrogen-enhanced fatigue crack growth, the model curve agrees well with the

experimental data. Again, the results shown in figure 3.9 indicate that the proposed corrosion-crack correlation model provides good prediction for the fatigue crack growth behaviour of medium-strength pipeline carbon steels.

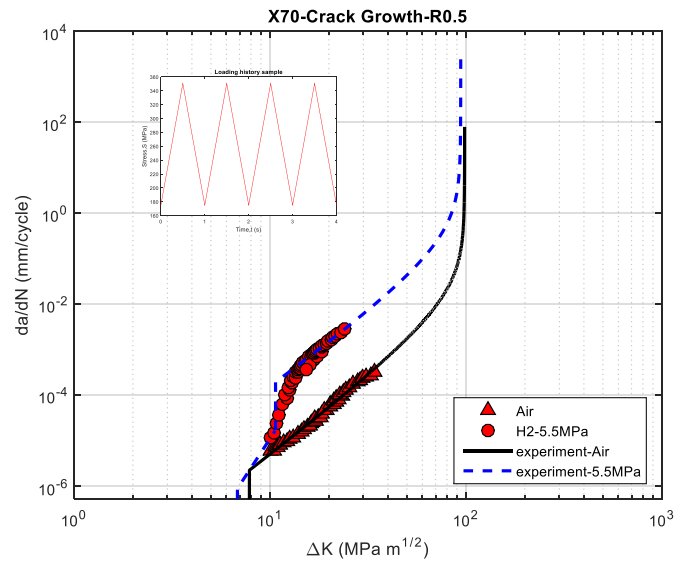


Figure 3.10 Comparison between model prediction and experimental data of X70 (Drexler et al., 2014)

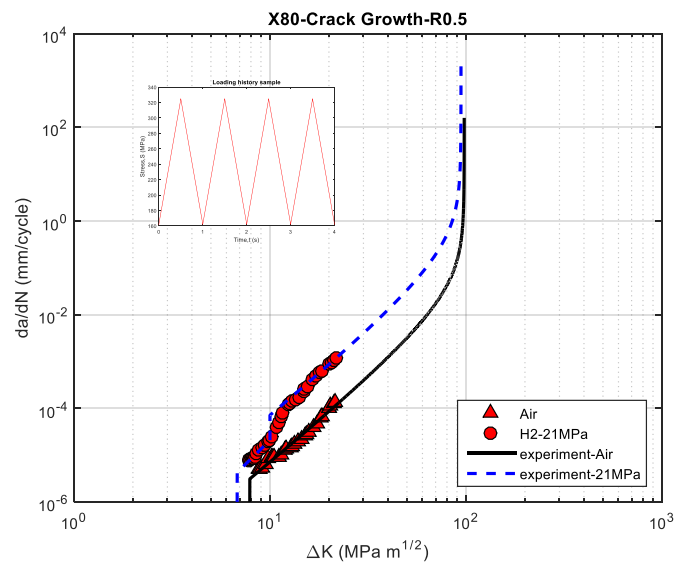


Figure 3.11 Comparison between model prediction and experimental data of X80 (Stalheim et al., 2010)

Figures 3.10 and 3.11 shows that the proposed model also works well for prediction of the hydrogen-enhanced fatigue crack growth behaviour of high-strength pipeline carbon steels X70 and X80. As predicted, table 3.2 also shows that the critical frequencies f_c estimated by equation (3 – 18) under their experimental conditions are smaller than the specific loading frequency f . It can be seen in figures 3.10 and 3.11 that both transitions of the hydrogen-enhanced fatigue crack growth curves happen at predicted K_{tran} listed in table 3.2. Both

figures also show that K_p calculated from equation (3 – 26) provides a good approximation to the stress intensity range over which the crack growth rate plateau phenomenon occurs. Good agreements are observed between the predicted hydrogen-enhanced fatigue crack growth curve and the actual experimental data of high-strength pipeline carbon steels.

3.1.5 Summary

In this 3.1 section, a corrosion-crack correlation model accounting for the influence from fracture toughness was developed based on the correlation model of environment-affected zone and plastic zone. The model is capable of modelling fatigue crack growth of pipeline carbon steels under gaseous hydrogen conditions. Experiments performed on X60 pipeline steel and corrosion fatigue tests on X65 pipelines steels were used to demonstrate the validity of the proposed formulae for predicting the critical frequency f_c and the transition stress intensity factor K_{tran} . A series of experiments for pipeline carbon steels of four API grades, X42 (low-strength), X65 (medium-strength), X70 (high-strength) and X80 (high-strength), were utilized for demonstrating the model effectiveness. The results show that

- 1) For the hydrogen-enhanced fatigue crack growth, the derived equations (3 – 18) and (3 – 23) provides good estimation for the critical frequency and the transition stress intensity factor.
- 2) The proposed corrosion-crack correlation model provides good prediction for the fatigue crack growth behaviour of low-strength, medium-strength, and also high-strength pipeline carbon steels.
- 3) Plateau stress intensity range K_p calculated from the proposed equation (3 – 26) provides a good approximation to the stress intensity range over which the crack growth rate plateau phenomenon occurs.

The research work in this section has been summarized and published by Cheng and Chen (2017a).

3.2 Corrosion Fatigue Crack Growth in Seawater

Corrosion fatigue is receiving more and more attention in recent years. A number of models have been developed for corrosion fatigue of metals in aqueous environments (Kim et al., 1998). However, most of them are just phenomenological because the material's corrosion fatigue cracking behavior is quite complicated and considerable variables can impose their impacts, while the involved mechanisms are not very clear. Based on the recent research on

the mechanisms and modelling of environment-assisted cracking (Rhodin, 1959; McEvily and Wei, 1972; Gerberich et al., 1988; Parkins, 1992; Rhodes, 2001; Gangloff, 2008; Wang et al., 2013), a two-component corrosion fatigue crack growth model for subsea pipeline steels is proposed in this section, in which the hydrogen embrittlement model established in the last section is integrated with an anodic dissolution model in the frame of fracture mechanics. The model is then applied to modelling the corrosion fatigue crack growth of X65 pipeline steel and the impact of loading frequency, stress ratio, temperature, and hydrogen concentration on the model performance is discussed.

3.2.1 Corrosion Fatigue Mechanisms

No metal is immune from some reduction of its resistance to cyclic loading if the metal is put in a corrosive environment. But different environment-material systems may exhibit distinct corrosion fatigue cracking behaviours. According to McEvily and Wei (1972), those behaviours belong to three types, type A, type B, and the mixed type. Each type is schematically plotted in figure 3.12.

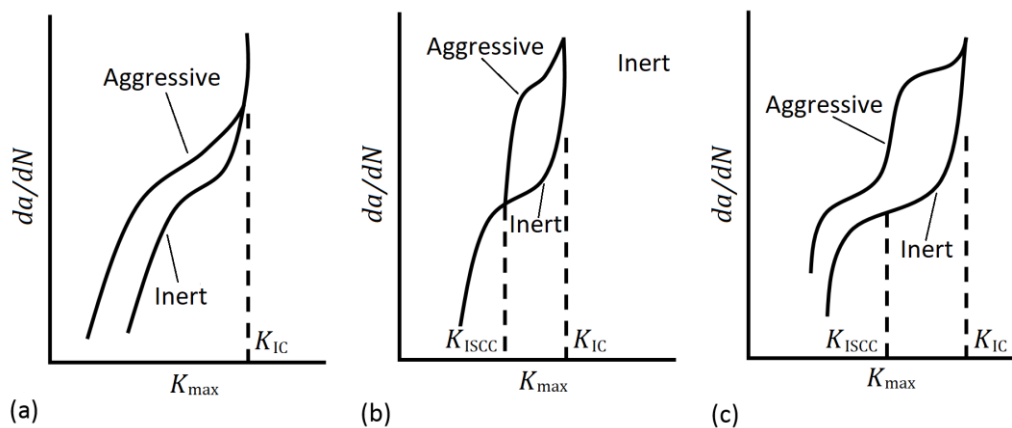


Figure 3.12 Corrosion fatigue behaviour: (a) Type A; (b) Type B; (c) Mixed type. (McEvily and Wei 1972, log-log plot).

Type A describes the behavior where the threshold K_{th} is reduced and crack growth rate is enhanced by the presence of the corrosive environment at all levels of K . Type B represents the behavior typified by the enhanced crack growth beyond the K_t and is characterized with a plateau in crack growth rate. The mixed type, where type B behavior happens above K_t with type C behavior superimposed on at all K levels below, is exhibited by a broad range of material-environment systems, and is typical of pipeline steels in seawater.

Due to the complicated nature of corrosion fatigue, current simplified corrosion fatigue crack growth models often provides predictions that are either over-conservative or under-estimated. For example, as shown in figure 3.13(a), the over conservatism in predictions by

linear models from BS 7910 (2015) and API 579-1/ASME FFS-1 (2016) is obvious. While in figure 3.13(b), both bilinear models provided by BS 7910 (2015) and API 579-1/ASME FFS-1 (2016) fail to predict the corrosion fatigue crack growth rate of X65 pipeline steels in seawater conservatively. The corrosion fatigue data under a loading frequency of 0.01 HZ and a stress ratio of 0.2 go beyond the prediction at relatively high stress intensity factor ranges. More attention should be paid to such problems since the lost corrosion fatigue crack growth rates are fairly high, thus greatly increasing the risk of sudden failure of the component.

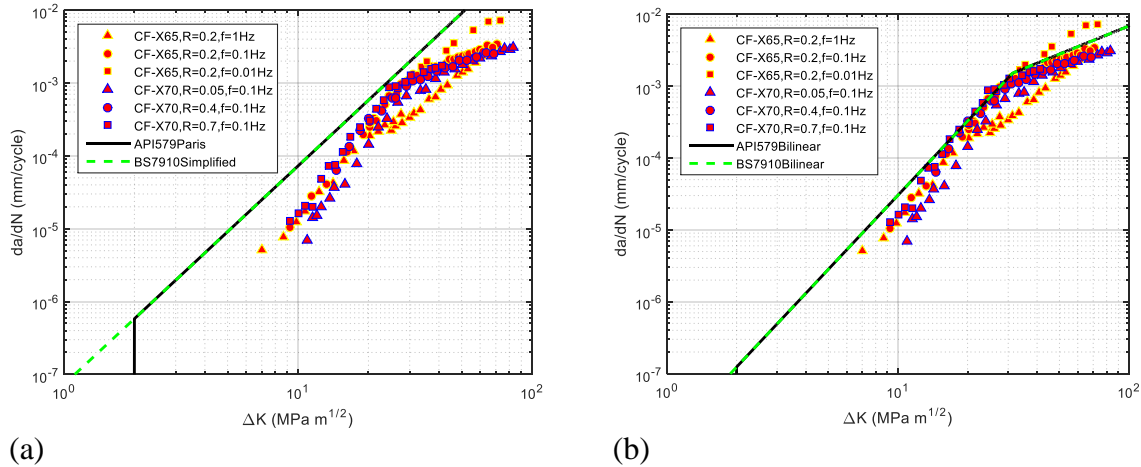


Figure 3.13 Experimental corrosion fatigue data of X65 (Vosikovsky, 1975) and X75 (Vosikovsky, 1981) in comparison with model predictions of API 579-1/ASME FFS-1 and BS 7910: (a) Simple linear model; (b) Bilinear model.

3.2.2 Model Development

To be consistent with engineering critical assessment, the model to be built should be in a framework of linear elastic fracture mechanics.

3.2.2.1 Fracture Mechanics

The theory of linear elastic fracture mechanics was developed in the 1950s by Irwin (1957) to describe the crack growth under sustained loads and introduce the concept of stress intensity factor

$$K = FS\sqrt{\pi a} \quad (3 - 32)$$

where F is the geometry function, S is the stress, and a is the characteristic dimension of the crack. For through-thickness cracks, a represents the half crack length, for surface cracks, a is the flaw height, and for embedded cracks, a is the half height.

The loading pattern of subsea pipelines is a combination of hydrostatic and cyclic loads. In some extreme cases, the ratio between the hydrostatic load contribution and the cyclic load

contribution in subsea pipelines may be greater than unity. This can be accounted for by the mean stress effects in fracture mechanics analysis (Bannantine et al., 1990).

The assumed fatigue crack growth rate at Stage II usually follows of Paris' law (Paris and Erdogan, 1963)

$$\frac{da}{dN} = C(\Delta K)^m \quad (3 - 33)$$

where m and C are constants for a specific material; ΔK is the so-called stress intensity factor range and is calculated by

$$\Delta K = (1 - R)K_{\max} \quad (3 - 34)$$

with R and K_{\max} being the stress ratio (i.e. S_{\min}/S_{\max}) and maximum stress intensity factor encountered in a stress cycle, respectively.

In a log-log plot of da/dN vs ΔK , Paris law represents a straight line of a slope m . Behavior of short cracks, i.e. cracks in stage I, departs from a simple Paris' law representation. Below a certain value of ΔK (known as the threshold value, ΔK_{th}) no macrocrack growth is expected. Whereas when K_{\max} approaches K_{IC} the crack growth rate increases rapidly. The fatigue life of a component in an inert environment can be roughly divided into two parts: crack initiation and crack growth. Fracture mechanics being applied to corrosion fatigue enables the corrosion fatigue life fractions to be defined within the criteria of crack initiation and propagation. For the engineering critical assessment applied at design stage, prediction of life before crack initiation is decisive, since the initiation process can cost much longer time. However, for the assessment applied in-service for to determine inspection intervals, since cracks already exist, prediction of life after crack initiation becomes decisive. In a typical corrosion fatigue situation, cracks initiate from corrosion sites and grows under the influence from environment, thus the initiation stage is often bypassed. Moreover, in practice, cracks detected on subsea pipelines are mostly at the propagation stage. Therefore, the research work of this section focuses on the crack growth in the stage of crack growth and linear elastic fracture mechanics is applied to establish a typical corrosion fatigue model for subsea pipelines at service.

3.2.2.2 General Model

Several attempts have been made to model environmentally-assisted crack growth under cyclic loading by superposing different processes. The classic model proposed by Landes and Wei (1969), as shown in equation (3 - 35), simply treats the rate of corrosion fatigue crack

growth $(da/dN)_{CF}$, as the algebraic sum of the rate of crack growth in an inert environment $(da/dN)_F$, and that of stress corrosion cracking $(da/dN)_{SCC}$ in the identical aggressive environment.

$$\left(\frac{da}{dN}\right)_{CF} = \left(\frac{da}{dN}\right)_F + \left(\frac{da}{dN}\right)_{SCC} \quad (3 - 35)$$

The process competition model of Austen and Walker (1977) is based on the assumptions that fatigue and stress corrosion cracking are two mutually competitive processes and that the crack will propagate at a faster rate pertinent to the prevailing stress intensity factor.

However, to ensure compatibility in terms of crack growth rate per cycle rather than per second, the plateau crack growth rate must be adjusted to the appropriate frequency or to the frequency, stress intensity and stress ratio. The influences of high frequencies on the crack growth rate plateau are predicted better than those of low frequencies. Other models (Hagn, 1988; Kim et al., 1998) modified these assumptions mostly by adding parameters.

3.2.2.3 Component Model

Based on the previous investigation on mechanisms of stress corrosion cracking and corrosion fatigue, the latter can be viewed as a joint action of stress corrosion and hydrogen embrittlement. A two-component physical model is proposed herein as

$$\left(\frac{da}{dN}\right)_{CF} = \left(\frac{da}{dN}\right)_{SC} + \left(\frac{da}{dN}\right)_{HAC} \quad (3 - 36)$$

where $(da/dN)_{HAC}$ is the crack growth rate by hydrogen-assisted cracking. The proposed model basically means that $(da/dN)_{CF}$ is an aggregate of the rates of stress corrosion, $(da/dN)_{SC}$ and hydrogen-assisted cracking, $(da/dN)_{HAC}$. The two-component description holds as long as corrosion fatigue is composed of stress corrosion and hydrogen-assisted cracking, in spite of possible interaction between the two processes. Anderson (2005) mentioned a similar superposition model, however, it superposed cycle-dependent corrosion fatigue with time-dependent corrosion fatigue, both of which are defined in a phenomenological way, leading to difficulty in implementing the model. In contrast, this proposed two-component model proposed is based upon physics while still being compatible with fracture mechanics.

Anodic Dissolution

Several models have been developed for explaining the crack growth in stress corrosion cracking due to anodic dissolution. A well-accepted one (Parkins, 1979) is the film rupture

model, which states while the metal surface is covered by a passive or protective layer, the crack tip is kept free from protective layers continuously or discontinuously by local chemical and mechanical effects, and this allows the accelerated anodic dissolution of local material. To a large extent, anodic dissolution models for corrosion fatigue are extension of those proposed for stress corrosion cracking. In such a view, the anodic dissolution process of corrosion fatigue is described as cyclic plastic strain ruptures a protective film at the crack tip, resulting in transient anodic dissolution, followed by possible re-passivation. The amount of environmental crack growth per fatigue cycle depends on the kinetics of the reaction on the clean metal surface as well as the time between film ruptures. All factors imposing influence on corrosion fatigue process seem to work through the film rupture mechanism. Based on the physical facts, a formula is proposed for the crack growth by stress corrosion over the whole regime of K_{\max}

$$\left(\frac{da}{dN}\right)_{SC} = \left(\frac{da}{dN}\right)_{AD} = h(\Delta K, R, f) = \begin{cases} h_1(\Delta K, R, f), & K_{\max} < K_t \\ h_2(\Delta K, R, f), & K_{\max} \geq K_t \end{cases} \quad (3 - 37)$$

where $(da/dN)_{AD}$ is the crack growth rate due to anodic dissolution, f is the stress cycle frequency, and K_t is the transition stress intensity factor, i.e. where the crack growth rate plateau starts in a abscissa of K_{\max} . Endo et al. (1981) conducted a series of experiments on carbon steels in NaCl solution to investigate the stress corrosion crack growth rate of steels due to anodic dissolution under fatigue loading conditions. They claimed that the observed corrosion fatigue crack growth followed the sequential model,

$$\left(\frac{da}{dN}\right)_{CF} = \left(\frac{da}{dN}\right)_F + \left(\frac{da}{dN}\right)_{AD} \quad (3 - 38)$$

where

$$\left(\frac{da}{dN}\right)_{AD} = Af^b(1 - R)^c\Delta K^m \quad (3 - 39)$$

A , b and c are the material-environment system coefficients. According to the experimental data, $A = 4.93 \times 10^{-12}$, $b = -0.36$, $c = 2$ and m is the same as that in the expression of crack growth in air, i.e. equation (3 - 33). The negative value of b is consistent with the experimental observation by Bartlett and Hudak (1990) that the higher the frequency, the lower the anodic dissolution rate, which means b is usually negative. It is suspected that the frequency and stress ratio dependence is determined by the solution conditions. Thus for a medium such as seawater, b may considered the same as that of the NaCl solution. So

$$h_1(\Delta K, R, f) = Af^{-0.36}(1 - R)^2\Delta K^m \quad (3 - 40)$$

Effects of coefficient A on the shape of the crack growth curve are shown in figure 3.14.

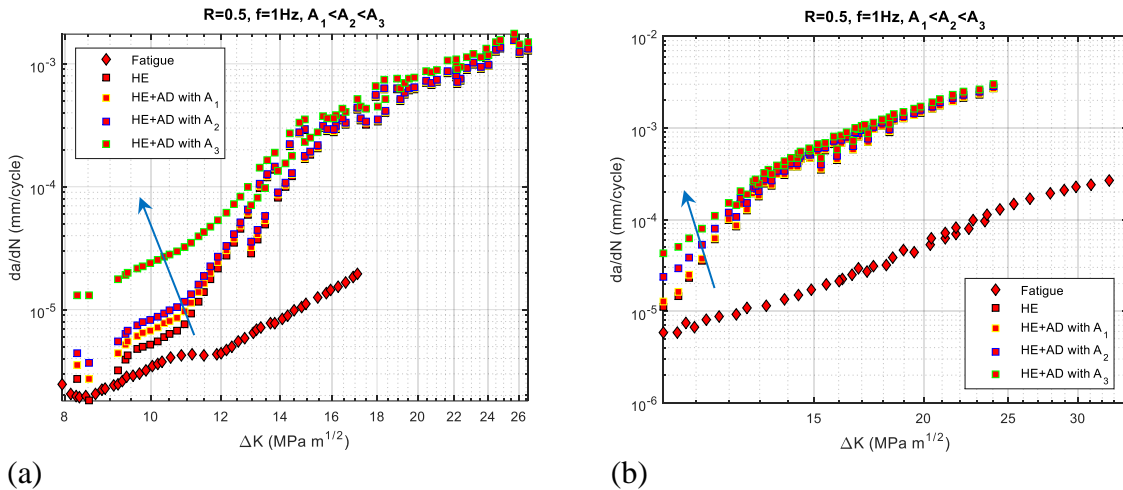


Figure 3.14 Anodic dissolution influence on the shape of crack growth curve: (a) X65 (Ronevich et al., 2016); (b) X70 (Drexler et al., 2014)

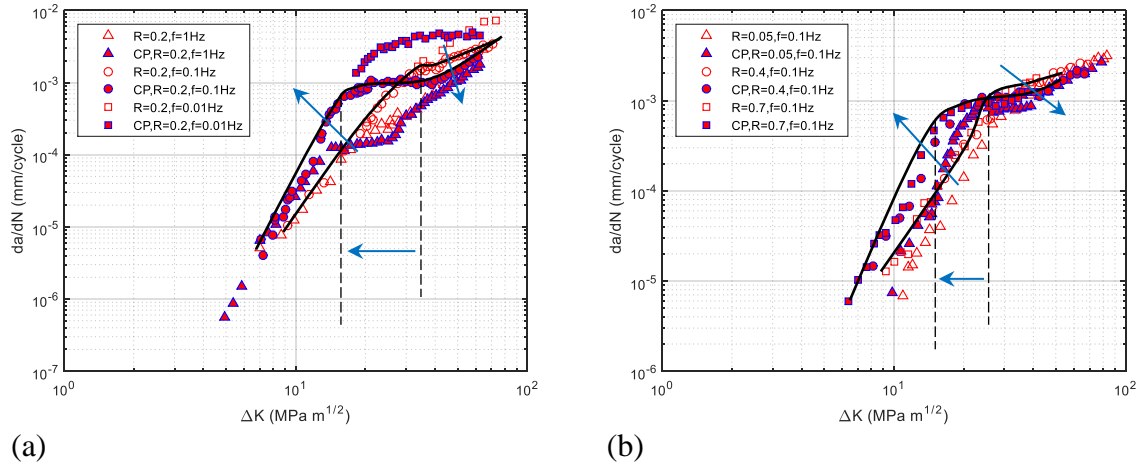


Figure 3.15 Pipeline steel specimens in seawater with and without cathodic protection (CP): (a) X65 (Vosikovsky, 1975); (b) X70 (Vosikovsky, 1981)

Aware that cathodic protection works through inhibiting the corrosion process. More specifically, cathodic protection prevents the occurrence of anodic dissolution at the crack tip. The corrosion fatigue crack growth data of X65 pipeline steel specimen in NaCl water with and without cathodic protection are plotted in figure 3.15, as well as those of X70 (Vosikovsky, 1975; Vosikovsky, 1981). As can be seen, the change of crack growth rates after imposing a cathodic protection is very small when ΔK goes beyond the plateau, thus roughly

$$h_2(\Delta K, R, f) \approx Af^{-0.36}(1 - R)^2 K_t^m \quad (3 - 41)$$

This is consistent with the aforementioned anodic dissolution mechanism. According to the anodic dissolution mechanism, as ΔK is growing, there is a critical value of ΔK where

repassivation disappears. Below this value, anodic dissolution occurs discontinuously; above this value, anodic dissolution effect will be constant. Compared with the increasing hydrogen-assisted cracking rate, this constant rate is very small and its ratio to the hydrogen-assisted cracking rate is still decreasing, evidenced as the pair of crack growth curves with and without cathodic protection approaching each other after the transition point, as shown in figure 3.15.

Hydrogen Embrittlement

As for hydrogen-assisted cracking, crack growth is associated with hydrogen impurity in the material. The hydrogen may be a by-product of corrosion reactions in aqueous solutions or cathodic protection. The absorbed hydrogen atoms diffuse to the region near the crack tip with stresses applied. The presence of hydrogen in metal is known to have an adverse effect on the material's properties, more specifically the concentration of hydrogen ahead of a crack tip can cause a significant reduction in the material's resistance to fracture (Humphries et al., 1989). In such a situation, cracking happens at a lower stress level compared to that of the same material without hydrogen absorption and crack propagates in an enhanced rate. This phenomenon is called hydrogen embrittlement. Although there is still controversy as to the extent to which hydrogen-assisted cracking explains subcritical crack growth in metals stressed in environments that support concurrent crack tip dissolution, passive film formation, and atomic hydrogen production. An agreement has been reached that hydrogen embrittlement normally prevail for subsea metal structures with cathodic protection as well as those exposed to gaseous hydrogen (Barnoush, 2011). Studies on the mechanism of hydrogen embrittlement started several decades ago and are still ongoing. Among the numerous mechanisms that have been raised so far, three have stood critical examinations and been widely accepted, i.e. hydrogen-enhanced de-cohesion, hydrogen-enhanced localized plasticity, and adsorption-induced dislocation emission. Arguments supporting each are not definitive, even not exclusive. For those who are interested, ample information can be found in a recent critical review by Lynch (2012). Not surprisingly, hydrogen-enhanced de-cohesion has been frequently used as the theoretical basis for modelling hydrogen embrittlement because of its explicit compatibility with fracture mechanics.

Hydrogen-enhanced de-cohesion provides the basic notion that hydrogen damage occurs in the crack-tip plastic zone when the local crack tip opening tensile stress exceeds the maximum-local atomic cohesion strength, which has been lowered by the presence of hydrogen (Oriani, 1972). Hence locations of hydrogen damage initial sites are at a distance ahead of the crack tip, i.e. the locations where tensile stresses are maximized. Thus mechanical characteristics of the region near the crack tip should be analyzed, since it can

control the precise damage location. A model based on the theory of hydrogen-enhanced de-cohesion should involve factors such as the tensile stress distribution in front of a crack tip, the plastic strain and the associated dislocation density profile about the crack tip, the distribution of hydrogen trap sites, and the concentration of environmentally produced hydrogen in the crack-tip area. To establish such a model, the mathematically formulated mechanism of hydrogen-enhanced de-cohesion by Lee and Unger (1988) was adopted, i.e.

$$\sigma_{\max H} = \sigma_{\max 0} - \beta C_H \quad (3 - 42)$$

where $\sigma_{\max H}$ and $\sigma_{\max 0}$ are the maximum principal stress at elastic-plastic boundary with and without hydrogen when cracking initiates, respectively. β is a parameter related to loss of critical cohesive stress by hydrogen impurity, and C_H is the local hydrogen concentration. It represents the assumption that fracture occurs when the maximum crack-tip-opening stress exceeds the hydrogen-reduced cohesive strength within an area in front of the crack tip.

C_H can be calculated by Fick's law with respect to the hydrostatic stress (Van Leeuwen, 1974)

$$C_H = C_{H0} \exp\left(\frac{\sigma_h V_H}{k_B T}\right) \quad (3 - 43)$$

where C_{H0} is the local hydrogen concentration in unstressed state, σ_h is the hydrostatic stress within plastic zone, V_H is the partial volume of hydrogen, k_B is the Boltzmann constant, and T is the temperature.

With the help of linear elastic fracture mechanics, expressions of the hydrostatic stress σ_h and the maximum crack-tip-opening stress in front of crack tip σ_{\max} under mode I with plane strain condition are (Broek, 1974),

$$\sigma_h = \frac{2}{3}(1 + \nu) \frac{K}{\sqrt{2\pi r}} \quad (3 - 44)$$

$$\sigma_{\max} = \sigma_{yy} = \frac{K}{\sqrt{2\pi r}} \quad (3 - 45)$$

where r is the radial distance from crack tip, ν is the Poisson's ratio, and σ_{yy} is the stress along the Y direction. Combining equations (3 - 41) ~ (3 - 44), with the assumption that the location of the crack initiation does not change with hydrogen concentration, Wang et al. (2013) obtained the following formula for predicting the hydrogen-degraded fracture toughness,

$$K_{IH} = K_{IC} \left\{ 1 - \left(\frac{\beta C_{H0}}{\omega \sigma_{ys}} \right) \exp \left[\frac{V_H \sigma_{ys}}{k_B T} \cdot \frac{2(1+\nu)}{3} \cdot \frac{K_{IH}}{K_{IC}} \right] \right\} \quad (3-46)$$

where ω is a magnification factor of value 3 ~ 5 accounting for the material's working hardening effect, and K_{IH} is the saturated fracture toughness, i.e. the fracture toughness fully degraded in the environment with a specific hydrogen concentration. This model has been applied to a series of steels to describe the dependence of fracture toughness on hydrogen concentration, and the predicted results match well with the experimental data.

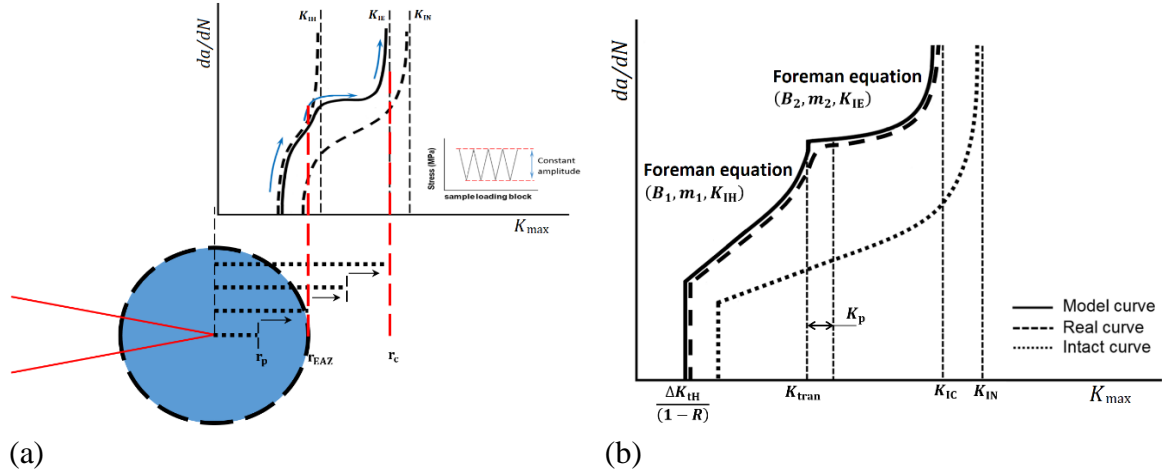


Figure 3.16 Model of crack growth for the hydrogen embrittlement part of corrosion fatigue: (a) Corrosion-crack correlation; (b) Two-stage Forman equation model.

Instead of Paris' law, Forman equation is adopted for its integration of mean stress influence via the stress ratio R and the static failure via K_{IC} in region II and region III,

$$\frac{da}{dN} = \frac{B(\Delta K)^m}{[(1-R)K_{IC} - \Delta K]} \quad (3-47)$$

In Section 3.1, a two-stage Forman equation model was proposed for the hydrogen-enhanced fatigue crack growth in hydrogen gas. It is based on the corrosion-crack correlation and the theory of hydrogen-enhanced de-cohesion, which is consistent with equation (3-45). The key assumption in this model is the stress-driven hydrogen diffusion, namely the absorption of the hydrogen ions into the crack tip is through transporting up the hydrostatic stress gradients. This process is schematically plotted in figure 3.16.

Such an assumption enables the model to calculate several crucial points to capture features of the hydrogen-enhanced fatigue crack growth. Note that this assumption is not applicable to the fatigue cracking of subsea pipeline steels under cathodic protection. Cathodic protection provides a potential intensifying the hydrogen absorption, which is mainly manifested as the decrease or left shift of K_t in the crack growth curve, as seen in figure 3.16.

The transition stress intensity factor K_t , i.e. the point where the environment affected zone is passed by the plastic zone in front of crack tip and the plateau section of the crack growth curve starts, can be calculated as

$$K_t = \min \left\{ \max \left\{ K_{\text{tran}}, \frac{\Delta K_0}{(1-R)} \right\}, K_{\text{IH}} \right\} \quad (3-48)$$

where ΔK_0 represents the threshold stress intensity factor range at $R = 0$ (usually obtained from experiments), and

$$K_{\text{tran}} = \omega \sigma_{\text{ys}} \frac{K_{\text{IH}}}{K_{\text{IC}}} \left(\frac{4\pi^2 DV_{\text{H}} \sigma_{\text{ys}}}{k_{\text{B}} T f} \right)^{\frac{1}{4}} \quad (3-49)$$

The range length of stress intensity factor over which the crack growth rate plateau lasts is approximated by

$$K_p = \frac{\Delta K_{\text{tH}}}{(1-R)} \quad (3-50)$$

where ΔK_{tH} is obtained by following equation

$$\Delta K_{\text{tH}} = \Delta K_{\text{th}} - 1 \quad (3-51)$$

The final fracture toughness displayed under a fatigue load, or alternatively the equilibrium fracture toughness K_{IE} , is proposed to be

$$K_{\text{IE}} = \begin{cases} \left[1 - \left(\frac{2\pi(\omega\sigma_{\text{ys}})^2}{K_{\text{IC}}^2} \sqrt{\frac{DV_{\text{H}}\sigma_{\text{ys}}}{k_{\text{B}}Tf}} \right)^{\lambda} \right] K_{\text{IN}}, & f > f_c \\ K_{\text{IH}}, & f \leq f_c \end{cases} \quad (3-52)$$

where λ is a non-negative parameter used to adjust the rate with which K_{IE} approaches K_{IC} , i.e. the inherent fracture toughness. In consistence with last section, λ is considered to be 1.0.

Then K_{IC} in equation (3-47) is substituted by K_{IH} and K_{IE} respectively for the first and second stage Forman equations. Good agreement can be seen from the application of the two-stage Forman equation model to a wide range of carbon pipeline steels in Section 3.1. Thus, the hydrogen-assisted cracking rate of the two-component corrosion fatigue model, is established as

$$\begin{aligned}
\left(\frac{da}{dN}\right)_{\text{HAC}} &= \left(\frac{da}{dN}\right)_{\text{HE}} \\
&= g(\Delta K, R, f, K_{\text{IC}}, C_{\text{H0}}) \\
&= \begin{cases} g_1(\Delta K, R, f, K_{\text{IH}}, C_{\text{H0}}), & K_{\text{max}} < K_{\text{t}} \\ g_2(\Delta K, R, f, K_{\text{IE}}, C_{\text{H0}}), & K_{\text{max}} \geq K_{\text{t}} \end{cases} \quad (3-53)
\end{aligned}$$

where

$$g_1(\Delta K, R, f, K_{\text{IH}}, C_{\text{H0}}) = \frac{B_1(\Delta K)^{m_1}}{[(1-R)K_{\text{IH}} - \Delta K]} \quad (3-54)$$

$$g_2(\Delta K, R, f, K_{\text{IE}}, C_{\text{H0}}) = \frac{B_2(\Delta K)^{m_2}}{[(1-R)K_{\text{IE}} - \Delta K]} \quad (3-55)$$

$(da/dN)_{\text{HE}}$ is the crack growth rate due to hydrogen embrittlement. Note that B_1 and m_1 are acquired from the crack growth data measured before ΔK reaches $(1-R)K_{\text{t}}$, while B_2 and m_2 are acquired from the crack growth data measured after the point $(1-R)(K_{\text{t}} + K_{\text{p}})$.

3.2.3 Model Applications

In terms of equations (3-36), (3-37), and (3-53), the two-component model can be reformulated as

$$\begin{aligned}
\left(\frac{da}{dN}\right)_{\text{CF}} &= \left(\frac{da}{dN}\right)_{\text{AD}} + \left(\frac{da}{dN}\right)_{\text{HE}} \\
&= \begin{cases} h_1(\Delta K, R, f) + g_1(\Delta K, R, f, K_{\text{IH}}, C_{\text{H0}}), & K_{\text{max}} < K_{\text{t}} \\ h_2(\Delta K, R, f) + g_2(\Delta K, R, f, K_{\text{IE}}, C_{\text{H0}}), & K_{\text{max}} \geq K_{\text{t}} \end{cases} \quad (3-56)
\end{aligned}$$

In this part, the proposed model will be applied to X65 pipeline steels to display its general performance. X65, the medium strength pipeline steel, is commonly adopted in offshore oil and gas production systems and is currently one of the highest API grade C-Mn steels for offshore service for its good ductility and toughness. In this application, the influence of wedge effect caused by the accumulation of corrosion product within the crack tip cavity is ruled out by using ΔK_{eff} as the default ΔK .

The two-component model allows the superposition of anodic dissolution and hydrogen embrittlement cracking rates. Due to a lack of exact experimental data for determining the anodic dissolution rate of corrosion fatigue in pipeline steels, the related coefficients will be given approximated values for the demonstrative purpose. On the other hand, corrosion fatigue in seawater shares the same hydrogen embrittlement nature with the hydrogen-assisted cracking of pipeline steels in hydrogen gas, while the experimental data of hydrogen-enhanced fatigue cracking in hydrogen gas are plentiful. Ronevich et al. (2016) performed a

series of tests on X65 pipeline steels and obtained the hydrogen-enhanced fatigue crack growth data. Experimental data of mechanical properties for X65 pipeline steels both in dry air and hydrogen gas were collected by Somerday and Marchi (2007). For the gaseous hydrogen environment, C_{H_0} is calculated as the product of solubility and the square root of pressure. The values of coefficients for determining the hydrogen embrittlement rate in the proposed model for X65 pipeline steel are adopted in accordance with the research work in the previous Section 3.1.

As for β , as stated in the notion of hydrogen-enhanced de-cohesion, β is a parameter related to the loss of critical cohesive stress by hydrogen impurity, which is a material property. Gutierrez-Solana and Elices (1982), and Cialone and Holbrook (1985), conducted a series of tests on the fracture toughness degradation of X42 and X70 pipeline steels in hydrogen gas of different pressures, respectively. Based on the fact that pipeline carbon steels usually share similar chemical composition and exhibit a common ferritic-pearlitic microstructure (Holtam, 2010). It is expected that the sensitivities of C-Mn steels of different strengths to hydrogen embrittlement should follow some relationship. In this research, linear interpolation between the β values of X42 and X70 is used with respect to the yield strength, and the β value of X65 pipeline steels is thus determined as $1.56 \times 10^4 \text{ MPa m}^3 (\text{mol H}_2)^{-1}$.

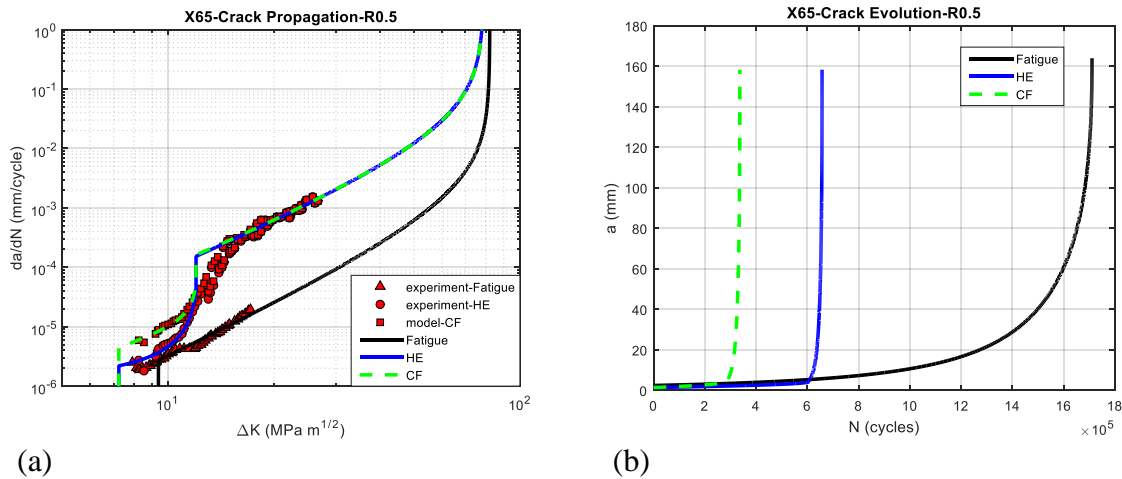


Figure 3.17 Model application to X65 pipeline steels with R=0.5 (Ronevich et al., 2016): (a) crack growth; (b) crack evolution.

The model implemented for X65 pipeline steel is shown in figure 3.17 and the related calculation results are listed in table 3.4 ($A = 3.93 \times 10^{-11}$ is adopted in the model calculation for demonstration). In the diagram of remaining fatigue life the effect of hydrogen embrittlement and corrosion fatigue on remaining fatigue life can be seen straightforward. The two-component model, by imposing the anodic dissolution rate to the hydrogen embrittlement rate, reasonably simulates the shape of the total crack growth curve. Obviously,

the anodic dissolution process gives a rise of the crack growth curve before $(1 - R)K_t$. This effect is quite significant at low ΔK regime. An analysis on the influence of the many factors involved in the proposed model is displayed below.

X65	R	K_t	Crack evolution time	Life reduction
<i>Fatigue</i>	0.5	-	1.7110×10^6	-
<i>Hydrogen embrittlement</i>	0.5	24	6.5756×10^5	61.568%
<i>Corrosion fatigue</i>	0.5	24	3.3674×10^5	80.318%
<i>Unit</i>	-	$\text{MPa}\sqrt{\text{m}}$	Cycle	-

Table 3.4 Model calculation results for X65 pipeline steel

3.2.3.1 Loading Frequency

For most of commonly used alloys, the effect of frequency on crack growth under constant-amplitude fatigue loads in inert environments is negligible. However in the presence of a corrosive environment, the effect of frequency is magnified since it is directly related to hydrogen diffusion and thus hydrogen embrittlement. The time dependent characteristic of hydrogen diffusion indicates that the loading frequency f may have an impact to the corrosion fatigue crack growth. More specifically, lowering the loading frequency increases the exposure time of the metal to the corrosive environment, thus within each load cycle more atomic hydrogen may enter the material via the crack tip and diffuse a longer distance. Observations from fatigue tests in corrosive environments have proven the existence of critical frequency f_c , below which the material always shows no frequency dependence. For a corrosion fatigue process at f_c , its propagation curve should be in a shape like that plotted in figure 3.13(a), which is not the typical type of corrosion fatigue behavior for pipeline steels in seawater. Hence this research puts its focus on the case where $f > f_c$, which is typical for corrosion fatigue of subsea pipeline steels in seawater.

In a typical situation, the influence of loading frequency can be divided into two parts, one is on the anodic dissolution process before ΔK reaches $K_t(1 - R)$. The decrease of f will cause the increase of anodic dissolution rates at each level of ΔK , as predicted by equation (3 - 39). This is because anodic dissolution rate is affected by the time available for chemisorption at the crack tip during each cycle. The higher growth rate result at lower frequencies occurs because the corrosive environment has more contact time with the crack surfaces, while at higher frequencies, the corrosive environment cannot fully penetrate the crack tip before the crack begins to close again. The experimental observation by Bartlett and

Hudak (1990) that a higher frequency resulted in lower fatigue crack growth rates than those at reduced frequencies supports this explanation. But in the log-log plot of da/dN vs ΔK , such increases are attenuated. The other part of the frequency influence is on the hydrogen embrittlement process, according to equation (3 – 49), the value of K_t decreases as f increases, manifesting as a left shift of the transition point on the crack growth curve, as seen in figure 3.18.

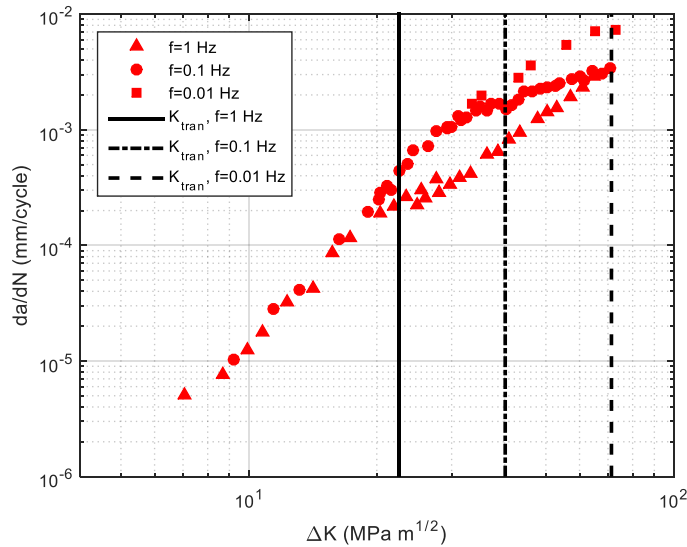


Figure 3.18 Loading frequency effect on K_t for X65 pipeline steels (Vosikovsky, 1975)

3.2.3.2 Hydrogen Concentration

The hydrogen concentration C_{H0} is specified as the local hydrogen concentration in the material in front of a crack tip with the unstressed state. Most previous experiments of corrosion fatigue for pipeline steels in seawater can hardly provide any information of C_{H0} . However, to some extent, the experimental data from tests conducted by Vosikovsky (1975) for API X65 pipeline steels under free corrosion in seawater with a series of loading frequencies can be used to investigate the influence of C_{H0} , since K_{IH} is calculated based on C_{H0} according to equation (3 – 46). Nevertheless, the K_{IH} for a component is hard to be decided under the free corrosion condition. For the purpose of demonstration, a degradation factor δ with a value of 0 ~ 1, representing the terms except K_{IN} at right hand side of equation (3 – 46), was used to multiply the inherent fracture toughness to approximate the remaining fracture toughness, namely

$$K_{IH} = \delta K_{IN} \quad (3 - 57)$$

Assume $\delta = 0.8$, i.e., 80 percent of the inherent fracture toughness is left providing a saturated hydrogen diffusion condition, then the predicted transitional points K_t on crack growth curves were calculated and plotted together with the test data in figure 3.18.

Good agreement between model prediction and experimental data is observed in figure 3.19. This means that if C_{H0} can be appropriately measured or determined, the corrosion fatigue behaviour of pipeline steels in seawater can be predicted pretty well. Also, if K_t is known or can be measured for a specific material-environment system, it may in turn help investigate the relationship of crack-cavity environment and the C_{H0} .

3.2.3.3 Stress Ratio

The experimental data of X42 pipeline steels in hydrogen gas provided by Gutierrez-Solana and Elices (1982) are used to investigate the influence of R on the model performance. The modelled crack growth processes and their evolution curves with different stress ratios in the situation of corrosion fatigue, hydrogen embrittlement, and fatigue, are plotted in figure 3.19.

Figure 3.19(a) and (b) show that the hydrogen embrittlement model can well capture the features of hydrogen-assisted cracking behavior of X42 pipeline steels under different stress ratios and the influence of anodic dissolution on cracking process is larger at lower stress ratios (e.g. $R = 0.1$) than that at higher ones (e.g. $R = 0.8$). Figure 3.19(c) ~ (f) show that both hydrogen embrittlement and anodic dissolution's influence on the crack evolution time (cycles) or the remaining fatigue life is closely related to the change of stress ratio R . More specifically, as shown in figure 3.19(c) and (d), at the low stress ratio $R = 0.1$, hydrogen embrittlement can cause a much larger reduction of crack evolution time or fatigue life than it at the high stress ratio $R = 0.8$, and thus anodic dissolution occupies a bigger portion of the life reduction in the latter case. Within each case, hydrogen embrittlement is more significant than anodic dissolution in reducing the fatigue life, while the critical crack size doesn't change much for fatigue, hydrogen-enhanced fatigue and corrosion fatigue. The little variation of critical crack size is attributed to the fact that when crack growth rate is high, hydrogen supply to the crack-tip region will be insufficient, leading to the recovery of material's fracture resistance, which is consistent with equation (3 – 52) for $f > f_c$. On the other hand, figure 3.19(e) and (f) indicate that the high stress ratio $R = 0.8$ provides a higher crack size where crack growth starts for either fatigue, hydrogen-enhanced fatigue or corrosion fatigue. Meanwhile the remaining life of either hydrogen-enhanced fatigue or corrosion fatigue decreases more heavily at the low stress ratio $R = 0.1$ than it at the high stress ratio $R = 0.8$ as the crack size extends. The model incorporates the effects of stress

ratio by equations (3 – 40) and (3 – 47). Equation (3 – 47), i.e. the Forman equation, includes the R effect in its denominator.

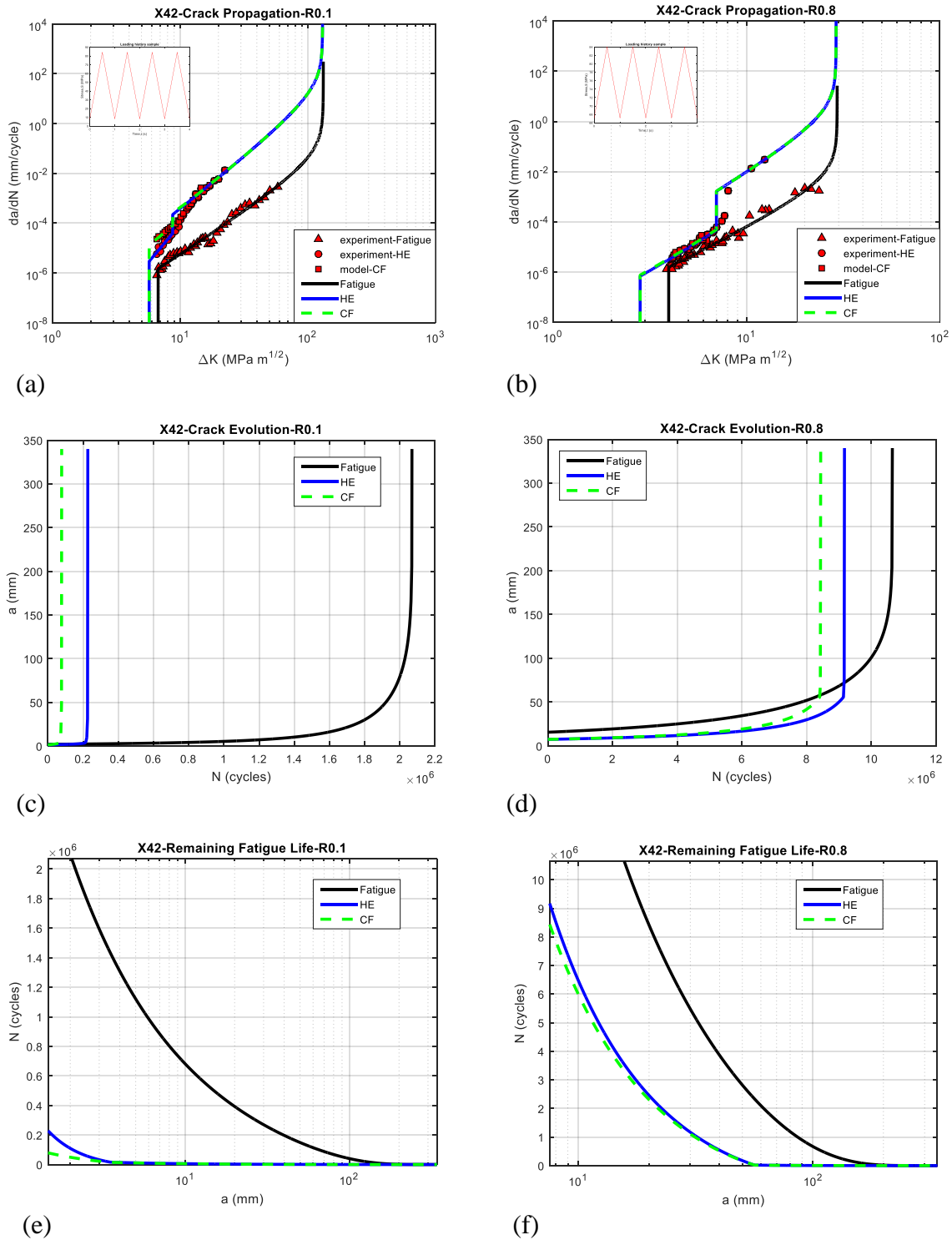


Figure 3.19 Stress ratio effect on model performance with experimental data collected from the work by Cialone and Holbrook (1985): (a) crack growth with $R = 0.1$; (b) crack growth with $R = 0.8$; (c) crack evolution with $R = 0.1$; (d) crack evolution with $R = 0.8$; (e) remaining fatigue life with $R = 0.1$; (f) remaining fatigue life with $R = 0.8$.

While equation (3 – 40) states that for corrosion fatigue, a high stress ratio can lead to a low anodic dissolution rate at crack tip. It seems that the hydrogen embrittlement process dominates the influence of R on corrosion fatigue, represented as the shifts of transition points as shown by Vosikovsky (1981). The accompanying changes in crack growth rates can be seen as well in the experimental data by Vosikovsky (1981) for X70 pipeline steel specimens tested in seawater. In conclusion, the increase of stress ratio can cause a left shift of the transition point in the crack growth curve and a decrease of fatigue life reduction due to corrosion fatigue. Detailed calculation results for X42 pipeline steel are listed in table 3.5.

X42	R	K_t	Crack evolution time	Life reduction
<i>Fatigue</i>	0.1	-	2.0684×10^6	-
<i>Hydrogen embrittlement</i>	0.1	9.7424	2.2721×10^5	89.016%
<i>Corrosion fatigue</i>	0.1	9.7424	7.8647×10^4	96.198%
<i>Fatigue</i>	0.8	-	1.0645×10^7	-
<i>Hydrogen embrittlement</i>	0.8	35	9.1655×10^6	13.902%
<i>Corrosion fatigue</i>	0.8	35	8.4309×10^6	20.803%
<i>Unit</i>	-	$\text{MPa}\sqrt{\text{m}}$	Cycle	-

Table 3.5 Model calculation results for X42 pipeline steels at different stress ratios

3.2.3.4 Temperature

Temperature has impacts on the structural integrity in a few aspects. On the one hand, as indicated by equations (3 – 46) and (3 – 49), temperature may affect the hydrogen diffusion process and furtherly impose an influence on K_t . On the other hand, the temperature variation may induce a stress/strain variation in the components (i.e. the so-called thermal load). Moreover, the temperature variation in the environment may even change the material's properties. For instance, at low temperatures steels could exhibit severe mechanical property degradation which is well known as ductile-brittle transition. The change of mechanical properties is usually obtained by tests and is out of this research's scope. To study the impact that temperature may have on K_t , a temperature range of 20 °C ~ 300 °C is selected. Within this temperature range, both ductile-brittle transition and creep are unlikely to happen to carbon steels (Moura et al., 2009).

The variation trend of K_t of X65 pipeline steels in such a temperature range is plotted in figure 3.20. Figure 3.20 shows that K_t increases as the environmental temperature increases, however, the increment is not very significant. When the temperature increases from 20 °C to 300 °C, K_t only increases from 19 MPa \sqrt{m} to a value less than 28 MPa \sqrt{m} . However, the increase of K_t doesn't necessarily mean the effects of environment-assisted cracking on the material under low temperature is less severe than that under high temperature. First, the environment temperature in this analysis only varies in a limited range where ductile-brittle transition and creep are unlikely to occur. Second, K_t is only used to assess the immediate structural integrity state and therefore can hardly give any information on the whole process of corrosion fatigue, especially if higher cracking rate appears. Lasebikan et al. (2013) concluded from a series of experiments conducted over a range of temperatures that the strain hardening index of steels can be reduced at elevated temperatures. Note that the strain hardening index has a negative correlation with the crack growth rate in an elastic-plastic way (J -integral). It is very likely that higher crack growth rate occurs at elevated environmental temperatures.

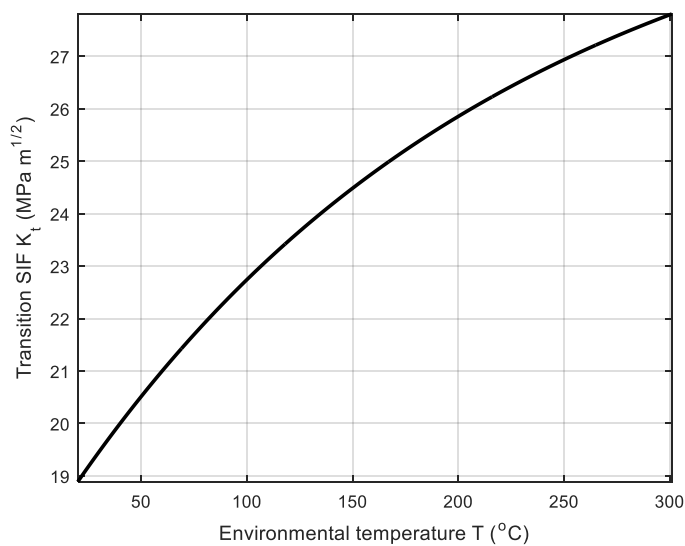


Figure 3.20 Environmental temperature effect on K_t

3.2.4 Summary

Subsea pipelines are vulnerable to corrosion fatigue which is a severe type of environment-assisted cracking. There is a practical need to develop constitutive models for describing the corrosion fatigue process of pipeline steels in seawater. In this 3.2 section, the mechanisms of corrosion fatigue for subsea pipeline steels were investigated and it was found that corrosion fatigue is driven by stress corrosion and hydrogen-assisted cracking. A two-component model was then proposed for subsea pipeline steels where both the anodic dissolution and hydrogen

embrittlement models are integrated based on fracture mechanics. The proposed model was applied to simulate the corrosion fatigue crack growth of X65 pipeline steels and the influences of factors of f , C_{H0} , R and T on the model performance were analyzed and discussed. The results show that

- 1) The proposed two-component model can reasonably simulate the total crack growth curve. Both the exacerbated cracking rate and behavior features can be well captured with appropriate consideration of the effects of mechanical and environmental parameters.
- 2) The increase of frequency will induce the decrease of anodic dissolution rates and a left shift of the transition point on the corrosion fatigue crack growth curve.
- 3) If C_{H0} can be properly measured, the transition behavior of the corrosion fatigue crack growth curves of pipeline steels in seawater can be well predicted.
- 4) The increase of stress ratio can cause a left shift of the transition point for the crack growth curve and a decrease in fatigue life reduction due to corrosion fatigue.
- 5) In a limited temperature range where ductile-brittle transition and creep are unlikely to occur, K_t increases with the increase of the environmental temperature.

The research work in this section has been summarized and published by Cheng and Chen (2017b).

3.3 Extended Engineering Critical Assessment for Corrosion Fatigue

Engineering critical assessment has been regularly performed in today's offshore oil and gas industry to ensure the safe operation of critical structures as well as to maximize their earning capabilities (Holtam, 2010). There are several industry standards that can provide guidance on conducting engineering critical assessments, such as SINTAP (2000), FITNET (2008), ISO 19902 (2014), BS 7910 (2015), API 579-1/ASME FFS-1 (2016) etc. Although these standards have specified corrosion fatigue as an important damage mechanism, they are not able to provide as detailed, in depth and generality, and accurate assessments to corrosion fatigue as to failure modes such as fracture/collapse, fatigue, creep fatigue, etc. (BS 7910, 2015). Such insufficiency often leads to overestimation or underestimation of the damage by corrosion fatigue to structural integrity. Offshore structures, for instance subsea pipelines, are vulnerable to corrosion fatigue. The excessive conservatism can ensure safe operation, but

also leads to unnecessary and costly underwater inspections; while the lack of conservatism will put the structure at a high risk of failure, which may result in enormous economic loss as well as catastrophic environmental disasters. There is thus a practical and pressing need to improve the traditional engineering critical assessment for the marine structures suffering corrosion fatigue.

Based upon previous research work in sections 3.1 and 3.2, a critical stress intensity factor is proposed in this section. It accounts for the influence of load frequency and initial crack size on the model selection in engineering critical assessments of marine structures subjected to corrosion fatigue. The critical stress intensity factor is calculated invoking the corrosion-crack correlation model established in Section 3.1 for different patterns of corrosion fatigue crack growth behaviour. While the subcritical crack growth is estimated using a three-stage model for corrosion fatigue crack growth based on the research work done in Section 3.2. Each stage of the model involves both the cracking processes assisted by anodic dissolution and by hydrogen embrittlement. Finally, X65 grade pipeline carbon steels subjected to corrosion fatigue in seawater is used to demonstrate the capability of the extended engineering critical assessment.

3.3.1 Traditional Approach

Since it was developed in the 1950s by Irwin (1957), linear elastic fracture mechanics has been widely applied to engineering critical assessments for steel structures. It introduces the concept of stress intensity factor K to describe the crack growth under sustained loads, where

$$K = YS\sqrt{\pi a} \quad (3 - 58)$$

with Y being the geometry function, S the applied stress perpendicular to the crack plane, and a the characteristic dimension of the crack. For through-thickness cracks, a represents the half crack length, for surface cracks, a is the flaw height, and for embedded cracks, a is the half height.

For the case of fatigue crack growth, the applied loading is characterized by an applied stress range ($\Delta S = S_{\max} - S_{\min}$) rather than a single value of stress, and in fracture mechanics terms, a given crack can then be considered to experience a stress intensity factor range (ΔK), which is calculated as

$$\Delta K = Y\Delta S\sqrt{\pi a} \quad (3 - 59)$$

where Y is the geometry function. ΔK also has a relationship with the maximum stress intensity factor K_{\max} in each load cycle as shown below,

$$K_{\max} = \frac{\Delta K}{(1 - R)} \quad (3 - 60)$$

For normal fatigue cracking (i.e. fatigue cracking in an inert environment), in principle, crack growth starts from the “stage I” (the “initiation” phase), mainly being “short crack”, and continues with the “propagation” phase of stage II and stage III (fast crack growth), being “long crack” towards final failure with K_{\max} in each load cycle approaching the fracture toughness K_{IC} (Pugno, 2006). Cracks detected at service are usually in the stage II. And it is generally agreed that linear elastic fracture mechanics can provide reasonable fatigue life prediction for long cracks (Stephens, 2000). Paris Law (Paris and Erdogan, 1963), which describes the relationship between cyclic crack growth rate da/dN and stress intensity factor range ΔK in stage II is the tool used in linear elastic fracture mechanics to predict the fatigue life, and has the expression as below,

$$\frac{da}{dN} = C(\Delta K)^m \quad (3 - 61)$$

where C and m are material constants.

Traditional guidelines for engineering critical assessment have noticed that fatigue crack growth in the presence of corrosion is different from that in an inert environment. However, they are still unable to provide treatments for corrosion fatigue in the same depth and generality as is provided for the aforementioned failure modes. For example, BS 7910 (2015) only offers a brief guideline in its Clause 10 for the assessment of corrosion fatigue as a part of environment-assisted cracking, which has a procedure as shown in figure 2.11. As in most other industry standards, the defects undergoing environment-assisted cracking are evaluated based on avoiding the phenomena by limiting K . More specifically, BS 7910 (2015) describes a crack acceptance criterion for mode I cracking as follows

$$K_I < \frac{K_{ISCC}}{F} \quad (3 - 62)$$

where K_I is the applied stress intensity factor, F is a factor of safety to be agreed between the parties involved in the structural integrity assessment and K_{ISCC} indicates the point when stress corrosion cracking happens. Following such an idea, the corresponding characterizing parameter for corrosion fatigue should be ΔK where corrosion fatigue starts. BS 7910 (2015) advises that the threshold stress intensity factor range at $R = 0$, ΔK_0 , for the growth of fatigue

cracks under the environmental and loading conditions of interest be chosen to assess the significance of cracks. To assessment the subcritical crack growth before the crack size (length or depth) reaches the failure criterion, the simplified model, which is actually a plot of Paris law in a log-log scale, and the bilinear model, which is a plot of a two-stage Paris equation, are recommended. However, it is often challenging to use ΔK_0 for assessment, because the fatigue crack growth rate is very small and hard to measure in the very low ΔK regime, and such an assessment approach is actually in a preliminary level. While the simplified model and bilinear model are not always good descriptions of the specified corrosion fatigue crack growth. Thus, it is often seen that traditional engineering critical assessment for corrosion fatigue may result in unnecessary cost as well as high risk of failure arising through the structure's service life.

3.3.2 Extended Approach

The fatigue crack growth process will be different in the presence of corrosion. According to McEvily and Wei (1972), corrosion fatigue crack growths of metals may be broadly categorized in three behaviour patterns as illustrated schematically in figure 3.13.

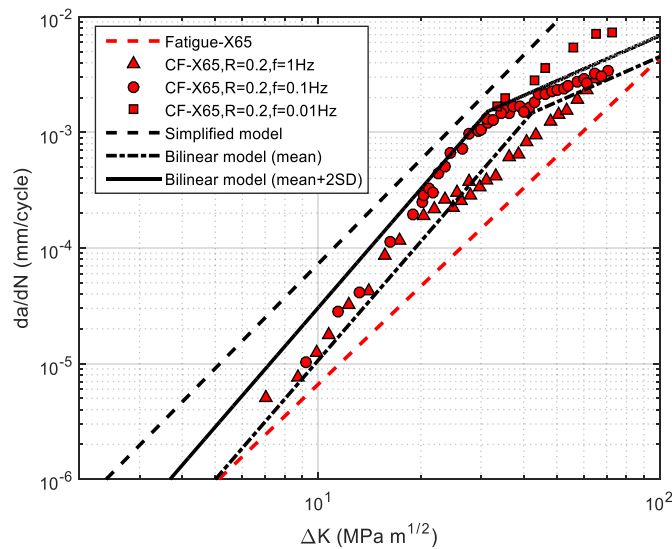


Figure 3.21 Comparison between BS 7910 model prediction and experimental data (Vosikovsky, 1975)

Type A pattern is typical as that of the aluminium-water system and is characterized by a reduction in the apparent threshold for crack growth and increases in the rate of crack growth at given K_{\max} levels. As K_{\max} approaches K_{IC} , the environmental influence diminishes. Type B pattern is typical for the steel-hydrogen systems. An abrupt increase of crack growth rate occurs somewhere along the abscissa, indicating quite strong environmental effects above some critical K_{\max} but negligible effects below this level. A broad range of material-

environment systems such as seawater-steel systems exhibit behaviours that fall in Type C pattern, with Type A behaviour at K_{\max} levels below the apparent threshold and Type B behaviour above.

For steels freely corroding in a marine environment, current industry standards suggest the simplified or bilinear models to be used in the engineering critical assessment of corrosion fatigue. Take BS 7910 for instance, it provides the simplified model, the mean bilinear model and the mean plus two standard deviations (mean+2SD) bilinear model for assessments of different accuracies. Two sets of parameters are available for the cases $R < 0.5$ and $R \geq 0.5$ respectively in the mean bilinear model as well as the mean+2SD bilinear model. However, as seen in figure 3.21, with the experimental data from Vosikovsky (1975) for fatigue crack growth of X65 pipeline carbon steels tested in seawater as the reference, the models are often not good descriptions of the whole corrosion fatigue crack growth. On the other hand, the experimental observation of fatigue crack growth curves of steels tested in seawater with and without CP clearly show that the hydrogen embrittlement induced degradation of fracture toughness is the reason causing crack behaviour features such as transition and plateau (Shipilov, 2002). But Paris law in itself doesn't link the crack growth behaviour with the fracture toughness degradation. In order to reasonably describe the hydrogen-enhanced fatigue crack growth of pipeline steels, a two-stage Forman equation model was developed in Section 3.1 as

$$\frac{da}{dN} = \begin{cases} \frac{B_1(\Delta K)^{n_1}}{[(1-R)K_{IH} - \Delta K]}, & K_{\max} < K_t \\ \frac{B_2(\Delta K)^{n_2}}{[(1-R)K_{IE} - \Delta K]}, & K_{\max} \geq K_t \end{cases} \quad (3-63)$$

where B_1 , B_2 , n_1 , and n_2 are material constants, f is the load frequency, K_{IH} is the saturated fracture toughness which is obtained with sufficient hydrogen supplement using procedures defined in ASTM E1820-17 (2017), K_{IE} is the equilibrium fracture toughness, namely the final fracture toughness displayed in the fatigue test conducted in hydrogen gas, and K_t is the transition stress intensity factor connecting the two stages, corresponding to the transition point in the corrosion fatigue crack growth curve.

This model is based on the fatigue cracking of steels in high-pressure hydrogen gas depicted by API 579-1/ASME FFS-1 (2016). Accordingly, the typical hydrogen-enhanced fatigue cracking process of steels with constant amplitude loading is divided into three stages, denoted as stage 1, 2 and 3 as shown in figure 3.22. In stage 1, the hydrogen delivered at the crack tip leads to an enhanced fatigue crack growth compared with the normal fatigue

4.93×10^{-12} was obtained by Endo et al. (1981) from their experiments. The other parameters have the same definition as in equation (3 – 63) but for corrosion fatigue in the seawater-steel system. As seen in equation (3 – 64), each stage involves both the cracking processes assisted by anodic dissolution and hydrogen embrittlement.

However, as seen in figure 3.21, the plateau in the crack growth curves of carbon pipeline steels such as X65 in seawater is not evident, and most importantly, the stress intensity factors of cracks detected at service usually locate within the range defined as long crack growth. Thus it may be reasonable and convenient to use Paris law for the specified range of ΔK , instead of Forman equation, from a view of practical engineering. Furthermore, a three-stage corrosion fatigue crack growth model, which has the expression shown below was built for corrosion fatigue of pipeline carbon steels in seawater,

$$\frac{da}{dN} = \begin{cases} Af^{-0.36}(1-R)^2(\Delta K)^3 + C_1(\Delta K)^{m_1}, & K_{\max} < K_t \\ Af^{-0.36}(1-R)^5(K_t)^3 + C_1[(1-R)K_t]^{m_1}, & K_t \leq K_{\max} < K_t + K_{pl} \\ Af^{-0.36}(1-R)^5(K_t)^3 + C_2(\Delta K)^{m_2}, & K_{\max} \geq K_t + K_{pl} \end{cases} \quad (3 - 65)$$

where A is set the same as in equation (3 – 64), C_1 , C_2 , m_1 , and m_2 are material constants, and the K_{\max} range $K_{pl} = \Delta K_{tH}/(1-R)$ according to Section 3.1, with the threshold stress intensity factor range for corrosion fatigue $\Delta K_{tH} = 2 \text{ MPa} \cdot \text{m}^{1/2}$ from API 579-1/ASME FFS-1 (2016).

Experimental observation shows that as K_{\max} increases, before each K_t is achieved, the crack with load frequencies of 1 Hz, 0.1 Hz, and 0.01 Hz, grows almost along the same curve, however, their growth curves deviate after K_t , which has an obvious dependence on the load frequency. Such a deviation has a direct influence on the crack growth rate and therefore the fatigue life. For the reasons stated above, K_t is proposed to be the critical value for stress intensity factor and particular check may be necessary on this value before conducting engineering critical assessments for critical structures under corrosion fatigue. The expression of K_t is derived from the corrosion-crack correlation model which is used to explain the process of hydrogen-enhanced fatigue cracking as shown in Section 3.1 and schematically plotted in figure 3.22.

In linear elastic fracture mechanics, the stress perpendicular to the crack plane in Mode I loading, σ_{yy} , is expressed by

$$\sigma_{yy} = \frac{K_I}{\sqrt{2\pi r}} \quad (3 - 66)$$

where r is the distance in front of the crack tip, and K_I is the stress intensity factor in Mode I.

And the maximum principal stress happens at the elastic-plastic boundary as,

$$\sigma_{\max} = \sigma_{yy} = \omega\sigma_{ys} \quad (3 - 67)$$

where ω is a magnification factor accounting for the material's working hardening effect and it is usually considered to be in a range of value 3 ~ 5 (Wang et al., 2013).

Thus the plastic zone size r_p has the expression

$$r_p = \frac{1}{2\pi} \frac{K_I^2}{(\omega\sigma_{ys})^2} \quad (3 - 68)$$

The concept of environment-affected zone is introduced to define the damaged zone where the material exhibits a property different from that of the bulk material due to the penetration of chemical agents into a localized crack-tip region (Liu, 2005). Assuming that the hydrogen diffusion in the material of crack-tip region is primarily stress-driven, then based on the work done in Section 3.1, r_{EAZ} has an expression as:

$$r_{\text{EAZ}} = \sqrt{\frac{DV_H\sigma_{ys}}{k_B T} \cdot \frac{1}{f}} \quad (3 - 69)$$

where D corresponds to the diffusion coefficient and is calculated from the ratio of hydrogen permeability and solubility for carbon steel (Gadgeel and Johnson, 1979), f is the load frequency, V_H is the partial volume of hydrogen, k_B is the Boltzmann constant, T is the temperature in Kelvins and σ_{ys} is the material's yield strength.

As can be seen from equation (3 - 68), r_p grows as K_I increases. In accordance with the corrosion-crack correlation model, the point where the crack growth curve starts transition is the very point where r_p grows to an equilibrium with the environment-affected zone size r_{EAZ} , i.e.

$$r_p = r_{\text{EAZ}} \quad (3 - 70)$$

Combining equations (3 - 66) ~ (3 - 70), it follows that

$$K_{\text{tran}} = \omega_H\sigma_{ys} \left(\frac{4\pi^2 DV_H\sigma_{ys}}{k_B T f} \right)^{1/4} \quad (3 - 71)$$

where ω_H accounts for the material's working hardening effect in the presence of hydrogen.

Note that fracture happens when K_I reaches the fracture toughness of the material, and the corresponding critical plastic zone size r_c keeps the same regardless of hydrogen ingress (Wang, et al., 2013), the following equation can be achieved

$$\frac{\omega}{\omega_H} = \frac{K_{IN}}{K_{IH}} \quad (3 - 72)$$

where K_{IN} is the inherent fracture toughness. Wang et al. (2013) gives an equation for calculating K_{IH} based on the theory of hydrogen-enhanced de-cohesion,

$$\frac{K_{IH}}{K_{IN}} = 1 - \frac{\beta c}{\omega \sigma_{ys}} \exp \left[\frac{2(1 + \nu)}{3} \frac{V_H}{k_B T} \frac{K_{IH}}{K_{IN}} \omega \sigma_{ys} \right] \quad (3 - 73)$$

where β is a parameter related to the loss of critical cohesive stress by hydrogen impurity, c refers to the hydrogen concentration in the material under a unstressed state, and ν is the Poisson ratio.

Inserting equation (3 – 72) into equation (3 – 71), a preliminary calculation of the transition stress intensity factor is performed, yielding

$$K_{tran} = \omega \sigma_{ys} \frac{K_{IH}}{K_{IN}} \left(\frac{4\pi^2 D V_H \sigma_{ys}}{k_B T f} \right)^{\frac{1}{4}} \quad (3 - 74)$$

To obtain the valid transition stress intensity factor K_t , the following formula is used

$$K_t = \min \left\{ \max \left\{ K_{tran}, \frac{\Delta K_0}{(1 - R)} \right\}, K_{IH} \right\} \quad (3 - 75)$$

3.3.3 Applications

For pipeline carbon steels, the frequency effect on the crack growth rate is normally negligible in dry-air environments. However, under corrosion fatigue, the frequency effect appears to be obvious for materials under constant-amplitude load. It is generally believed that in an environment with stable corrosiveness, the fatigue crack growth rate increases with the decrease of the frequency. But as mentioned in Yu et al. (2015), observations from fatigue tests in corrosive environments showed that there exists a critical frequency f_c , under which the material properties show the same level of degradation. According to the corrosion-crack correlation model, the lower cyclic load frequency extends the exposure time of the material to the corrosive environment, and this allows more hydrogen atoms to diffuse to a longer distance in front of the crack tip within each loading cycle and thus a higher K_t . When $f < f_c$,

the whole corrosion fatigue crack growth maintains high crack growth rate, namely no transition appears in the growth curve. Thus, f_c is decided by the relationship below:

$$K_{\text{tran}} = K_{\text{IH}} \quad (3 - 76)$$

Combining equations (3 – 74) and (3 – 76), it follows that

$$f_c = \frac{4\pi^2 D V_H \sigma_{ys}}{k_B T} \left(\frac{\omega \sigma_{ys}}{K_{\text{IN}}} \right)^4 \quad (3 - 77)$$

To validate the corrosion-crack correlation model, the results of an experiment conducted by Yu et al. (2015) are compared with the prediction by equation (3 – 77) for f_c . The experiment was performed on X60 pipeline steel and the measured critical frequency was 1.04×10^{-3} Hz. According to the experimental conditions and material properties provided, the f_c of X60 pipeline carbon steels is calculated to be in the range of 4.4×10^{-4} to 3.4×10^{-3} Hz, with a consideration of ω ranging from 3 to 5. While the measured f_c is 1.04×10^{-3} Hz that exactly falls in the predicted range of 4.4×10^{-4} and 3.4×10^{-3} Hz, which shows the critical frequency of the experiment is captured by equation (3 – 77).

Material	<i>Yield strength</i> (σ_{ys})	<i>Poisson ratio</i> (ν)	<i>Diffusion coefficient</i> (D)	<i>Threshold stress intensity factor range</i> (ΔK_0)	<i>Inherent fracture toughness</i> (K_{IN})	<i>Partial volume of hydrogen</i> (V_H)
X65	458.5	0.3	5.3×10^{-9}	2.0	197.9	2.0×10^6
<i>Unit</i>	MPa	-	(mol H ₂) /m ³ · MPa ^{1/2}	MPa · m ^{1/2}	MPa · m ^{1/2}	m ³ mol ⁻¹

Table 3.6 Material properties of API X65 steel (Guedri et al., 2004; Yu et al., 2015)

Similarly, using the material in table 3.6, the f_c of X65 pipeline carbon steels falls in a range of 1.8×10^{-4} to 1.4×10^{-3} Hz, which is reasonable since it is well below the sample frequency 0.01 Hz. Furthermore, the validity of equation (3 – 74) can be confirmed by the experimental data from tests conducted by Vosikovskiy (1975) for API X65 pipeline steels freely corroding in seawater with a series of load frequencies. As the saturated fracture toughness is hard to be decided for a component with free corrosion in seawater, a degradation factor δ , with a value of 0 ~ 1.0, is multiplied by the inherent fracture toughness to approximate the remaining fracture toughness, namely

$$K_{\text{IH}} = \delta K_{\text{IN}} \quad (3 - 78)$$

Assuming $\delta = 0.8$, i.e. 80 percent of the inherent fracture toughness is left providing a saturated diffusion condition, which corresponds to the worst corrosion fatigue case where $\text{pH}=5$, K_t are calculated using the material property data provided in table 3.6 and then plotted together with the experimental data in figure 3.23. Good agreement between the model prediction and experimental data is observed as shown in figure 3.23, which indicates that equation (3 – 74) is an effective formula to predict the K_t for corrosion fatigue crack growth curves above f_c . The results of the model prediction are summarized in table 3.7.

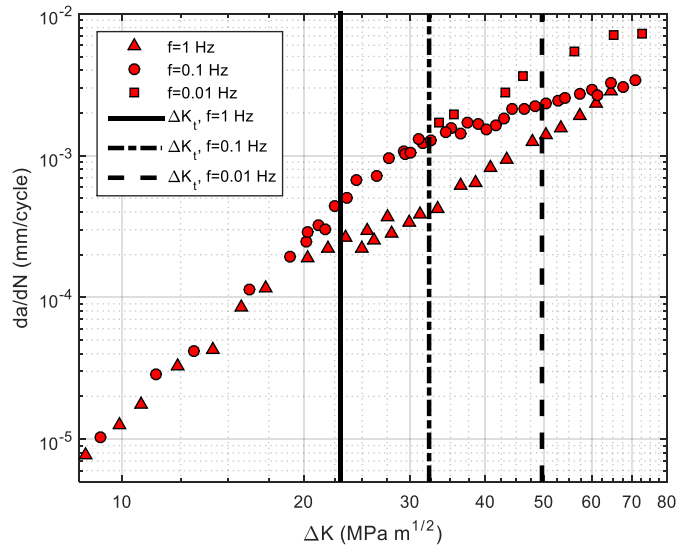


Figure 3.23 Prediction of transition stress intensity factors for X65 under corrosion fatigue with various load frequencies (Vosikovsky, 1975)

Material	Stress Ratio (R)	Load frequency (f)	Transition SIF (K_t)	Transition SIF range (ΔK_t)
X65	0.2	1	28.8	23.0
X65	0.2	0.1	40.3	32.3
X65	0.2	0.01	62.0	49.6
Unit	-	Hz	$\text{MPa} \cdot \text{m}^{1/2}$	$\text{MPa} \cdot \text{m}^{1/2}$

Table 3.7 Predicted transition stress intensity factors for X65 pipeline carbon steels under corrosion fatigue

Crack growth curve	$K_{max} < K_t$		$K_{max} \geq K_t$		K_t
	C_1	m_1	C_2	m_2	
X65, $f = 1 \text{ Hz}$	2.30×10^{-9}	3.69	2.67×10^{-8}	2.76	28.8
X65, $f = 0.1 \text{ Hz}$	4.01×10^{-10}	4.34	9.72×10^{-6}	1.36	40.3
X65, $f = 0.01 \text{ Hz}$	8.79×10^{-11}	4.58	4.15×10^{-7}	2.17	62.0
Unit	-	-	-	-	$\text{MPa} \cdot \text{m}^{1/2}$

Table 3.8 Parameters of corrosion fatigue crack growth curves regressed from test data

The initial crack size a_i in this research is defined as the size when the crack is detected using a reliable non-destructive technique. It characterizes the initial state of the crack in the

engineering critical assessment to be conducted. The initial crack size in pressure vessels may range from several millimetres to some centimetres (Visser, 2002). Three cases where the initial crack size $a_i = 1$ mm, 4 mm, 12 mm are investigated based on experimental data (Vosikovsky, 1975). Since K_t of corrosion fatigue crack growth curves of X65 pipeline carbon steels under various load frequencies have been acquired, the experimental data are regressed to follow the three-stage corrosion fatigue model. The parameter values from regression are summarized in table 3.8. Crack growth curves generated by each model are plotted in figure 3.24, with the experimental data plotted as reference.

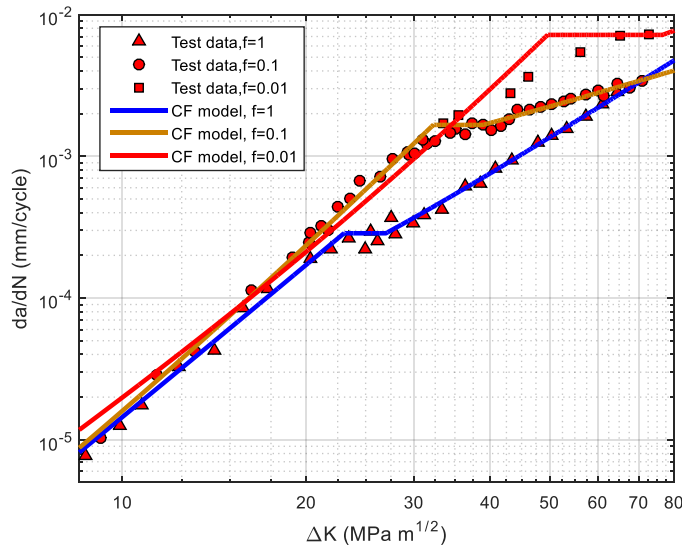


Figure 3.24 Crack growth curves of X65 under corrosion fatigue with various load frequencies (Vosikovsky, 1975)

The fatigue life in cycles over the range of crack sizes a_i to a_f is calculated as:

$$N_{if} = \int_{a_i}^{a_f} \frac{1}{C(Y\Delta S\sqrt{\pi a})^m} \frac{da}{a^{m/2}} \quad (3 - 79)$$

Vosikovsky (1975) used single-edge notched specimens, with a width b of 76.2 mm and a half length h of 580 mm, in his tests. The specimen is plotted in figure 3.25. Accordingly, the following function for calculating the geometry factor Y is used (Dowling, 2012):

$$Y = \left(1 + 0.122\cos^4 \frac{\pi\alpha}{2}\right) \sqrt{\frac{2}{\pi\alpha} \tan \frac{\pi\alpha}{2}} \quad (3 - 80)$$

where α is the ratio of crack length a to the width of specimen. Equation (3 – 80) is also plotted in figure 3.25. It is obvious that the geometry effect is relatively stable before α reaches 0.6, i.e. before the length of crack grows to a length of 0.6 times the width. So the failure criteria in this case is set as the crack grows to a length of 45.7 mm, i.e. $a_f =$

45.7 mm. The ratio of applied stress to the material's yield strength is adjusted to 0.4 so that the range of ΔK_I for evaluation approximately equals that where experimental data are available and the small yielding assumption of linear elastic fracture mechanics is met.

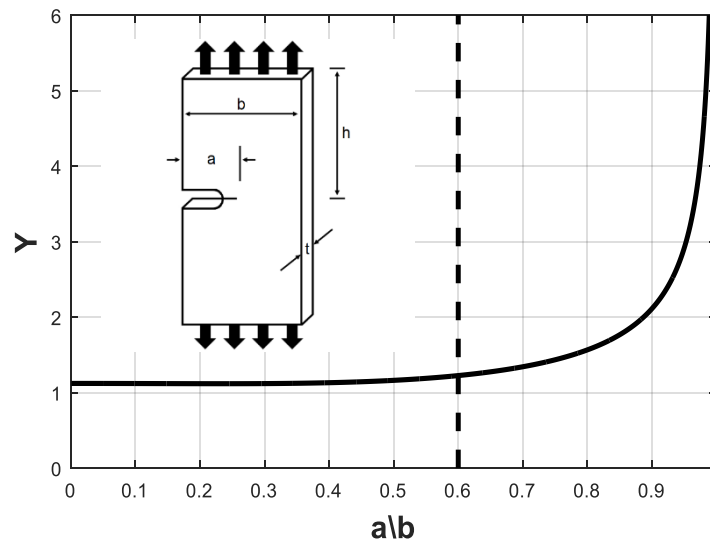


Figure 3.25. Geometry and the geometry function of the single-edge notched specimen

To evaluate the influence from the load frequency as well as the initial crack size on the performance of standard models in predicting corrosion fatigue life, a comparison is made among each group in terms of load frequency and initial crack size. Conservatism is used as the evaluation parameter, which is defined as:

$$\text{Conservatism} = \frac{\text{Experimental prediction} - \text{Model prediction}}{\text{Experimental prediction}} \times 100\% \quad (3 - 81)$$

Negative conservatism means the model predicts a larger life than that of the experiment, i.e. the prediction by standard model is unconservative, which is usually not allowed in engineering practices. In other words, a negative conservatism indicates that the model should be rejected for the engineering critical assessment. Conversely, positive conservatism stands for a redundancy in life prediction of the model, and the smaller the conservatism the better the performance of the model in the engineering critical assessment. Only the simplified model and the bilinear model of mean plus two standard deviations (mean+2SD) are used for fatigue life prediction and comparison with experimental data, since the mean bilinear model is obviously short of conservatism for engineering critical assessments of corrosion fatigue, as indicated in figure 3.21. The values of parameters of the simplified and bilinear models suggested in BS 7910 (2015) are summarized in table 3.9 for the experimental case where $R = 0.2$. The calculation results for each case are summarized in table 3.10.

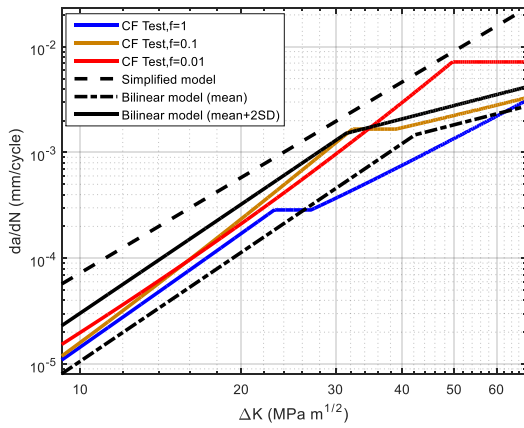
<i>Standard Model</i>	<i>Stage 1</i>		<i>Stage 2</i>		K_t
	C_1	m_1	C_2	m_2	
Simplified	2.30×10^{-12}	3	2.3×10^{-12}	3	-
Bilinear (mean)	3.0×10^{-14}	3.42	1.27×10^{-7}	1.30	1336
Bilinear (mean+2SD)	8.55×10^{-14}	3.42	1.93×10^{-7}	1.30	993
<i>Unit</i>	-	-	-	-	$N \cdot mm^{3/2}$ for da/dN in mm/cycle

Table 3.9 Parameters of crack growth curves with $R < 0.5$ from BS 7910 (2015)

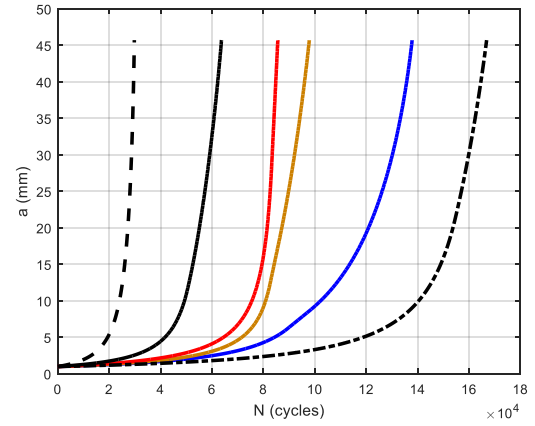
<i>Initial crack size (mm)</i>	<i>Crack growth curve</i>	$f = 1.0$ Hz	$f = 0.1$ Hz	$f = 0.01$ Hz	<i>Unit</i>
1	Test	1.38×10^5	9.78×10^4	8.56×10^4	cycles
	Simplified model	2.98×10^4			cycles
	Conservatism	78.4%	69.6%	65.2%	-
	Bilinear model (mean)	1.67×10^5			cycles
	Conservatism	-21.0%	-70.5%	-90.4%	-
	Bilinear model (mean+2D)	6.37×10^4			cycles
	Conservatism	53.8%	34.9%	25.6%	-
4	Test	6.00×10^4	3.10×10^4	2.63×10^4	cycles
	Simplified model	1.23×10^4			cycles
	Conservatism	79.6%	60.5%	53.4%	-
	Bilinear model (mean)	5.77×10^4			cycles
	Conservatism	3.83%	-86.2%	-119%	-
	Bilinear model (mean+2D)	2.54×10^4			cycles
	Conservatism	57.7%	18.1%	3.55%	-
12	Test	3.04×10^4	1.55×10^4	8.14×10^3	cycles
	Simplified model	4.83×10^3			cycles
	Conservatism	84.1%	68.8%	40.7%	-
	Bilinear model (mean)	2.23×10^4			cycles
	Conservatism	26.7%	-44.0%	-174%	-
	Bilinear model (mean+2D)	1.30×10^4			cycles
	Conservatism	57.4%	16.3%	-59.1%	-

Table 3.10 Prediction of BS 7910 simplified and bilinear models and experimental results

The crack growth curves as well as the corresponding crack evolution curves are plotted in figures 3.26, 3.27 and 3.28 respectively for cases where $a_i = 1$ mm, $a_i = 4$ mm and $a_i = 12$ mm. It can be clearly observed from figures. 3.26 ~28 that the difference in initial crack sizes may result in different crack evolution behaviours and corrosion fatigue lives even though the overall crack growth behaviour keeps the same.

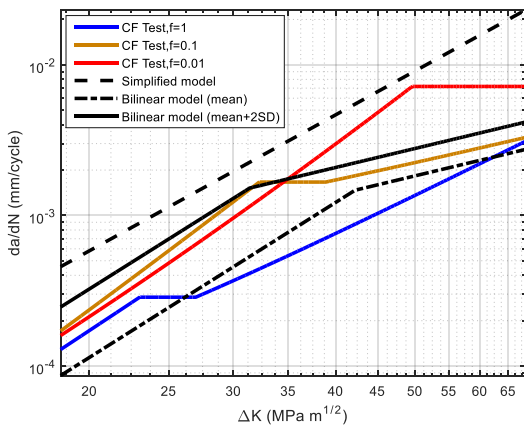


(a)

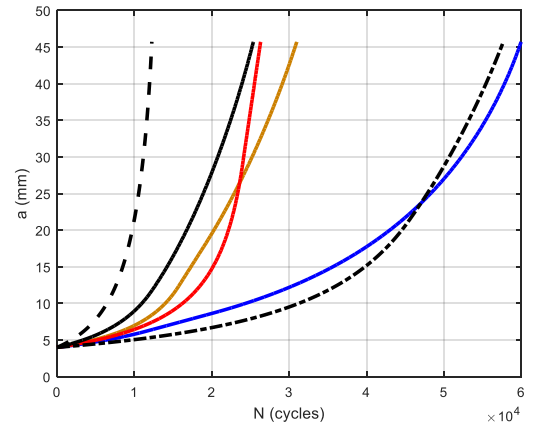


(b)

Figure 3.26 Corrosion fatigue crack curves for X65 steels with initial crack size $a_i = 1$ mm: (a) Crack growth; (b) Crack evolution.

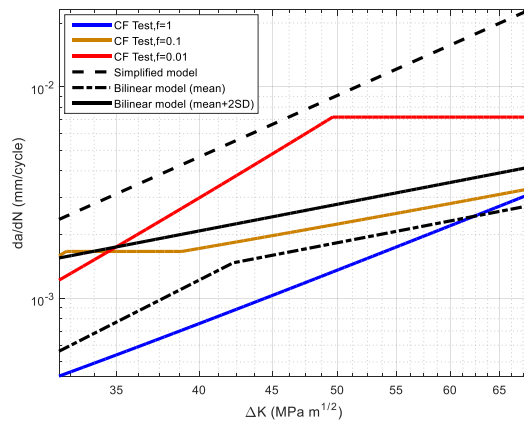


(a)

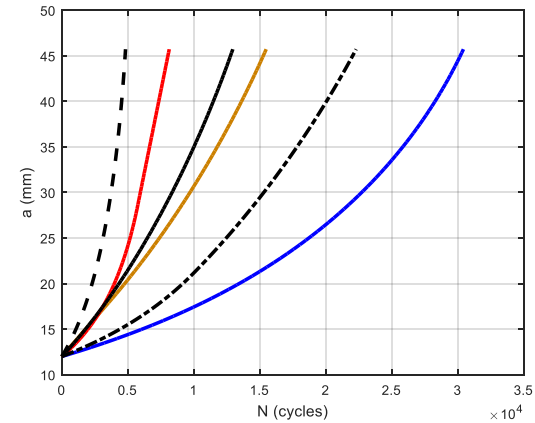


(b)

Figure 3.27 Corrosion fatigue crack curves for X65 steels with initial crack size $a_i = 4$ mm: (a) Crack growth; (b) Crack evolution.



(a)



(b)

Figure 3.28 Corrosion fatigue crack curves for X65 steels with initial crack size $a_i = 12$ mm: (a) Crack growth; (b) Crack evolution.

Corrosion fatigue lives calculated based on the experiment data are plotted in figure 3.29 and those predicted using standard models from BS 7910 are plotted in figure 3.30. Conservatism calculated from equation (3 – 81) for each model are plotted in figure 3.31 as histograms. The histograms are clustered in terms of load frequencies, and within each cluster the histograms are lined in a sequence of initial crack size 1 mm, 4 mm, and 12 mm from left to right.

As shown in figure 3.29, the fatigue life of structures subjected to corrosion fatigue is tightly related with the load frequency f . The lower the frequency, the higher the crack growth rate and thus the lower the fatigue life, represented by the experiment based prediction. This is believed to be caused by the increase in the value of ΔK_t resulting from the decrease of load frequency. However, the standard models from industrial standards such as BS 7910 (2015), ignore the load frequency effect in corrosion fatigue, causing either overestimation or underestimation of the structure's fatigue life. Figure 3.29 also implies that the corrosion fatigue life in low regime of ΔK occupies a much bigger fraction in overall fatigue life than that in high ΔK regime, which means more cycles are spent to drive the crack growth when the crack size is small. Combining the aforementioned two findings with the observation, it is found that the increase of fatigue life accelerates as f increases.

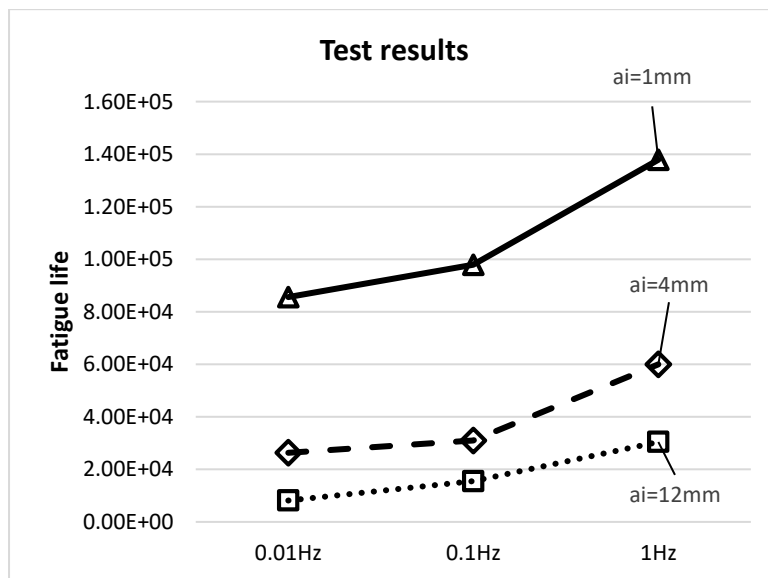


Figure 3.29 Load frequency effect on corrosion fatigue life prediction for X65 steels under various initial crack sizes

Figure 3.30 shows that among the corrosion fatigue lives predicted by the standard models using the parameter values provided by BS 7910, the corrosion fatigue life predicted by the bilinear model (mean) is always the highest, and then comes that by the bilinear model (mean+2SD), and the corrosion fatigue life predicted by the simplified model is the lowest.

All the three predicted values decrease as the initial crack size increases. And quite obviously, the difference among them decreases as well.

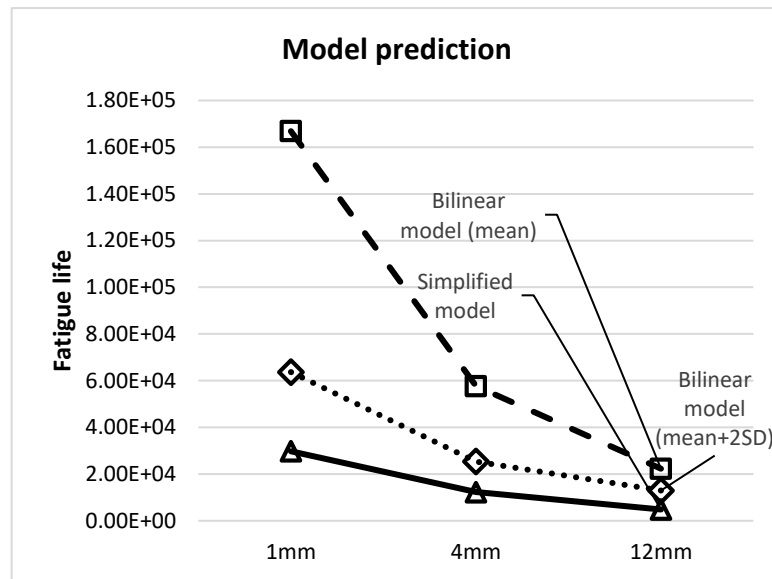


Figure 3.30 Prediction by standard models for corrosion fatigue life of X65 steels with various initial crack sizes

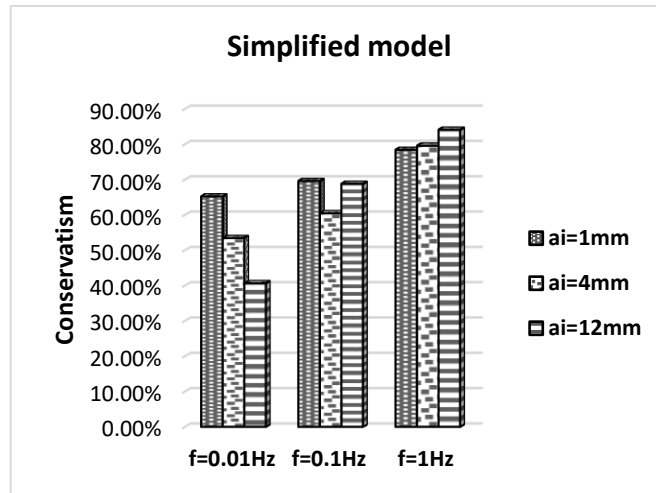
As seen in figure 3.21 that there is some underestimation of the corrosion fatigue crack growth rate from the bilinear model in the high ΔK regime for low load frequencies, while the simplified model always overestimates the crack growth rate. But this doesn't mean the simplified model is better than the bilinear model, because the underestimation of the corrosion fatigue crack growth rate for low frequencies such as 0.01Hz from the bilinear model in high ΔK regime can be balanced by the overestimation from the bilinear model in low ΔK regime. Keeping in mind that the crack growth in low ΔK regime contributes much more than that in high ΔK regime, the bilinear model may give a prediction that is overall conservative, but with a much better performance in the view of conservatism. For example, the conservatism of the prediction by bilinear model (mean+2SD) for a crack of the initial size 4 mm with a load frequency of 0.01 Hz is as low as 3.55%, as indicated in table 3.10.

Figure 3.31(a) shows that the simplified model always give a conservative life prediction for corrosion fatigue cracks with various initial crack sizes. While the conservatisms in the life prediction by the simplified model remain relatively large, they decrease as the load frequency decreases. Additionally, the sensitivity of the conservatism to load frequency is higher for a larger initial crack size, and this is also true for figures 3.31(b) and (c). Figure 3.31(b) implies that among all the possible 9 combinations of load frequencies and initial crack sizes, the bilinear model (mean) can only be used for engineering critical assessments of two cases, i.e. $f = 1$ Hz with $a_i = 4$ mm, and $f = 1$ Hz with $a_i = 12$ mm. In figure 3.31(c),

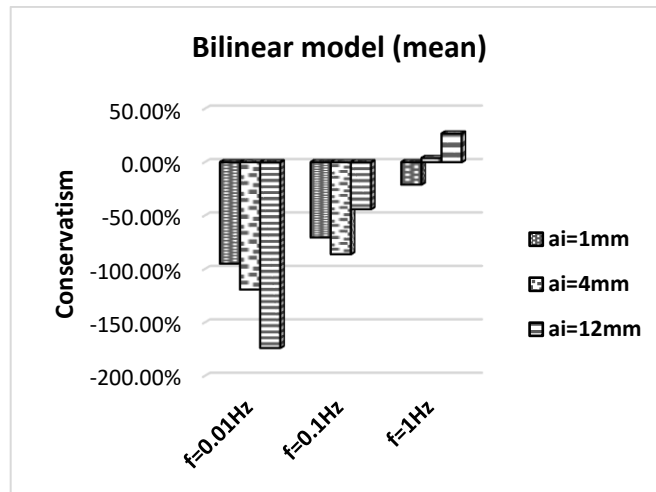
only the case where $f = 0.01$ Hz with $a_i = 12$ mm is not fit for engineering critical assessment conducted using the bilinear model (mean+2SD). In a general view, with the load frequency decreasing, the conservatisms of the simplified, bilinear (mean) as well as bilinear (mean+2SD) models decrease, and the bilinear model (mean+2SD) performs best. The conservatism generated by the standard models in life prediction accumulates with the crack growth. The inefficient performance of the simplified model, indicated by its large conservatisms on average, is due to the ignorance of the transition in the corrosion fatigue crack growth curve. As revealed by equation (3 – 74), the transition stress intensity factor is determined by the load frequency. Depending on both the load frequency and the initial crack size/stress intensity factor range, the corrosion fatigue life, as seen in figure 3.29, may be heavily influenced, and so is the conservatism. The transition stress intensity factor specified in the bilinear model (mean+2SD) happens to be close to that of the crack growth curve with a load frequency of 0.1 Hz, as seen in figure 3.21, which makes the conservatism in life prediction by the bilinear model (mean+2SD) small overall. But for cases where the load frequencies are lower than 0.1 Hz, the bilinear model (mean+2SD) tends to underestimate the crack growth rate after ΔK_t , contributing a negative value to the overall conservatism afterward; while for the cases where load frequencies are higher than 0.1 Hz, the bilinear model tends to overestimate the crack growth rate after ΔK_t , contributing a positive value to the overall conservatism afterward. Based on the conclusion drawn for figure 3.29, the increase of the sensitivity of conservatism to load frequency with the increasing initial crack size, which has been shown in figure 3.31, is explained to be due to the increase in initial crack size reducing the portion of the low- ΔK crack growth in the predicted life.

Figure 3.31 also shows that a large initial crack size combined with a low load frequency tend to provide small even negative conservatism. Caution is needed when the case to be assessed involves either low frequency or large initial crack size or both. When assessing cases where $f \leq 0.01$ Hz, the simplified model is suggested to be used. If more accuracy is required, it may work to use the bilinear model (mean+2SD) before ΔK reaches ΔK_t specified by BS 7910 (2015) and then use the simplified model. Large initial crack size implies a high ΔK . Even though most cracks found at service are in a scale of several millimetres, this doesn't equivalently mean that their ΔK usually falls in the regime of low ΔK range. It is also necessary to consider the stress history and future working load conditions. For cracks detected with high ΔK , the simplified model is suggested to be used for engineering critical assessment since it can always provide positive conservatism. As shown in table 3.10, in the case where the crack has an initial size of 12 mm under a load frequency of 0.01 Hz, the use

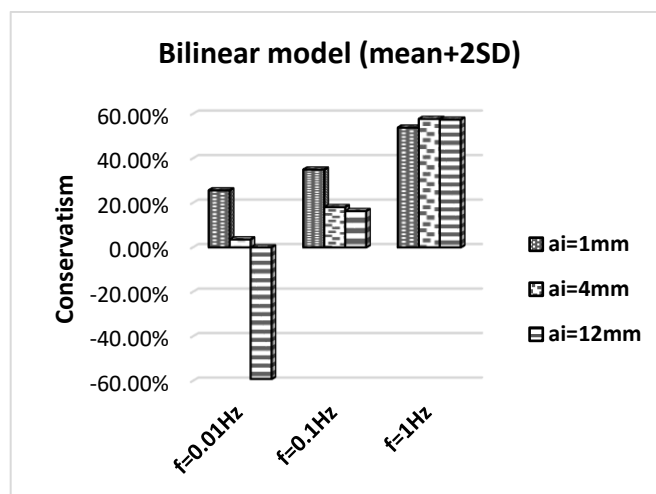
of the bilinear model provides unconservative life prediction (conservatism = -59.1%), however, the use of the simplified model still provides conservative life prediction (conservatism = 40.7%).



(a)



(b)



(c)

Figure 3.31 Comparison of corrosion fatigue life prediction for X65 under various load frequencies

In traditional engineering critical assessments, the effect of the load frequency and initial crack size (in long-crack domain) is ignored due to their little influence on fatigue crack growth in an inert environment. However, for a structure subjected to corrosion fatigue, the effect of the load frequency and initial crack size on the corrosion fatigue crack growth is important. Such an effect can be taken into account through the parameter K_t or ΔK_t . According to equation (3 – 74), K_t or ΔK_t is directly related to the load frequency. The higher the load frequency, the smaller the value of K_t or ΔK_t . Meanwhile, the initial crack size may be well above the crack size corresponding to K_t or ΔK_t . As analysed before, conservatism accumulates as the crack grows, thus the crack growth curve after K_t or ΔK_t may impose a significant influence on the performance of the model. Equation (3 – 74), which is derived from the corrosion-crack correlation model, provides an effective way of calculating K_t or ΔK_t . It is thus believed that the calculation of K_t or ΔK_t and an analysis on the fatigue crack growth behaviour for the structures under corrosion fatigue would benefit the subsequent engineering critical assessment.

3.3.4 Summary

An extended engineering critical assessment was developed in this 3.3 section, in which a critical stress intensity factor was proposed, accounting for the influence of load frequency and initial crack size, to direct the model selection within current industrial standards for assessing the integrity of structures subjected to corrosion fatigue. For the specific corrosion fatigue cracking behavior pattern, a three-stage fracture mechanics based corrosion fatigue crack growth model is used to predict the subcritical crack growth. This extended engineering critical assessment was applied to X65 grade pipeline carbon steels and the results indicate that

- 1) The load frequency and initial crack size impose significant impact on the corrosion fatigue crack growth.
- 2) The proposed critical stress intensity factor K_t extends the traditional engineering critical assessment for corrosion fatigue in that it accounts for the influence of load frequency and initial crack size on the model selection for the engineering critical assessments of marine structures under corrosion fatigue.
- 3) For X65 pipeline steels, the simplified model always gives a conservative life prediction for corrosion fatigue cracks with various initial crack sizes
- 4) When assessing corrosion fatigue cases of X65 pipeline steels where $f \geq 1$ Hz, the life prediction by the bilinear model (mean) from BS 7910 (2015) is conservative only

if the initial crack size is larger than the crack size corresponding to K_t or ΔK_t under the specified load history.

- 5) When assessing cases of X65 pipeline steels where $f \leq 0.01$ Hz, the simplified model is suggested to be used. If more accuracy is required, it may work to use the bilinear model (mean+2SD) before ΔK reaches ΔK_t values specified by BS 7910 (2015) and the simplified model afterward.

In summary, the proposed approach of engineering critical assessments in particular for subsea pipelines suffering corrosion fatigue has procedures as shown in figure 3.32. It includes two parts: a strategy of selecting crack growth models and their parameters from current industrial standards for corrosion fatigue in seawater; and a three-stage corrosion fatigue crack growth model, which is used in this Section 3.3 to provide basis for comparisons among various models, for corrosion fatigue of other cases.

The detailed procedure of proposed engineering critical assessment for corrosion fatigue in seawater are furtherly demonstrated in figure 3.32. In words it would be as follows: in the beginning of assessment, the ΔK_t of the component's material should be calculated and then be compared with the values for the bilinear (mean+2D) model from industrial standards such as BS 7910 (2015). If the calculated value of ΔK_t is smaller than the provided value, then the bilinear model (mean+2D) is proper to be used. But if the calculated value is larger than the provided value, then the bilinear model (mean+2D) should not be simply applied. It is suggested that the initial ΔK of the aimed inspection interval should then be determined using the detected characteristic dimension of the crack together with the component's load information. If the initial ΔK is larger than the provided ΔK_t , the simplified linear model is recommended for use, otherwise, the bilinear model (mean+2D) may be used before ΔK reaches the provided ΔK_t , but afterward the simplified linear model is again recommended for use.

Note that the material ΔK_t is related to the loading frequency and the initial ΔK is actually related the initial crack size. Hence the proposed approach actually extends the traditional ECA approach to account for the influence from both loading frequency and initial crack size. The research work in this section has been summarized and published by Cheng and Chen (2018a).

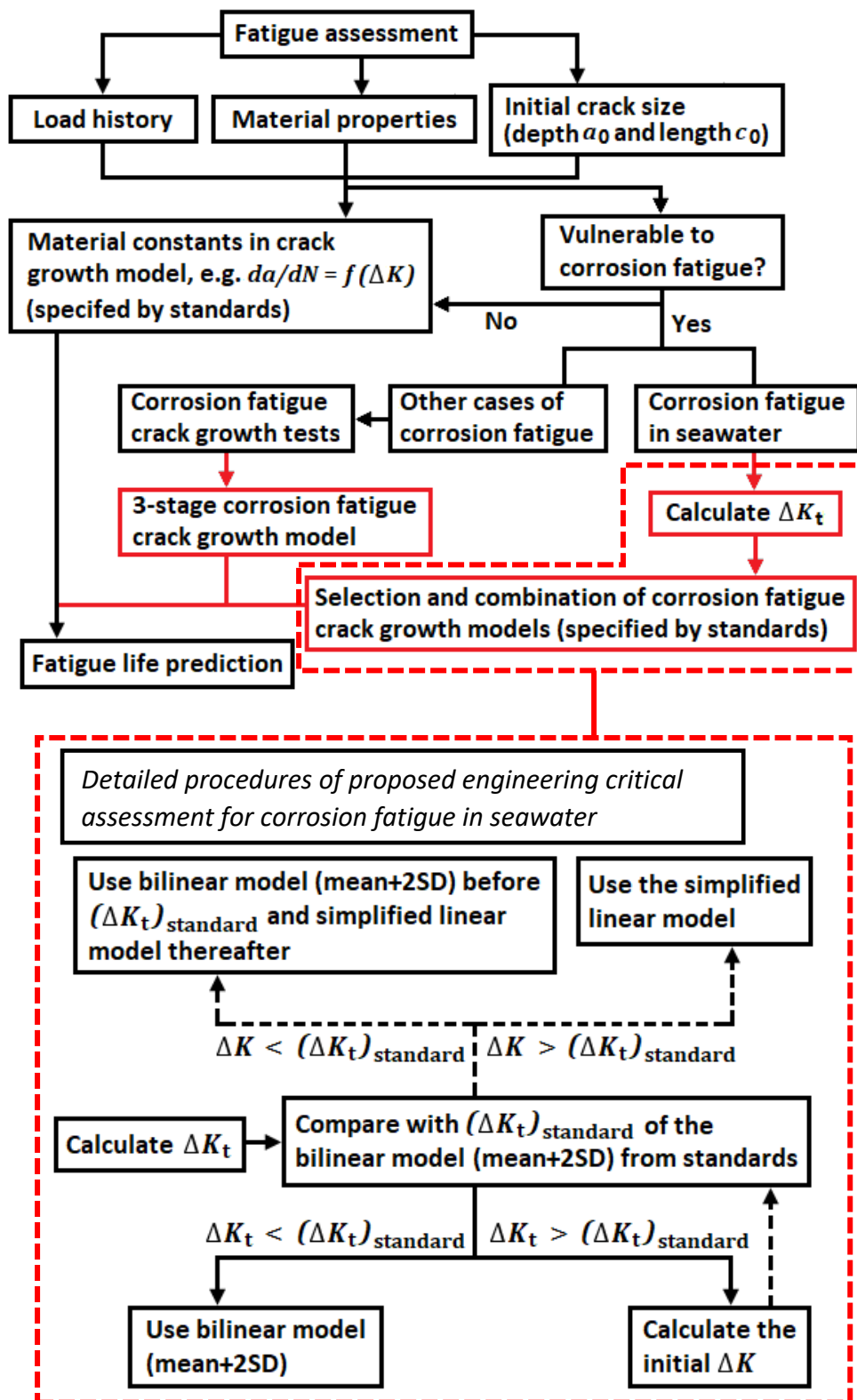


Figure 3.32 Proposed approach of engineering critical assessment for corrosion fatigue

Chapter 4. FATIGUE ASSESSMENT

While most engineering structures are designed to withstand loads well below the material's yield strength, low-cycle fatigue in practice is still possible to happen. For subsea pipelines under high-pressure/high-temperature service conditions, cyclic buckling may happen either as planned or unexpectedly. In each way, the structures can suffer cyclic operational stresses close to or larger than the material's yield strength, which in this thesis is called low-cycle fatigue loads. In such cases, the small-scale yielding assumption of linear elastic fracture mechanics is violated. Therefore, linear elastic fracture mechanics and models based on it can no longer be applied. Unfortunately, most current industrial standards adopt fatigue crack growth models based on linear elastic fracture mechanics to predict the subcritical growth of detected flaws.

The research work to be presented in this Chapter is centred on establishing a prediction model of fatigue crack growth applicable for low-cycle fatigue. It consists of 2 sections. In Section 4.1, an energy principles based model is built up using the characteristic parameter of linear elastic fracture mechanics, ΔK to predict the crack growth of metallic materials under high-cycle fatigue loads. In Section 4.2, crack growth under low-cycle fatigue loads is predicted through establishing a model following a similar idea of last section, but using the characteristic parameter of elastoplastic fracture mechanics, ΔJ to ensure the model's applicability to crack growth under both high-cycle and low-cycle fatigue loads.

4.1 Crack Growth under High-cycle Fatigue Loads

Following the pioneering work of Paris and Erdogan (1963), a number of models relating the range of stress intensity factor, ΔK and the crack growth rate, da/dN , have been developed to describe the fatigue crack growth under small-scale yielding conditions (Nguyen et al., 2001; Pugno et al., 2006; Beden et al., 2009; Santecchia et al., 2016). For most of these models, fatigue crack growth data from tests are required to determine the empirical curve-fitting parameters within the models.

Many researchers have recognized that it is possible to build models capable of predicting fatigue crack growth primarily from the fundamental deformation properties including low-cycle fatigue properties and monotonic and cyclic tensile properties, which are easier to be obtained experimentally and are often required for the purpose of design (Kaisand and Mowbray, 1984; Li et al., 1998; Pandey and Chand, 2003; Hurley and Evans, 2007; Ellyin,

2012; Shi et al., 2016; Huffman, 2016; Wu et al., 2017). Some of them also tapped energy principles in their model development (Pandey and Chand, 2003; Shi et al., 2016; Huffman, 2016). However, in addition to the aforesaid fundamental deformation properties, the threshold range, ΔK_{th} of the material is often required by these models as an input parameter, for calculating either the length of the fracture process zone ahead of crack tip (Li et al., 1998; Pandey and Chand, 2003; Ellyin, 2012) or the critical crack blunting radius (Shi et al., 2016; Wu et al., 2017). Notably, ΔK_{th} is obtained by fatigue crack growth tests and it is thus not widely available due to the high complexity and cost of the tests. Moreover, fatigue crack growth rates will be generated along the tests, undermining the necessity of model prediction.

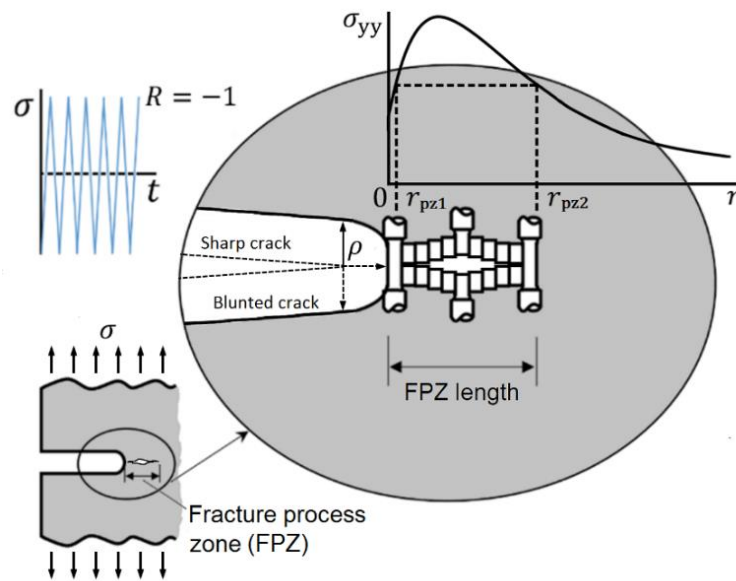


Figure 4.1 Fatigue crack growth with $R = -1$

In this section, a model based on energy principles for fatigue crack growth prediction is developed. As schematically illustrated in figure 4.1, the model is developed for Mode-I cracking under constant-amplitude cyclic loading. Fracture process zone is defined as the region where microscopic events that lead to fracture processing occur. In light of the law of energy conservation, for each load cycle the strain energy released accompanying fatigue crack growth may be attributed to the stored energy accumulated along the length of fracture process zone. By the definition, fatigue crack growth rate da/dN is the crack growth per load cycle, and thus it can be calculated through dividing the accumulated stored energy by the elementary fracture released energy. The length of fracture process zone is determined from the critical stored energy that is obtained by integrating the stresses normal to crack plane over the length of fracture process zone. The stress distribution of stresses normal to crack plane is constructed on the ground of blunting and re-sharpening fatigue crack growth

mechanism and fracture mechanics within the length of fracture process zone. Only fundamental deformation properties are required for the model prediction.

The description of the proposed model is divided into two parts in the present section: the part based on fracture mechanics (4.1.1) and the part based on energy principles (4.1.2); 4.1.3 shows comparison between the model prediction and the test data of metallic materials; Conclusions are drawn in 4.1.4.

4.1.1 Fracture Mechanics Based Model Development

The model development work based on fracture mechanics roots in the widely accepted blunting and re-sharpening theory explaining the fatigue crack growth. The theory states that during loading, the crack tip is blunted by slips along two slip planes with approximately 45° to the crack plane respectively at the same time; upon unloading, the crack tip is re-sharpened by reversed slips; thus the fatigue crack growth is controlled through the repeating process of blunting and re-sharpening under cyclic loads.

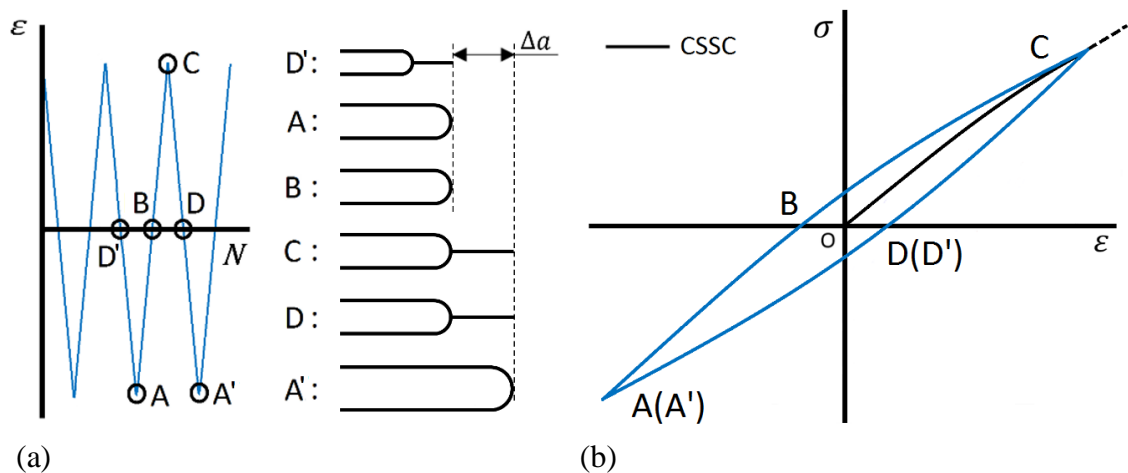


Figure 4.2 (a) Mechanism of fatigue crack growth under constant amplitude cyclic load; (b) Stress-strain relationship under constant-amplitude cyclic load

The process described by the theory may be reasonably restructured, as briefly depicted in figure 4.2(a):

- 1) in each load cycle, upon the start of loading (point A), crack is blunted to some radius;
- 2) as the load keeps increasing (point B), the blunted crack keeps static and crack-tip radius stays constant;
- 3) right at the end of loading (point C), crack growth occurs along the crack plane with a sharp crack tip;
- 4) as the load decreases (point D), the re-sharpened crack keeps static;
- 5) Another load cycle starts and the newly formed crack repeats the process.

To give a clearer illustration, the crack status at point D' in the previous load cycle and at the point A' in the next load cycle are also plotted.

In this section, the restructuring of the fatigue crack growth process based on the blunting and re-sharpening mechanism is important for establishing the prediction model. It defines a fatigue crack growth in a step-wise way, which allows to link the change of strain energy release rate with the fatigue crack growth rate. Also, the notch-like blunted crack before crack growth enables the distribution of stresses normal to the crack plane to be constructed utilizing the methods used for notch analysis. This is based on the fact that there is no fundamental difference in the cracking behaviours of notch and crack, indicating that the methods for notch analysis may also be applicable for cracks, as supported by the theory of critical distance proposed by David Taylor (1999) and its applications in fatigue (Taylor, 2008; Susmel, 2008; Araújo et al., 2017; Benedetti and Santus, 2019).

4.1.1.1 Strain-life and Stress-strain Relationships

The strain-life relationship is often expressed in the form of Basquin-Coffin-Manson equation

$$\frac{\Delta\varepsilon}{2} = \frac{\sigma'_f}{E} (2N_f)^b + \varepsilon'_f (2N_f)^c \quad (4 - 1)$$

where $\Delta\varepsilon$ is the strain range, E the Young's modulus, $2N_f$ the reversals to failure, σ'_f , ε'_f , b and c refer to the cyclic fatigue strength coefficient, the fatigue ductility coefficient, the fatigue strength exponent and the fatigue ductility exponent. The strain-life relationship is normally curve fitted from low-cycle fatigue test data and thus σ'_f , ε'_f , b and c are also called as the low-cycle fatigue properties of the material.

The stress-strain relationship of metallic materials is often described using a power law model. In the context of cyclic loading, the cyclic stress-strain curve is drawn by joining the tip locus of the stabilized hysteresis loops obtained via fatigue tests, and its mathematical expression is

$$\varepsilon_a = \frac{\sigma_a}{E} + \left(\frac{\sigma_a}{H'}\right)^{\frac{1}{n'}} \quad (4 - 2)$$

where ε_a is the strain amplitude, σ_a the stress amplitude, H' the cyclic strength coefficient, and n' the cyclic strain hardening exponent. Figure 4.2(b) is a nominal stress-nominal strain plot. With reference to equation (4 - 2), it is not unexpected to see the stabilized hysteresis loop. The cyclic stress-strain curve is also plotted in the figure. Assuming the material exhibits a Masing behaviour, equation (4 - 2) can be rewritten into

$$\frac{\Delta\varepsilon}{2} = \frac{\Delta\sigma}{2E} + \left(\frac{\Delta\sigma}{2H'}\right)^{1/n'} \quad (4-3)$$

where the strain range $\Delta\varepsilon = 2\varepsilon_a$ and the stress range $\Delta\sigma = 2\sigma_a$.

4.1.1.2 Crack-tip Stress Distribution

Under monotonical loading conditions, the crack-tip stress field of a material described by Hutchinson-Rice-Rosengren or briefly HRR solution (Hutchinson, 1968; Rice and Rosengren, 1968) may be written as

$$\sigma_{ij} = \sigma_0 \left(\frac{K^2}{\alpha \sigma_0^2 I_n r} \right)^{n/(n+1)} \tilde{\sigma}_{ij} \quad (4-4)$$

with

$$\alpha = \frac{E}{\sigma_0} \left(\frac{\sigma_0}{H} \right)^{1/n} \quad (4-5)$$

where σ_0 is the yield strength, K the stress intensity factor, r the distance off the crack tip along the crack plane, n the strain-hardening exponent, I_n an integration constant depending on n , and $\tilde{\sigma}_{ij}$ the non-dimensional angular distribution function. For details of calculating $\tilde{\sigma}_{ij}$ and I_n , please refer to the works by Guo (1993a; 1993b) and Galkiewicz and Graba (2006). Note that the implicit assumption of the HRR solution is that the material behaviours following the monotonic stress-strain curve, which is mathematically expressed as

$$\varepsilon = \frac{\sigma}{E} + \left(\frac{\sigma}{H} \right)^{1/n} \quad (4-6)$$

where σ and ε are the stress and strain respectively, and H is the strength coefficient.

HRR solution is valid to describe the stress distribution from some small distance off the crack tip through the fracture process zone but not appropriate for the region very close to the crack tip (Anderson, 2017) since it predicts singularity at the crack tip. In reality an infinite stress is impossible due to the crack-tip blunting and the strain hardening effect. Hill solution (Hill, 1998) has been widely adopted to describe the stress distribution very close to the root of notch with a radius r_0 . For the stress normal to the crack plane, σ_{yy} , it follows that

$$\sigma_{yy} = \sigma_0 \left[1 + \ln \left(1 + \frac{r}{r_0} \right) \right] \quad (4-7)$$

Tetelman and McEvilly (1967) modified equation (4-7) with $2/\sqrt{3}\sigma_c$ replacing σ_0 , where σ_c represents the flow stress. Considering the crack blunting, r_0 may be replaced by ρ . It is

easy to tell that at the blunted crack tip, $\sigma_{yy} = 2/\sqrt{3}\sigma_c$, i.e. the crack-tip local stress equals $2/\sqrt{3}\sigma_c$. Hence if the crack-tip local stress is known, σ_c can be obtained.

4.1.1.3 Crack-tip Radius

As sketched in figure 4.1, the crack-tip radius ρ caused by blunting has an approximate relationship with the crack tip opening displacement (CTOD) as below

$$\rho = CTOD/2 \quad (4 - 8)$$

While J -integral, which is the two-dimensional path-independent line integral around the crack tip, is widely used to correlate with $CTOD$, Well's (1961) original estimate of $CTOD$ under small-scale yielding conditions is in the form as

$$CTOD = \frac{G}{m\sigma_0} \quad (4 - 9)$$

where m is a dimensionless constant that depends on the stress state and material properties, and G is the crack extension force or strain energy release rate (in SI units J/m^2 or equivalently $Pa \cdot m$). The experimental observation by Dawes (1979) and the finite element analysis results by Shih and German (1981) clearly show that the linear relationship between G and $CTOD$ indicated by equation (4 - 9) is extended to elastoplastic conditions. Different expressions of m have been formulated as functions of crack aspect ratios from extensive experiments and elastic-plastic finite element analyses (Zhu and Joyce, 2012; ASTM E1820-17, 2017). To consider the strain hardening effect, the yield strength σ_0 in equation (4 - 9) is commonly replaced by the effective yield strength σ_Y that is the average of σ_0 and the ultimate tensile strength σ_u .

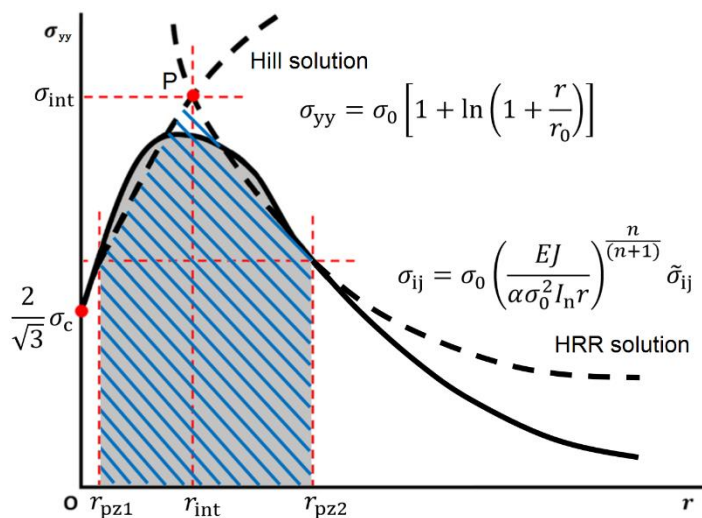


Figure 4.3 Crack-tip stress distribution at the peak stress of a load cycle

Combining equations (4 – 1) ~ (4 – 9), the distribution of σ_{yy} in front of crack tip can thus be constructed, as sketched in figure 4.3. The abscissa coordinate of the intersection point P, r_{int} can be obtained and the corresponding peak stress σ_{int} can be also calculated by either equation (4 – 4) or equation (4 – 7). Note that in reality the peak stress along the crack plane, σ_{yy}^{max} may occur at the point with the abscissa coordinate r_{max} , different from the point P predicted by equation (4 – 4) and (4 – 7), but the shaded areas under the predicted stress distribution curve and the real may be viewed as approximately equal. This is supported by the work of De Jesus and Correia (2013). They compared the stress distribution ahead of the crack tip along the crack plane obtained analytically using a similar local-strain method and that obtained numerically using the finite element analysis. It was found that for the case of small-scale yielding conditions, the portions before σ_{yy}^{max} of both stress distribution curves are very small and agree well with each other in general.

Assuming the linear relationship represented by equation (4 – 9) applies in the case of cyclic loading, the cyclic strain energy release rate, ΔG should be used in place of G in equation (4 – 9). The model development work based on fracture mechanics now has been fulfilled.

4.1.2 Energy Principles Based Model Development

In this section, details of the model development work based on energy principles are presented, including the calculation of crack-tip local stress, determination of the length of fracture process zone, and the prediction of fatigue crack growth rate. In addition, it should be pointed out herein that in this research the term “energy” is commonly used in analysis based on energy principles particularly for material elements. But strictly speaking, when the bulk material is considered, either “energy per unit area” (J/m^2 or equivalently $Pa \cdot m$) or “energy per unit volume” (J/m^3 or equivalently Pa) may be more appropriate depending on the situation.

4.1.2.1 Crack-tip Local Stress

It is possible to obtain the local stresses at blunted crack tip invoking energy principles. Molski and Glinka (1981) proposed the equivalent strain energy density rule, which assumes that the strain energy density at the notch root is nearly the same for linear elastic notch behaviour (W_n) and elastic-plastic notch behaviour (W_t) and it has achieved good results in calculating the local stresses at notch roots (Stephens et al., 2000). In the case of monotonic loading, the equivalent strain energy density rule can be expressed in the form as

$$(K_t)^2 W_n = W_t \quad (4 - 10)$$

where K_t is the stress concentration factor at the crack tip, and

$$\left\{ \begin{array}{l} W_n = \frac{Se}{2} \end{array} \right. \quad (4 - 11a)$$

$$\left\{ \begin{array}{l} W_t = \frac{\sigma^2}{2E} + \frac{\sigma}{n+1} \left(\frac{\sigma}{H} \right)^{1/n} \end{array} \right. \quad (4 - 11b)$$

where S and e is the nominal elastic stress and strain respectively, and σ is the local stress.

In the case of cyclic loading condition, W_n and W_t in equations (4 - 10) and (4 - 11) are replaced by ΔW_n and ΔW_t , where

$$\left\{ \begin{array}{l} \Delta W_n = \frac{\Delta S \Delta e}{2} \end{array} \right. \quad (4 - 12a)$$

$$\left\{ \begin{array}{l} \Delta W_t = \frac{\Delta \sigma^2}{2E} + \frac{2\Delta \sigma}{n'+1} \left(\frac{\Delta \sigma}{2H'} \right)^{1/n'} \end{array} \right. \quad (4 - 12b)$$

with ΔS and Δe being the nominal elastic stress and strain ranges respectively, and $\Delta \sigma$ the local stress range. This enables the equivalent strain energy density rule, i.e. equation (4 - 10) to be re-written as

$$(K_t)^2 \Delta S \Delta e = \Delta \sigma \Delta \varepsilon + \Delta W_h \quad (4 - 13)$$

where $\Delta \varepsilon$ has the expression indicated by equation (4 - 3) and ΔW_h actually corresponds to the hysteresis energy calculated by

$$\Delta W_h = \frac{(1 - n') 2 \Delta \sigma}{n' + 1} \left(\frac{\Delta \sigma}{2H'} \right)^{1/n'} \quad (4 - 14)$$

From the perspective of thermodynamics, equation (4 - 13) states that the theoretical work $\Delta S \Delta e$ applied to the material element at the notch root due to the nominal stress range is transformed into the real total strain energy $\Delta \sigma \Delta \varepsilon$ absorbed by the notch-root material element and the dissipated hysteresis energy ΔW_h . However, it has been pointed out that actually a part of ΔW_h will also contribute to the local stress and strain ranges at the notch root, and therefore only the remaining part of ΔW_h will be dissipated into heat at the notch root due to plasticity (Ye et al., 2004). Accordingly, the modified rule of equivalent strain energy density for cyclic loading conditions was proposed, i.e.

$$(K_t)^2 \Delta S \Delta e = \Delta \sigma \Delta \varepsilon + \Delta W_q \quad (4 - 15)$$

where the part of hysteresis energy dissipated into heat is denoted as ΔW_q , and has an expression as the following

$$\Delta W_q = \frac{2(1 - 2n')\Delta\sigma}{1 + n'} \left(\frac{\Delta\sigma}{2H'} \right)^{1/n'} \quad (4 - 16)$$

Combining equations (4 – 10) ~ (4 – 16), the modified rule of equivalent strain energy density, i.e. equation (4 – 15) can be rewritten into

$$(K_f)^2 \frac{\Delta S^2}{E} = \frac{\Delta\sigma^2}{E} + \frac{2(2 - n')\Delta\sigma}{1 + n'} \left(\frac{\Delta\sigma}{2H'} \right)^{1/n'} \quad (4 - 17)$$

The modified rule of equivalent strain energy density, represented by equation (4 – 15), is adopted in this research to calculate the local stress range at “notch” root under small-scale yielding conditions. But instead of K_t , K_f , which is called the fatigue stress concentration factor (Arola and Williams, 2002; Chen, 2016), is used in equation (4 – 15) to account for the “notch” size effect (Topper et al., 1967) since the crack-tip radius due to blunting is very small. According to Neuber (1958), K_f can be calculated by

$$K_f = 1 + \frac{K_t - 1}{1 + \sqrt{\rho_0/\rho}} \quad (4 - 18)$$

where ρ represents the crack-tip radius instead of the notch root radius. ρ_0 is the so-called Neuber’s material characteristic length. As indicated by equation (4 – 18), the larger ρ is, the smaller difference between K_f and K_t is. Approximating the blunted crack tip by an elliptical notch, K_t can be calculated as (Pilkey and Pilkey, 2008)

$$K_t = 0.855 + 2.21\sqrt{a/\rho} \quad (4 - 19)$$

with a being the crack’s characteristic dimension. For through-thickness cracks, a represents the half crack length, for surface cracks, a is the flaw height, and for embedded cracks, a is the half height.

The crack-tip local stresses and thus σ_c can be found following the steps mentioned above. Obviously σ_c is not a constant like σ_0 , which is also supported by the study of Ganesh et al. (2019). With σ_c is known, the construction of σ_{yy} distribution along the length of fracture process zone ahead of a crack tip is accomplished.

4.1.2.2 Length of Fracture Process Zone

It has been experimentally proven that when a notched metallic specimen is monotonically loaded to be plastically deformed, the bulk of the supplied plastic strain energy is dissipated in the form of heat and vibration, and perhaps slip along the crystallographic planes and dislocation movements in front of the notch, while the remaining part is stored in the material along the loading path (Ellyin, 2012). With the introduction of unloading, the elastic part of the stored energy is recovered, and the remaining part of the stored energy may be associated with residual stresses generated in the metal after unloading (Kim, 1990; Klesnil and Lukac, 1992; Ye et al., 2004). Therefore, the supplied strain energy can be viewed as the sum of two types of energy: the recoverable type and the irrecoverable type. The recoverable energy is the elastic part of the energy stored along loading. The irrecoverable energy includes the remainder part of the stored energy and the dissipated energy. For a cracked specimen, as the crack grows under cyclic loads, the irrecoverable stored energy of the fractured material could be released (Benaarbia et al., 2014). Under cyclic loads, the hysteresis energy, represented by the area enclosed by ABCD in figure 4.2(b) or figure 4.4, is often taken to represent the total irrecoverable energy (Ellyin, 2012).

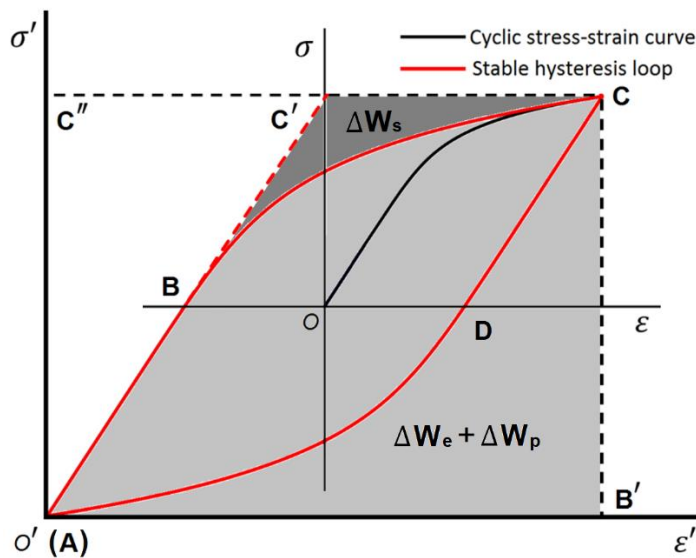


Figure 4.4 Strain energy density required for material elements to fracture

According to Skelton (1987), for a material element, the irrecoverable stored energy, denoted as ΔW_s corresponds only to its tension half cycle of the hysteresis loop as illustrated in figure 4.4 by the area shaded in dark grey. Thus ΔW_s is expressed by

$$\Delta W_s = \text{Area ABC} = \int_0^{\Delta\sigma} \varepsilon' d\sigma' - \frac{\Delta\sigma^2}{2E} \quad (4 - 20)$$

Combined with equation (4 - 3), ΔW_s can be rewritten into

$$\Delta W_s = \frac{2n'\Delta\sigma}{n'+1} \left(\frac{\Delta\sigma}{2H'} \right)^{1/n'} \quad (4-21)$$

In front of a crack tip, the accumulation of irrecoverable stored energy starts from the point where it must be released or can no more be stored, and ends at the point where it must be released or can no more be stored. The limit of irrecoverable stored energy for the material in a load cycle is the ΔW_s of the special case where $N_f = 1/2$. Denoted as $\Delta W_{\bar{s}}$, this limit is called the critical stored energy and it is adopted to define the range of fracture process zone along the crack plane. The boundary conditions are therefore given by

$$\begin{cases} \Delta W_s|_{r_{prz1}} = \Delta W_{\bar{s}} & \text{with } \Delta\sigma = \frac{2}{\sqrt{3}}\sigma_c \left[1 + \ln \left(1 + \frac{r}{\rho} \right) \right] \\ \Delta W_s|_{r_{prz2}} = \Delta W_{\bar{s}} & \text{with } \Delta\sigma = \Delta\sigma_0 \left(\frac{\Delta K^2}{\alpha' \Delta\sigma_0^2 I_n r} \right)^{n'/(n'+1)} \tilde{\sigma}_{ij} \end{cases} \quad (4-22)$$

$$\tilde{\sigma}_{ij} \quad (4-23)$$

where r_{prz1} and r_{prz2} are the abscissa coordinates of the left and right boundary points, respectively, and α' corresponds to α in equation (4-5) but it is derived based on equation (4-3) as

$$\alpha' = \frac{2E}{(2H')^{1/n'} \Delta\sigma_0^{(n'-1)/n'}} \quad (4-24)$$

where $\Delta\sigma_0 \sim 2\sigma'_0$, σ'_0 is the cyclic yield strength calculated as the 0.2% offset value if not specified. Equations (4-22) and (4-23) indicate that length of fracture process zone or $[r_{pz1}, r_{pz2}]$ may vary with the level of applied stresses, which is supported by the observations of Li et al. (1998) and Ellyin (2012) et al.

4.1.2.3 Fatigue Crack Growth Rate

Called the cyclic strain energy release rate, ΔG could be physically interpreted as the energy released per unit of newly created crack surface area under cyclic loads. It should be noted that $\Delta G \neq G_{\max} - G_{\min}$. ΔG is more like an “equivalent” strain energy release rate which is calculated based on the “equivalent” stress $\Delta\sigma$ and the “equivalent” strain $\Delta\varepsilon$. As per the analysis in 4.1.2.2, for a load cycle ABCD in figure 4.2(b), the cyclic strain energy released accompanying the crack growth at B could be attributed to the irrecoverable strain energy stored along the loading branch. Then for each load cycle, the energy conservation law yields

$$\Delta a \Delta W_{\bar{f}} = \Delta \Pi_{FPZ} \quad (4-25)$$

where Δa is the increment of a at the end of load cycle, $\Delta W_{\bar{f}}$ is the elementary fracture released energy or more specifically the unit of energy per unit volume, which will be explained and calculated later in this part, and $\Delta \Pi_{\text{FPZ}}$ is the total irrecoverable stored strain energy accumulated along the length of fracture process zone, or briefly the accumulated stored energy, in the load cycle before Δa occurs. Therefore Δa equals the fatigue crack growth rate by its definition. Correspondingly equation (4 – 25) is rewritten as

$$\frac{da}{dN} = \frac{\Delta \Pi_{\text{FPZ}}}{\Delta W_{\bar{f}}} \quad (4 - 26)$$

Elementary fracture released energy ($\Delta W_{\bar{f}}$)

To find $\Delta W_{\bar{f}}$, recall that for linear elastic materials under plane stress condition,

$$\Delta G = \frac{\Delta K^2}{E} \quad (4 - 27)$$

where the stress intensity factor range ΔK is calculated through

$$\Delta K = F \Delta S \sqrt{\pi a} \quad (4 - 28)$$

with F accounting for stress amplification by net-section (Chandran, 2017). However, when fracturing the material element within one load cycle, significant plasticity will be introduced and the material will behave in an elastoplastic manner, invalidating the equilibrium indicated by equation (4 – 27). The approach proposed by Dowling (1977) is adopted herein to estimate ΔG under elastoplastic conditions. ΔG is first split into two components,

$$\Delta G = \Delta G_e + \Delta G_p \quad (4 - 29)$$

ΔG_e and ΔG_p represents the contributions of the elastic and plastic terms in equation (4 – 3), respectively. ΔG_e can be approximated using equation (4 – 27). Note that the elastic strain energy of a material element is

$$\Delta W_e = \frac{\Delta S^2}{2E} \quad (4 - 30)$$

Upon substituting equations (4 – 29) and (4 – 30) into equation (4 – 27), it follows that

$$\Delta G_e = 2\pi a F^2 \Delta W_e \quad (4 - 31)$$

Assuming the energy correction factor F^2 is also applied to ΔG_p , then referring to equation (4 – 31), ΔG_p may be approximated by

$$\Delta G_p = 2\pi a F^2 f(n') \Delta W_p \quad (4 - 32)$$

where $f(n')$ is introduced to consider the influence of plasticity, and ΔW_p is the plastic strain energy. Various formulae have been derived for estimating $f(n')$ (Shih and Hutchinson, 1976; Ngoula et al., 2018). Considering the stress-strain relationship represented by equation (4 - 3), ΔW_p has the expression as below

$$\Delta W_p = \frac{2\Delta S}{n' + 1} \left(\frac{\Delta S}{2H'} \right)^{\frac{1}{n'}} \quad (4 - 33)$$

Then equation (4 - 29) is rewritten into

$$\Delta G = 2\pi a F^2 [\Delta W_e + f_{n'} \Delta W_p] \quad (4 - 34)$$

As indicated by the above equation, ΔG is a function of a when the nominal stress ΔS is constant. In fact ΔG , similar to G , is uniquely defined for a specimen cyclic loaded under the nominal stress range ΔS with a crack of characteristic dimension a . In this sense, ΔG is a global concept. Assuming there is a small increment of a , denoted as δa , occurs at the end of some load cycle, ΔG will be increased by $\delta \Delta G$ accordingly, which is calculated as

$$\delta \Delta G = 2\pi \left[\frac{\Delta S^2}{2E} + 2f_{n'} \Delta S \left(\frac{\Delta S}{2H'} \right)^{\frac{1}{n'}} \right] [F|_{a+\delta a}^2 (a + \delta a) - F|_a^2 a] \quad (4 - 35)$$

Note that before the crack shows unstable growth, F usually has a flat slope. Hence when δa is small, $F|_{a+\delta a} \cong F|_a$. Thus equation (4 - 35) becomes

$$\Delta W_f = \frac{\delta \Delta G}{\delta a} = 2\pi (F|_a^2) \left[\frac{\Delta S^2}{2E} + 2f_{n'} \Delta S \left(\frac{\Delta S}{2H'} \right)^{\frac{1}{n'}} \right] \quad (4 - 36)$$

The above equation can be explained as that an increase ΔW_f of the energy released per unit volume is required globally to grow the crack by δa in its characteristic dimension. Note that while the crack grows by δa globally, locally the crack-tip material element is fractured.

Therefore, particular analysis on the crack-tip material element is needed.

Different from the global specimen, for the material element to be fractured in one load cycle ahead of the crack tip, there is no crack in the element at the beginning of the load cycle. Thus $F|_a^2 = 1$. With reference to the reconstructed process of fatigue crack growth, the strain range that can fracture the material element by a loading half cycle is found through equation (4 - 1) by setting $N_f = 1/2$. Combined with equation (4 - 3), the specific stress range can

be found. Substituting this specific stress range into equation (4 – 36), the energy released by fracturing the material element of unit volume, i.e. the elementary fracture released energy, $\Delta W_{\bar{f}}$ is obtained.

Accumulated stored energy ($\Delta\Pi_{\text{FPZ}}$)

Based on the previous work, $\Delta\Pi_{\text{FPZ}}$ can be calculated by integrating ΔW_s over the domain of $[r_{\text{pz1}}, r_{\text{pz2}}]$, i.e.

$$\Delta\Pi_{\text{FPZ}} = \int_{r_{\text{pz1}}}^{r_{\text{pz2}}} F^2 \Delta W_s dr \quad (4 - 37)$$

Combining equations (4 – 3) and (4 – 21), the equation (4 – 37) can be rewritten into

$$\Delta\Pi_{\text{FPZ}} = \frac{2n'}{1+n'} \left(\frac{1}{2H'} \right)^{1/n'} F^2 \int_{r_{\text{pz1}}}^{r_{\text{pz2}}} \Delta\sigma^{1+1/n'} dr \quad (4 - 38)$$

The distribution of $\Delta\sigma$ within $[r_{\text{pz1}}, r_{\text{pz2}}]$ under a constant-amplitude cyclic load is estimated based on the model development work in fracture mechanics,

$$\Delta\sigma = \begin{cases} \frac{2}{\sqrt{3}} \sigma_c \left[1 + \ln \left(1 + \frac{r}{\rho} \right) \right] & r \in [r_{\text{pz1}}, r_{\text{int}}] \quad (4 - 39a) \\ \Delta\sigma_0 \left(\frac{\Delta K^2}{\alpha' \Delta\sigma_0^2 I_{n',r}} \right)^{n'/(n'+1)} \tilde{\sigma}_{ij} & r \in [r_{\text{int}}, r_{\text{pz2}}] \quad (4 - 39b) \end{cases}$$

In the context of cyclic loading, the effective yield strength σ_Y in equation (4 – 9) should be calculated as the average of σ'_0 and σ'_f . The later applications of the proposed model in different metals find the peak stresses normal to the crack plane σ_{yy}^{max} agrees with the expectation that $\sigma_{yy}^{\text{max}} = 3 \sim 5 \sigma_0$ (Ritchie and Thompson, 1985).

4.1.3 Model Application and Discussion

Figure 4.5 is the flow diagram of main routine implementing the proposed model. In the manner of cycle-by-cycle calculation, ΔN equals 1 and Δa is then the value of the fatigue crack growth rate. The fatigue crack growth begins as the calculated $\Delta\Pi_{\text{FPZ}} > 0$. The subroutine used to find the corresponding ΔK threshold is given in figure 4.6, where a self-adaptive iterative algorithm in response to the applied stress is illustrated. It requires the same input material properties and loading conditions as provided for the main procedure. Both the main routine and subroutine are coded using MATLAB. As long as the subroutine finishes, the main routine begins.

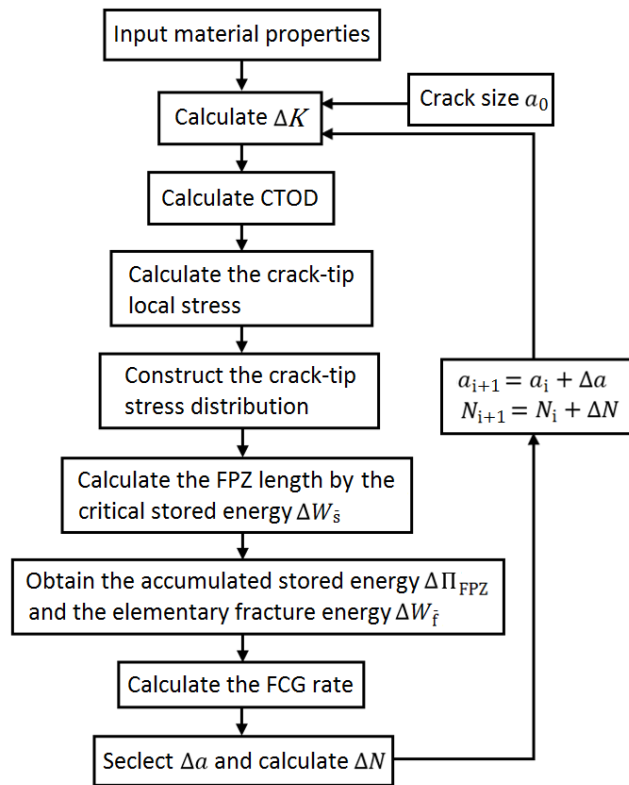


Figure 4.5 Main routine implementing the proposed model for predicting fatigue crack growth (FCG) rate

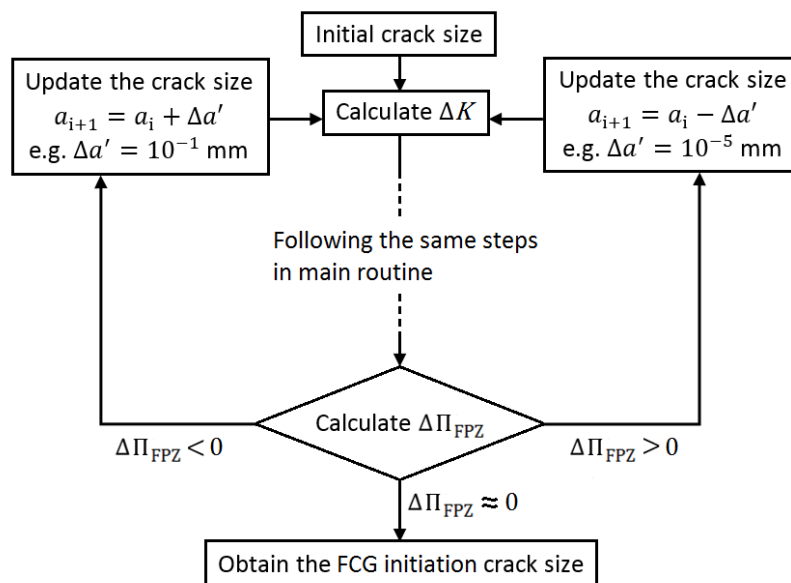


Figure 4.6 Subroutine for calculating the initiation crack size of fatigue crack growth

While the test data of materials' fundamental deformation properties for different materials generated are plentiful in literature, and the fatigue crack growth rate data generated by tests for some materials under fully reversed constant-amplitude cyclic loads are available, there is a lack of research where both types of data are provided for the same material. Hence, only following metals are used for model validation, i.e. A533-B1 steel, AISI 4340 steel, AISI

4140 steel, 25CrMo4 steel, 2024-T351 aluminium, 7075-T6 aluminium, 7175-T6 aluminium and Ti6Al4V alloy. Their fundamental deformation properties, i.e. monotonic and cyclic tensile material properties and low-cycle fatigue material properties, and the test data of fatigue crack growth rates are collected from literature, with the data compatibility confirmed by either previous researchers (Li et al., 1998; Silva, 2005; Wu et al., 2017) or the author. After model validation, AISI 4340 steel and 7075-T6 aluminium are utilized to investigate the potential model application under different stress ratios ($R = -1, 0, 0.5$). The input parameters of the model for each material is tabulated in table 4.1 together with the data sources. The information of the fatigue crack growth tests for each material is listed in table 4.2. For more testing details, please refer to the references given in table 4.2.

Parameters	Monotonic and cyclic tensile properties					Low-cycle fatigue properties				Data source
	σ_0	E	σ_u	K'	n'	σ'_f	b	ϵ'_f	c	
A533-B1 Steel	482	200	627	1047	0.165	869	-0.085	0.32	0.52	Li et al., 1998
AISI 4340 Steel	634	192	826	1384	0.17	1232	-0.10	0.53	0.56	Noroozi et al., 2005
SAE 4140 Steel	1341	201	1474	1110	0.036	1424	0.053	2.65	0.84	Rteil and Topper, 2005
25CrMo4 Steel	512	206	674	892	0.11	900	0.072	0.90	0.69	Wu et al., 2017
2024-T351 Al	379	73	469	662	0.07	927	0.113	0.41	0.71	Noroozi et al., 2005
7075-T6 Al	520	71	578	977	0.106	1466	0.143	0.26	0.62	Dowling, 2012
7175 Al	611	72	656	779	0.038	814	0.059	0.67	1.18	Salerno, 2007
Ti6Al4V Alloy	805	122	845	1288	0.095	1293	0.088	0.26	0.72	ASM, 1996
<i>Unit</i>	MPa	GPa	MPa	MPa	-	MPa	-	-	-	

Table 4.1 Material input parameters for model application

Material	Stress ratio	Test data(Δ)	Data source
A533-B1 Steel	-1	Yes	Dowling, 1977
AISI 4340 Steel	-1	Yes	Newman, 2007
	0	Yes	
	0.5	Yes	
SAE 4140 Steel	-1	Yes	Stephens et al., 1979
25CrMo4 Steel	-1	Yes	Luke, 2010
2024-T351 Al	-1	Yes	Forman et al., 2005
7075-T6 Al	-1	Yes	Newman et al., 1994
	0	Yes	
	0.5	Yes	
7175 Al	-1	Yes	Silva, 2005
Ti6Al4V Alloy	-1	Yes	Silva, 2005

Table 4.2 Fatigue crack growth test information

4.1.3.1 General Application

The fatigue crack growth curves of materials of A533-B1 steel, AISI 4340 steel, AISI 4140 steel, 25CrMo4 steel, 2024-T351 aluminium, 7075-T6 aluminium, 7175-T6 aluminium and Ti6Al4V alloy under constant-amplitude cyclic loads with $R = -1$ were predicted by the proposed model and plotted in figures 4.7 ~ 4.14 against the corresponding test data.

As can be seen in those figures, the model predictions for all those metallic materials are pretty good in spite of some local deviations. The predicted fatigue crack growth curves agree well with the test data in both the near-threshold regime and the stable-growth regime of ΔK . More specifically, for those materials of which the start of fatigue crack growth may not be well defined by their test data, such as AISI 4340 steel, 25CrMo4 steel, 7075-T6 aluminium, and Ti6Al4V alloy, the predicted curve by the proposed model provides good prediction. For those materials of which the start of fatigue crack growth may be clearly observed in the test data provided, such as A533-B1 steel, AISI 4140 steel, 2024-T351 aluminium, and 7175 aluminium, the proposed model not only works well to predict the fatigue crack growth but also captures the start of real fatigue crack growth with good accuracy. In general, figures 4.7 ~ 4.14 show that the proposed model can provide good prediction for the fatigue crack growth and its start for metallic materials under constant-amplitude cyclic loads with $R = -1$.

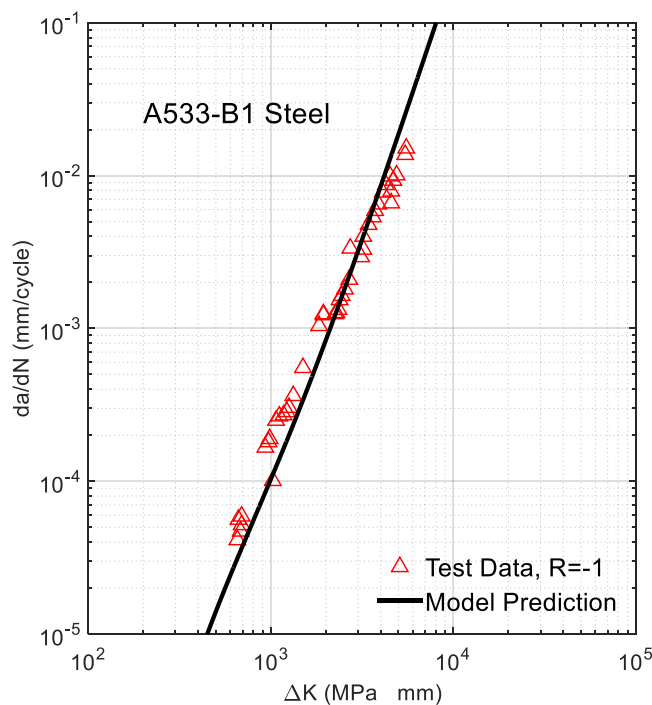


Figure 4.7 Comparison between model prediction and test data (Dowling, 1977) for A533-B1

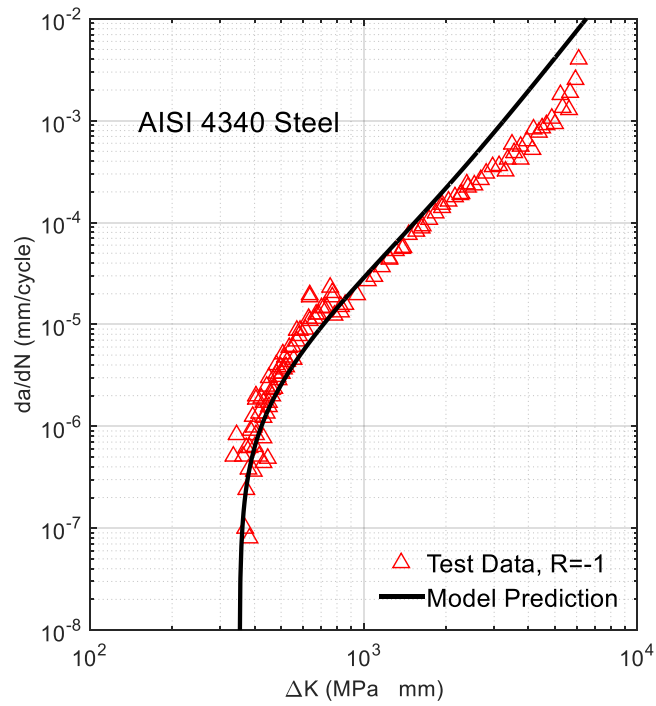


Figure 4.8 Comparison between model prediction and test data (Newman, 2007) for AISI 4340 Steel

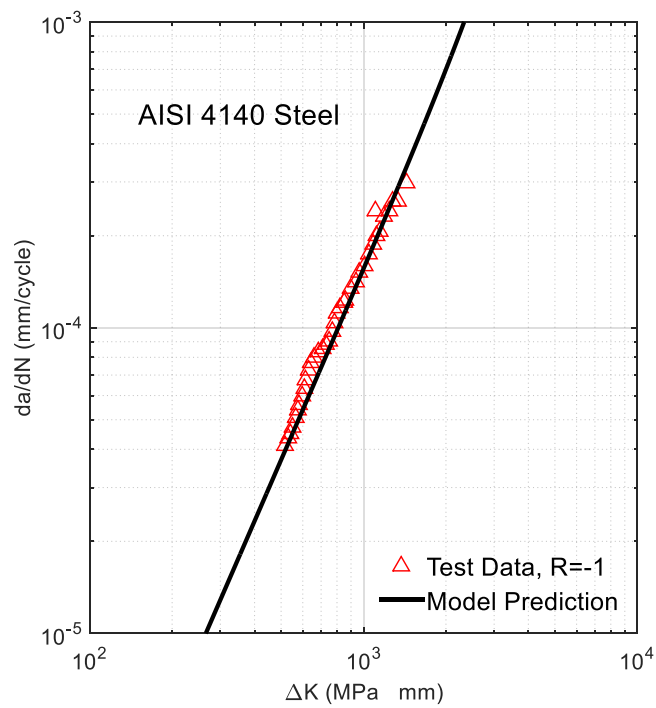


Figure 4.9 Comparison between model prediction and test data (Stephens et al., 1979) for AISI 4140 Steel

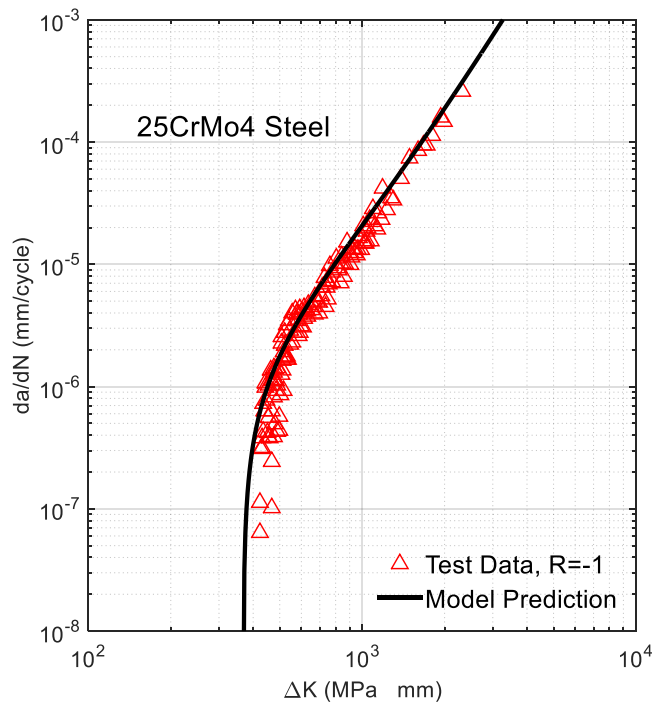


Figure 4.10 Comparison between model prediction and test data (Luke et al., 2010) for 25CrMo4 Steel

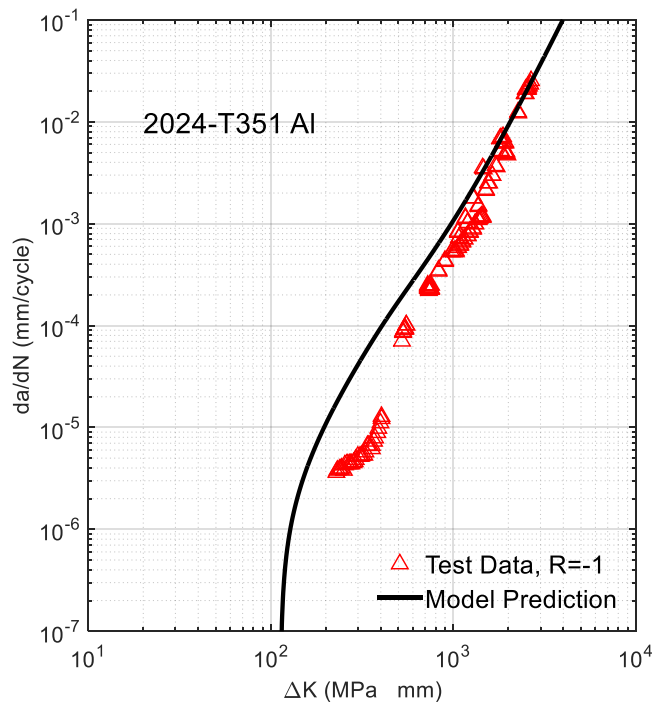


Figure 4.11 Comparison between model prediction and test data (Forman et al., 2005) for 2024-T351 Al

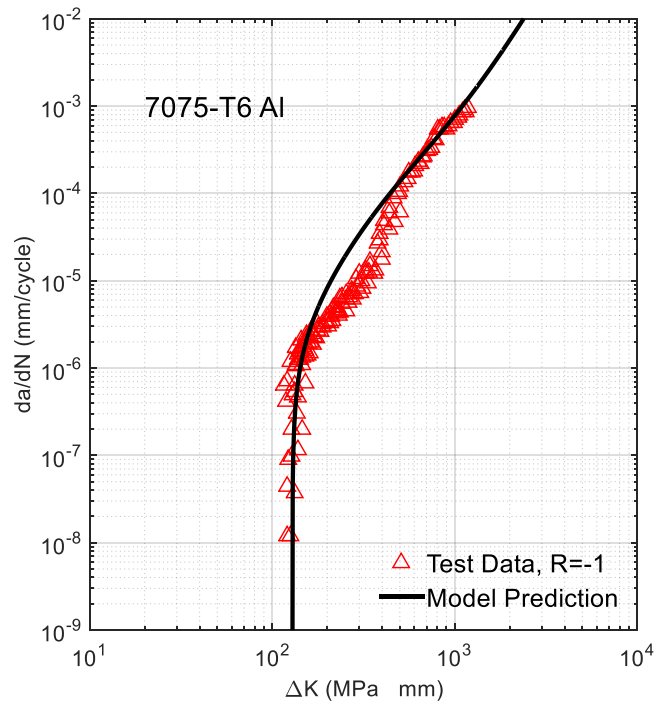


Figure 4.12 Comparison between model prediction and test data (Newman et al., 1994) for 7075-T6 Al

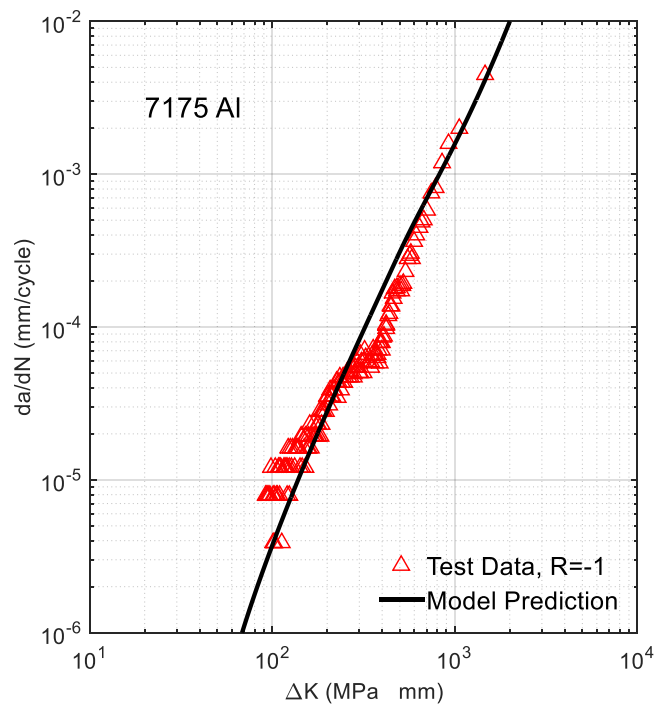


Figure 4.13 Comparison between model prediction and test data (Silva, 2005) for 7175 Al

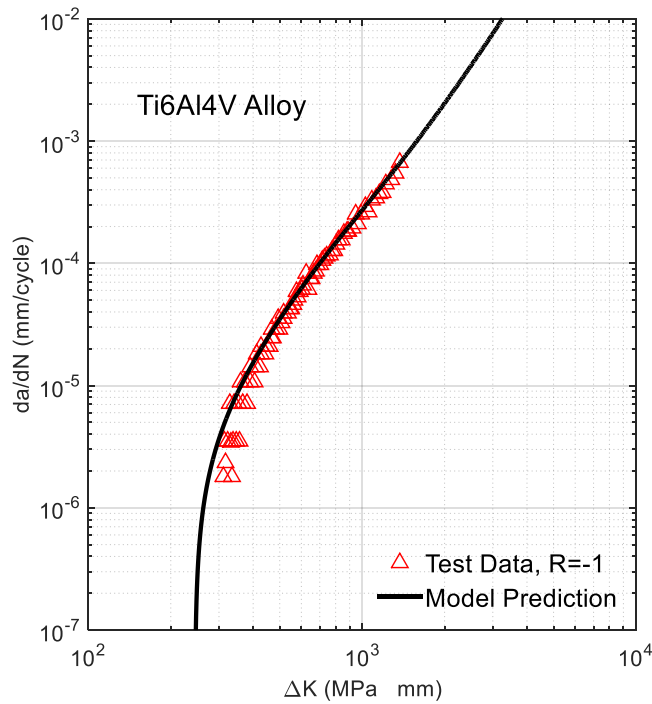


Figure 4.14 Comparison between model prediction and test data (Silva, 2005) for Ti6Al4V Alloy

4.1.3.2 Stress Ratio Effect

In the case of constant-amplitude fatigue loading, the stress ratio R can have a significant effect on the fatigue crack growth. An increase in R usually causes growth rates for a given ΔK to be larger, as illustrated by figure 4.15(a) and figure 4.16(a) for AISI 4340 steel and 7075-T6 aluminium respectively. While the proposed model is developed for the case of fully reversed constant-amplitude cyclic loading, i.e. $R = -1$, it is possible to be used for predicting the fatigue crack growth rates for metallic materials loaded at different R levels.

Various relationships have been proposed to characterize the effect of R on fatigue crack growth rates. Walker equation is one of the most widely accepted. Based on Paris' law, the fatigue crack growth data at each R level can be described using a straight line in the log-log plot. Basically, the Walker equation consolidates all the fatigue crack growth data at different R levels along one single straight line, i.e. the one plotted when $R = 0$. Walker equation may be written as below,

$$\frac{da}{dN} = C(\overline{\Delta K})^m \quad (4 - 40)$$

where C and m are material constants. $\overline{\Delta K}$ is called the equivalent zero-to-constant stress intensity factor and is calculated by

$$\overline{\Delta K} = \frac{\Delta K}{(1 - R)^{1-\gamma}} \quad (4 - 41)$$

with γ being a material constant.

Since the proposed model is developed for the case of fatigue crack growth under fully reversed constant-amplitude cyclic loads, i.e. $R = -1$. To match with the proposed model, Walker equation should be modified by reformulating equation (4 - 41) into

$$\overline{\Delta K} = \left(\frac{2}{1 - R} \right)^{1-\gamma} \Delta K \quad (4 - 42)$$

The above equation consolidates the fatigue crack growth data at different R levels along the straight line of which $R = -1$. Thus, the proposed model can be applied in combination with the modified Walker equation when accounting for the R effect is required as follows: the fatigue crack growth curve for $R = -1$ is first obtained using the proposed model; based on the fatigue crack growth curve and equation (4 - 42), the fatigue crack growth rates at different R levels can then be calculated. To illustrate the effectiveness of the method, AISI 4340 steel and 7075-T6 aluminium are used.

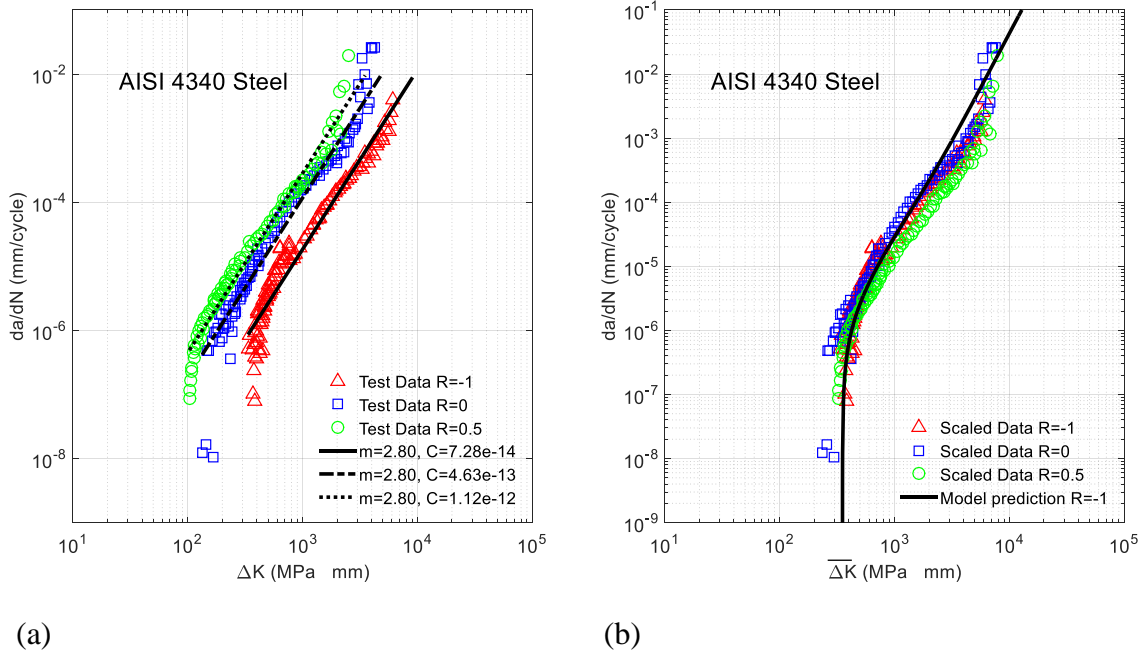


Figure 4.15 Model application to consider the R effect for AISI 4340 Steel: (a) R effect on fatigue crack growth rates (Newman, 2007); (b) model application.

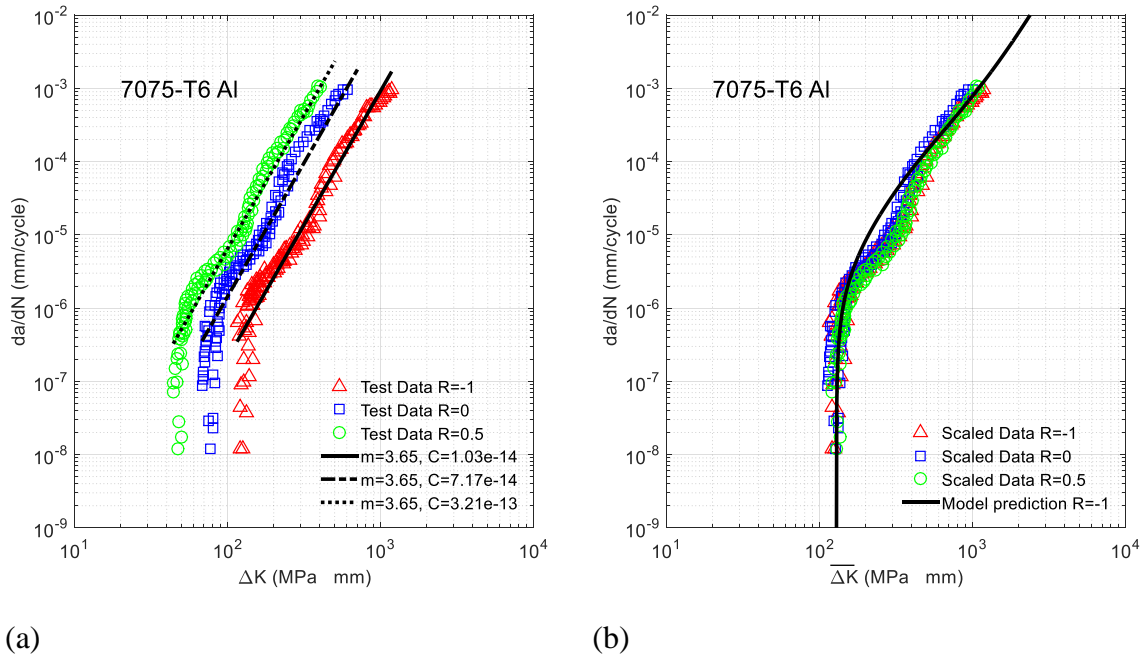


Figure 4.16 Model application to consider the R effect for 7075-T6 Al: (a) R effect on fatigue crack growth rates (Newman et al., 1994); (b) model application.

Figures 4.15 and 4.16 show the model applications to AISI 4340 steel and 7075-T6 aluminium respectively. For each material, three sets of fatigue crack growth data at different R levels ($R = -1, 0, 0.5$) are provided. As shown in figure 4.15(a) and figure 4.16(a), the R effect on the fatigue crack growth is significant. The increase of R causes the increase of fatigue crack growth rates for a given ΔK . The data of fatigue crack growth rates at different R levels can be regressed into parallel straight lines using the Paris' law. By introducing equation (4 – 42), those parallel straight lines can be consolidated into a single straight line. Instead of the Pars' law, the proposed model predicts the material's fatigue crack growth curve from the its fundamental deformation properties for $R = -1$ with higher accuracy, as illustrated in figure 4.15(b) and figure 4.16(b). The fatigue crack growth rates at different R levels can thus be found using $\overline{\Delta K}$ calculated by equation (4 – 42). While for AISI 4340 steel and 7075-T6 aluminium, the starts of fatigue crack growth at different R levels seem to be consolidated well following the equation (4 – 42), it should be noted that they may vary in a slightly different extent for other materials. In conclusion, the proposed model has a good potentiality of considering the R effect.

4.1.4 Summary

In this 4.1 section, a model based on elastoplastic fracture mechanics and energy principles was proposed for predicting fatigue crack growth of metallic materials under small-scale yielding conditions. Only monotonic and cyclic tensile material properties and low-cycle

fatigue properties are required for the model prediction. The test data of A533-B1 steel, AISI 4340 steel, AISI 4140 steel, 25CrMo4 steel, 2024-T351 aluminium, 7075-T6 aluminium, 7175-T6 aluminium and Ti6Al4V alloy were chosen for the comparison with model prediction. The results show that

- 1) The proposed model works well to predict the fatigue crack growth under fully reversed constant-amplitude cyclic loads where $R = -1$.
- 2) In combination with Walker equation, the proposed model can provide good prediction for fatigue crack growth accounting for the R effect.
- 3) The proposed model only needs fundamental deformation properties of the material, i.e. monotonic and cyclic tensile material properties and low-cycle fatigue material properties, to predict the fatigue crack growth.

The research work in this section has been summarized and published by Cheng et al. (2019).

4.2 Crack Growth under Low-cycle Fatigue Loads

Engineering critical assessment is gaining popularity in industries nowadays (BS 7910, 2015). As a fitness-for-service procedure, it invokes fracture mechanics to determine the defect tolerance of safety critical items. Among the many models developed in particular for assessing fatigue, those based on linear elastic fracture mechanics are the most welcomed for their capability of predicting fatigue crack growth (Santecchia et al., 2016). They are often expressed in some formats of Paris' law and give good performance as evidenced by both lab experiments and engineering practices (Dowling, 2012; BS 7910, 2015). Such a success is mainly attributed to the fact that engineering structures are usually designed to withstand loads well below the material's yield strength, justifying the small-scale yielding assumption of linear elastic fracture mechanics and hence qualifying its application.

However, in engineering practice fatigue with non-small-scale yielding crack-tip conditions is still possible to happen. Subsea pipelines serving high-pressure/high-temperature reservoirs are highly possible to suffer cyclic operational stresses comparable to or even larger than the material's yield strength, which means the non-small-scale yielding conditions may occur (Bai and Bai, 2014; Cheng and Chen, 2018b). On the one hand, the plasticity introduced will significantly reduce the number of load cycles to be experienced by the structure, thus causing the so-called low-cycle fatigue. On the other hand, non-small-scale yielding conditions violates the assumption of linear elastic fracture mechanics. Therefore, linear elastic fracture

mechanics and models based on it can no longer be applied. Elastoplastic fracture mechanics and its characteristic parameter J -integral, for being capable of describing the crack-tip plasticity under both small-scale yielding and non-small-scale yielding conditions, has received much attention over the past several decades. (Dowling, 1977; Tanka, 1983; Ljustell, 2007; Ngoula et al., 2018).

Meanwhile, various models have been established to use fundamental deformation properties, i.e. a material's monotonic and cyclic tensile properties and the low-cycle fatigue properties, to predict fatigue crack growth (Kujawski and Ellyin, 1984; Li et al., 1998; Pandey and Chand, 2003; Shi et al., 2016; Wu et al., 2017). This is because compared with the parameters in Paris' law, fundamental deformation properties are easy to be obtained by test. Also, they are routinely asked in engineering practice for the purpose of structure design and hence are widely available in literature (ASM, 1996). But this type of fatigue crack growth models mostly adopts ΔK as the characteristic parameter, limiting their applicability to small-scale yielding conditions only. Besides, the threshold stress intensity factor range, ΔK_{th} often has to be introduced in addition to fundamental deformation properties, requiring fatigue crack growth tests to be carried out and thus contradicting the original intention.

With these facts being recognized, a prediction model for fatigue crack growth of metals using the cyclic J -integral, ΔJ is developed in this section in the frame of elastoplastic fracture mechanics. The model is inspired by the blunting and re-sharpening mechanism of fatigue crack growth and only needs fundamental deformation properties as material inputs. For each load cycle, ΔJ is first estimated to obtain the crack-tip radius. Invoking the modified rule of equivalent strain energy density, the crack-tip normal stress distribution along the crack plane is constructed. Then the fatigue crack growth process is re-arranged. Based on the energy balance and the re-arranged fatigue crack growth process, a governing equation for fatigue crack growth is proposed. The elementary fracture released energy and the critical stored energy required for calculating the fatigue crack growth rate are derived from fundamental deformation properties.

4.2.1 Model Development

Before introducing the detailed work of model development, it should be pointed out that the term “energy” in this thesis is commonly used in energy-based analysis particularly for material elements. But in a strict sense, when the bulk material is considered, either “energy per unit area” or “energy per unit volume” may be more appropriate depending on the situation. Dimensional consistency of equations has been thoroughly checked and assured.

Fracture mechanics predicts singularity at crack tip where r and θ both equal to 0. However, in reality an infinite stress is impossible due to the crack-tip blunting and the strain hardening effect. Since there is no fundamental difference between in the cracking behaviours of notch and crack (Taylor, 1999), the methods for notch analysis may also be applicable for cracks, or more specifically the notch-like blunted cracks, and vice versa (Shin et al., 1994). This enables the construction of a close-to-reality stress distribution in front of the crack tip.

4.2.1.1 Cyclic Material Behaviour

Material behaviour often can be described in some format of Ramberg-Osgood equation. For the case of monotonic loading, the material behaviour is described by the monotonic stress-strain curve, as shown in figure 4.17(a), which is mathematically expressed as follows

$$\varepsilon_a = \frac{\sigma_a}{E} + \left(\frac{\sigma_a}{H}\right)^{1/n} \quad (4 - 43)$$

where σ_a is the stress amplitude, ε_a the strain amplitude, E the Young's modulus, H the strength coefficient, and n the strain-hardening exponent.

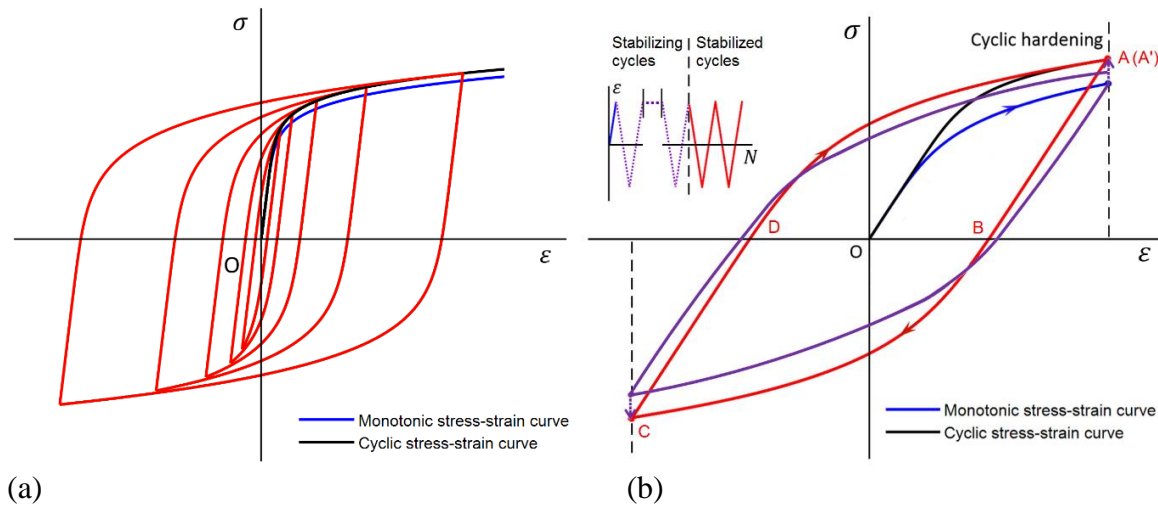


Figure 4.17 (a) Stress-strain curves under monotonic and cyclic loads; (b) stress-strain response under a specified cyclic strain load

For the case of cyclic loading, the cyclic stress-strain curve, also shown in figure 4.17(a), is obtained by joining the tip locus of a series of stabilized hysteresis loops (ASTM E606M-12, 2012). The cyclic stress-strain curve can be described by

$$\varepsilon_a = \frac{\sigma_a}{E} + \left(\frac{\sigma_a}{H'}\right)^{1/n'} \quad (4 - 44)$$

where H' is the cyclic strength coefficient, and n' is the cyclic strain hardening exponent.

Assuming the material exhibits a Masing behaviour, equation (4 - 44) can be rewritten into

$$\frac{\Delta\varepsilon}{2} = \frac{\Delta\sigma}{2E} + \left(\frac{\Delta\sigma}{2H'}\right)^{1/n'} \quad (4 - 45)$$

since the strain range $\Delta\varepsilon = 2\varepsilon_a$ and the stress $\Delta\sigma = 2\sigma_a$. Note that the stress-strain curve is not closed in the beginning. As the number of load cycles increases, the material response finally achieves a stabilized state and generates a hysteresis loop, as illustrated in figure 4.17(b). Hence, strictly speaking equations (4 – 44) and (4 – 45) describes the material's stabilized stress-strain behaviour.

4.2.1.2 Strain-life Correlation

For the case of low-cycle fatigue, the Basquin-Coffin-Manson (BCM) equation, which correlates the load strain range $\Delta\varepsilon$ and fatigue life N_f , is often used in practice when estimating fatigue life is required. The BCM equation is written as

$$\frac{\Delta\varepsilon}{2} = \frac{\sigma_f'}{E}(2N_f)^b + \varepsilon_f'(2N_f)^c \quad (4 - 46)$$

where σ_f' , ε_f' , b and c refer to the cyclic fatigue strength coefficient, the fatigue ductility coefficient, the fatigue strength exponent and the fatigue ductility exponent, respectively. The four parameters are also called low-cycle fatigue properties as a whole since they are curve fitted from the data obtained by low-cycle fatigue tests where the loads are constant-amplitude strain with fully reversed cycles (Stephens, 2000).

4.2.1.3 Crack-tip stress field

According to Hutchinson (1968), and Rice and Rosengren (1968) the crack-tip stress field of nonlinear elastic solids obeying the power-law stress-strain relationship (equation (4 – 48)), is represented by

$$\sigma_{ij} = \sigma_0 \left(\frac{EJ}{\alpha\sigma_0^2 I_n r} \right)^{n/(n+1)} \tilde{\sigma}_{ij} \quad (4 - 47)$$

where r is the radial distance off the crack tip in the direction of crack plane, σ_0 is the yield strength, $\tilde{\sigma}_{ij}$ is the non-dimensional angular distribution function, I_n is the non-dimensional parameter of exponent n , J is the two-dimensional path-independent line integral around the crack tip and α is an equation derived based on equation (4 – 43) and has an expression as

$$\alpha = \frac{E}{\sigma_0} \left(\frac{\sigma_0}{H} \right)^{1/n} \quad (4 - 48)$$

For details of calculating $\tilde{\sigma}_{ij}$ and I_n , please refer to the work by Guo (1993a; 1993b) and Galkiewicz and Graba (2006). Hill (1998) proposed a formula for the stress normal to the crack plane, σ_{yy} based on the slip line theory to describe the distribution of σ_{yy} off the notch root but before it reaches its peak value. Tetelman and McEvilly (1967) modified Hill's solution with $2/\sqrt{3}\sigma_c$ replacing σ_0 to account for strain hardening and reached

$$\sigma_{yy} = \frac{2}{\sqrt{3}}\sigma_c \left[1 + \ln \left(1 + \frac{r}{r_0} \right) \right] \quad (4 - 49)$$

where σ_c represents the flow stress and r_0 represents the notch radius. Considering the crack blunting effect, r_0 may be replaced by the crack-tip radius due to blunting ρ . Then combining equations (4 – 47) ~ (4 – 49), the abscissa coordinate of the intersection point P shown in figure 4.3, r_{int} can be obtained and the corresponding peak stress σ_{int} can be also calculated by either equation (4 – 47) or equation (4 – 49). Note that in reality, the peak stress along the crack plane, σ_{yy}^{max} may occur at the point with a distance, r_{max} , different from the location of P predicted by equations (4 – 47) and (4 – 49), but the shaded areas under the artificial stress distribution curve and the real may be viewed as approximately equal. σ_c can be obtained following equation (4 – 49) if the local stress at the blunted crack-tip root is known.

The finite displacement at the crack tip generated from blunting is commonly referred as the crack tip opening displacement (CTOD). As depicted in figure 4.18, ρ can then be approximated by a half of CTOD, i.e.

$$\rho = CTOD/2 \quad (4 - 50)$$

It has been experimentally proven that CTOD is uniquely related to J -integral via the following equation (Rice and Rosengren, 1968)

$$J = m\sigma_0 CTOD \quad (4 - 51)$$

where m is a dimensionless constant that depends on the stress state and material properties. To consider the strain hardening effect, σ_0 in the equation upon is commonly replaced by the effective yield strength σ_y that is the average of σ_0 and the ultimate tensile strength σ_u . Dawes (1979) observed that the linear relationship between J and CTOD indicated by equation (4 – 51) keeps well even under elastoplastic conditions where mild plasticity exists. Different expressions of m have been formulated as functions of crack aspect ratios from extensive elastoplastic finite element analyses (Zhu and Joyce, 2012; ASTM E1820-17, 2017). In the case of cyclic loading, ΔJ should replace J in constructing the crack-tip stress distribution

normal to the crack plane, and the associated σ_Y is calculated as the average of σ_f' and the cyclic yield strength σ_0' .

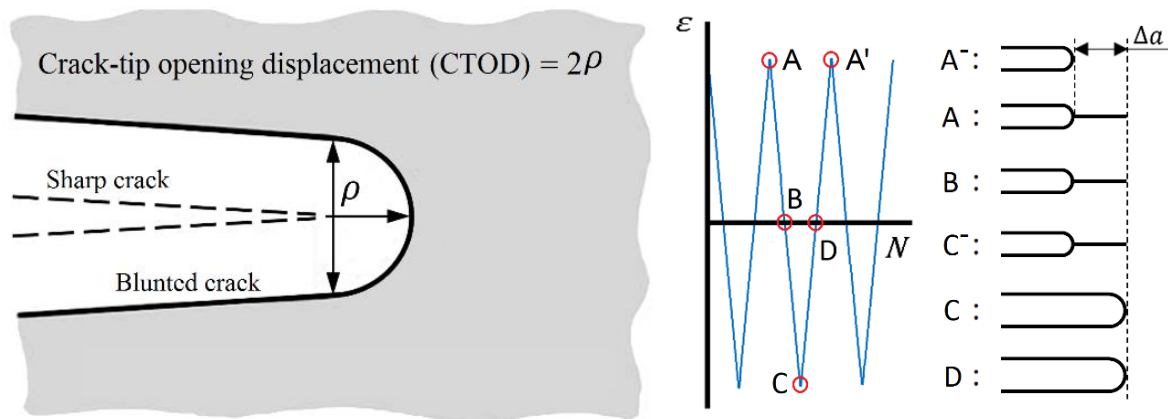


Figure 4.18 Mechanism of crack growth under low-cycle fatigue conditions

Different from the case of static loading, crack blunting is alternated with re-sharpening and thus controls the process of fatigue crack growth under cyclic loads. During loading, slip takes place along the two slip planes approximately 45° to the crack plane at the same time, blunting the crack tip; Upon unloading, reversed slip occurs, re-sharpening the crack tip. To allow for a clear definition of ΔJ and the application of notch based methods, the fatigue crack growth process in each load cycle is simply rearranged as schematically depicted in figure 4.19:

- 1) in each load cycle, upon the start of unloading (point A), crack growth occurs along the crack plane with a sharp crack tip;
- 2) as the load decreases (point B and point C^-), the sharp crack keeps static;
- 3) right at the start of loading (point C), crack is blunted to some radius;
- 4) as the load keeps increasing (point D), the blunted crack keeps static and crack-tip radius stays constant.
- 5) As the load finishes increasing (point A'), another load cycle starts and the crack grows with re-sharpened tip, repeating the above process.

In essence, J -integral is a way of calculating the energy release rate G (in SI units J/m^2 or equivalently $Pa \cdot m$). Based on the rearranged fatigue crack growth process, ΔJ may also be interpreted as ΔG or physically the rate at which energy is released as crack growth occurs per load cycle (following the path illustrated above), which is consistent with that of G . Dowling (1977) proposed an approach to estimate ΔJ invoking the concept of strain energy. It actually corresponds to ΔJ 's aforesaid physical meaning, as supported by the work of Yao et al. (2007)

where ΔG is decomposed into strain energy items. In Dowling's approach, ΔJ is split into an elastic component ΔJ_e and a fully-plastic component ΔJ_p , i.e.

$$\Delta J = \Delta J_e + \Delta J_p \quad (4 - 52)$$

Assuming plane stress, ΔJ_e is related to ΔK as follows

$$\Delta J_e = \frac{\Delta K^2}{E} \quad (4 - 53)$$

where ΔK is given by

$$\Delta K = F\Delta S\sqrt{\pi a} \quad (4 - 54)$$

where F is the geometric function, ΔS is the range of nominal stress normal to the crack plane, and a is the characteristic dimension of the crack. For through-thickness cracks, a represents the half crack length, for surface cracks, a is the flaw height, and for embedded cracks, a is the half height. Note that the elastic strain energy of a material element can be calculated as

$$\Delta W_e = \frac{\Delta S^2}{2E} \quad (4 - 55)$$

Substituting equations (4 - 54) and (4 - 55) into equation (4 - 53), it follows that

$$\Delta J_e = 2\pi a F^2 \Delta W_e \quad (4 - 56)$$

Assuming the geometric correction factor F also applies to ΔJ_p . Referring to equation (4 - 56), it yields that

$$\Delta J_p = 2\pi a F^2 f_{n'} \Delta W_p \quad (4 - 57)$$

where $f_{n'}$ is a function of the cyclic strain hardening exponent n' considering the influence of plasticity, and ΔW_p is the plastic strain energy. Considering the stress-strain relationship indicated by equations (4 - 44) and (4 - 45), ΔW_p is calculated by

$$\Delta W_p = \frac{2\Delta S}{n' + 1} \left(\frac{\Delta S}{2H'} \right)^{\frac{1}{n'}} \quad (4 - 58)$$

Then equation (4 - 52) is rewritten as

$$\Delta J = 2\pi a F^2 [\Delta W_e + f_{n'} \Delta W_p] \quad (4 - 59)$$

For different geometries of specimens, F and $f_{n'}$ can be found in the works by Shih and Hutchinson (1976), Kumar et al. (1981), Dowling (2012) et al..

4.2.1.3 Crack-tip radius

Neuber's rule (Neuber, 1961) has been frequently used to obtain local stresses at notch roots since its proposal. From the perspective of strain energy (Stephens et al., 2000), Neuber's rule states that for the material element at notch root,

$$(K_t)^2 W_n = W_t \quad (4 - 60)$$

where

$$\begin{cases} W_n = \frac{Se}{2} & (4 - 61) \\ W_t = \frac{\sigma^2}{2E} + \frac{\sigma}{n+1} \left(\frac{\sigma}{H}\right)^{1/n} & (4 - 62) \end{cases}$$

with K_t being the elastic stress concentration factor at the crack tip and the nominal stress in the linear elastic range.

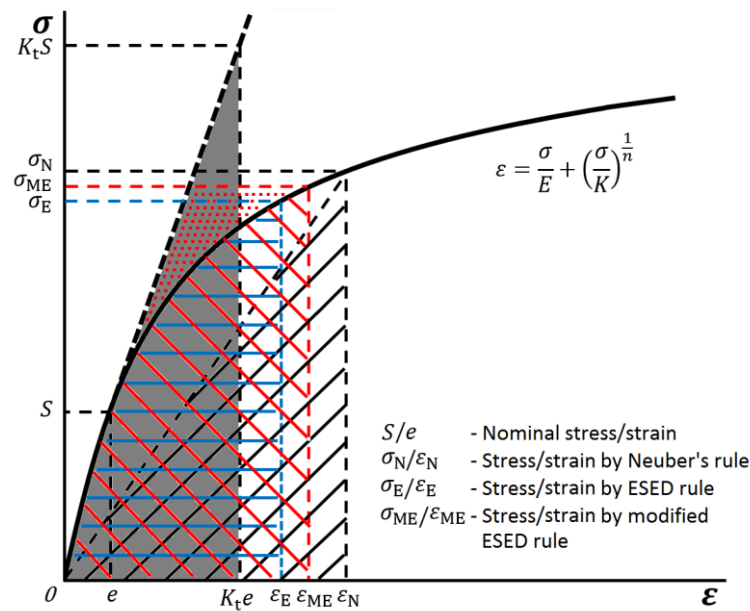


Figure 4.19 Graphical interpretation of Neuber's rule, equivalent strain energy density (ESED) rule, and modified ESED rule

More straightforward, in figure 4.19, the grey shadowed area is the nominal applied strain energy W_n and the black hatched area the secant strain energy W_t . Later, Molski and Glinka (1981) proposed the equivalent strain energy density rule, which suggests the use of the elastoplastic strain energy W_σ on the right hand side of equation (4 - 60). W_σ is calculated as

$$W_\sigma = \frac{\sigma^2}{2E} + \frac{\sigma}{n+1} \left(\frac{\sigma}{H}\right)^{1/n} \quad (4 - 63)$$

In figure 4.19, the area hatched in blue represents the strain energy W_σ calculated based on the equivalent strain energy density rule. In the case of cyclic loading, W_n and W_σ in the equivalent strain energy density rule are changed into their cyclic counterparts, ΔW_n and ΔW_σ , where

$$\Delta W_\sigma = \frac{\Delta\sigma^2}{2E} + \frac{2\Delta\sigma}{n'+1} \left(\frac{\Delta\sigma}{2H'} \right)^{1/n'} \quad (4 - 64)$$

while ΔW_n is calculated by replacing S and e with their cyclic counterparts, ΔS and Δe . Ye et al. (2004) proposed that the equivalent strain energy density rule should be modified with consideration of thermodynamics. In the case of cyclic loading, the theoretical work ΔW_n applied to the material element at the notch root due to the nominal stress range is transformed into the real total strain energy $\Delta\sigma\Delta e$ absorbed by the element and the portion of hysteresis energy dissipated by the element during cyclic plastic deformation, ΔW_q , which can be calculated by

$$\Delta W_q = \frac{2(1-2n')\Delta\sigma}{1+n'} \left(\frac{\Delta\sigma}{2H'} \right)^{1/n'} \quad (4 - 64)$$

Therefore, the mathematical expression of modified rule of equivalent strain energy density for cyclic loading is

$$(K_t)^2 \frac{\Delta S^2}{E} = \frac{\Delta\sigma^2}{E} + \frac{2(2-n')\Delta\sigma}{1+n'} \left(\frac{\Delta\sigma}{2H'} \right)^{1/n'} \quad (4 - 65)$$

The strain energy on the right hand side of equation (4 - 65) is the red hatched area subtracting the red dashed area in figure 4.19. The graphical interpretations of Neuber's rule, equivalent strain energy density rule, and Modified rule of equivalent strain energy density are plotted together in figure 4.19. In this research, the modified rule of equivalent strain energy density is adopted. But given the potential non-small-scale yielding conditions, equation (4 - 64) is further written into

$$(K_t)^2 \left[\frac{\Delta S^2}{E} + \frac{4(1-n')\Delta S}{1+n'} \left(\frac{\Delta S}{2H'} \right)^{1/n'} \right] = \frac{\Delta\sigma^2}{E} + \frac{2(2-n')\Delta\sigma}{1+n'} \left(\frac{\Delta\sigma}{2H'} \right)^{1/n'} \quad (4 - 66)$$

To account for the notch size effect, Topper et al. (1969) suggested the use of the fatigue stress concentration factor K_f , in place of K_t when evaluating the notch-root stress. The replacement was supported by the better agreement with experimental fatigue life data as they observed. Therefore, K_f is used in this research when applying equation (4 - 66). K_f is calculated according to Neuber (1958),

$$K_f = 1 + \frac{K_t - 1}{1 + \sqrt{\rho_0/\rho}} \quad (4 - 67)$$

where ρ_0 is the so-called Neuber's material characteristic length. K_t is obtained based on fracture mechanics (Shin et al., 1994)

$$K_t = 1 + 2F\sqrt{a/\rho} \quad (4 - 68)$$

Note that K_t in the above equation is derived from the gross section, while K_t in equation (4 - 67) is defined using the net section. Hence conversion may be necessary. The crack-tip distribution of σ_{yy} along the length of fracture process zone is thus be constructed.

4.2.1.4 Fatigue crack growth

Ellyin (2012) pointed out that for a notched metallic specimen undergoes plastic deformation, the bulk of the supplied strain energy is dissipated into heat, while the remaining part is stored in the material. If unloading comes subsequently, the elastic part of the stored energy will be recovered, but the plastic part of stored energy is irrecoverable and most possibly associated with the residual stresses after unloading (Chrysochoos et al., 1989; Kim, 1990; Klesnil and Lukac, 1992). Similarly in the case of a cracked specimen under cyclic loads, following the path ABCDA' as shown in figure 4.20, the only energy retained by the material element before crack growing through is the irrecoverable stored energy (Oilferuk et al., 2001; Ye et al., 2004). Therefore the energy to be released as the crack grows may be attributed to the irrecoverable stored energy, which goes back to the definition of ΔJ being the change in the stored energy per unit change in crack surface area (Bever et al., 1973; Mars and Fatemi, 2002; Benaarbia et al., 2014). Assuming that for a material element of unit volume, the irrecoverable stored energy along the loading path is ΔW_s , and the energy released by fracturing it is ΔW_f . Obviously, there exists a relationship between ΔW_s and ΔW_f (Morrow, 1965). The following equation is hence proposed for a crack to grow at arbitrary load cycle,

$$\Delta W_{\bar{f}}\Delta a = \Delta \Pi_{FPZ} \quad (4 - 69)$$

where Δa is the extension of crack characteristic dimension a in the load cycle, $\Delta W_{\bar{f}}$ is the elementary fracture released energy, i.e. the energy released by fracturing the material element of unit volume, and $\Delta \Pi_{FPZ}$ is the total irrecoverable stored strain energy accumulated along the length of fracture process zone before Δa occurs, or briefly the accumulated stored energy. The above equation is thought as the governing equation of fatigue crack growth. Physically it states that the accumulated irrecoverable energy stored before crack grows provides the energy to be released during the crack growth.

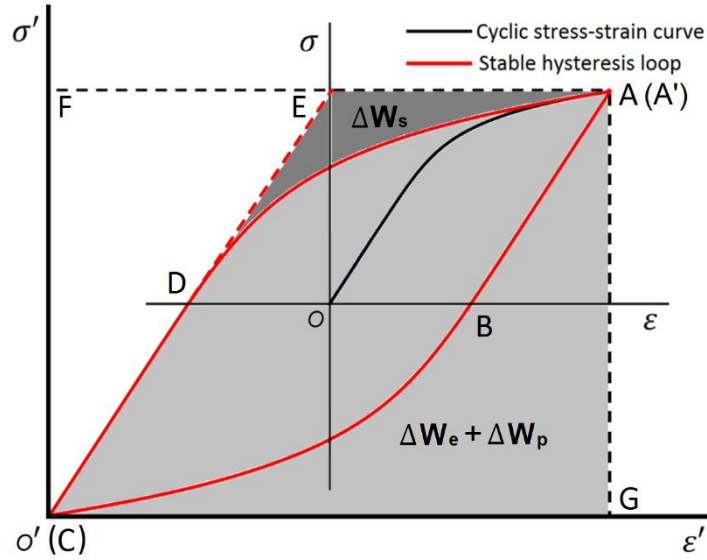


Figure 4.20 Strain energy density required for material elements to fracture

According to Skelton (1987), the stored energy ΔW_s of a material element can be represented by area ADE, which is shaded in heavy grey in figure 4.20. Therefore

$$\Delta W_s = \text{Area ABC} = \int_0^{\Delta\sigma} \varepsilon' d\sigma' - \frac{\Delta\sigma^2}{2E} \quad (4-70)$$

Combined with equation (4-45), it follows that

$$\Delta W_s = \frac{2n'\Delta\sigma}{n'+1} \left(\frac{\Delta\sigma}{2H'} \right)^{1/n'} \quad (4-71)$$

Fracture process zone is where the microscopic events that lead to fracture processing occur. Its length is the dimension in the direction of crack plane. In this thesis the length of fracture process zone is defined to start from the material point of which ΔW_s must be released or ΔW_s can no more be stored, and end at the material point of which ΔW_s must be released or ΔW_s can no more be stored. Obviously the limit of storing energy for a material point in one cycle is the ΔW_s of the special case where the reversal number $2N_f = 1$. Denoting this critical energy as $\Delta W_{\bar{s}}$, the boundary conditions of fracture process zone are thus given by

$$\left\{ \begin{array}{l} \Delta W_s|_{r_{prz1}} = \Delta W_{\bar{s}} \quad \text{with} \quad \Delta\sigma = \frac{2}{\sqrt{3}} \sigma_c \left[1 + \ln \left(1 + \frac{r}{\rho} \right) \right] \end{array} \right. \quad (4-72)$$

$$\left\{ \begin{array}{l} \Delta W_s|_{r_{prz2}} = \Delta W_{\bar{s}} \quad \text{with} \quad \Delta\sigma = \Delta\sigma_0 \left(\frac{E\Delta J}{\alpha' \Delta\sigma_0^2 I_n r} \right)^{n'/(n'+1)} \quad \tilde{\sigma}_{ij} \end{array} \right. \quad (4-73)$$

where r_{prz1} and r_{prz2} are the abscissa coordinates of the left and right boundary points, respectively, and α' corresponds to α in equation (4-47) but is derived based on equation (4-45) and thus has the following expression

$$\alpha' = \frac{2E}{(2H')^{1/n'} \Delta\sigma_0^{(n'-1)/n'}} \quad (4-74)$$

where $\Delta\sigma_0 = 2\sigma'_0$. Equations (4-72) and (4-73) indicate that length of fracture process zone or $[r_{pz1}, r_{pz2}]$ may vary depends on the level of applied stress, which is supported by the observations of Li et al. (1998) and Ellyin (2012) et al. With the boundaries known, $\Delta\Pi_{FPZ}$ can be calculated mathematically as an integral in the domain $[r_{pz1}, r_{pz2}]$,

$$\Delta\Pi_{FPZ} = F^2 \int_{r_{pz1}}^{r_{pz2}} \Delta W_s dr \quad (4-75)$$

where F^2 is introduced following equation (4-59). Combining equations (4-45) and (4-72), the equation (4-75) is rewritten into

$$\Delta\Pi_{FPZ} = \frac{2n'}{1+n'} \left(\frac{1}{2H'}\right)^{1/n'} F^2 \int_{r_{pz1}}^{r_{pz2}} \Delta\sigma^{1+1/n'} dr \quad (4-76)$$

The stress distribution along the length of fracture process zone in the direction of crack path under constant-amplitude cyclic loads is estimated from equations (4-47) ~ (4-49) as

$$\Delta\sigma = \begin{cases} \frac{2}{\sqrt{3}} \sigma_c \left[1 + \ln\left(1 + \frac{r}{\rho}\right)\right] & r \in [r_{pz1}, r_{int}] \quad (4-77a) \\ \Delta\sigma_0 \left(\frac{E\Delta J}{\alpha' \Delta\sigma_0^2 I_n, r}\right)^{n'/(n'+1)} \tilde{\sigma}_{ij} & r \in [r_{int}, r_{pz2}] \quad (4-77b) \end{cases}$$

The later application finds that for different types of metals, the amplitude of the peak stress normal to the crack plane σ_{yy}^{\max} usually falls into the expected range of $3\sim 5\sigma_0$ (Ritchie and Thompson, 1985).

As indicated by equation (4-59), ΔJ is a function of a when the amplitude of the load stress is constant. If a small increment of a , denoted as δa occurs, ΔJ will increase accordingly by $\delta\Delta J$, which has the expression as

$$\delta\Delta J = 2\pi \left[\frac{\Delta S^2}{2E} + 2f_{n'} \Delta S \left(\frac{\Delta S}{2H'}\right)^{\frac{1}{n'}} \right] [F|_{a+\delta a}^2 (a + \delta a) - F|_a^2 a] \quad (4-78)$$

Before the crack shows unstable growth, F usually stays stable providing δa is small, therefore $F|_{a+\delta a} \cong F|_a$. Then equation (4-78) becomes

$$\delta\Delta J = 2\pi \left[\frac{\Delta S^2}{2E} + 2f_{n'}\Delta S \left(\frac{\Delta S}{2H'} \right)^{\frac{1}{n'}} \right] (F|_a)^2 \delta a \quad (4 - 79)$$

As explained in 4.2.1.3, ΔJ accounts for the cyclic energy release rate, hence the physical interpretation of $\delta\Delta J$ may be the change of cyclic energy release rate due to δa in some load cycle. In other words, the change of energy release rate comes from fracturing the material of unit area in a length δa ahead of the crack tip. Based on the physical meaning of $\delta\Delta J$, $\delta\Delta J/\delta a$ should be seen as the change of released energy per fracturing a unit volume of the crack-tip material. Denote this averaged energy change as ΔW_f , then

$$\Delta W_f = 2\pi(F|_a)^2 \left[\frac{\Delta S^2}{2E} + 2f_{n'}\Delta S \left(\frac{\Delta S}{2H'} \right)^{\frac{1}{n'}} \right] \quad (4 - 80)$$

For the use of ΔS in the above equation, ΔW_f is still a global concept as ΔJ . While the whole specimen may experience many cycles before the failure criteria is reached, the crack tip advances and hence crack grows under each load cycle, which means locally the crack-tip material elements are fractured by only one cycle. By setting $2N_f = 1$, the elementary fracture released energy $\Delta W_{\bar{f}}$, i.e. the energy to be released by fracturing the material element with one load cycle, can be found using equation (4 - 80) in combination with equations (4 - 45) and (4 - 46). It should be noted that since no cracks are assumed to exist in the crack-tip material elements at the beginning of arbitrary load cycle, $F|_a^2 = 1$.

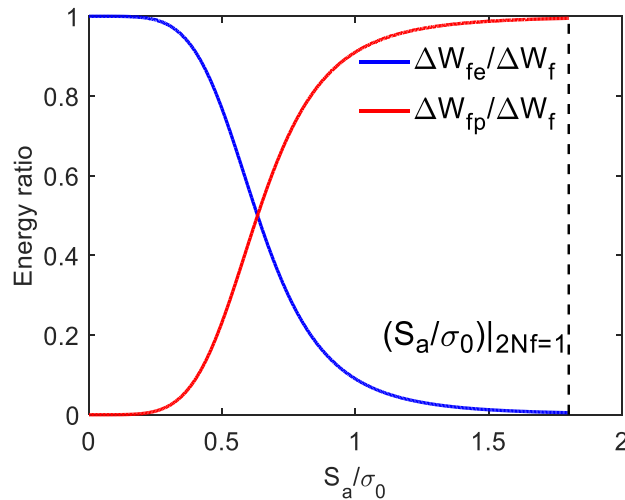


Figure 4.21 Variation of energy ratios with stress amplitude ratio

Equation (4 - 80) indicates that ΔW_f is composed of two parts, i.e. the part associated with elastic strain energy ΔW_{fe} and the part associated with plastic strain energy ΔW_{fp} . If the ratios of both parts to ΔW_f are the plotted as functions of S_a/σ_0 in the same figure, as shown in

figure 4.21 using A533-B1 steel for instance, it can be found that at $2N_f = 1$ ΔW_{fp} contributes most, if not all, to ΔW_f . This actually suggests that the elementary fracture released energy $\Delta W_{\bar{f}}$ is provided by the plastic strain energy, or equivalently the energy to be released by fracturing the material element with one load cycle is provided by the plastic strain energy. This is consistent with the governing equation, i.e. equation (4 – 68), in that both energies on the two sides of the equation are from plastic strain energy. Such a consistency agrees with Morrow’s suggestion that plastic strain energy is closely related to the fatigue process (Morrow, 1965) and the models developed based on it (Ellyin and Kujawski, 1984; Dasgupta et al., 1992; Ellyin, 2012). Thus to some extent it supports the governing equation.

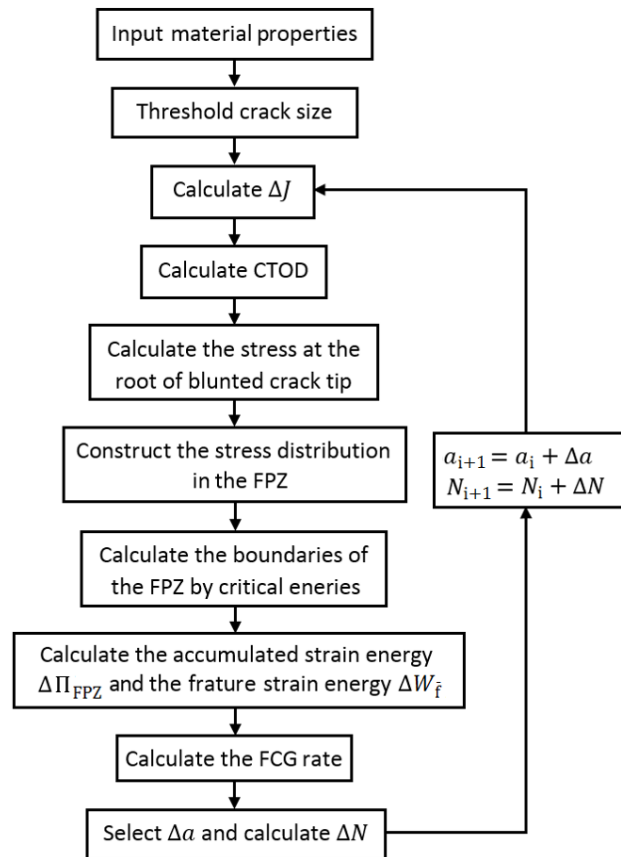


Figure 4.22 Flow diagram of the proposed model for predicting fatigue crack growth (FCG) rate

Note that for a specific load cycle, Δa by definition is the fatigue crack growth rate, thus with $\Delta \Pi_{FPZ}$ and $\Delta W_{\bar{f}}$ determined, the law of energy conservation, i.e. equation (4 – 68) yields

$$\frac{da}{dN} = \frac{\Delta \Pi_{FPZ}}{\Delta W_{\bar{f}}} \quad (4 – 81)$$

Clearly, by using ΔJ and energy principles the above steps bypass the discussion on the crack-tip yielding conditions during fatigue crack growth. Figure 4.22 is the flow diagram of how to

implement the model. In the cycle-by-cycle calculation, ΔN equals 1 and Δa has the value of the fatigue crack growth rate. $\Delta \Pi_{FPZ} > 0$ is set as the criterion when fatigue crack growth starts. The corresponding crack size is taken as the threshold crack size.

4.2.2 Model Application and Discussion

Given the availability of fatigue crack growth test data at $R = -1$ in the published literature, the proposed model is first applied to A533-B1 steel and then modified based on the application result. General application of the modified model is carried out afterward on several other metallic materials such as AISI 4340 steel, 2024-T3 aluminium, 2024-T351 aluminium, 7075-T6 aluminium, and Ti6Al4V alloy. The predicted curves are always plotted against the applied material's test data for the purpose of validation.

4.2.2.1 Model Correction

The proposed model was first applied to A533-B1 steel. The monotonic and cyclic tensile properties and the low-cycle fatigue properties of A533-B1 steel to be input into the model are tabulated in table 4.3. The fatigue crack growth test data of A533-B1 steel were collected from the work by Dowling (1977), as indicated in table 4.4, and plotted against the predicted curves by the proposed model. Since S_{\max} is critical to determining the yielding scale, three load cases where $S_{\max} = 0.2\sigma_0$, $0.7\sigma_0$ and $1.2\sigma_0$ respectively were chosen to apply the proposed model. $S_{\max} = 0.7\sigma_0$ can be roughly regarded as the small-scale yielding load limit. Below this limit, for instance $S_{\max} = 0.2\sigma_0$, the fatigue crack growth is considered under small-scale yielding conditions; above this limit, for instance $S_{\max} = 1.2\sigma_0$, the fatigue crack growth is considered under non-small-scale yielding conditions. Thus the validity of the model is checked for both small-scale and non-small-scale yielding conditions.

As can be seen in figure 4.23, the predicted curves agree pretty well with the test data at $S_{\max} = 0.2\sigma_0$. However, it was found that as S_{\max} changes, some deviation occurs between the predicted curve and the test data. As observed in area A that is boxed by green dot lines in figure 4.23, the predicted curve rises above the test data as S_{\max} increases. While obviously in area B boxed by blue dot lines, the predicted curve falls below the test data as S_{\max} increases. In both regimes, the higher value of S_{\max} , the larger deviation of the predicted fatigue crack growth rate from the test data. Such discrepancies among different load cases are not unexpected. According to the review by Cui (2002), 1 mm could be treated as the consent boundary between short and long cracks. In the case of A533-B1 steel, it corresponds to a ΔJ of 24.3 MPa · mm for $S_{\max} = 0.7\sigma_0$ and 708 MPa · mm for $S_{\max} = 1.2\sigma_0$.

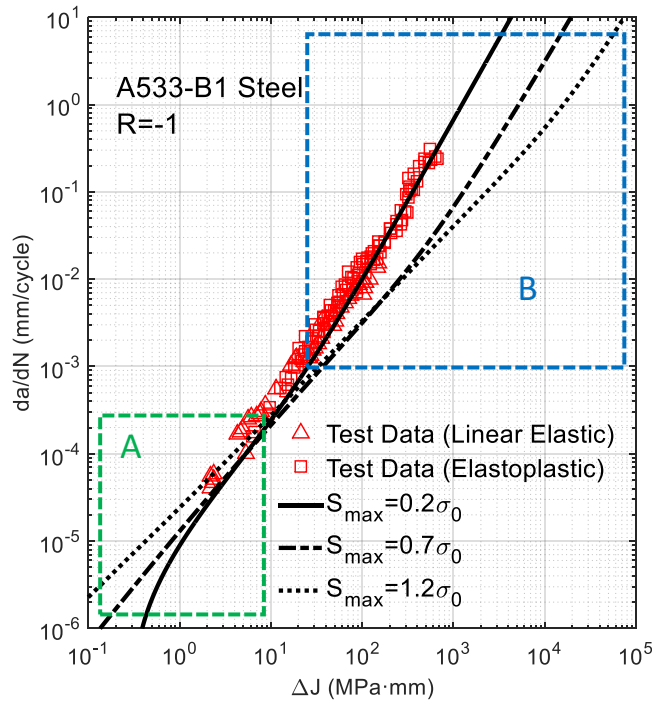


Figure 4.23 Comparison between the test data (Dowling, 1977) and the model prediction for A533-B1 Steel without modification

Checking these ΔJ values in figure 4.23, it is easy to see that both of them are outside area A, implying that cracks with calculated ΔJ fell in area A may be viewed as short cracks. For short cracks more factors such as the microstructure may come into effect, causing remarkably different fatigue crack growth behaviours. Hence in such scenarios, the proposed model which is based on macro-mechanics could be improper. Stable fatigue crack growth usually occurs after short cracks transformed into long cracks, as shown in area B. The increasing deviation of the predicted curve from the test data along with the increasing load level indicates that the underestimation may result from the increase of crack-tip plasticity. De Jesus and Correia (2013) performed a series of experimental tests and finite element analysis to investigate the local stresses and strains of P355NL1 steel at crack tips. By comparing the crack-tip stress distributions obtained analytically using the local-strain method and numerically by finite element analysis, it was found that the elastic portions of the two distributions agree well with each other in general, while the plastic portions deviates. Such findings basically indicate that as the plastic portion of crack-tip stress increases, the approximation represented by figure 4.3 will bring about increasing inaccuracy. Hence the model built in Section 4.1 for predicting fatigue crack growth under small-scale yielding conditions achieved a success: comparison between model prediction and fatigue crack growth test data for several metals showed good agreement. But when it comes to the non-small-scale yielding conditions, where plasticity is no longer negligible, the use of F^2 as a

correction factor for $\Delta\Pi_{FPZ}$ may be insufficient. Since F only considers the geometric amplification of stress (Chandran, 2017). In order to diminish such deviation and hence provide better prediction, a more proper correction factor should be considered. Instead of F^2 , a new correction factor, C_p is proposed as

$$C_p = \left[1 + \sqrt{\frac{\rho}{\rho_0}} \right]^{1/n'} \quad (4 - 82)$$

Since ρ is linearly related to ΔJ which incorporates F for calculation, the above equation in fact takes account of both the geometric effect and strain hardening effect (n').

Applying the proposed model with C_p in place of F^2 in equation (4 - 74) to A533-B1 steel, another set of predicted curves for three load levels, i.e. $S_{max} = 0.2\sigma_0$, $0.7\sigma_0$ and $1.2\sigma_0$ were obtained respectively using the same input parameters by Li et al. (1998). The newly obtained fatigue crack growth curves were plotted with the test data by Dowling (1977) in figure 4.24.

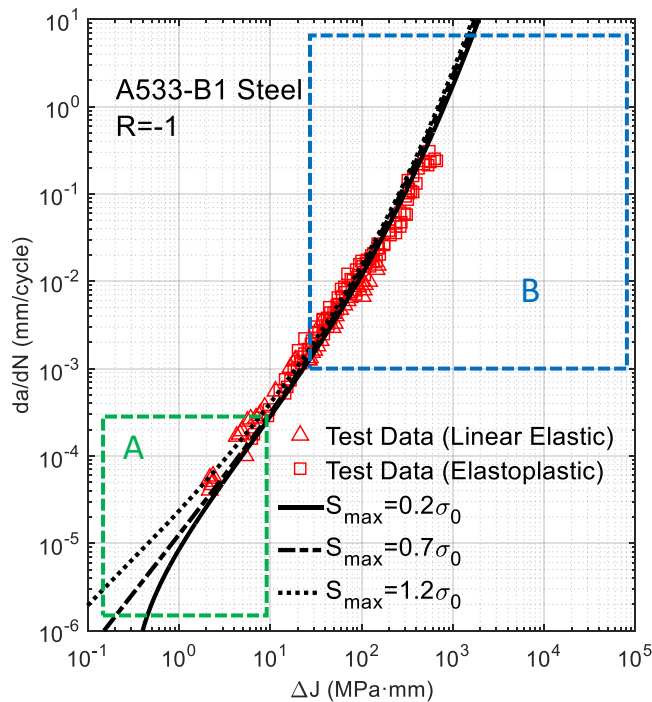


Figure 4.24 Comparison between the test data (Dowling, 1977) and the model prediction for A533-B1 Steel with modification

Observation shows that while the modified proposed model gives good prediction of fatigue crack growth for the load case where $S_{max} = 0.2\sigma_0$, no obvious change presents in area A for load cases where $S_{max} = 0.7\sigma_0$ and $1.2\sigma_0$. This is believed due to the fact that the proposed model is not designed for short cracks. Checking the ΔJ values corresponding to the boundary crack size $a = 1$ mm for load levels of $S_{max} = 0.7\sigma_0$ and $1.2\sigma_0$ respectively in figure 4.24, it

is easy to see that both of them are outside the regime of low ΔJ where the modified proposed model generates discrepancies for different load levels. In contrast to figure. 4.23, the improvement in area B is quite impressive. The deviations among the predicted curves under different load levels have been significantly diminished by introducing the modification. While in Dowling's elastoplastic tests, the smallest crack size recorded is about 0.05 mm, in practical engineering the detectable flaw size using the technique of non-destructive test with satisfactory confidence level is usually larger than 1 mm. Therefore, the part of fatigue crack growth curve in the regime of low ΔJ for load cases where $S_{\max} = 0.7\sigma_0$ and $1.2\sigma_0$ may not important or even not meaningful from the point of view of engineering practice.

For further validating the modified proposed model, a plot of crack characteristic length (depth in Dowling's work) versus fraction of fatigue life, i.e. N/N_f is produced, as shown figure 4.25. N is the number of load cycles experienced when the crack characteristic length a is reached. N is found by integrating the inverse of da/dN over a finite growth of a . N_f is calculated by equation (4 – 46). Generally good agreement can be observed between predicted crack evolution curve by the modified proposed model and Dowling's experimental measurements.

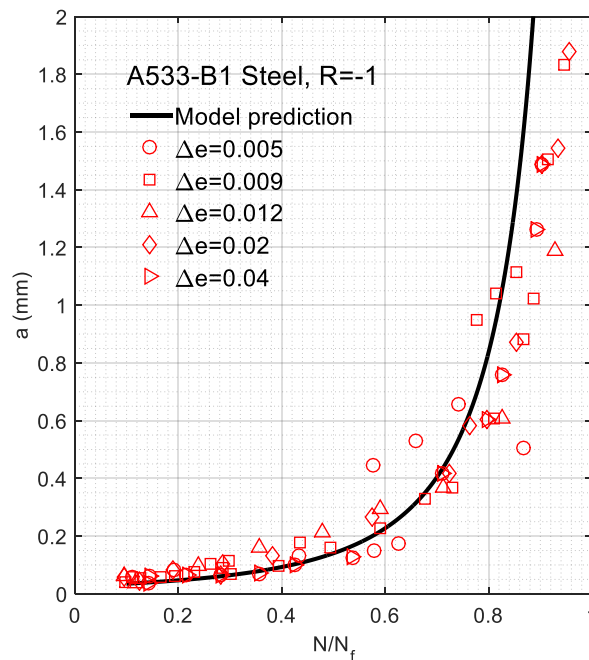


Figure 4.25 Comparison of crack evolution data generated by tests (Dowling, 1977) and model for A533-B1 Steel

4.2.2.2 General Application

General model applications are performed to AISI 4340 steel, 2024-T3 aluminium, 7075-T6 aluminium, and Ti6Al4V alloy. These metals are selected for their availability of test data of

both fundamental deformation properties and fatigue crack growth rates in literature. The model input parameters, i.e. fundamental deformation properties for each material are collected and tabulated in table 4.3. Their source information is also given in the table. In addition, some fatigue crack growth test information is listed for each material in table 4.4. It is worth noting that the fatigue crack growth rate data of all selected materials plotted in the figures as reference were obtained by linear elastic tests. This is because no fatigue crack growth rate data generated by elastoplastic tests has been found for those materials in literature. Recall equation (4 – 52), ΔJ is a unified characteristic parameter covering both linear elastic and elastoplastic conditions. It is thus believed that the fatigue crack growth rate data acquired by linear elastic tests and elastoplastic tests should fall around the same straight line described by the Paris' law in a log-log plot of ΔJ and da/dN , as evidenced by the case of A533-B1 steel (Dowling, 1977). Thus, the data by linear elastic test can still be used as an indicator of the straight line even if no data by elastoplastic test is available. Therefore the fatigue crack growth rate data of selected materials, which were generated originally in the measure of ΔK , are converted into ΔJ for the convenience of comparison, according to equation (4 – 53) before being plotted in figures.

Parameters	Monotonic and cyclic tensile properties					Low-cycle fatigue properties				Data source
	Material	σ_0	E	σ_u	K'	n'	σ'_f	b	ϵ'_f	
A533-B1 Steel	482	200	627	1047	0.165	869	-0.085	0.32	-0.52	Li et al., 1998
AISI 4340 Steel	710	200	1172	1910	0.123	1879	-0.0895	0.64	-0.636	Noroozi et al., 2005
2024-T3 Al	370	72	536	605	0.065	850	-0.086	0.22	-0.462	Karakas and Szusta, 2016
7075-T6 Al	469	71	578	977	0.106	1466	-0.143	0.262	-0.619	Dowling, 2012
Ti6Al4V Alloy	805	121.5	845	1288	0.095	1293	-0.088	0.26	-0.721	ASM, 1996
Unit	MPa	GPa	MPa	MPa	-	MPa	-	-	-	

Table 4.3 Input parameters of some materials for model application

Materials	A533-B1 Steel	AISI 4340 Steel	2024-T3 Al	7075-T6 Al	Ti6Al4V Alloy
Stress ratio	-1	-1	-1	-1	-1
Linear elastic test (Δ)	Yes	Yes	Yes	Yes	Yes
Elastoplastic test (\square)	No	No	No	No	No
Data source	Dowling, 1977	Newman, 2007	Forman et al., 2005	Newman et al., 1994	Silva, 2005

Table 4.4 Information of fatigue crack growth tests for applied materials

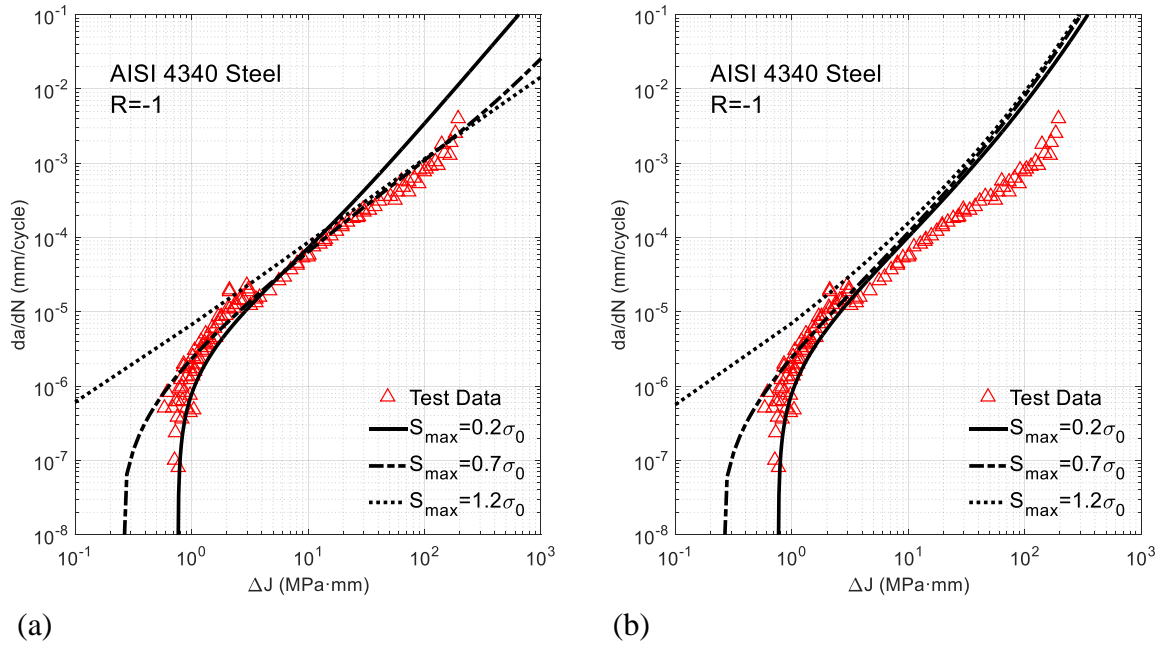


Figure 4.26 Comparison between the test data (Newman, 2007) and the model prediction for AISI 4340 Steel (a) without modification; (b) with modification

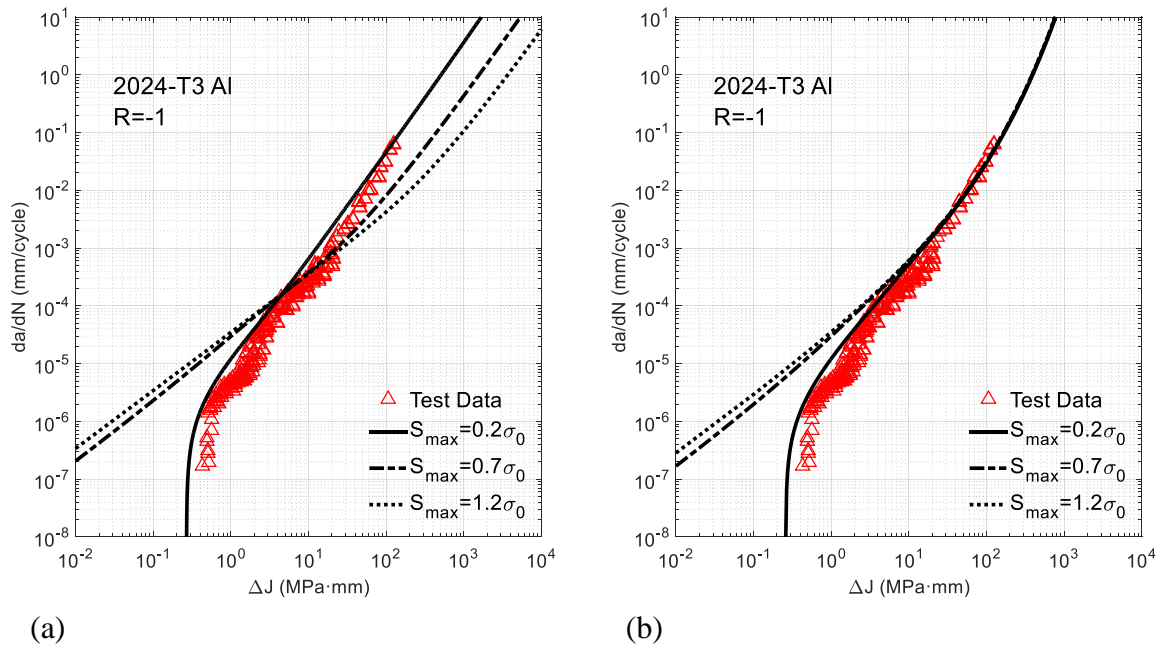


Figure 4.27 Comparison between the test data (Forman et al., 2005) and the model prediction for 2024-T3 Al (a) without modification; (b) with modification

For each material, both models without and with modification were used to predict the fatigue crack growth curves for three load levels, i.e. $S_{max} = 0.2\sigma_0$, $0.7\sigma_0$ and $1.2\sigma_0$. The predicted curves have been plotted against the test data of the applied material in figures 4.26 ~ 4.29. It can be observed that compared with the other two load levels, when $S_{max} = 0.2\sigma_0$ the

proposed model without modification can give pretty good prediction for fatigue crack growth in both low and high ΔJ regimes, or alternatively, the proposed model without modification works well for predicting the fatigue crack growth under small-scale yielding conditions. As S_{\max} increases across the small-scale yielding load limit, trends similar to that in the case of A533-B1 steel are demonstrated: the predicted curve goes above the test data in the regime of high ΔJ ; the predicted curve falls below the test data in the regime of high ΔJ ; in both regimes, a higher S_{\max} usually causes larger deviation between the predicted curve and the test data. It is also illustrated in figures 4.26 ~ 4.29 that the deviation of the model prediction from the test data in the regime of high ΔJ can be eliminated by replacing F^2 with the newly proposed correction factor C_p expressed by equation (4 – 81) in the proposed model. The predicted curves by the proposed model with modification generally have good agreements with the test data of the applied material despite the change of S_{\max} in the regime of high ΔJ . The modified proposed model works well for predicting fatigue crack growth in both high and low ΔJ regimes for the case of $S_{\max} = 0.2\sigma_0$. While the deviation among the predicted curves exist in the regime of low ΔJ , it is suggested that they may not have of significant engineering importance and hence could be neglected. Based on those facts, it is achieved that the modified proposed model works well for predicting the stable fatigue crack growth of metals with $R = -1$ under both small-scale yielding and non-small-scale yielding conditions.

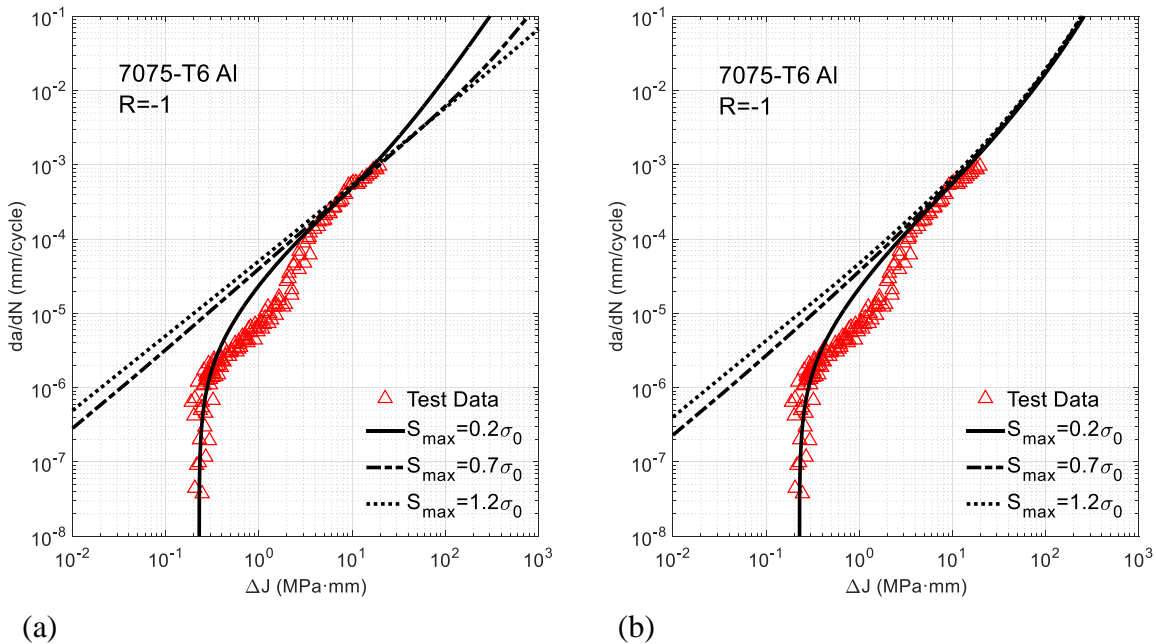


Figure 4.28 Comparison between the test data (Newman et al., 1994) and the model prediction for 7075-T6 (a) without modification; (b) with modification

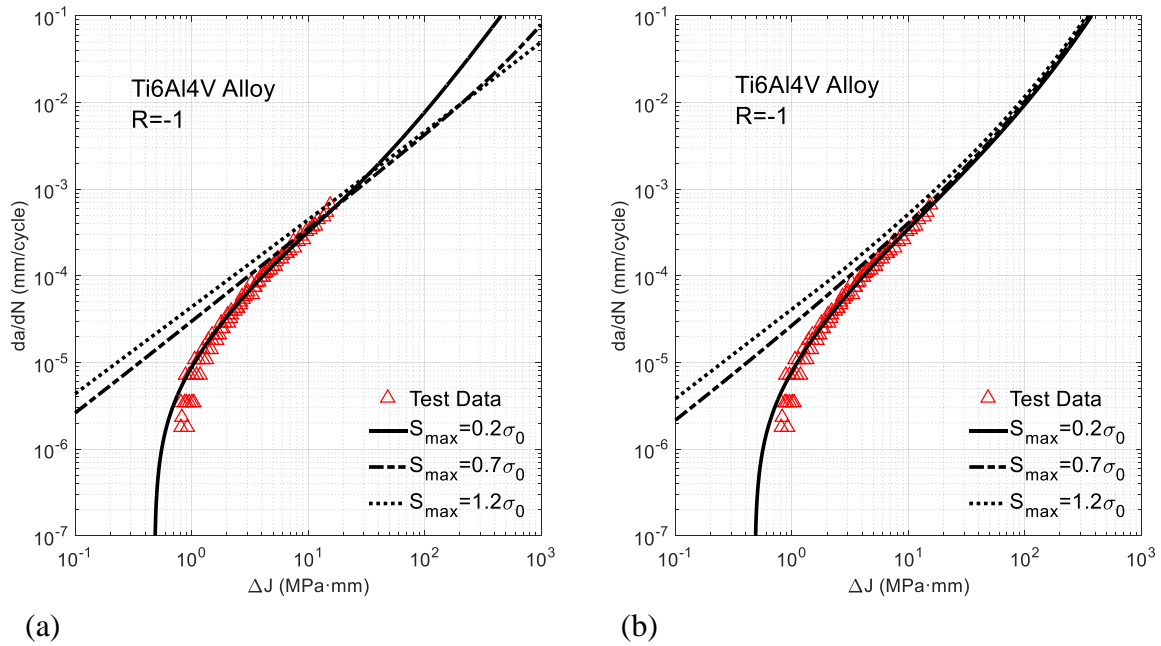


Figure 4.29 Comparison between the test data (Silva, 2005) and the model prediction for Ti6Al4V Alloy (a) without modification; (b) with modification

Figures 4.26 ~ 4.29 also illustrate that the aforementioned trends have been significantly moderated by replacing F^2 with newly proposed correction factor C_p into calculation as implied in equation (4 – 84). The fatigue crack growth curves predicted by the proposed model with modification generally have good agreements with the test data of the applied material despite the change of S_{max} in the regime of high ΔJ . While the deviation among the predicted curves exist in the regime of low ΔJ , it is suggested that they may not have of significant engineering importance and hence could be neglected. Based on those facts, it is achieved that the proposed model with modification works well for predicting fatigue crack growth rates of metallic materials under both small-scale yielding and non-small-scale yielding conditions with $R = -1$.

4.2.3 Summary

In this 4.2 section, a prediction model was established based on energy principles and elastoplastic fracture mechanics for fatigue crack growth in metallic materials with $R = -1$. Several types of metals such as A533-B1 steel, AISI 4130 steel, 2024-T3 aluminium, 7075-T6 aluminium, and Ti6Al4V alloy were chosen to apply the model given the availability of their fatigue crack growth test data as well as fundamental deformation properties. For each material, both predicted fatigue crack growth curves from the models without and with correction were plotted against its fatigue crack growth test data for comparison. The results show that

- 1) The proposed model based on energy principles represented by equation (4 – 68) can predict the fatigue crack growth of metals with $R = -1$ using ΔJ and only needs the fundamental deformation properties as the material inputs.
- 2) The proposed model without modification works well to predict the fatigue crack growth of metals under small-scale yielding conditions, but under non-small-scale yielding conditions, discrepancies occur in both the low and high ΔJ regimes, and the higher the load level, i.e. S_{\max} , the larger the deviation of the predicted fatigue crack growth curve from the test data.
- 3) By introducing the new correction factor C_p expressed by equation (4 – 81), the modified proposed model is enabled to give generally good predictions for stable fatigue crack growth in metals under both small-scale yielding and non-small-scale yielding conditions.

The research work in this section has been summarized by Cheng et al. and is under review for publication in journal.

Chapter 5. Conclusions

Subsea pipelines serving high-pressure/high-temperature oil and gas reservoirs often have to face serious challenges from both the internal and external environments since the date of their commissioning, which may seriously endanger the structural integrity and finally lead to premature failures. Foremost among those challenges are corrosion fatigue and low-cycle fatigue. Therefore, corrosion fatigue and low-cycle fatigue are two crucial issues that must be carefully dealt with when assessing the structural integrity of subsea pipelines under high-pressure/high-temperature service conditions using engineering critical assessments.

However, current industrial standards for conducting engineering critical assessments provide only limited guidance in particular for corrosion fatigue. Low-cycle fatigue is even out of their scope.

This PhD thesis is an attempt to bridge such gaps between current industrial standards and engineering practices. In the thesis, the environmental loads and corrosion mechanisms of subsea pipelines serving high-pressure/high-temperature reservoirs are analysed first. Further research work has been carried out in two stages centring on the engineering critical assessments of subsea pipelines under high-pressure/high-temperature service conditions, as illustrated by figure 5.1.

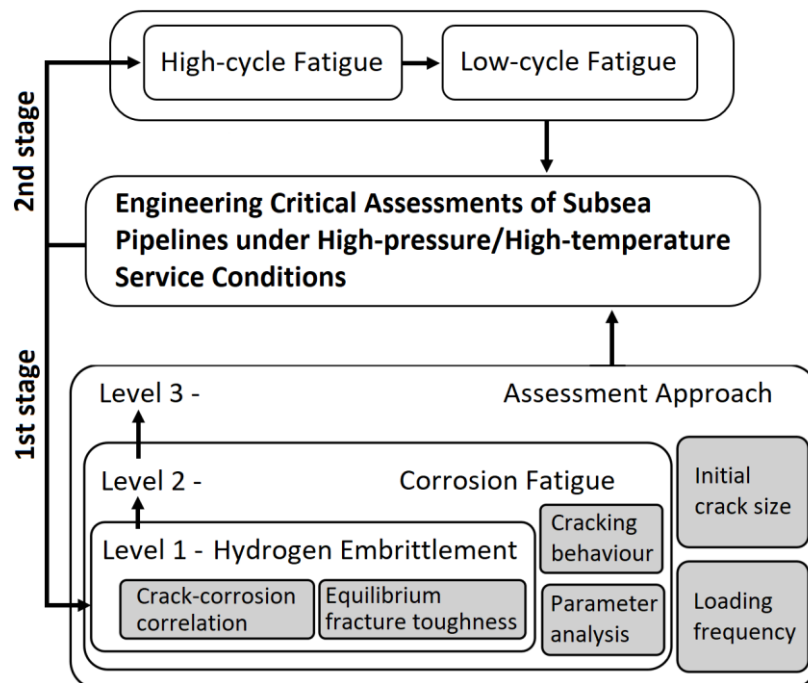


Figure 5.1 Whole structure of the PhD research

In the first stage, an extended approach of engineering critical assessment for corrosion fatigue is developed consistently in 3 levels. In level 1, a model describing the fatigue crack

growth under the impact of hydrogen embrittlement is built with the corrosion-crack correlation mathematically constructed. Then a two-component corrosion fatigue crack growth model considering both the contribution from anodic dissolution and hydrogen embrittlement is established in level 2. On those foundations, the approach of engineering critical assessment in particular for corrosion fatigue is finally proposed, with effects of both initial crack size and loading frequency accounted for.

In the second stage, a fatigue crack growth model for low-cycle fatigue based on low-cycle fatigue properties, energy principles and elastoplastic fracture mechanics is developed. It's applicability to fatigue crack growth under small-scale yielding conditions, i.e. high-cycle fatigue is first checked and then is modified and applied to predicting the fatigue crack growth under non-small-scale yielding conditions, i.e. low-cycle fatigue.

5.1 Contributions

The contributions of each section of the research work are briefly summarised here,

- 1) In developing the approach of engineering critical assessment in particular for corrosion fatigue, the author first studied the fatigue crack growth of pipeline carbon steels under gaseous hydrogen conditions, where a new corrosion-crack correlation model for fatigue behaviour is established based on the concept of environment-affected zone and the theory of linear elastic fracture mechanics. The model is applied to different API grade pipeline steels and it is found that the fatigue crack growth behaviour of those pipeline carbon steels in hydrogen gas can be well captured.
- 2) Then a two-component model is proposed for the corrosion fatigue crack growth of subsea pipeline steels considering both the stress corrosion and hydrogen-assisted cracking. The model is constructed within the frame of linear elastic fracture mechanics, characterizes both environmental and mechanical conditions and bridges the physics of corrosion fatigue and the corrosion fatigue crack growth behaviour. Based on the application of the model to X65 pipeline carbon steel, the influence of factors such as load frequency f , hydrogen concentration C_{H_0} , stress ratio R and temperature T is analysed.
- 3) On the foundation of previous research, an extended approach of engineering critical assessment in particular for corrosion fatigue is developed, in which a critical stress intensity factor was suggested to account for the influence of load frequency and initial

crack size, thus directing the model selection within current industrial standards (e.g. BS 7910) for assessing the integrity of structures suffering corrosion fatigue. The extended approach is applied to X65 grade pipeline carbon steels and the results indicate that it can provide reasonable results with significantly reduced conservatism.

- 4) In establishing the prediction model of fatigue crack growth applicable for low-cycle fatigue, the author started his research from building up an energy principles based model for predicting the fatigue crack growth of metallic materials subjected to high-cycle fatigue. The model built only requires the material's fundamental deformation properties, such as monotonic and cyclic tensile material properties and low-cycle fatigue material properties as input parameters. Application of the model to different types of materials shows that the model can predict the high-cycle fatigue crack growth under fully reversed constant amplitude cyclic loads. In combination with the Manson-Halford equation, the model can provide good prediction for high-cycle fatigue crack growth in cases of negative stress ratios (i.e. $R \leq 0$), which is typical for offshore structures.
- 5) Following a similar idea in building up the prediction model of fatigue crack growth in high-cycle fatigue, the author established a model using the cyclic J -integral ΔJ to predict fatigue crack growth in low-cycle fatigue. The model is applicable for both small-scale yielding and non-small-scale yielding fatigue crack growth as long as J -integral is applicable. Application of the model to different types of metallic materials shows that the model works well for predicting fatigue crack growth under small-scale yielding conditions from the materials' fundamental deformation properties. By introducing a correction factor C_p , the model works roughly well for predicting the fatigue crack growth under non-small-scale yielding conditions, i.e. low-cycle fatigue crack growth as well.

5.2 Future Research

Future research may be conducted in:

- 1) verifying the effectiveness of the proposed approach of engineering critical assessment in the presence of different chemicals and their combination experimentally,
- 2) extending the applicability of the proposed fatigue crack growth model to wider range of stress ratios,

- 3) modifying the proposed fatigue crack growth model to take the load sequence effect into consideration,
- 4) correlating the cracking process with corrosion under the circumstances of low-cycle fatigue, and so on.

As discussed in the literature review, high-pressure/high-temperature reservoirs are increasingly encountered in recent years as the exploration and exploitation activities of offshore oil and gas heading into deep waters, while there is no well accepted industrial standards for engineering critical assessments that can give reasonably consideration of the critical issues faced by subsea pipelines under high-pressure/high-temperature service conditions. This research is an attempt to tackle some of the most critical issues faced by current industrial standards.

Environment-assisted cracking and low-cycle fatigue are complex issues that involves multidisciplinary knowledge, and widely exist in various industries. For safety critical structures of which the failures could result tremendous economic loss and catastrophic environmental disasters, the possibility of suffering environment-assisted cracking and low-cycle fatigue should be seriously taken into account. Good understandings on the mechanisms and behaviours of environment-assisted cracking and low-cycle fatigue are crucial to achieving high-quality engineering critical assessments. Therefore environment-assisted cracking and low-cycle fatigue deserve researchers' continuous research effort. The outcomes of this research may, at least to some extent, bridge the gaps between the current industrial standards and the engineering practice in developing high-pressure/high-temperature offshore oil and gas sources, meanwhile providing useful reference for engineering critical assessment of metallic welded structures in a broader sense.

References

- ABS, 2014. ABS Rules for building and classing: Floating production installations. American Bureau of Shipping, Houston, US.
- ABS, 2018. ABS Guide for building and classing subsea pipeline systems. American Bureau of Shipping, Houston, US.
- Amaro, R.L., Rustagi, N., Findley, K.O., Drexler, E.S. and Slifka, A.J., 2014. Modeling the fatigue crack growth of X100 pipeline steel in gaseous hydrogen. *International Journal of Fatigue*, 59, pp.262-271.
- Anderson, T.L., 2017, *Fracture mechanics: fundamentals and applications*. CRC press.
- API, 2009. API Recommended Practice 17N: Subsea production system reliability and technical risk management. American Petroleum Institute, Houston, US.
- API, 2013. API Standard 1104: Welding of pipelines and related facilities. American Petroleum Institute, Houston, US.
- API, 2015. API Technical Report 17TR8: High-pressure high-temperature design guidelines. American Petroleum Institute, Houston, US.
- API, 2016. API Standard 579-1/ASME FFS-1: Fitness-for-service. American Petroleum Institute, Houston, US.
- Araújo, J.A., Susmel, L., Pires, M.S.T. and Castro, F.C., 2017. A multiaxial stress-based critical distance methodology to estimate fretting fatigue life. *Tribology International*, 108, pp.2-6.
- Arola, D. and Williams, C.L., 2002. Estimating the fatigue stress concentration factor of machined surfaces. *International Journal of fatigue*, 24(9), pp.923-930.
- ASM, 1996. Handbook, vol. 19, Fatigue and fracture. American Society for Metals (ASM) International, Cleveland, US.
- ASTM International, 2012. E606M-12 Standard test method for strain-controlled fatigue testing. West Conshohocken, US.
- ASTM International, 2017. E1820-17 Standard test method for measurement of fracture toughness. West Conshohocken, US.

Austen, I.M. and Walker, E.F., 1977, Quantitative understanding of the effects of mechanical and environmental variables on corrosion fatigue crack growth behaviour. In *The Influence of Environment on Fatigue*. I Mech E Conference Publications, London, pp.1-10.

Bai, Y. and Bai, Q. eds., 2005. *Subsea pipelines and risers*. Elsevier.

Bai, Q. and Bai, Y., 2014. *Subsea pipeline design, analysis, and installation*. Gulf Professional Publishing.

Bannantine, J.A., Comer, J.J., and Handrock, J.L., 1990. *Fundamentals of metal fatigue analysis*. Prentice Hall.

Barnoush, A., 2011. *Hydrogen embrittlement*. Saarland University.

Bartlett, M.L. and Hudak, Jr S.J., 1990. The Influence of Frequency-Dependent Crack Closure on Corrosion Fatigue Crack Growth (Retroactive Coverage). *Fatigue* 90, pp.1783-1788.

Baxter, D.P., Maddox, S.J. and Pargeter, R.J., Corrosion fatigue behaviour of welded risers and pipelines. *Stress*, 2007, 10(100), p.1000.

Beavers, J.A. and Harle, B.A., 2001. Mechanisms of high-pH and near-neutral-pH SCC of underground pipelines. *Journal of Offshore Mechanics and Arctic Engineering*, 123(3), pp.147-151.

Beden, S.M., Abdullah, S. and Ariffin, A.K., 2009. Review of fatigue crack propagation models for metallic components. *European Journal of Scientific Research*, 28(3), pp.364-397.

Benaarbia, A., Chrysochoos, A. and Robert, G., 2014. Kinetics of stored and dissipated energies associated with cyclic loadings of dry polyamide 6.6 specimens. *Polymer Testing*, 34, pp.155-167.

Benedetti, M. and Santus, C., 2019. Notch fatigue and crack growth resistance of Ti-6Al-4V ELI additively manufactured via selective laser melting: A critical distance approach to defect sensitivity. *International Journal of Fatigue*, 121, pp.281-292.

Bever, M.B., Holt, D.L. and Titchener, A.L., 1973. The stored energy of cold work. *Progress in Materials Science*, 17, pp.5-177.

Bomba, J., Chin, D., Kak, A. and Meng, W., 2018, April. Flow Assurance Engineering in Deepwater Offshore-Past, Present, and Future. In *Offshore Technology Conference*. Offshore Technology Conference.

- British Energy, 2001. R6: Assessment of the integrity of structures containing defects.
- Broek, D., 2012. Elementary engineering fracture mechanics. Springer Science & Business Media.
- BSI, 2015. BS 7910: Guidance on methods for assessing the acceptability of flaws in fusion welded structures. British Standards Institution, London, UK.
- Buitrago, J., Hudak, S. and Baxter, D., 2008. High-cycle and low-cycle fatigue resistance of girth welds in sour service. In ASME 2008 27th International Conference on Offshore Mechanics and Arctic Engineering (pp. 365-372). American Society of Mechanical Engineers.
- Cabrini, M. and Pastore, T., 2006. Hydrogen diffusion and EAC of pipeline steels under cathodic protection. Fracture of Nano and Engineering Materials and Structures, pp. 1005-1006. Springer, Netherlands.
- CSA, 2015. CSA Z662: Oil & gas pipeline systems. Canadian Standards Association, Mississauga, Canada.
- Carr, M., Bruton, D. and Leslie, D., 2003, February. Lateral buckling and pipeline walking, a challenge for hot pipelines. In Offshore Pipeline Technology Conference (pp. 1-36), Amsterdam.
- Chandran, K.R., 2017. Insight on physical meaning of finite-width-correction factors in stress intensity factor (K) solutions of fracture mechanics. Engineering Fracture Mechanics, 186, pp.399-409.
- Chandrasatheesh, C., Jayapriya, J., George, R.P. and Mudali, U.K., 2014. Detection and analysis of microbiologically influenced corrosion of 316 L stainless steel with electrochemical noise technique. Engineering Failure Analysis, 42, pp.133-142.
- Chang, K.M., 1988. An empirical model for environmental damage at the crack tip. In MRS Proceedings (Vol. 125, p. 243). Cambridge University Press.
- Chen, N.Z., Wang, G., Guedes Soares, C., 2011. Palmgren-Miner's rule and fracture mechanics based inspection planning. Engineering Fracture Mechanics, 78, pp.3166-3182.
- Chen, N.Z., 2016. A stop-hole method for marine and offshore structures. International Journal of Fatigue, 88, pp.49-57.

- Cheng, A. and Chen, N.Z., 2017a. Fatigue crack growth modelling for pipeline carbon steels under gaseous hydrogen conditions. *International Journal of Fatigue*, 96, pp.152-161.
- Cheng, A. and Chen, N.Z., 2017b. Corrosion fatigue crack growth modelling for subsea pipeline steels. *Ocean Engineering*, 142, pp.10-19.
- Cheng, A. and Chen, N.Z., 2018a. An extended engineering critical assessment for corrosion fatigue of subsea pipeline steels. *Engineering Failure Analysis*, 84, pp.262-275.
- Cheng, A. and Chen, N.Z., 2018b, June. A benchmark study on applying extended finite element method to the structural integrity assessment of subsea pipelines at HPHT service conditions. In *ASME 2018 37th International Conference on Ocean, Offshore and Arctic Engineering*. Paper NO. V11BT12A037. American Society of Mechanical Engineers.
- Cheng, A., Chen, N.Z. and Pu, Y., 2019. An energy principles based model for fatigue crack growth prediction. *International Journal of Fatigue*, 128, p.105198.
- Chong, T.V.S., Kumar, S.B., Tronskar, J.P., Lai, M.O. and Loh, W.L., 2016. Engineering critical assessment of nickel-based clad pipeline girth welds in a wet H₂S-containing environment. *Engineering Fracture Mechanics*, 160, pp.42-51.
- Chrysochoos, A., Maisonneuve, O., Martin, G., Caumon, H. and Chezeaux, J.C., 1989. Plastic and dissipated work and stored energy. *Nuclear Engineering and Design*, 114(3), pp.323-333.
- Cialone, H.J. and Holbrook, J.H., 1985. Effects of gaseous hydrogen on fatigue crack growth in pipeline steel. *Metallurgical Transactions A*, 16(1), pp.115-122.
- Cui, W., 2002. A state-of-the-art review on fatigue life prediction methods for metal structures. *Journal of marine science and technology*, 7(1), pp.43-56.
- Dasgupta, A., Oyan, C., Barker, D. and Pecht, M., 1992. Solder creep-fatigue analysis by an energy-partitioning approach. *Journal of Electronic Packaging*, 114(2), pp.152-160.
- Dauskardt, R.H. and Ritchie, R.O., 1986. Fatigue crack propagation behavior in pressure-vessel steels for high-pressure hydrogen service. *Properties of High-Strength Steels for High-Pressure Containments*, American Society of Mechanical Engineers, pp.17-28.
- Davenport, R.T. and Brook, R., 1979. The threshold stress intensity range in fatigue. *Fatigue & Fracture of Engineering Materials & Structures*, 1(2), pp.151-158.
- Dawes, M.G., 1979. Elastic-plastic fracture toughness based on the COD and J-contour integral concepts. In *Elastic-plastic fracture*. ASTM International.

- De Jesus, A.M. and Correia, J.A., 2013. Critical assessment of a local strain-based fatigue crack growth model using experimental data available for the P355NL1 steel. *Journal of Pressure Vessel Technology*, 135(1), p.011404.
- DNVGL, 2017. DNVGL-RP-F108: Assessment of flaws in pipeline and riser girth welds. Det Norske Veritas, Oslo, Norway.
- DNVGL, 2017. DNVGL-ST-F101: Submarine pipeline systems. Det Norske Veritas, Oslo, Norway.
- Dowling, N.E. and Begley, J.A., 1976. Fatigue crack growth during gross plasticity and the J-integral. In *Mechanics of crack growth*. ASTM International.
- Dowling, N.E., 1977. Crack growth during low-cycle fatigue of smooth axial specimens. In *Cyclic stress-strain and plastic deformation aspects of fatigue crack growth*. ASTM International.
- Dowling, N.E., 2012. *Mechanical behavior of materials: engineering methods for deformation, fracture, and fatigue*. Pearson.
- Drexler, E.S., Slifka, A.J., Amaro, R.L., Barbosa, N., Lauria, D.S., Hayden, L.E. and Stalheim, D.G., 2014. Fatigue crack growth rates of API X70 pipeline steel in a pressurized hydrogen gas environment. *Fatigue & Fracture of Engineering Materials & Structures*, 37(5), pp.517-525.
- Ellyin, F. and Kujawski, D., 1984. Plastic strain energy in fatigue failure. *Journal of Pressure Vessel Technology*, 106(4), pp.342-347.
- Ellyin, F., 2012. *Fatigue damage, crack growth and life prediction*. Springer Science & Business Media.
- Endo, K., Komai, K. and Matsuda, Y., 1981. Mechanical effects of corrosion products in corrosion fatigue crack growth of a steel. *Bulletin of Japanese Society of Mechanical Engineers*, 24(194), pp.1319-1325.
- Fahr, A., 2013. *Aeronautical applications of non-destructive testing*. DEStech Publications, Inc.
- Fang, B.Y., Atrens, A., Wang, J.Q., Han, E.H., Zhu, Z.Y. and Ke, W., 2003. Review of stress corrosion cracking of pipeline steels in “low” and “high” pH solutions. *Journal of Materials Science*, 38(1), pp. 127-132.

- Fatemi, A. and Yang, L., 1998. Cumulative fatigue damage and life prediction theories: a survey of the state of the art for homogeneous materials. *International journal of fatigue*, 20(1), pp.9-34.
- Fontana, M.G., 2005. *Corrosion engineering*. Tata McGraw-Hill Education.
- Forman, R.G., Shivakumar, V., Cardinal, J.W., Williams, L.C. and McKeighan, P.C., 2005. Fatigue crack growth database for damage tolerance analysis (Final Report No. DOT/FAA/AR-05/15). US Department of Transportation Federal Aviation Administration (FAA), Office of Aviation Research Washington, US.
- Gadgeel, V.L. and Johnson, D.L., 1979. Gas-phase hydrogen permeation and diffusion in carbon steels as a function of carbon content from 500 to 900 K. *Journal of Materials for Energy Systems*, 1(2), pp.32-40.
- Galkiewicz, J. and Graba, M., 2006. Algorithm for determination of $\tilde{\sigma}_{ij}(n, \theta)$, $\tilde{\varepsilon}_{ij}(n, \theta)$, $\tilde{u}_i(n, \theta)$, $d_n(n, \theta)$ and $I_n(n)$ functions in Hutchinson Rice Rosengren solution and its 3D generalization. *Journal of Theoretical and Applied Mechanics*, 44, pp.19-30.
- Ganesh Kumar, J., Ganesan, V. and Laha, K., 2019. High temperature tensile properties of 316LN stainless steel investigated using automated ball indentation technique. *Materials at High Temperatures*, 36(1), pp.48-57.
- Gangloff, R.P., 1990. *Corrosion fatigue crack propagation in metals* (No. NASA-CR-4301). National Aeronautics and Space Administration (NASA), Langley Research Center, Hampton, US.
- Gangloff, R.P., 2008. Critical issues in hydrogen assisted cracking of structural alloys. In *Environment-induced cracking of materials*, pp. 141-165. Elsevier.
- Garbatov, Y., As, S. K., Branner, K., Choi, B. K., den Besten, J. H., Dong, P., ... Yuan, Y., 2018. Committee III.2: Fatigue and fracture. In M. L. Kaminski, & P. Rigo (Eds.), *Proceedings of the 20th International Ship and Offshore Structures Congress (ISSC 2018)* (Vol. 1, pp. 441-547). CRC Press.
- Gavem, T., Kumar, A., Panga, V., Stratton, M. and Harry, J.J., 2015, May. Critical HP/HT flowline design challenges associated with deepwater miocene GoM fields. In *Offshore Technology Conference*. Offshore Technology Conference.

- Gerberich, W. W., Livne, T., Chen, X. F. and Kaczorowski, M., 1988. Crack growth from internal hydrogen-temperature and microstructure effects in 4340 steel. *Metallurgical and Materials Transactions A*, 19(5), pp.1319-1344.
- Godefroid, L.B., Cândido, L.C., Toffolo, R.V.B. and Barbosa, L.H.S., 2014. Microstructure and mechanical properties of two API steels for iron ore pipelines. *Materials Research*, 17, pp.114-120.
- Guedri, A., Merzoug, B. and Zegloul, A., 2004. Improving mechanical properties of API X60/X70 welded pipeline steel. *Sciences & Technologie B*, (29), pp.51-58.
- Guo, W., 1993a. Elastoplastic three dimensional crack border field—I. Singular structure of the field. *Engineering Fracture Mechanics*, 46(1), pp.93-104.
- Guo, W., 1993b. Elastoplastic three dimensional crack border field—II. Asymptotic solution for the field. *Engineering Fracture Mechanics*, 46(1), pp.105-113.
- Gutierrez-Solana, F. and Elices M., 1982, High-pressure hydrogen behavior of a pipeline steel. In *Current solutions to hydrogen problems in steels*, pp.181-185.
- Haritos, G.K., Nicholas, T. and Lanning, D.B., 1999. Notch size effects in HCF behavior of Ti-6Al-4V. *International Journal of Fatigue*, 21(7), pp.643-652.
- Hill, R., 1998. *The mathematical theory of plasticity* (Vol. 11). Oxford university press.
- Holtam, C., 2010. Structural integrity assessment of C-Mn pipeline steels exposed to sour environments. PhD thesis, Loughborough University, UK.
- Holtam, C., Saraswat, R., Thodla, R. and Gui, F., 2018. A modified engineering critical assessment approach for offshore pipelines. In *ASME 2018 37th International Conference on Ocean, Offshore and Arctic Engineering* (pp. V004T03A011-V004T03A011). American Society of Mechanical Engineers.
- Huffman, P.J., 2016. A strain energy based damage model for fatigue crack initiation and growth. *International Journal of Fatigue*, 88, pp.197-204.
- Humphries, M.J., McLaughlin, J.E. and Pargeter, R., 1989. Toughness characteristics of hydrogen charged pressure vessel steels. In *International Conference on Interaction of Steels with Hydrogen in Petroleum Industry Pressure Vessel Service*, Paper No. 243.
- Hurley, P.J. and Evans, W.J., 2007. A new method for predicting fatigue crack propagation rates. *Materials Science and Engineering: A*, 466(1-2), pp.265-273.

- Hutchinson, J.W., 1968. Singular behaviour at the end of a tensile crack in a hardening material. *Journal of the Mechanics and Physics of Solids*, 16(1), pp.13-31.
- Iannuzzi, M., 2011. Environmentally assisted cracking (EAC) in oil and gas production. In *Stress Corrosion Cracking* (pp. 570-607). Woodhead Publishing.
- Irwin, G. R., 1957. Analysis of stresses and strains near the end of a crack traversing a plate. *Journal of Applied Mechanics* 24, pp.361-364.
- ISO, 2014. ISO 19902 (2014): Petroleum and natural gas industries-fixed steel offshore structures. International Organization for Standardization, Geneva, Switzerland.
- Jia, L.J. and Ge, H., 2018. *Ultra-Low Cycle Fatigue Failure of Metal Structures Under Strong Earthquakes*. Springer.
- Kaisand, L.R. and Mowbray, D.F., 1979. Relationships between low-cycle fatigue and fatigue crack growth rate properties. *Journal of Testing and Evaluation*, 7(5), pp.270-280.
- Kaminski, M.L., 2007, January. Sensing and understanding fatigue lifetime of new and converted FPSOs. In *Offshore Technology Conference*. Offshore Technology Conference.
- Kang, P.S., Lee, D.G. and Lim, J.S., 2014, August. Status of wax mitigation technologies in offshore oil production. In *The Twenty-fourth International Ocean and Polar Engineering Conference*. International Society of Offshore and Polar Engineers.
- Karakaş, Ö. and Szusta, J., 2016. Monotonic and low cycle fatigue behaviour of 2024-T3 aluminium alloy between room temperature and 300°C for designing VAWT components. *Fatigue & Fracture of Engineering Materials & Structures*, 39(1), pp.95-109.
- Kim, Y.H. and Manning, S.D., 1983, January. A superposition model for corrosion-fatigue crack propagation in aluminum alloys. In *Fracture Mechanics: Fourteenth Symposium—Volume I: Theory and Analysis*. ASTM International.
- Kim, K.S. and Leckie, F.A., 1990. On the calculations of the stored energy of cold work. *Journal of Engineering Materials and Technology*, 112, p.465.
- Kim S.S., Choe S.J., Shin K.S., 1998. Quantitative models on corrosion fatigue crack growth rates in metals: Part I. Overview of quantitative crack growth models. *Metals and Materials International*, 4(1), pp.1-13.
- Klesnil, M. and Lukac, P., 1992. *Fatigue of metallic materials* (Vol. 71). Elsevier.

- Kuhn, P. and Hardrath, H.F., 1952. An engineering method for estimating notch-size effect in fatigue tests on steel (Technical Note 2805). National Advisory Committee for Aeronautics (NACA), Langley Aeronautical Laboratory, Langely Field, US.
- Koçak, M., Webster, S., Janosch, J.J., Ainsworth, R.A., and Koers, R., 2008. FITNET fitness-for-service (FFS) – procedure. GKSS Research Center, Germany.
- Kuhn, P. and Figge, I.E., 1962. Unified notch-strength analysis for wrought aluminum alloys (No. NASA-TN-D-1259). National Aeronautics and Space Administration (NASA), Langley Research Center, Hampton, US.
- Kumar, S.B., Chong, S., Tornqvist, R., Tronskar, J.P., Lai, M.O. and Loh, W.L., 2014. ECA of high pressure and high temperature (HP/HT) CRA pipelines. In Offshore Technology Conference-Asia. Offshore Technology Conference.
- Kumar, V.G.M.D., German, M.D. and Shih, C.F., 1981. Engineering approach for elastic-plastic fracture analysis. No. EPRI-NP—1931, General Electric Co..
- Kujawski, D. and Ellyin, F., 1984. A fatigue crack propagation model. *Engineering Fracture Mechanics*, 20(5-6), pp.695-704.
- Lam, P., 2006. Gaseous hydrogen effects on the mechanical properties of carbon and low alloy steels (U) (No. WSRC-TR-2006-00119). SRS.
- Lamba, H.S., 1975. The J-integral applied to cyclic loading. *Engineering Fracture Mechanics*, 7(4), pp.693-703.
- Landes, J.D. and Wei, R.P., 1969. Correlation between sustained-load and fatigue crack growth in high-strength steels. National Aeronautics and Space Administration (NASA), Langley Research Center, Hampton, US.
- Lasebikan, B.A., Akisanya, A.R. and Deans, W.F., 2013. The mechanical behavior of a 25Cr super duplex stainless steel at elevated temperature. *Journal of Materials Engineering and Performance*, 22(2), pp.598-606.
- Lee, S.L. and Unger, D.J., 1988. A decohesion model of hydrogen assisted cracking. *Engineering Fracture Mechanics*, 31, pp.647-660.
- Leighty, W., Holloway, J., Merer, R., Somerday, B., San Marchi, C., Keith, G., White, D. and Economics, S.E., 2006, April. Compressorless hydrogen transmission pipelines deliver large-scale stranded renewable energy at competitive cost. In *Proceedings of the 16th World Hydrogen Energy Conference*, Lyon, FR, June (Vol. 6).

- Li, D.M., Nam, W.J. and Lee, C.S., 1998. An improvement on prediction of fatigue crack growth from low cycle fatigue properties. *Engineering Fracture Mechanics*, 60(4), pp.397-406.
- Liu, A.F., *Mechanics and mechanisms of fracture: an introduction*. ASM International, 2005.
- Liu, Q. and Atrens, A., 2013. A critical review of the influence of hydrogen on the mechanical properties of medium-strength steels. *Corrosion Reviews*, 31(3-6), pp.85-103.
- Ljustell, P., 2007. Large scale yielding fatigue crack growth: A literature survey.
- Logan, H.L., 1952. Film-rupture mechanism of stress corrosion. *Journal of Research of the National Bureau of Standards*, 48(2), pp.99-105.
- Loginow, A.W. and Phelps, E.H., 1975. Steels for seamless hydrogen pressure vessels. *Journal of Engineering for Industry*, 97(1), pp.274-282.
- Luke, M., Varfolomeev, I., Lütkepohl, K. and Esderts, A., 2010. Fracture mechanics assessment of railway axles: experimental characterization and computation. *Engineering Failure Analysis*, 17(3), pp.617-623.
- Lynch, S.P., 2011. Hydrogen embrittlement (HE) phenomena and mechanisms. In *Stress Corrosion Cracking*, pp. 90-130. Woodhead Publishing.
- Ma, F.Y., 2012. Corrosive effects of chlorides on metals. In *Pitting corrosion*. IntechOpen.
- Makogon, T.Y., 2019. *Handbook of Multiphase Flow Assurance*. Gulf Professional Publishing.
- Manson, S.S. and Halford, G.R., 1981. Practical implementation of the double linear damage rule and damage curve approach for treating cumulative fatigue damage. *International Journal of Fracture*, 17(2), pp.169-192.
- Martinez, X., Oller, S., Barbu, L.G., Barbat, A.H. and De Jesus, A.M.P., 2015. Analysis of Ultra Low Cycle Fatigue problems with the Barcelona plastic damage model and a new isotropic hardening law. *International Journal of Fatigue*, 73, pp.132-142.
- Masson, C., Lou, J., Saranyasoontorn, K., Jesudasan, A.S., Zeng, W., Wang, L. and Hahn, G.D., 2015, October. A review of fitness-for-service and life extension assessment methodologies relating to corrosion features in fatigue sensitive risers and pipelines. In *OTC Brasil. Offshore Technology Conference*.

- Mars, W.V. and Fatemi, A., 2002. A literature survey on fatigue analysis approaches for rubber. *International Journal of fatigue*, 24(9), pp.949-961.
- McEvily, A. J. and Wei, R.P., 1972. *Fracture mechanics and corrosion fatigue*. Connecticut University Storrs Department of Metallurgy.
- Mokhatab, S., Wilkens, R.J. and Leontaritis, K.J., 2007. A review of strategies for solving gas-hydrate problems in subsea pipelines. *Energy Sources, Part A*, 29(1), pp.39-45.
- Molski, K. and Glinka, G., 1981. A method of elastic-plastic stress and strain calculation at a notch root. *Materials Science and Engineering*, 50(1), pp.93-100.
- Morrow, J., 1965. Cyclic plastic strain energy and fatigue of metals. In *Internal friction, damping, and cyclic plasticity*. ASTM International.
- Moura, C.M., Vilela, J.J., Rabello, E.G., Martins, D.G.P. and Carneiro, J.R.G., 2009. Evaluation of the ductile-to-brittle transition temperature in steel low carbon. *International Nuclear Atlantic Conference (INAC)*, 2009.
- Nanninga, N., Slifka, A., Levy, Y. and White, C., 2010. A review of fatigue crack growth for pipeline steels exposed to hydrogen. *Journal of research of the National Institute of Standards and Technology*, 115(6), p.437.
- Neuber, H., *Kerbspannungstehre*, Springer, Berlin, 1958. Translation theory of notch stresses. U.S. Office of Technical Services, Washington, US.
- Neuber, H., 1961. Theory of stress concentration for shear-strained prismatical bodies with arbitrary nonlinear stress-strain law. *Journal of Applied Mechanics*, 28(4), pp.544-550.
- Newman, J.C., Wu, X.R., Venneri, S.L. and Li, C.G., 1994. Small-crack effects in high-strength aluminum alloys (NASA-RP-1309). National Aeronautics and Space Administration (NASA), Langley Research Center, Hampton, VA.
- Newman, J.C., 2007. Analyses of fatigue crack growth databases for use in a damage tolerance approach for aircraft propellers and rotorcraft. US Department of Transportation, Federal Aviation Administration.
- Ngoula, D.T., Madia, M., Beier, H.T., Vormwald, M. and Zerbst, U., 2018. Cyclic J-integral: Numerical and analytical investigations for surface cracks in weldments. *Engineering Fracture Mechanics*, 198, pp.24-44.

- Nguyen, O., Repetto, E.A., Ortiz, M. and Radovitzky, R.A., 2001. A cohesive model of fatigue crack growth. *International Journal of Fracture*, 110(4), pp.351-369.
- Nip, K.H., Gardner, L., Davies, C.M. and Elghazouli, A.Y., 2010. Extremely low cycle fatigue tests on structural carbon steel and stainless steel. *Journal of constructional steel research*, 66(1), pp.96-110.
- Noroozi, A.H., Glinka, G. and Lambert, S., 2005. A two parameter driving force for fatigue crack growth analysis. *International Journal of Fatigue*, 27(10-12), pp.1277-1296.
- Oh, C.K., Kim, Y.J., Baek, J.H., Kim, Y.P. and Kim, W., 2007. A phenomenological model of ductile fracture for API X65 steel. *International Journal of Mechanical Sciences*, 49(12), pp.1399-1412.
- Oliferuk, W., Korbel, A. and Bochniak, W., 2001. Energy balance and macroscopic strain localization during plastic deformation of polycrystalline metals. *Materials Science and Engineering: A*, 319, pp.250-253.
- Oriani, R.A., 1972. A mechanistic theory of hydrogen embrittlement of steels. *Berichte der Bunsengesellschaft für physikalische Chemie*, 76(8), pp.848-857.
- Oriani, R.A. and Josephic, P.H., 1977. Equilibrium and kinetic studies of the hydrogen-assisted cracking of steel. *Acta Metallurgica*, 25(9), pp.979-988.
- Ossai, C.I., Boswell, B. and Davies, I.J., 2015. Pipeline failures in corrosive environments—A conceptual analysis of trends and effects. *Engineering Failure Analysis*, 53, pp.36-58.
- Palmer, A.C. and King, R.A., 2004. *Subsea pipeline engineering*. Penn Well Books.
- Pandey, K.N. and Chand, S., 2003. An energy based fatigue crack growth model. *International Journal of Fatigue*, 25(8), pp.771-778.
- Pargeter, R.J. and Baxter, D.P., 2009, January. Design of pipelines subject to lateral buckling to resist corrosion fatigue. In *Corrosion 2009*. NACE International.
- Paris, P.C. and Erdogan, F., 1963. A critical analysis of crack propagation laws. *Journal of Basic Engineering*, 85(4), pp.528-533.
- Parkins, R.N., 1979. Environment sensitive fracture and its prevention. *British Corrosion Journal*, 14(1), pp.5-14.
- Parkins, R.N., 1992. Current understanding of stress-corrosion cracking. *Journal of the Mineral, Metals and Materials Society*, 44(12), pp.12-19.

- Parkins, R.N., 2000, January. A review of stress corrosion cracking of high pressure gas pipelines. In Corrosion 2000. NACE International.
- Pendse, R.D. and Ritchie, R.O., 1985. A study of fatigue crack propagation in prior hydrogen attacked pressure vessel steels. *Metallurgical Transactions A*, 16(8), pp.1491-1501.
- Pilkey, W.D. and Pilkey, D.F., 2008. *Peterson's stress concentration factors*. John Wiley & Sons.
- Pugno, N., Ciavarella, M., Cornetti, P. and Carpinteri, A., 2006. A generalized Paris' law for fatigue crack growth. *Journal of the Mechanics and Physics of Solids*, 54(7), pp.1333-1349.
- Reda, A.M., Forbes, G.L. and Sultan, I.A., 2011. Characterisation of slug flow conditions in pipelines for fatigue analysis. In *ASME 2011 30th International Conference on Ocean, Offshore and Arctic Engineering* (pp. 535-547). American Society of Mechanical Engineers.
- Rhodes, P.R., 2001. Environment-assisted cracking of corrosion-resistant alloys in oil and gas production environments: a review. *Corrosion*, 57(11), pp.923-966.
- Rhodin, T. N. (ed.), 1959. *Physical metallurgy of stress corrosion fracture*. Interscience, New York, US.
- Rice, J.R., 1968. A path independent integral and the approximate analysis of strain concentration by notches and cracks. *Journal of applied mechanics*, 35(2), pp.379-386.
- Rice, J. and Rosengren, G.F., 1968. Plane strain deformation near a crack tip in a power-law hardening material. *Journal of the Mechanics and Physics of Solids*, 16(1), pp.1-12.
- Ritchie, R.O. and Thompson, A.W., 1985. On macroscopic and microscopic analyses for crack initiation and crack growth toughness in ductile alloys. *Metallurgical Transactions A*, 16(1), pp.233-248.
- Robinson, S.L. and Stoltz, R.E., 1980. Toughness losses and fracture behavior of low-strength carbon-manganese steels in hydrogen. *Hydrogen Effects in Metals*, pp.987-995.
- Ronevich, J.A., Somerday, B.P. and San Marchi, C.W., 2016. Effects of microstructure banding on hydrogen assisted fatigue crack growth in X65 pipeline steels. *International Journal of Fatigue*, 82, pp.497-504.
- Rteil, A.A. and Topper, T.H., 2005. Fatigue behavior, monotonic properties and microstructure data for SAE 4140, quenched and Tempered Steel (Iteration No. 69). American Iron and Steel Institute (AISI), Washington, US.

- Salerno, G., Magnabosco, R. and de Moura Neto, C., 2007. Mean strain influence in low cycle fatigue behavior of AA7175-T1 aluminum alloy. *International Journal of Fatigue*, 29(5), pp.829-835.
- San Marchi, C. and Somerday, B.P., 2008. Technical reference on hydrogen compatibility of materials. SAND2008-1163, Sandia National Laboratories, Livermore, US.
- Santecchia, E., Hamouda, A.M.S., Musharavati, F., Zalnezhad, E., Cabibbo, M., El Mehtedi, M. and Spigarelli, S., 2016. A review on fatigue life prediction methods for metals. *Advances in Materials Science and Engineering*, 2016.
- Santos, T.F.A., Hermenegildo, T.F.C., Afonso, C.R.M., Marinho, R.R., Paes, M.T.P. and Ramirez, A.J., 2010. Fracture toughness of ISO 3183 X80M (API 5L X80) steel friction stir welds. *Engineering Fracture Mechanics*, 77(15), pp.2937-2945.
- Schütz, W., 1993. Fatigue life prediction—a review of the state of the art. *Structural Failure, Product Liability and Technical Insurance*, 4.
- Shi, K.K., Cai, L.X., Qi, S. and Bao, C., 2016. A prediction model for fatigue crack growth using effective cyclic plastic zone and low cycle fatigue properties. *Engineering Fracture Mechanics*, 158, pp.209-219.
- Shih, C.F. and Hutchinson, J.W., 1976. Fully plastic solutions and large scale yielding estimates for plane stress crack problems. *Journal of Engineering Materials and Technology*, 98(4), pp.289-295.
- Shih, C.F. and German, M.D., 1981. Requirements for a one parameter characterization of crack tip fields by the HRR singularity. *International Journal of Fracture*, 17(1), pp.27-43.
- Shin, C.S., Man, K.C. and Wang, C.M., 1994. A practical method to estimate the stress concentration of notches. *International Journal of Fatigue*, 16(4), pp.242-256.
- Silva, F.S., 2005. The importance of compressive stresses on fatigue crack propagation rate. *International journal of fatigue*, 27(10-12), pp.1441-1452.
- SINTAP, November 1999. Structural integrity assessment procedures for European industry, final procedure. European Union Brite-Euram Programme (Project No. BE95-1426), British Steel, Rotherham, UK.
- Shipilov, S.A., 2002. Mechanisms for corrosion fatigue crack propagation. *Fatigue & Fracture of Engineering Materials & Structures*, 25(3), pp.243-259.

- Skeels, H.B., 2014. API 17TR8-HPHT design guideline for subsea equipment. In Offshore Technology Conference. Offshore Technology Conference.
- Skelton, R.P., 1987. Cyclic stress-strain properties during high strain fatigue. In High Temperature Fatigue (pp. 27-112). Springer, Dordrecht.
- Smith, A.T., Schneider, C.R.A., Bird, C.R., Wall, M., 2019. Use of non-destructive testing for engineering critical assessment: Background to the advice given in BS 7910:2013, International Journal of Pressure Vessels and Piping, 169, pp. 153-159.
- Somerday, B.P., 2008. Technical reference on hydrogen compatibility of materials-Plain Carbon Ferritic Steels: C-Mn Alloys (Code 1100) (Report No. SAND2008-1163). Sandia National Laboratories, Livermore, CA.
- Song, J. and Curtin, W.A., 2011. A nanoscale mechanism of hydrogen embrittlement in metals. Acta Materialia, 59(4), pp.1557-1569.
- Song, Y., Palencsár, A., Svenningsen, G., Kvalekvål, J. and Hemmingsen, T., 2012. Effect of O₂ and temperature on sour corrosion. Corrosion, 68(7), pp.662-671.
- Stalheim, D., Boggess, T., San Marchi, C., Jansto, S., Somerday, B., Muralidharan, G. and Sofronis, P., 2010, January. Microstructure and mechanical property performance of commercial grade API pipeline steels in high pressure gaseous hydrogen. In 2010 8th International Pipeline Conference (pp. 529-537). American Society of Mechanical Engineers.
- Stephens, R.I., Benner, P.H., Mauritzson, G. and Tindall, G.W., 1979. Constant and variable amplitude fatigue behavior of eight steels. Journal of Testing and Evaluation, 7(2), pp.68-81.
- Stephens, R.I., Fatemi, A., Stephens, R.R. and Fuchs, H.O., 2000. Metal fatigue in engineering. John Wiley & Sons.
- Sun, J., Jukes, P. and Shi, H., 2012, January. Thermal expansion/global buckling mitigation of HPHT deepwater pipelines, sleeper or buoyancy? In The Twenty-second International Offshore and Polar Engineering Conference. International Society of Offshore and Polar Engineers.
- Suresh, S. and Ritchie, R.O., 1984. Propagation of short fatigue cracks. International Metals Reviews, 29(1), pp.445-475.
- Susmel, L., 2008. The theory of critical distances: a review of its applications in fatigue. Engineering Fracture Mechanics, 75(7), pp.1706-1724.

Tanaka, K., 1983. The cyclic J-integral as a criterion for fatigue crack growth. *International Journal of Fracture*, 22(2), pp.91-104.

Tavares, S.M.O. and De Castro, P.M.S.T., 2017. An overview of fatigue in aircraft structures. *Fatigue & Fracture of Engineering Materials & Structures*, 40(10), pp.1510-1529.

Taylor, D., 1999. Geometrical effects in fatigue: a unifying theoretical model. *International Journal of Fatigue*, 21(5), pp.413-420.

Taylor, D., 2008. The theory of critical distances. *Engineering Fracture Mechanics*, 75(7), pp.1696-1705.

Tetelman, A.S. and McEvily, A.J., 1967. *Fracture of structural materials*. Science & Technology of Materials.

Topper, T., Wetzel, R.M. and Morrow, J., 1967. Neuber's rule applied to fatigue of notched specimens. Illinois University at Urbana Department of Theoretical and Applied Mechanics.

Turnbull, A., 2014. Corrosion pitting and environmentally assisted small crack growth. *Proceedings of the Royal Society A: Mathematical, Physical and Engineering Sciences*, 470(2169), p.20140254.

Van Leeuwen, H.P., 1974. The kinetics of hydrogen embrittlement: a quantitative diffusion model. *Engineering Fracture Mechanics*, 6, pp.141 - 161.

Visser, W., 2002. *POD/POS curves for non-destructive examination*. HSE Books.

Vosikovsky, O., 1975. Fatigue-crack growth in an X-65 line-pipe steel at low cyclic frequencies in aqueous environments. *Journal of Engineering Materials and Technology*, 97(4), pp.298-304.

Vosikovsky, O., 1981. Fatigue crack closure in an X70 steel. *International Journal of Fracture*, 17(3), pp.301-309.

Wang, Y., Gong, J. and Jiang, W., 2013. A quantitative description on fracture toughness of steels in hydrogen gas. *International Journal of Hydrogen Energy*, 38(28), pp.12503-12508.

Wang, Y., Duan, M., Xu, M., Wang, D. and Feng, W., 2012. A mathematical model for subsea wells partition in the layout of cluster manifolds. *Applied Ocean Research*, 36, pp.26-35.

Wells, A., 1961, September. Unstable crack propagation in metals: cleavage and fast fracture. In *Proceedings of the crack propagation symposium (Vol. 1, No. 84)*.

- Weng, L., Zhang, J., Kalnaus, S., Feng, M. and Jiang, Y., 2013. Corrosion fatigue crack growth of AISI 4340 steel. *International Journal of Fatigue*, 48, pp.156-164.
- Westergaard, H.M., 1939. Bearing pressures and cracks. *Journal of Applied Mechanics*, Vol. 6, pp. 49–53.
- Williams, M.L., 1952. Stress singularities resulting from various boundary conditions in angular corners of plates in extension. *Journal of Applied Mechanics*, Vol. 19, pp. 526–528.
- Williams, M.L., 1957. On the stress distribution at the base of a stationary crack. *Journal of Applied Mechanics*, Vol. 24, pp. 109–114.
- Woodtli, J. and Kieselbach, R., 2000. Damage due to hydrogen embrittlement and stress corrosion cracking. *Engineering Failure Analysis*, 7(6), pp.427-450.
- Woollin, P. and Murphy, W., 2001. Hydrogen embrittlement stress corrosion cracking of superduplex stainless steel. *Stainless Steel World*, 13(JUN), pp.48-58.
- Wu, S.C., Xu, Z.W., Yu, C., Kafka, O.L. and Liu, W.K., 2017. A physically short fatigue crack growth approach based on low cycle fatigue properties. *International Journal of Fatigue*, 103, pp.185-195.
- Yao, Y., Fine, M.E. and Keer, L.M., 2007. An energy approach to predict fatigue crack propagation in metals and alloys. *International Journal of Fracture*, 146(3), pp.149-158.
- Ye, D., Matsuoka, S., Suzuki, N. and Maeda, Y., 2004. Further investigation of Neuber's rule and the equivalent strain energy density (ESED) method. *International Journal of Fatigue*, 26(5), pp.447-455.
- Yu, M., Xing, X., Zhang, H., Zhao, J., Eadie, R., Chen, W., Been, J., Van Boven, G. and Kania, R., 2015. Corrosion fatigue crack growth behavior of pipeline steel under underload-type variable amplitude loading schemes. *Acta Materialia*, 96, pp.159-169.
- Zhao, J., Chen, W., Keane, S., Been, J. and Van Boven, G., 2014, December. Development and validation of load-interaction based models for crack growth prediction. In 2014 10th International Pipeline Conference. American Society of Mechanical Engineers Digital Collection.
- Zhu, X.K. and Joyce, J.A., 2012. Review of fracture toughness (G, K, J, CTOD, CTOA) testing and standardization. *Engineering Fracture Mechanics*, 85, pp.1-46.

Yuyama, S. and Kishi, T., 1983. AE analysis during corrosion, stress corrosion cracking and corrosion fatigue processes. *Journal of Acoustic Emission* 2, 71.